On-axis Self-calibration of Angle Measurement Errors in Precision Rotary Encoders

by

Richard J. Graetz

B.A.Sc., University of British Columbia, 2008

A THESIS SUBMITTED IN PARTIAL FULFILLMENT
OF THE REQUIREMENTS FOR THE DEGREE OF

Master of Applied Science

in

THE FACULTY OF GRADUATE STUDIES
(Mechanical Engineering)

The University Of British Columbia
(Vancouver)

February 2011

Abstract

Incremental angle encoders are widely used in industry as a standard sensor to measure rotational axis angular position and velocity. The best commercially available angle encoders have achieved measurement accuracy on the order of 1 arc-sec with proper installation. Higher-accuracy encoders are needed to measure rotational axis angular position and velocity in ultra-precision rotary table based manufacturing and measurement applications. One specific application is to enable the development of maskless lithography technology used for mass manufacture of next generation semiconductors.

In order to achieve accuracy well below 1 arc-sec, repeatable errors in the encoder measurement need to be removed through a calibration process. Numerous high-accuracy encoder calibration techniques have been developed, but the fundamental problem of calibrating angle encoders remains unsolved; their calibration results cannot be directly applied to the manufacturing machine. Existing calibration methods involve calibrating the encoder on a specially designed angle comparator, but the calibrated error is useless after transferring the encoder back to its application axis, due to the sensitivity of encoder error on the installation condition. Other calibration methods capable of calibrating the encoder on its application axis cannot determine all the encoder error harmonics. There still does not exist a calibration method to quickly calibrate an angle encoder on its application axis, providing all encoder error harmonics.

In this thesis the development of a Time-measurement Dynamic Reversal (TDR) encoder calibration technique is presented and its accuracy is validated, through simulation and experiment, and shown to improve encoder accuracy to the thousandth of an arc-sec level. Integration enhancement and rotary vibration removal methods are introduced to improve upon uncertainties caused by limited time measurement resolution and an assumption of free-response dynamics. The accuracy of this method is analyzed in detail, and an accuracy limitation based purely on time measurement resolution and angle measurement repeatability identified. Through experiments performed on a custom-built precision rotary table, experimental accuracy of several thousandths of an arc-sec is validated through uncertainty analysis and spindle radial error motion comparison. A comparison with the the industry standard, the Equal Division Averaged (EDA) calibration method, shows agreement within 0.01 arc-sec for error harmonics not multiple of four. Due to the missing multiple of four harmonics, the EDA method is found to be 0.3 arc-sec less accurate than the TDR method in calibrating this experimental setup.

Table of Contents

Abstract . . . ii

Table of Contents . . . iii

List of Tables . . . vi

List of Figures . . . vii

Glossary . . . xi

List of Acronyms . . . xii

List of Symbols . . . xiii

Acknowledgments . . . xvi

1 Introduction . . . **1**
- 1.1 Next Generation Semiconductor Manufacture . . . 2
- 1.2 Incremental Angle Encoder Limitations . . . 3
- 1.3 Angle Encoder Operation . . . 6
  - 1.3.1 Image Scanning Principle . . . 6
  - 1.3.2 Interferential Scanning Principle . . . 7
  - 1.3.3 Encoder Signal Interpolation . . . 8
- 1.4 Prior Art in Encoder Calibration . . . 9
  - 1.4.1 Angle Comparator Calibration . . . 9
  - 1.4.2 On-axis Self-Calibration . . . 10
- 1.5 Thesis Overview . . . 11

2 Calibration Theory . . . **13**
- 2.1 Time-measurement Dynamic Reversal Calibration . . . 13
  - 2.1.1 TDR Integration Enhancement . . . 18
  - 2.1.2 TDR Rotary Vibration Removal . . . 19
  - 2.1.3 Low-speed Calibration Accuracy Enhancement . . . 22
- 2.2 Spindle Radial Error Motion Extraction . . . 24
- 2.3 Calibration Uncertainty . . . 25
  - 2.3.1 Marking Repeatability . . . 26

2.3.2 Timing Uncertainty . . . 30
2.3.3 Scanning Unit Alignment Uncertainty . . . 32
2.4 Calibration Comparison . . . 34

3 Simulation . . . 37
3.1 Simulation Method . . . 37
3.2 Simulation Parameters . . . 38
3.3 Simulation Results . . . 40
3.3.1 Calibration Inaccuracy . . . 41
3.3.2 Damping Estimation and Error Map Inaccuracy . . . 42
3.3.3 Experimental Calibration Inaccuracy Metrics . . . 45

4 Experimental Setup . . . 50
4.1 Precision Rotary Table . . . 51
4.2 Heidenhain's ERA4282c Incremental Angle Encoder . . . 52
4.2.1 Theoretical Operation and Design . . . 54
4.2.2 High Frequency Encoder Error . . . 56
4.3 Motor Control and Ripple Compensation . . . 59
4.4 Custom Electronics . . . 63
4.4.1 Tsunami Daughter Board Detailed Design . . . 63
4.5 Scanning Unit Alignment . . . 66

5 Experimental Results . . . 69
5.1 Damping Estimation . . . 69
5.2 Calibration Before Rotary Vibration Removal . . . 70
5.3 Rotary Vibration Removal . . . 76
5.3.1 Harmonic Cancellation vs. Prediction . . . 78
5.3.2 Possible Causes of Rotary Vibration . . . 79
5.4 Calibration After Rotary Vibration Removal . . . 83
5.4.1 High Frequency Error Components Analysis . . . 90
5.4.2 Experimental Photocell Spatial Offset . . . 95
5.5 Calibration Performance . . . 96
5.5.1 Inaccuracy from RMS Set Repeatability . . . 96
5.5.2 Inaccuracy from Error Motion Estimation . . . 97
5.5.3 Calibration Comparison . . . 98
5.5.4 Experimental Setup Uncertainty . . . 105
5.6 Analog Encoder Signal Averaging . . . 108
5.7 Calibration Installation Sensitivities . . . 110

6 Conclusion . . . 114
6.1 Future Work . . . 114

Bibliography . . . 116

Appendices . . . .

A Simultaneous Scanning Unit Damping Estimation 119

B Encoder Signal Derivation 120

List of Tables

Table 1.1 ITRS predicted embedded memory requirements near and far-term 2

Table 3.1 Coefficients of the simulated dynamics. 39
Table 3.2 Torque disturbance input harmonics. 40
Table 3.3 Spindle radial error motion input harmonics. 40

Table 4.1 Motor torque constant ripple harmonics. 61

Table 5.1 Error map harmonics peak locations and amplitudes. 89
Table 5.2 Error map harmonic amplitudes for TDR and EDA calibration methods. 102

List of Figures

Figure 1.1	Basic operating principle of rotary angle encoder and its output signals.	3
Figure 1.2	Incremental angle encoder error sources.	4
Figure 1.3	Sensitivity of scanning unit to installation error.	5
Figure 1.4	Incremental angle encoder measurement error due to installation eccentricity.	5
Figure 1.5	Image scanning principle for incremental angle encoders.	6
Figure 1.6	Interferential scanning principle for incremental angle encoders.	7
Figure 1.7	Spatial interval markings with no interpolation.	8
Figure 1.8	Spatial interval markings with two times interpolation.	8
Figure 1.9	Spatial interval markings with quadrature decoding interpolation.	9
Figure 1.10	PTB's Angle Comparator.	10
Figure 2.1	Rotary encoder spatial and temporal sampling events.	13
Figure 2.2	Ideal vs. realistic spatial sampling events.	14
Figure 2.3	Sampled data sets used to perform dynamic reversal in the self-calibration method.	17
Figure 2.4	The 4-head setup used in removing rotary vibration component from calibration results.	20
Figure 2.5	Spindle speed between count intervals.	23
Figure 2.6	Iterative procedure for accuracy enhanced calibration.	24
Figure 2.7	Spatial sampling event uncertainty.	26
Figure 2.8	Linear manufacturing tolerance for writing on a rotary table.	27
Figure 2.9	Predicted linear uncertainty for encoders without signal processing.	28
Figure 2.10	Predicted angular uncertainty for encoders without signal processing.	29
Figure 2.11	Predicted linear uncertainty for encoders with aggressive signal processing.	29
Figure 2.12	Time measurement uncertainty.	30
Figure 2.13	Predicted angular uncertainty in spatial sampling events due to finite time resolution.	31
Figure 2.14	Predicted linear uncertainty in spatial sampling events due to finite time resolution.	31
Figure 2.15	Relative alignment of each scanning unit.	32
Figure 2.16	Inaccuracy of rotary vibration removal and calibration due to misalignment.	33
Figure 2.17	Inaccuracy of rotary vibration removal over a range of scanning unit misalignments.	34
Figure 2.18	Cumulative angle measurement errors.	35
Figure 2.19	Angle measurement differences relative to scanning unit H1.	35
Figure 3.1	Simulation block diagram	38
Figure 3.2	Graduation error input of simulation.	39
Figure 3.3	Torque disturbance input of simulation.	39

Figure 3.4 Spindle radial error motion input of simulation. 40
Figure 3.5 Simulated calibration inaccuracy curves at 500 rpm. 41
Figure 3.6 Simulated calibration inaccuracy over range from 1,000rpm down to 100 rpm. 42
Figure 3.7 First-order damping coefficient simulation results. 43
Figure 3.8 Second-order damping coefficient simulation results. 43
Figure 3.9 Simulated calibration inaccuracy at 500 rpm, considering perfect damping estimation. . 44
Figure 3.10 Perfect damping calibration simulation over range from 1,000 rpm down to 100 rpm. . . 44
Figure 3.11 Simulated calibration set repeatability at 500 rpm. 45
Figure 3.12 Simulated calibration rms set repeatability over range from 1,000 rpm down to 100 rpm. 46
Figure 3.13 Simulated error motion extracted from calibration results for -1 component. 47
Figure 3.14 Simulated error motion extracted from calibration results for +3 component. 47
Figure 3.15 Simulated error motion extracted from calibration results for -5 component. 48
Figure 3.16 Simulated spindle error motion estimation inaccuracy for a range of speeds. 48
Figure 3.17 Comparison of error map inaccuracy to error motion inaccuracy 49

Figure 4.1 Flow of data int the experimental setup. block diagram. 50
Figure 4.2 Encoder calibration experimental setup designed by Darya Amin-Shahidi. 51
Figure 4.3 Heidenhain's calibrated error map for the ERA4282c angle encoder. 52
Figure 4.4 Single field imaging scanning principle of Heidenhain's ERA4282c angle encoder. . . . 52
Figure 4.5 Inside the ERA4282c scanning unit. 53
Figure 4.6 Photovoltaic cell array structure of the ERA4282c encoder. 53
Figure 4.7 Differential combination of photovoltaic cell signals. 53
Figure 4.8 Encoder operation coordinate definition. 54
Figure 4.9 Ideal sinusoidal encoder signals with relative 90° phase-shift and no signal unbalance. . 56
Figure 4.10 Unbalance of sinusoidal encoder signal phase A as cause of high frequency encoder error. 57
Figure 4.11 Phase misalignment of sinusoidal encoder signals causing encoder error. 58
Figure 4.12 ThinGAP TG8263 DC brushless motor installed on the air bearing spindle. 59
Figure 4.13 Slanted profile of the motor coils, designed to reduce motor torque ripple. 60
Figure 4.14 Three phase coil configuration cancels harmonic in the magnetic field. 60
Figure 4.15 Experimentally measured motor torque constant. 61
Figure 4.16 Spindle velocity control system. 61
Figure 4.17 Position ripple for constant constant velocity control dominated by commutation error. . 62
Figure 4.18 Position ripple for constant constant velocity control. 62
Figure 4.19 Tsunami, multi-rate multiprocessor control platform developed by Kris Smeds. 63
Figure 4.20 Three generations of the NanoRAD daughter board. 64
Figure 4.21 Analog encoder signal processing on the NanoRAD daughter board. 64
Figure 4.22 PCB design of NanoRAD. 66
Figure 4.23 Relative alignment of each scanning unit to be evenly spaced around the circular scale. . 67
Figure 4.24 Normalized cross-correlation of spatial intervals. 68
Figure 4.25 Normalized cross-correlation of angle measurement error. 68

Figure 5.1 Experimentally measured spindle free response. 69

Figure 5.2 Experimental constant normalized damping coefficient. 70
Figure 5.3 Experimental spindle speed dependent normalized damping coefficient. 70
Figure 5.4 Calibrated error maps with rotary vibration, at 200 rpm. 71
Figure 5.5 Calibrated error maps with rotary vibration, showing only the first 500 cpr harmonics. . 71
Figure 5.6 Calibrated error maps for H1, at spindle rotation speeds between 300 rpm and 200 rpm. . 72
Figure 5.7 Calibrated error maps for H2, at spindle rotation speeds between 300 rpm and 200 rpm. . 72
Figure 5.8 Calibrated error maps for H4, at spindle rotation speeds between 300 rpm and 200 rpm. . 73
Figure 5.9 Calibrated error maps for H3, at spindle rotation speeds between 300 rpm and 200 rpm. . 73
Figure 5.10 Amplitude and phase for calibrated error maps of scanning unit H1. 74
Figure 5.11 Amplitude and phase for calibrated error maps of scanning unit H2. 74
Figure 5.12 Amplitude and phase for calibrated error maps of scanning unit H3. 75
Figure 5.13 Amplitude and phase for calibrated error maps of scanning unit H4. 75
Figure 5.14 Rotary vibration amplitude spectrum for the first six harmonics. 76
Figure 5.15 Rotary vibration component removed from calibration results. 77
Figure 5.16 Estimated speed independent, rotary position dependent disturbance torque. 77
Figure 5.17 Comparison of the first harmonic of rotary vibration extracted. 78
Figure 5.18 Comparison of the second harmonic of rotary vibration extracted. 79
Figure 5.19 Comparison of the third harmonic of rotary vibration extracted. 79
Figure 5.20 Experimental setup with air bearing rotor and stator highlighted. 80
Figure 5.21 Out of parallel deformation of spindle rotor causing 1cpr rotary vibration harmonic. . . . 80
Figure 5.22 Elliptic deformation of spindle rotor causing 2cpr rotary vibration harmonic. 81
Figure 5.23 Experimental setup for measuring stator expansion. 81
Figure 5.24 Experimentally measured stator expansion. 82
Figure 5.25 Calibrated error maps without rotary vibration. 83
Figure 5.26 Calibrated error maps for H1, at spindle rotation speeds between 300 rpm and 200 rpm. . 84
Figure 5.27 Calibrated error maps for H2, at spindle rotation speeds between 300 rpm and 200 rpm. . 84
Figure 5.28 Calibrated error maps for H3, at spindle rotation speeds between 300 rpm and 200 rpm. . 85
Figure 5.29 Calibrated error maps for H4, at spindle rotation speeds between 300 rpm and 200 rpm. . 85
Figure 5.30 Calibrated error maps for H1, at spindle rotation speeds between 300 rpm and 200 rpm. . 86
Figure 5.31 Calibrated error maps for H2, at spindle rotation speeds between 300 rpm and 200 rpm. . 86
Figure 5.32 Calibrated error maps for H3, at spindle rotation speeds between 300 rpm and 200 rpm. . 87
Figure 5.33 Calibrated error maps for H4, at spindle rotation speeds between 300 rpm and 200 rpm. . 87
Figure 5.34 Fourier amplitude spectrum of calibrated encoder error map H1 without rotary vibration. 88
Figure 5.35 Comparison of the Fourier amplitude spectrum of calibrated encoder error maps. 89
Figure 5.36 Typical calibrated encoder error map with rotary vibration removal, at 200 rpm. 90
Figure 5.37 Deviations of each spatial interval from the nominal spacing on scanning unit H1. 90
Figure 5.38 Offset between odd and even count deviations. 91
Figure 5.39 Comparison of error map with and without high frequency phase misalignment error. . . 92
Figure 5.40 Count deviations of encoder signal phase A. Rising to falling edge of encoder signal A. . 92
Figure 5.41 Count deviations of encoder signal phase B. Rising to falling edge of encoder signal B. . 93
Figure 5.42 between odd and even count deviations of encoder signal A, showing phase unbalance. . 93

Figure 5.43 between odd and even count deviations of encoder signal B, showing phase unbalance. . 94
Figure 5.44 Comparison of error map without phase misalignment and signal unbalance. 95
Figure 5.45 Difference of count deviations between encoder signal phase A and phase B. 95
Figure 5.46 RMS set repeatability improvements due to developments in the experimental setup . . . 96
Figure 5.47 RMS set repeatability in the final experimental setup. 97
Figure 5.48 Experimental spindle radial error motion measurement. 98
Figure 5.49 Error motion estimation without simultaneous encoder measurements. 98
Figure 5.50 TDR and EDA calibration results at 200 rpm showing first 500 cpr harmonics. 99
Figure 5.51 TDR and EDA calibration difference at 200 rpm showing first 500 cpr harmonics. 99
Figure 5.52 TDR and EDA calibration results at 200 rpm. 100
Figure 5.53 TDR and EDA calibration difference at 200 rpm. 100
Figure 5.54 Low frequency error map harmonic amplitudes for TDR and EDA calibration methods. . 101
Figure 5.55 High frequency error map harmonic amplitudes for TDR and EDA calibration methods. 101
Figure 5.56 First encoder error harmonic for scanning unit H1 from TDR and EDA methods. 102
Figure 5.57 First encoder error harmonic for scanning unit H2 from TDR and EDA methods. 103
Figure 5.58 First encoder error harmonic for scanning unit H3 from TDR and EDA methods. 104
Figure 5.59 First encoder error harmonic for scanning unit H4 from TDR and EDA methods. 104
Figure 5.60 Calibrated error maps from uncertainty experiment. 105
Figure 5.61 Calibrated error maps, with the first 500 cpr harmonics, from uncertainty experiment. . . 106
Figure 5.62 Sequential experiment error map differences from mean. 107
Figure 5.63 Sequential experiment error map differences from mean, with only first 500cpr harmonics.107
Figure 5.64 Averaging multiple scanning unit signals to improve calibration repeatability. 108
Figure 5.65 Two analog scanning signal average error map. 109
Figure 5.66 Four analog scanning signal average error map. 109
Figure 5.67 RMS set repeatability of calibration results with analog encoder signal averaging. 110
Figure 5.68 Initial installation of the circular scale on the spindle rotor with support shims. 111
Figure 5.69 Error map from encoder mounted on uneven mating surface. 111
Figure 5.70 Error map dependency on bolt torque. 112
Figure 5.71 Calibration result with large 1cpr harmonic due to 5μm installation eccentricity. 112
Figure 5.72 Error map dependency on clean circular scale. 113

Glossary

arc-sec A unit of angular measurement. 3600 arc-sec is equal to 1 degree.

encoder Incremental rotary angle encoder. Consists of two pieces of equipment: (a) the circular scale, written with periodic physical markings, is mounted on the rotor of the spindle while (b) the scanning unit, with electronics to image the physical markings, is mounted on the stator of the spindle.

error map Incremental angle encoder error map defines the cumulative measurement error using an angle encoder. The calibrated error map is used to compensate the raw measurements on the angle encoder to improve measurement accuracy.

List of Acronyms

ADC	Analog to Digital Converter.
CPR	cycles per revolution.
DAC	Digital to Analog Converter.
DRAM	Dynamic Random Access Memory.
DSP	Digital Signal Processor.
e-beam	electron beam.
EDA	Equal Division Averaged method.
EMF	Electromotive Force.
EMI	electromagnetic interference.
EUV	Extreme Ultraviolet.
HDD	Hard Disk Drive.
IC	Integrated Circuit.
ITRS	International Technology Roadmap for Semiconductors.
MFB	multiple feedback.
ML	maskless.
NMIJ	National Metrology of Japan.
PCB	printed circuit board.
PTB	Physikalisch-Technische Bundesanstalt.
SNR	signal to noise ratio.
TDR	Time-measurement Dynamic Reversal.

List of Symbols

a	First-order damping coefficient estimated with the TDR calibration method.
a_1	First-order damping coefficient of first revolution estimated with the TDR calibration method.
a_2	First-order damping coefficient of second revolution estimated with the TDR calibration method.
A_n	Predicted complex rotary vibration coefficient at spindle rotation speed n.
B	Spindle air bearing damping coefficient.
b	Second-order damping coefficient estimated with the TDR calibration method.
b_1	Second-order damping coefficient of first revolution estimated with the TDR calibration method.
b_2	Second-order damping coefficient of second revolution estimated with the TDR calibration method.
c	Normalized damping coefficient, ratio of damping coefficient to rotational inertia.
c_0	First-order damping coefficient, constant with spindle speed.
c_1	Second-order damping coefficient, dependent on spindle speed.
D	Diameter of the circular scale.
Δ	[Nx1] vector of spatial intervals.
$d_{i,j}$	[Nx1] vector of angle measurement differences of j-th scanning unit to the i-th scanning unit.
$d\theta$	Measured spindle rotation from encoder signal variation.
dV	Variation of analog encoder voltage signal or voltage noise, independent of spindle rotation.
dx	Linear manufacturing tolerance, from angle measurement uncertainty.
e	Circular scale mounting eccentricity.
f_c	Time measurement clocking frequency.
f_s	Spatial frequency of grating lines on the circular scale.
f_w	Spatial frequency of lines on the window grating.
G	Active filter gain.
$g(k)$	Grating error component of angular measurement error at the k-th spatial sampling event.
$G(n)$	n-th Fourier coefficient of grating error component of the angular measurement error.
i	Imaginary unit.

$int(\ldots)$	Cumulative summation without mean value operation.
J	Spindle rotor rotational inertia.
$\mathbf{k}$	[Nx1] vector of counts over one spindle revolution (1 to N).
L_s	Variable describing regions on the circular scale of an angle encoder where is reflected or absorbed.
L_w	Variable describing regions on the grating window of an angle encoder where light passes through or is blocked.
M	Amplitude of analog encoder voltage signal.
$\mathbf{m}$	[Nx1] scaled vector of time measurement intervals over one spindle revolution.
M_0	Amplitude of analog encoder voltage signal without signal filtering.
$M(s)$	Position dependent, spindle speed independent disturbance torque.
N	Number of spatial sampling events around the circular scale of the incremental rotary angle encoder.
ω	Rotational axis speed [rpm].
n_{min}	minimum e-beam spindle writing speed.
$\mathbf{p}$	[Nx1] vector of angular measurement errors at each spatial sampling event.
$\overline{\mathbf{p}}$	[Nx1] vector of estimated angular measurement errors at each spatial sampling event.
ϕ_j	Misalignment of j-th scanning unit to scanning unit H1.
$p(k)$	Angular measurement error at the k-th spatial sampling event.
$p_{Hj}(k)$	Derived angular measurement error of the j-th scanning unit at the k-th spatial sampling event.
$p_{Hj}(k,\omega)$	Derived angular measurement error of the j-th scanning unit at the k-th spatial sampling event and spindle rotation speed ω.
$P_{Hj}(n)$	n-th Fourier coefficient of derived angular measurement error of the j-th scanning unit.
$P_{Hj}(n,\omega)$	n-th Fourier coefficient of derived angular measurement error of the j-th scanning unit at spindle rotation speed ω.
$q_{Hj}(k)$	Calibrated angular measurement error of the j-th scanning unit at the k-th spatial sampling event compensated for rotary vibration.
$\overline{q}_{Hj}(k)$	EDA calibration method, partial angular measurement error of the j-th scanning unit at the k-th spatial sampling event.
$Q_{Hj}(n)$	n-th Fourier coefficient of calibrated angular measurement error of the j-th scanning unit compensated for rotary vibration.
$\overline{Q}_{Hj}(n)$	EDA calibration method, n-th Fourier coefficient of partial angular measurement error of the j-th scanning unit.
R	Radius of the circular scale.
R_i	inner e-beam writing radius.
$r(k)$	Spindle radial error motion component (arbitrary direction) of angular measurement error at the k-th spatial sampling event.
R_w	e-beam writing radius.
S	Spatial interval offset defining the start of a revolution of data.
s	Laplace operator, representing complex frequency components.

SNR_0	signal to noise ratio measured on the analog encoder signals.
$\mathbf{T}$	[Nx1] vector of time measurement intervals over one spindle revolution.
θ	Rotational axis angular position.
T_k	Time measurement interval of k-th spatial sampling interval. Time measurement between when the previous sampling event and the k-th event are detected.
$\widehat{T}_k$	Actual time interval between spatial events.
$t_{k,Hj}$	Time measurements when k-th spatial event is detected on the j-th scanning unit.
T_p	Period of the photocell pattern inside the scanning unit.
T_s	Period of grating lines on the circular scale.
T_w	Period of lines on the window grating.
$\mathbf{U}$	[Nx1] vector of scaled first-order time measurement intervals and counts over one spindle revolution.
V	Analog encoder voltage signal.
$v(k)$	Rotary vibration error component of the calibrated angular measurement error at the k-th spatial sampling event.
$v(k,\omega)$	Speed dependent rotary vibration error component of the calibrated angular measurement error at the k-th spatial sampling event.
$V(n)$	n-th Fourier coefficient of rotary vibration error component of the calibrated angular measurement error.
$v(s)$	Measured spindle rotary vibration, complex frequency domain.
$\mathbf{V}$	[Nx1] vector of second-order scaled time measurement intervals and counts over one spindle revolution.
$x(k)$	Spindle radial error motion component (along the x-direction) of angular measurement error at the k-th spatial sampling event.
$X(n)$	n-th Fourier coefficient of spindle radial error motion component (along the x-direction) of the angular measurement error.
$y(k)$	Spindle radial error motion component (along the y-direction) of angular measurement error at the k-th spatial sampling event.
$Y(n)$	n-th Fourier coefficient of spindle radial error motion component (along the y-direction) of the angular measurement error.
Δ_0	Nominal angular spacing of spatial events measured on the angular encoder.
Δ_k	Actual angular spacing of the k-th spatial event measured on the angular encoder.
$\widehat{\Delta}_k$	Angular spacing of the k-th spatial event without measurement error.
ω	Rotational axis speed [rad/sec].
ω_0	Rotational axis speed at the start of a spindle revolution [rad/sec].
ω_k	Instantaneous rotational axis speed [rad/sec].
θ_0	Rotational axis angular position at the start of a spindle revolution.
θ_e	Rotational axis angular position measurement error due to imperfect installation resulting in circular scale mounting eccentricity.
θ_k	Discrete rotational axis angular position measured with incremental angle encoder, by counting the spatial events passing the scanning unit.

Acknowledgments

I would like to thank my thesis supervisor, Dr. Xiaodong Lu, for the opportunity to study at the University of British Columbia in pursuit of my Master degree. He has given me a solid introduction into the field of Precision Engineering and has been instrumental in the success of this research. His work ethic and passion for engineering are an inspiration.

I am thankful to Professor Yusuf Altintas and Dr. Hsi-Yung Feng for being in my examination committee. Professor Altintas has been present since the beginning of my university career and I have a lot, thanks to him, in the Mechatronics program.

A special thanks to my fellow lab mates for their friendship and contributions over the past two years. Darya Amin-Shahidi designed and manufactured the Precision Rotary Table; both mechanical and electrical systems. Without his contribution this research would remain untested on precision metrology axes. Kris Smeds has made significant contributions to the software design of the experimental setup and more recently developed the multi-rate multiprocessor control platform necessary for accurate measurements. With his help the most accurate results of this research have been obtained. Arash Jamalian's research on spindle radial error motion provided a means to validate the accuracy of our results. In addition, his help in maintaining and modifying the experimental setup was invaluable. Additional thanks to Irfan-ur-rab Usman, Niankun Rao, Mathew Paone and others for their feedback and helpful advice.

It was a privilege to work closely with KLA-Tencor and the REBL team of Marek Zynwo, Upendra Ummethala, Joshua Clyne, and Tao Zhang in the beginning of this research. Their support and external analysis allowed very quick progress in my research and developed my professionalism. Most importantly their project gave the research a direct practical application.

I am very fortunate to have a great family and many loyal friends, who continue to supported me in every way. My family is the reason I have gotten to where I am today and I appreciate their enormous sacrifices. I have fond memories of shared time with friends in Vancouver. I will miss you all dearly as I start a new life in California.

This research has been sponsored by KLA-Tencor and Canada Foundation for Innovation.

To my grand dads

Chapter 1

Introduction

Incremental angle encoders are widely used in industry as a standard sensor to measure rotational axis angular position and velocity. The best commercially available angle encoders have achieved measurement accuracy on the order of 1 arc-sec (3,600 arc-sec is equal to 1 degree) with proper installation [1–4]. Higher-accuracy encoders are needed to measure rotational axis angular position and velocity in ultra-precision manufacturing and measurement applications, such as optical disk mastering, maskless nanolithography [5] or trajectory generation for fast tool servos [6]. Specifically, higher rotational accuracy is necessary to enable the development of maskless rotary lithography technology used for next generation semiconductor manufacture.

In order to achieve accuracy well below 1 arc-sec, repeatable errors in the encoder measurement need to be removed through a calibration process. Numerous high-accuracy encoder calibration techniques have been developed over the last few decades [7–13]. Although these methods have demonstrated repeatability of a few thousandths of an arc-sec, their calibration results cannot be directly applied to the manufacturing machine due to missing error components. Existing calibration methods involve calibrating the encoder on a specially designed angle comparator, but the calibrated error is useless after transferring the encoder back to its application axis, due to the sensitivity of encoder error on the installation condition. Other calibration methods capable of calibrating the encoder on its application axis cannot determine all the encoder error harmonics. There still does not exist a calibration method to quickly calibrate an angle encoder on its application axis, providing all encoder error harmonics.

In this thesis the development of a Time-measurement Dynamic Reversal (TDR) encoder calibration technique is presented and its accuracy is validated through simulation and experiment, and shown to improve encoder accuracy to the thousandth of an arc-sec level. The theoretical accuracy of this method is analyzed in simulation, and an accuracy limitation based purely on time measurement resolution is identified. Through experiments performed on a custom-built precision rotary table [14], experimental accuracy of a few thousandths of an arc-sec is validated through uncertainty analysis and spindle radial error motion comparison.

The application of this research in the semiconductor industry is discussed next.

1.1 Next Generation Semiconductor Manufacture

The semiconductor industry is distinguished from other industries by its rapid pace of improvements in its products. Improvements in cost, speed, power consumption, compactness and functionality result principally from the exponential decrease in minimum feature sizes used to fabricated circuits. The most significant trend is decreasing cost, which has led to significant improvement in quality of life through proliferation of computers, communication, and other industrial and consumer electronics.

In 1965 Gordon E. Moore first described a trend in the industry that the number of components in integrated circuits doubles every two years [15]. The trend has been accurate for more than four decades and has become a self-fulfilling prophecy as research and development efforts are set to meet the trend. The International Technology Roadmap for Semiconductors (ITRS) is an association, consisting of industry experts from Europe, Japan, Korea, Taiwan and the U.S.A, which helps the advancement of the semiconductor industry by directing the efforts of industry research and development. The ITRS publishes a Roadmap each year which defines what technical capabilities the industry needs to develop and by when, in order to keep up with Moore's Law and the other trends. Dynamic Random Access Memory (DRAM) half-pitch is a historical indicator of Integrated Circuit (IC) scaling and the ITRS predicts the following reduction in feature size in their Roadmap in the near and far term (Table 1.1). To meet this reduction in feature size the ITRS

Table 1.1: ITRS predicted embedded memory requirements near and far-term [16].

Year of Production	*2007*	*2008*	*2009*	*2010*	*2011*	*2012*	*2013*	*2014*	*2015*
DRAM Half-pitch (nm)	65	55	52	45	40	36	32	28	25
Year of Production	*2016*	*2017*	*2018*	*2019*	*2020*	*2021*	*2022*	*2023*	*2024*
DRAM Half-pitch (nm)	22.5	20	17.9	15.9	14.2	12.6	11.3	10	8.9

have highlighted several feasible solutions. The move from 65 nm to 45 nm half-pitch has been possible with the development of Immersion Optical Lithography at 193 nm wavelength. Unfortunately the Optical Lithography process is limited in feature size by the wavelength of the light source and no proven optical solutions are available past 22 nm half-pitch. Extreme Ultraviolet (EUV), maskless (ML), and imprint lithography are potential successors to optical-lithography. EUV lithography is considered by the ITRS as the most probable solution for 22 nm and 16 nm half-pitch but breakthroughs in ML lithography that allow throughput increases could bring a paradigm shift [17].

KLA-Tencor, a leader in development of semiconductor manufacturing and inspection equipment, is developing a ML electron beam (e-beam) lithography technique which can significantly increase the throughput of the ML methods and lead to this paradigm shift. Existing e-beam lithography technology already exists, but is considered not suitable for high-volume manufacturing because of its limited throughput. A main limit in throughput of e-beam lithography is due to the smaller field for e-beam writing, less than $1mm^2$ compared to optical lithography which can write fields greater than $40mm^2$. Massive parallel e-beam writing schemes are being developed [18–20], but the writing field is still small enough that raster scanning is necessary to pattern a large area. This adds complications to the metrology system where two degrees of freedom are required where before only a single degree of freedom motion was needed. A feasible solution, being developed by KLA-Tencor, is a rotary version of the e-beam lithography machine where a rotary and linear stage provide both degrees of motion, similar to the operation of a Hard Disk Drive (HDD).

A key component to this design is an angular encoder with accuracy of a few thousandths of an arc-sec at speeds up to 600 rpm. To meet the needs of next generation semiconductor manufacture this machine is aimed to produce DRAM half-pitch of 10 nm. The angular encoder will require angular accuracy of 2 thousandths of an arc-sec (for 0.5 m writing radius) at 180 rpm, to meet linear manufacturing tolerances of 5 nm. Currently, there are no rotation measurement solutions which have approached such high accuracy requirements at such high speeds.

The accuracy of angle encoders is limited due to measurement errors of the standard rotation measurement sensor, the incremental angle encoder. Both repeatable and non-repeatable measurement errors exists, but the repeatable error components are dominant. The objective of this research is to accurately calibrate the repeatable errors of any incremental angle encoder, use them to compensate the angle measurement and improve the accuracy of the angle measurement needed for precision manufacturing or measurement applications.

The next section describes incremental angle encoder operation and the repeatable errors in angle measurement.

1.2 Incremental Angle Encoder Limitations

An incremental angle encoder is composed of two pieces of equipment: (a) the circular scale, written with periodic physical markings, is mounted on the rotor of the spindle while (b) the scanning unit, with electronics to image the physical markings, is mounted on the stator of the spindle. When the circular scale is moved past the scanning unit, the encoder provides two sinusoidal signals, phase-shifted by 90°, and an index signal marking the absolute rotary position shown in Figure 1.1. The physical creation of these signals

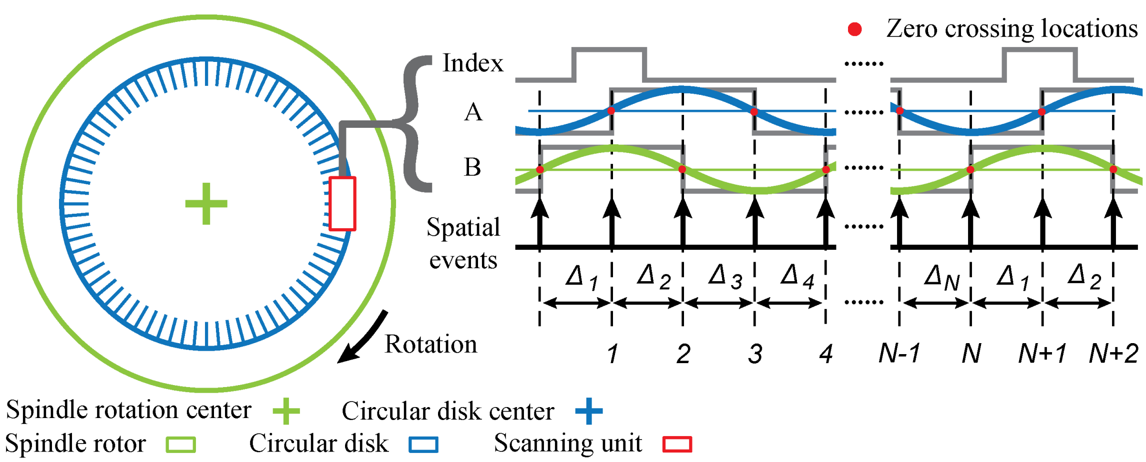

Figure 1.1: Basic operating principle of rotary angle encoder and its output signals.

is discussed later in Section 1.3 and Section 4.2. The most basic form of interpolation, quadrature decoding, marks the zero-crossings of each encoder signal as spatial sampling events. Higher interpolation electronics can be used but are not considered because of increased uncertainty due to encoder signal harmonic distortion. Ideally, spatial sampling events are evenly spaced around the circular scale with nominal spacing of, $\Delta_0 = 1/N$ revolution, where N is the number of spatial events in one revolution. The rotational angle is easily found by counting the number of spatial events read by the scanning unit, $\theta_k = k\Delta_0$.

This is the case for an ideal rotary metrology system, where the encoder's circular scale is mounted on the spindle rotor so that the geometric center of the scale aligns with the spindle rotation axis, the spindle does not exhibit any radial error motion and the periodic physical markings on the circular scale are evenly spaced apart (Figure 1.2a). Each spatial event, read by the scanning unit, is then treated as an increment in rotational angular position of the spindle. This ideal situation has no angle encoder error, but is not realistic

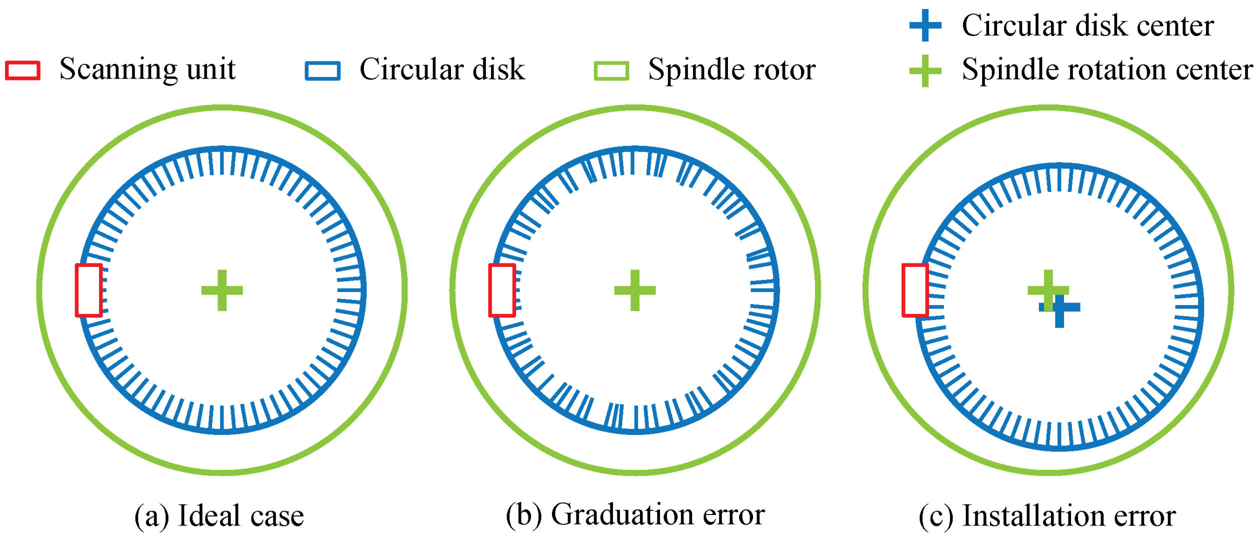

Figure 1.2: Incremental angle encoder error sources.

for a real world installation. The circular scale will always be mounted with some eccentricity on the spindle rotor, all realistic spindles have error motion and practical manufacturing and operation limitations of the angle encoder cannot guarantee even spacing of the physical markings.

In reality the physical markings on the circular scale are not evenly spaced apart. Due to manufacturing limitations, successive markings could be closer together or farther apart than the assumed average (Figure 1.2b), leading to repeatable errors in the rotational angular position measured. This component is not restricted to the physical error in the placement of lines on the circular scale but is also related to the imaging of the lines by the scanning unit. This component can experimentally contribute as much as 0.6 arc-sec error.

Imperfect installation of the circular scale on the rotor of the spindle leads to repeatable measurement errors. Installation can be affected by the installation offset or mounting eccentricity of the circular scale where the geometric center of the circular scale is not concentric with the rotation axis of the spindle rotor (Figure 1.2c). This offset is read by the scanning unit as an equivalent rotation of the spindle. The scanning unit is most sensitive to this error when the installation offset is parallel to the scanning direction (Figure 1.3a), and insensitive to motion that moves the circular scale closer or further away from the unit (Figure 1.3b). Installation encoder error is synchronous to spindle rotation and has been seen to dominate over the other errors in the system. The amount of installation error, $\theta_e = \theta - \theta_k$, for a given spindle rotation angle θ is illustrated in Figure 1.4 and is found as

$$\theta_e = \frac{e \sin\theta}{\frac{1}{2}D} \tag{1.1}$$

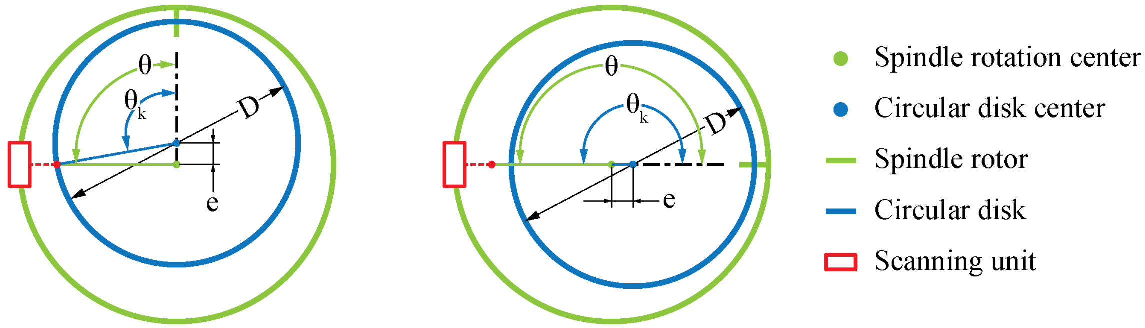

(a) Worst case installation error
θ = 90°

(b) Best case installation error
θ = 180°

Figure 1.3: Sensitivity of scanning unit to installation error.

where θ_e is given in radians, e is the installation eccentricity and D is the diameter of the circular scale. Even with very precise mounting alignment, resulting in $0.5\mu m$ installation offset, the installation error will contribute 1 arc-sec of measurement error with a typical encoder circular scale diameter of 200 mm. Installation error can also be affected by deformation of the circular scale, when rigidly attaching the circular scale to the spindle rotor. Deformation of the circular scale would in turn cause deformation of the physical markings, increasing any uneven spacing of the markings. Flatness of mating surfaces and torque of mounting bolts are important factors to reduce the deformation of the circular scale and its contribution to angle encoder error.

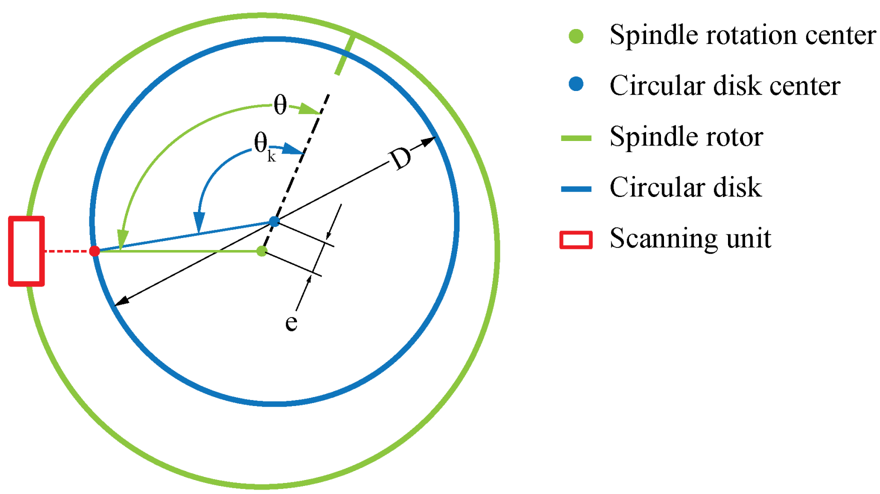

Figure 1.4: Incremental angle encoder measurement error due to installation eccentricity.

The last repeatable error source is due to spindle radial error motion. The spindle axis does not rotate perfectly and during rotation the axis will move radially, due to interaction between spindle rotor and stator. This radial motion component in the encoder scanning direction will be seen from the scanning unit as equivalent rotation, similar to the effect of installation error. Precision spindles typically exhibit radial error motion on the order of a few dozens of nano-meters therefore this error source does not dominate, but can contribute on the order of a hundredth of a arc-sec to encoder error.

The measurement error on an encoder is not a property of the encoder itself but is a combination of the encoder and the rotational axis it is installed on. Graduation, installation and spindle motion error exist in all incremental angle encoder systems and limit the angle measurement accuracy that can be achieved by state of the art angle encoders to ± 1 arc-sec. However the grating error component is solely a property of the angle encoder. The specific design and operating principle of the encoder can make this component a dominant factor in measurement accuracy.

The following section introduces common operating principle of angle encoders, to form a better understanding of encoder operation and the angle measurement errors.

1.3 Angle Encoder Operation

The operating principle of an angle encoder describes how the physical lines on the circular scale are imaged and ultimately converted to electrical signals that are then interpreted by electronics to determine rotation angle. Two common operating principles of incremental angle encoders exist: The image scanning principle and the interferential scanning principle.

1.3.1 Image Scanning Principle

The most common operating principle of angle encoders is the image scanning principle and is generally used for encoders with grating scale periods of more than $10\mu m$. A simplified schematic of the operation is shown in Figure 1.5. Inside the scanning unit, infrared light is collimated and then passes out of the scanning

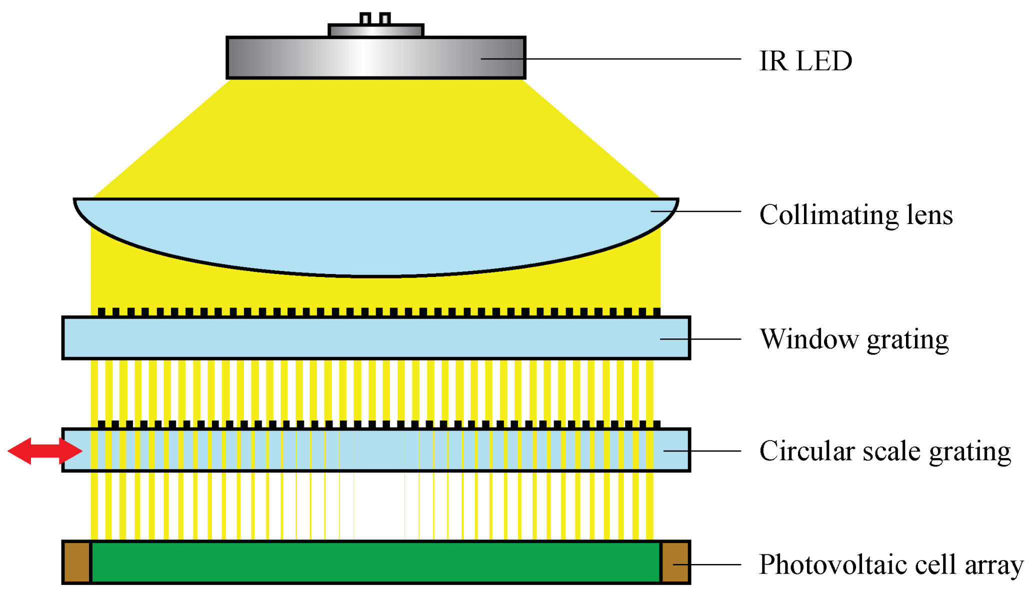

Figure 1.5: Image scanning principle for incremental angle encoders. Note that the window grating and the circular scale grating have different pitches.

unit through a window grating. This window grating modulates the light to the period of the grating on the window. This period slightly differs from the period of the circular scale grating and when the light hits the circular scale an optical beat is created due to the differing grating periods. The light reflects off the circular scale and back into the scanning unit where a photovoltaic cell transforms the detected light into electrical signals. Relative motion of the circular scale to the scanning unit causes a change in the light intensity that falls on the photovoltaic cell, creating a nearly sinusoidal output signal. The output signal changes one period from the relative motion of one grating period.

Heidenhain [2, 3] and Renishaw [4] produce a selection of precision angle encoders, some of which operate on the image scanning principle. The ERA4282c incremental angle encoder, commercially produced by Heidenhain GmbH, is used in this thesis to experimentally validate angle encoder calibration techniques and operates on the image scanning principle described in further detail in Section 4.2.

1.3.2 Interferential Scanning Principle

The interferential scanning principle is relatively less common operating principle among angle encoders, reserved for encoders that require very fine resolution and high accuracy, featuring circular scale graduations of $10\mu m$ or less.

The interferential scanning principle, rather than relying on interfering opaque patterns, relies on diffraction and interference of light waves as shown in Figure 1.6. Similar to the image scanning principle, light is first collimated and passes out of the scanning unit through a window grating. The window grating is patterned with a transparent grating of periodic steps. The light waves passing through the window are diffracted and concentrate into beams of the orders -1, 0 and +1. The circular grating is similarly patterned as the window grating but with reflective lines making up the stepped profile, with identical period as the window grating. The beams fall onto the circular scale and are again diffracted with most of the light inten-

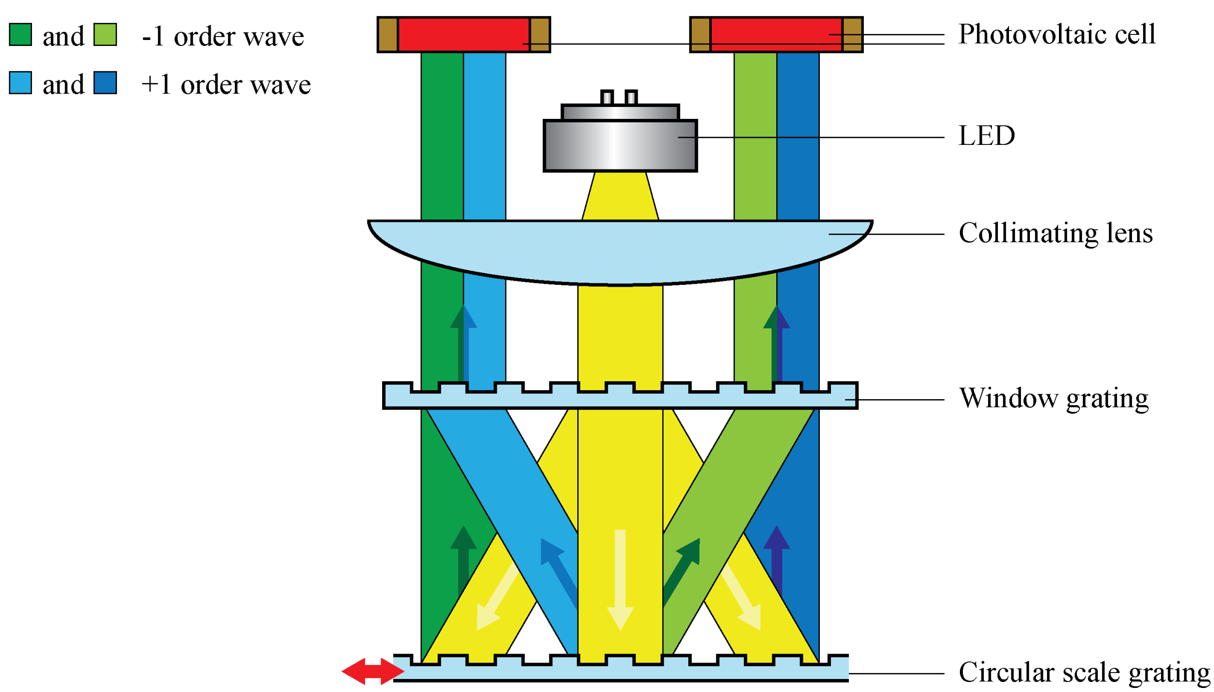

Figure 1.6: Interferential scanning principle for incremental angle encoders. Adapted from [3].

sity being in the -1 and +1 orders. Each light beam reflected back into the scanning unit, through the window grating are diffracted one last time and finally fall on photovoltaic cells inside the scanning unit that convert the alternating light intensity into electrical signals. Motion of the circular scale relative to the scanning unit cause the diffracted waves to shift in phase. The wave front of the +1 and -1 order are affected in opposite directions. Motion of one grating period causes phase shift of one wavelength in the positive direction for the +1 order beam and one wavelength in the negative direction for the -1 order beam. Due to interference of the beams, the waves are shifted relative to each other by two wavelengths thus the output signal changes two periods from relative motion of one grating period.

Heidenhain [2, 3] and Canon [1] produce a selection of precision angle encoders, some of which operate on the interferential scanning principle.

1.3.3 Encoder Signal Interpolation

The two operating principles discussed, produce sinusoidal encoder signals with very limited harmonic distortion. Relying on very small harmonic distortions, interpolation techniques can be used to increase the resolution of the incremental angle encoder. However, increased angle resolution usually results in lower measurement accuracy. This inaccuracy, if repeatable, can also be calibrated.

Without interpolation only a single edge of the digitized analog encoder signal is counted, shown in Figure 1.7. The resolution can be increase two times by counting both the rising and falling edges of

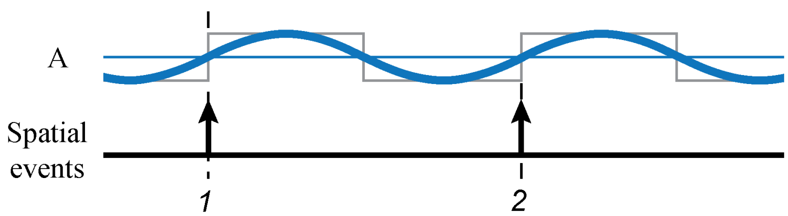

Figure 1.7: Spatial interval markings with no interpolation, relying on a single edge of the encoder signal.

the digitized analog encoder signal, shown in Figure 1.8. Accurate angle measurement with two times interpolation requires very low signal unbalance or offset. Signal unbalance causes a repeating pattern of smaller then larger spatial intervals. Most angle encoders provide two encoder signals with a relative

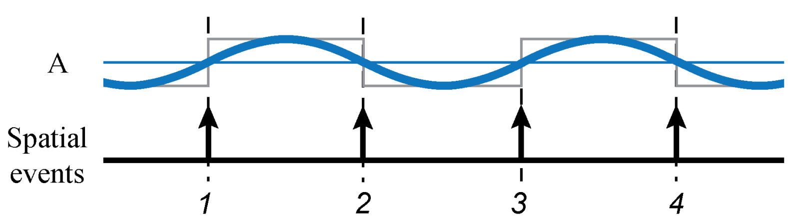

Figure 1.8: Spatial interval markings with two times interpolation, relying on the rising and falling edges of the encoder signal.

phase shift of 90° or $\frac{1}{4}$ wavelength. These signals are used together to determine the direction of spindle rotation but can also be used to increase the encoder's resolution. Termed quadrature decoding, this increases encoder resolution by four times, shown in Figure 1.9, but requires precise alignment of the A and B phases as well as low signal unbalance on both phases for reliable accuracy. These interpolation techniques cause

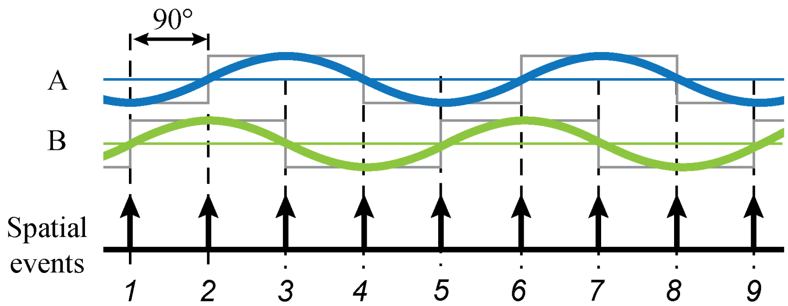

Figure 1.9: Spatial interval markings with quadrature decoding interpolation, relying on the rising and falling edges of two encoder signals.

a decrease in the angle measurement accuracy, due to signal unbalance and phase misalignment, but the inaccuracies are repeatable and can also be calibrated. More importantly these interpolation techniques do not significantly reduce the repeatability of angle measurements because they all rely on zero-crossing locations of the encoder signals. The zero-crossing locations are most insensitive the signal noise. Higher interpolation techniques rely on the encoder signal at locations other than the zero crossing which are more sensitive to voltage noise, further discussed in Section 2.3.1. For this reason higher interpolation techniques are not considered.

Both high and low frequency encoder error harmonics exist. Low frequency harmonics are mostly caused by installation error. While high frequency error components are caused due to circular scale graduation quality, quality of the scanning process and signal interpolation techniques. A high accuracy calibration technique therefore needs to capture all of the error components.

In the following section prior calibration techniques are discussed.

1.4 Prior Art in Encoder Calibration

The goal of angle encoder calibration is to correct for repeatable angle measurement errors and ultimately obtain a more precise rotational angular position measurement. If encoder calibration is used to guide a manufacturing operation it is important to perform the calibration on the manufacturing machine (application axis), under similar conditions that would be encountered during the manufacturing operation.

Two classes of calibration technique have been identified in literature: Angle Comparator calibration and On-axis Self-calibration.

1.4.1 Angle Comparator Calibration

An angle comparator is an angle metrology system specifically designed to calibrate for angle encoder measurement errors. The angle comparator is significantly different from the application machine and could incorporate stacked indexing tables [7] or multiple rotary encoders coaxially mounted on two rotary axes [8–13]. One variation of an angle comparator developed by the German metrology institute Physikalisch-Technische Bundesanstalt (PTB) is shown in Figure 1.10. These systems have demonstrated very high

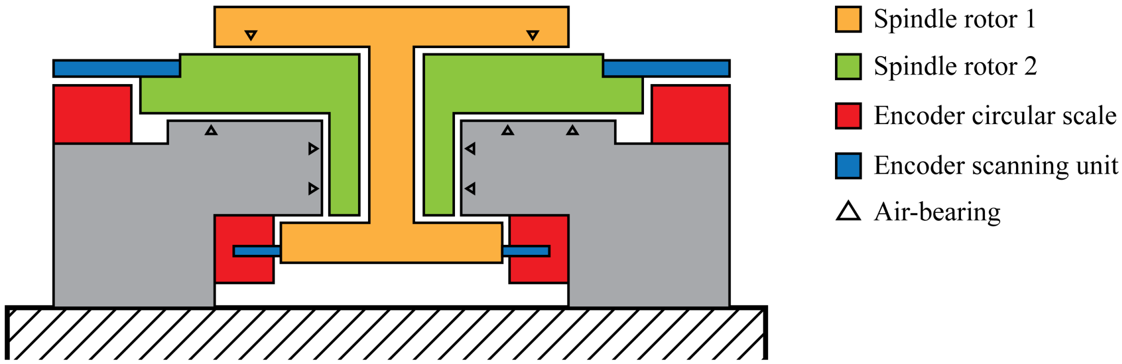

Figure 1.10: PTB's Angle Comparator with multiple angle encoders and coaxial rotary axes, adapted from [21].

calibration repeatability of a few thousandths of an arc-sec, but significant modifications would need to be made to incorporate an angle comparator into the application machine. Alternatively, transferring the calibrated error from the angle comparator to the application machine is counterproductive. Due to differing installation, rotational axis error motion and operating conditions, the error calibrated on the angle comparator is useless to improve measurement accuracy on the application machine. This technique finds better application in quality assurance of the accuracy of a manufactured encoder.

1.4.2 On-axis Self-Calibration

Ideally, the encoder should be calibrated on its application axis to ensure the conditions are most similar to those encountered during the manufacturing process. Several on-axis calibration techniques that meet the criteria have been identified, where calibration can be performed directly on the application machine. These methods are ideal to improve measurement accuracy for a manufacturing process. These methods can be identified as angle measurement, time measurement and dynamic calibration methods.

Along with the angle comparator presented in [12], a self-calibration method was also introduced utilizing 16 scanning units mounted in a special arrangement around the circular scale. Although a 16 scanning unit setup is excessive, this calibration method can also be adapted to lower scanning unit numbers as shown in [22] for a 5 scanning unit setup. Angle measurements are used from each scanning unit and either a linear combination of the measurements [22] or a Fourier analysis [11, 23–25] yields a discrete representation of the true encoder error. This is a main limitation of the method as the full encoder error map cannot be obtained and the completeness of the calibrated error is proportional to the number of scanning units used. For the 16 scanning unit setup only 128 points of the total 2^{18} scanning periods (less than 0.05%) are obtained and even less for the 5 scanning unit setup where only 16 points are obtained. Thus, any high frequency error components are missed in this calibration technique, making it impractical for high accuracy calibration.

Based on theEqual Division Averaged method (EDA) [9, 10], a self-calibratable encoder is presented using 5 scanning units [26]. The time that each of the grating lines passes the scanning unit is measured and using measurements from each scanning unit, evenly spaced around the circular scale the encoder error can be identified. However, due to harmonic cancellation of error harmonics between the scanning unit measurements a complete error map cannot be obtained. The calibrated error misses harmonics multiple of the number scanning units, for example all 5th order multiple harmonics are missed in the presented setup

[26].

A dynamic on-axis calibration method is first presented in [27]. The time intervals between successive grating lines passing the scanning unit, T_k are measured. The spatial distance between each grating line, Δ_k, is found, assuming the angular velocity of the spindle is constant during the entire spindle revolution. The accuracy of this method is limited due to the constant velocity assumption. This assumption is violated in realistic spindles due to damping and rotary disturbance torque due to interaction between spindle rotor and stator. To address these uncertainties a second method was presented relying on constant velocity assumption between successive grating lines and the angle between phase A and B detectors being smaller than the grating line period. Theoretically this second method is very promising as the second phase B sensor provides a means to directly solve for the encoder error without any spindle dynamic assumptions. However, practical encoder manufacturing limitations invalidate this second assumption. Although the phase A and B signals are designed to be phase-shifted by 90° or one quarter of the grating period, the detectors are often placed much wider apart for practical design considerations, discussed in Section 4.2. For example in a single field image scanning principle encoder, the 90° phase-shift is created through an optical beat and not directly from the spacing of phase A and B sensors. This causes significant limitations of the method and even the authors of [27] could not obtain consistent calibration results for the publication, possibly due to these practical encoder limitations.

Another dynamic on-axis calibration method was introduced in [28]. Relying again on time interval measurements, this method uses a dynamic model of the spindle including inertia and rotary damping to derive the encoder error. The free response velocity profile of the spindle speed is estimated with the dynamic model and encoder error is found from the time measurements. This is an improvement of the model compared to the constant velocity assumption of [27]. However, uncertainties caused by limited timing resolution and an assumption of free-response rotation were not addressed.

Through this literature search we see that there still does not exist a calibration method to quickly calibrate an angle encoder on its application axis, providing all encoder error harmonics (high and low) with an accuracy on the order of a thousandth of an arc-sec. Based on previous work [28] a novel encoder self-calibration algorithm is developed for these purposes.

1.5 Thesis Overview

This thesis introduces a novel self-calibration method for incremental angle encoders to very quickly self-calibrate an encoder on its application axis at any rotating speed, providing all encoder error harmonics.

Chapter 2 presents the theory behind the TDR calibration method and introduces two improvements that increase the accuracy of the method in calibrating precision angle encoders: (a) integration enhancement and (b) rotary vibration removal. A novel method for extracting spindle radial error motion from calibration results is presented and is proposed as a method to indirectly determine the accuracy of experimental calibration. The uncertainty in calibration is also investigated as a function of encoder signal repeatability, time measurement uncertainty and scanning unit alignment.

Chapter 3 presents simulation results used to validate the feasibility of the calibration method without added experimental complexity. Form simulation results the fundamental limitation of this method is found, purely due to repeatability of encoder and time measurements and not a function of dynamic estimation. Calibration inaccuracy is investigated and two metrics, readily found in experiment, are introduced to indirectly determine experimental uncertainty: (a) set repeatability and (b) spindle radial error motion estimation.

Chapter 4 presents the experimental setup used as a practical application for the calibration method. The operating principle of Heidenhain's ERA4282c angle encoder, installed on the setup, is analyzed and several sources of additional repeatable encoder errors and found due to the design. A method to align the scanning units evenly on the setup to less than 10 arc-sec (1 count) misalignment is discussed. The design of the encoder signal processing and time measurement electronics is presented.

Chapter 5 presents experimental calibration results and shows with calibration the angle measurement accuracy has been improved by more than 100 times.

Chapter 6 concludes this thesis and presents areas for improvement in the experimental setup that allow further study encoder calibration.

Chapter 2

Calibration Theory

2.1 Time-measurement Dynamic Reversal Calibration

The TDR self-calibration method is based on the free response dynamics of the encoder rotation axis, i.e. during the freely slowing down rotation of the spindle on which the encoder to be calibrated is mounted. The spindle speed decreases solely due to damping and inertia characteristics of the rotation axis. This assumption is most accurate for precision rotary axes that are supported by non-rolling element bearings, such as aerostatic or magnetic bearings, and with any rotary motors turned off. Figure 2.1 shows the output signals from a single encoder head: two quadrature signals A and B with N zero crossings per revolution and an index signal with one pulse per revolution. The zero crossing points in A and B mark the unique encoder angular position. Higher interpolation electronics can be used but are not considered because of increased uncertainty due to encoder signal harmonic distortion. Ideally, spatial sampling events are evenly

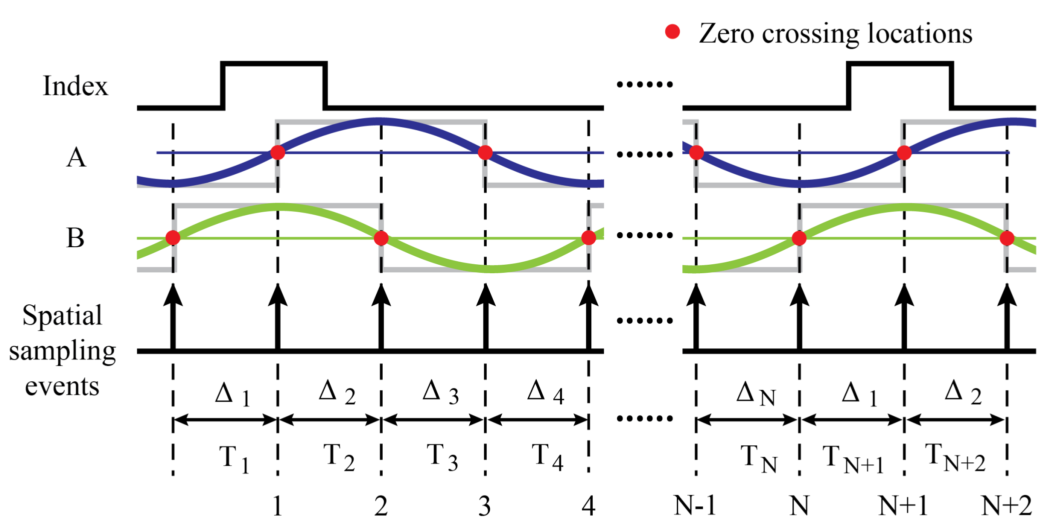

Figure 2.1: Rotary encoder spatial and temporal sampling events.

spaced around the circular scale with nominal spacing of, $\Delta_0 = 1/N$ revolution. In this situation, the angle of the rotation axis can easily be found by counting the number of spatial events, $\theta_k = k\Delta_0$. Realistically the spatial sampling events are not evenly spaced (Figure 2.2). The actual spatial sampling locations, Δ_k (for k =

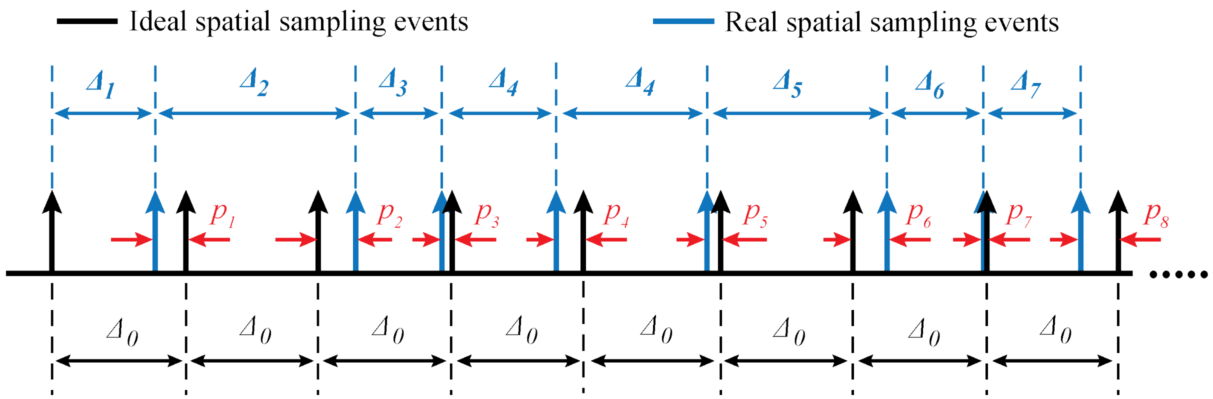

Figure 2.2: Ideal vs. realistic spatial sampling events (grating line locations) of an increment angle encoder.

1 to N), deviates from the nominal value and is the main cause of encoder error, causing angle measurement error. To accurately determine the angle of the rotation axis it is necessary to determine the exact spatial sampling intervals, $\theta_k = \sum_{i=1}^{k} \Delta_k$. In practice, the angle of the rotation axis would still be found by counting the number of spatial events but, digital electronics would compensate for measurement error with a lookup table of the encoder error at each spatial sampling event. The lookup table is referred to as the encoder error map, $p(k)$, which is the cumulation of deviations between the actual and nominal spatial sampling events,

$$p(k) = \sum_{i=1}^{k} (\Delta_k - \Delta_0). \tag{2.1}$$

It is important to note that the the error map does not have a mean value. The mean value of the error map would just redefine the start of the spindle revolution, indicating that all the graduation lines should be shifted by this value. In the experimental results this mean value is removed to be consistent with the definition and obtain a fair comparison of results.

$$p(k) = \sum_{i=1}^{k} (\Delta_k - \Delta_0) - \frac{1}{N} \sum_{k=1}^{N} \sum_{i=1}^{k} (\Delta_k - \Delta_0). \tag{2.2}$$

Using the encoder error map, the angle of the rotation axis at each spatial sampling event is

$$\theta_k = k\Delta_0 + p(k). \tag{2.3}$$

Spatial sampling intervals cannot be directly measured. Instead the time intervals between successive spatial sampling events, T_k, are captured with custom high-speed processing electronics. A dynamic model of the system is then used to relate spatial sampling intervals to the time measurements. The spindle dynamics are expressed as

$$d\omega/dt + c\omega = 0. \tag{2.4}$$

Where ω is spindle speed and c is the normalized damping coefficient (ratio of spindle damping to rotor inertia). This dynamic model is only accurate for free-response rotation without significant torque disturbance. The dominant source of torque disturbance, motor torque ripple, is removed by turning the motor off at a certain speed and letting the spindle slow down freely. Removing the effects of any additional torque disturbance, i.e. due to interaction between spindle rotor and stator, is discussed in Section 2.1.2. As the spindle speed is the temporal derivative of spindle rotational angular position, $\omega = d\theta/dt$, the dynamics of the spindle (Equation 2.4) are transformed into the angle domain

$$d\omega/d\theta = -c. \tag{2.5}$$

The unknown dynamics of the system are more accurately estimated when spindle speed is written in the spatial domain, where the normalized damping coefficient is found as the slope of the spindle speed function. Alternatively, the spindle speed function in the time domain is an exponentially decaying function, making the estimation more difficult. The normalized damping coefficient can be modeled to include any order of speed dependent damping and is shown here with second-order damping,

$$c = c_0 + c_1(\omega - \omega_0), \tag{2.6}$$

where ω_0 is the initial spindle speed of that revolution and c_0 and c_1 are constant and spindle speed dependent damping coefficients respectively. Solution of the spindle speed to Equation 2.5 and Equation 2.6 is given as

$$\omega(\theta) = \omega_0 + \frac{c_0}{c_1}\left[e^{-c_1(\theta-\theta_0)} - 1\right]. \tag{2.7}$$

Using a Taylor series expansion the angular speed can be approximated as ,

$$\omega(\theta) = \omega_0 - c_0(\theta - \theta_0)\left[1 - c_1\frac{(\theta-\theta_0)}{2}\right] + \omega_e. \tag{2.8}$$

where $|\omega_e| < c_0{c_1}^2(\theta-\theta_0)^3/6$ represents the higher order terms of the expansion. These higher order terms are negligible and the spindle speed at each sampling event is found,

$$\omega(\theta) = \omega_0 + a\left(\frac{\theta_k - \theta_0}{\Delta_0}\right) + b\left(\frac{\theta_k - \theta_0}{\Delta_0}\right)^2, \tag{2.9}$$

where $a = -c_0\Delta_0$ and $b = c_0 c_1 {\Delta_0}^2/2$ are damping parameters to be estimated. The spatial sampling events are approximately evenly spaced apart, $\theta_k \approx \theta_0 + k\Delta_0$, so that the spindle speed can be approximated at each sampling event as

$$\omega_k = \omega_0 + ak + bk^2. \tag{2.10}$$

From time measurements of each sampling event the spindle speed is given as

$$\omega_k = \Delta_k/T_k. \tag{2.11}$$

Combining Equation 2.10 and 2.11 the spatial distance between each count is written as,

$$\Delta_k = T_k\left(\omega_0 + ak + bk^2\right). \tag{2.12}$$

Circular closure constrains the sum of all count intervals to be one revolution and allows solution of the initial speed.

$$\sum_{i=S+1}^{S+N} \Delta_i = N \cdot \Delta_0 \tag{2.13}$$

Another perspective of the circular closure constraint is that there is no error in the rotational measurement from any sampling event to that same sampling event one revolution later. This also constrains the encoder error map as periodic over one spindle revolution. Combining Equation 2.12 and 2.13 yields

$$N \cdot \Delta_0 = \omega_0 \sum_{i=S+1}^{S+N} T_i \cdot i + a \sum_{i=S+1}^{S+N} T_i \cdot i + b \sum_{i=S+1}^{S+N} T_i \cdot i^2, \tag{2.14}$$

which can be rewritten to solve for the initial speed of each revolution as

$$\omega_0 = \frac{N \cdot \Delta_0}{\sum_{i=S+1}^{S+N} T_i} - a \frac{\sum_{i=S+1}^{S+N} T_i \cdot i}{\sum_{i=S+1}^{S+N} T_i} - b \frac{\sum_{i=S+1}^{S+N} T_i \cdot i^2}{\sum_{i=S+1}^{S+N} T_i}. \tag{2.15}$$

Replacing the initial speed found in Equation 2.12 with that in Equation 2.15

$$\frac{N \cdot \Delta_0}{\sum_{i=S+1}^{S+N} T_i} \mathbf{T} = \Delta_k + a \left(\frac{\sum_{i=S+1}^{S+N} T_i \cdot i}{\sum_{i=S+1}^{S+N} T_i} - k \right) \mathbf{T} + b \left(\frac{\sum_{i=S+1}^{S+N} T_i \cdot i^2}{\sum_{i=S+1}^{S+N} T_i} - k^2 \right) \mathbf{T}, \tag{2.16}$$

where $k = S+1 \ldots S+N$ and the time measurements are written in vector form as

$$\mathbf{T} = \begin{bmatrix} T_N + 1 \\ \vdots \\ T_N + S \\ T_S + 1 \\ \vdots \\ T_N \end{bmatrix} \tag{2.17}$$

T. Reordering these N equations of Equation 2.18 according to Δ_k index from $k = 1$ to N, Equation 2.16 can be rewritten in vector form as

$$\mathbf{m} = \Delta + a \cdot \mathbf{U} + b \cdot \mathbf{V}, \tag{2.18}$$

where $\mathbf{m}$, $\mathbf{U}$ and $\mathbf{V}$ are vectors composed of time measurements

$$\mathbf{m} = \frac{N \cdot \Delta_0}{\sum_{i=S+1}^{S+N} T_i} \mathbf{T} \tag{2.19a}$$

$$\mathbf{U} = \frac{\sum_{i=S+1}^{S+N} T_i \cdot i}{\sum_{i=S+1}^{S+N} T_i} \mathbf{T} - \mathbf{kT} \tag{2.19b}$$

$$\mathbf{V} = \frac{\sum_{i=S+1}^{S+N} T_i \cdot i^2}{\sum_{i=S+1}^{S+N} T_i} \mathbf{T} - \mathbf{k^2 T} \tag{2.19c}$$

and each vector has the following form

$$\Delta = \begin{bmatrix} \Delta_1 \\ \vdots \\ \Delta_S \\ \Delta_S + 1 \\ \vdots \\ \Delta_N \end{bmatrix} \mathbf{kT} = \begin{bmatrix} (N+1)\,T_N + 1 \\ \vdots \\ (N+S)\,T_N + S \\ (S+1)\,T_S + 1 \\ \vdots \\ NT_N \end{bmatrix} \mathbf{k^2T} = \begin{bmatrix} (N+1)^2\,T_N + 1 \\ \vdots \\ (N+S)^2\,T_N + S \\ (S+1)^2\,T_S + 1 \\ \vdots \\ N^2 T_N \end{bmatrix}. \tag{2.20}$$

Two revolutions of time data are used to isolate the artifact, $a \cdot \mathbf{U} + b \cdot \mathbf{V}$, from the spatial intervals, Δ, and solve for the unknown damping coefficients. Each revolution of data is offset by one and a half revolutions to ensure no overlap or correlation between data sets, Figure 2.3. Equation 2.18 is applied to both data sets,

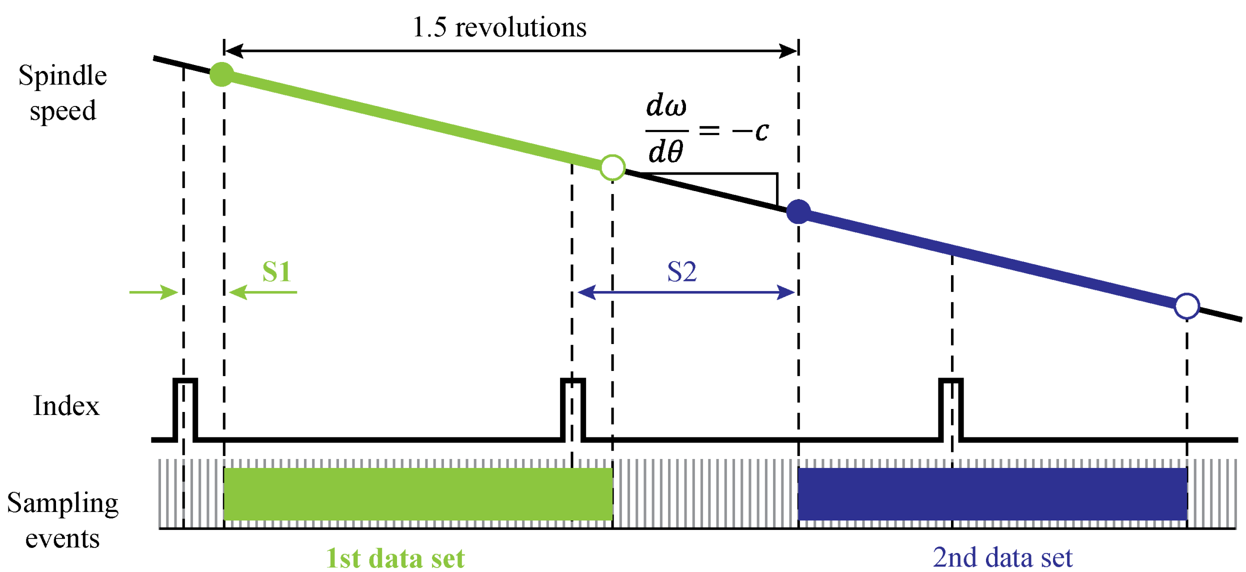

Figure 2.3: Sampled data sets used to perform dynamic reversal in the self-calibration method.

$$\mathbf{m_1} = \Delta + a_1 \cdot \mathbf{U_1} + b_1 \cdot \mathbf{V_1} \tag{2.21a}$$

$$\mathbf{m_2} = \Delta + a_2 \cdot \mathbf{U_2} + b_2 \cdot \mathbf{V_2}. \tag{2.21b}$$

Due to the different starting locations of each data set, the second data set is reorganized to align the spatial interval vector between data sets. The difference of the two equations, removes spatial interval vector, Δ, common to each data set. This is referred to as dynamic reversal and gives the following linear equation.

$$\underbrace{\begin{bmatrix} \mathbf{U_1} & \mathbf{V_1} & -\mathbf{U_2} & -\mathbf{V_2} \end{bmatrix}}_{\mathbf{W}} \begin{bmatrix} a_1 \\ b_1 \\ a_2 \\ b_2 \end{bmatrix} = \mathbf{m_1} - \mathbf{m_2} \tag{2.22}$$

In early work [28], the damping estimation is based on the least square fitting of Equation 2.22 and the encoder error map is calculated with the estimated damping coefficients from Equation 2.21. This damping estimation can minimize the estimation error for graduation vector Δ, but can possibly bring large error to the encoder error map. An integration enhancement method is proposed to provide a better estimate of the encoder error map.

2.1.1 TDR Integration Enhancement

The encoder error map, $p(k)$, represents the error in the angle measurement at each spatial sampling event and is found as the cumulative sum of deviations between the actual and ideal spatial sampling intervals without mean value (Equation 2.2). The encoder error map written in vector form is

$$\mathbf{p} = \begin{bmatrix} \Delta_1 - \Delta_0 \\ \Delta_1 + \Delta_2 - 2\Delta_0 \\ \Delta_1 + \Delta_2 + \Delta_3 - 3\Delta_0 \\ \vdots \\ \sum_{i=1}^{S} \Delta_i - S\Delta_0 \\ \sum_{i=1}^{S+1} \Delta_i - (S+1)\Delta_0 \\ \vdots \\ \sum_{i=1}^{N} \Delta_i - N\Delta_0 \end{bmatrix} - \frac{1}{N}\sum_{k=1}^{N}\sum_{i=1}^{k}(\Delta_k - \Delta_0). \tag{2.23}$$

To simplify notation of the cumulative summation without mean value, the $int(\cdots)$ operator is introduced, and the encoder error map can be presented as,

$$\mathbf{p} = int(\Delta - \Delta_0). \tag{2.24}$$

In order to eliminate the accumulated calibration error caused by the damping estimation, Equation 2.21 is rewritten, to replace the graduation vector Δ with the error map $\mathbf{p}$.

$$int(\mathbf{m_1}) = \mathbf{p} + int(\Delta_0) + a_1 \cdot int(\mathbf{U_1}) + b_1 \cdot int(\mathbf{V_1}) \tag{2.25a}$$

$$int(\mathbf{m_2}) = \mathbf{p} + int(\Delta_0) + a_2 \cdot int(\mathbf{U_2}) + b_2 \cdot int(\mathbf{V_2}). \tag{2.25b}$$

Dynamic reversal for two data sets is applied and the linear equation used for damping estimation is then written as,

$$\underbrace{int\left(\begin{bmatrix} \mathbf{U_1} & \mathbf{V_1} & -\mathbf{U_2} & -\mathbf{V_2} \end{bmatrix}\right)}_{\mathbf{W}} \begin{bmatrix} a_1 \\ b_1 \\ a_2 \\ b_2 \end{bmatrix} = int(\mathbf{m_1} - \mathbf{m_2}). \tag{2.26}$$

A least squares fitting is applied to Equation 2.26 and the damping parameters are estimated as

$$\begin{bmatrix} \overline{a_1} \\ \overline{b_1} \\ \overline{a_2} \\ \overline{b_2} \end{bmatrix} = \left(\mathbf{W}^T\mathbf{W}\right)^{-1}\left[int(\mathbf{m_1} - \mathbf{m_2})\right]. \tag{2.27}$$

The damping estimates found through Equation 2.27 minimize the error between error maps, instead of count intervals. This results in a much more accurate prediction of the error map which will ultimately be used to improve measurement accuracy. Two sets of damping coefficients are obtained and thus two estimated encoder error maps are found

$$\mathbf{p_1} = int\left(\mathbf{m_1}\right) - int\left(\Delta_0\right) - \overline{a_1} \cdot int\left(\mathbf{U_1}\right) - \overline{b_1} \cdot int\left(\mathbf{V_1}\right) \tag{2.28a}$$

$$\mathbf{p}_2 = int\left(\mathbf{m_2}\right) - int\left(\Delta_0\right) - \overline{a_2} \cdot int\left(\mathbf{U_2}\right) - \overline{b_2} \cdot int\left(\mathbf{V_2}\right). \tag{2.28b}$$

The derivation assumes that both these error maps are identical. Any difference in the two error maps, defined as set repeatability, can be used as a metric of the uncertainty of the calibration results.

Integration enhancement improves upon performance limitations caused by limited timing resolution. In the following section, a limitation caused by assuming free-response dynamics (Equation 2.4) is addressed.

2.1.2 TDR Rotary Vibration Removal

The main assumption of this calibration method is in free response dynamics of Equation 2.4. In reality, there may exist a position dependent disturbance torque due to an interaction between the spindle rotor and stator as the spindle rotates. This disturbance torque causes the spindle rotor to vibrate rotationally, increasing or decreasing in rotational speed at different spindle rotational angular positions. This causes a significant degradation of the calibrated encoder error map of Equation 2.28. The estimated encoder error map $p(k)$, will be the combination of encoder graduation error $g(k)$, spindle radial error motion divided by scale radius $r(k)$, and rotary vibration $v(k)$:

$$p(k) = g(k) + r(k) + v(k). \tag{2.29}$$

The first two terms $g(k) + r(k)$ represent the encoder errors, and can be used in an application to improve the accuracy of angle measurement. The third term $v(k)$ is an artifact due to the free response assumption and degrades the calibration accuracy. The rotary vibration compensated error map $q(k)$, is a much better estimate of the angle measurement errors given as

$$q(k) = g(k) + r(k). \tag{2.30}$$

The 4-head setup shown in Figure 2.4,consisting of scanning units H1, H2, H3 and H4 all evenly installed around the circular scale, is used to develop a method to remove the rotary vibration component. Calibration is performed on data from each scanning unit and each derived error map is uniquely composed of graduation, spindle radial error motion and rotary vibration components expressed as:

$$\begin{array}{rcccccc} p_{H1}(k) = & g(k) & + & y(k)/R & + & v(k) \\ p_{H2}(k) = & g(k-N/4) & - & x(k)/R & + & v(k) \\ p_{H3}(k) = & g(k-N/2) & - & y(k)/R & + & v(k) \\ p_{H4}(k) = & g(k-3N/4) & + & x(k)/R & + & v(k) \end{array} \tag{2.31}$$

where $x(k)$ and $y(k)$ are spindle radial error motions along the X and Y direction and R is the radius of the circular scale. The graduation component rotates with the spatial position of the scanning unit on the

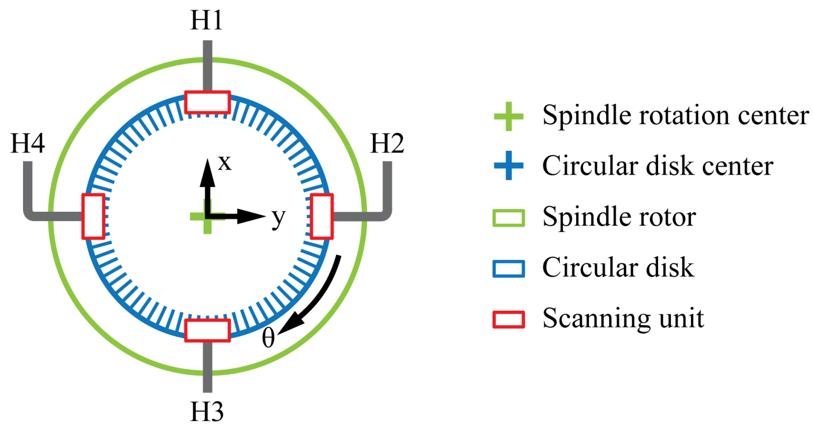

Figure 2.4: The 4-head setup used in removing rotary vibration component from calibration results.

rotor while the rotary vibration component is synchronous to the spindle rotation and is independent of the scanning unit position. As discussed in Section 1.2 the scanning unit is only sensitive to spindle radial error motion that is parallel to the scanning direction, thus opposing heads see equal but opposite radial error motion components.

A harmonic cancellation method and a rotary vibration prediction method are used to isolate the rotary vibration component from the calibration result.

Harmonic cancellation

Harmonic-cancellation can be applied to an arbitrary periodic curve. In general, the average of h identical periodic function, each evenly distributed on 2π, shows the sum of integer multiples of Fourier components of the original curve multiple of h. This is shown for the discrete periodic function $f(k)$ and the evenly distributed curves, $f_m(k)$ for $m = 0$ to $h-1$,

$$\begin{aligned}
f_0(k) &= f(k) \\
f_1(k) &= f(k - N/h) \\
f_2(k) &= f(k - 2N/h) \\
&\cdots \\
f_{h-1}(k) &= f(k-(h-1)N/h)
\end{aligned} \tag{2.32}$$

The Fourier coefficients of the evenly distributed curves, $F_m(n)$, can be written as

$$F_m(n) = \sum_{k=1}^{N} f_m(k) \cdot e^{-2\pi ikn/N} \tag{2.33}$$

where n is the harmonic number. Each distributed curve is simply delayed by $e^{-2\pi i(m-1)/h}$ with respect to the first and can be written as,

$$F_m(n) = F_0(n) \cdot e^{-i2\pi mn/h}. \tag{2.34}$$

Finally, the average of the distributed curves is found

$$\frac{1}{h}\sum_{m=0}^{h-1} F_m(n) = \frac{1}{h} F_0(n) \sum_{m=0}^{h-1} e^{-i2\pi mn/h} = \begin{cases} F_0(n) & \text{if } n = hj \\ 0 & \text{if } n \neq hj \end{cases} \tag{2.35}$$

for j equal to any integer.

This can be applied to cancel the graduation component of the derived encoder error map, except for harmonics integer multiple of four, the number of scanning units. The periodic curve is the graduation error and each of the derived encoder error maps from each scanning unit provides an even distribution of this curve. At each spindle speed ω, the n-th Fourier coefficients $P_{Hj}(n,\omega)$ of the derived error map $p_{Hj}(k,\omega)$ can be calculated for the j-th scanning unit as:

$$P_{Hj}(n,\omega) = \sum_{k=1}^{N} p_{Hj}(k,\omega) \cdot e^{-2\pi ikn/N} \tag{2.36}$$

From the Fourier coefficients of the four error maps in Equation 2.31, the rotary vibration Fourier coefficients can be extracted according to harmonic cancellation as the average of error map harmonics from each scanning unit,

$$\frac{P_{H1}(n) + P_{H2}(n) + P_{H3}(n) + P_{H4}(n)}{4} = \begin{cases} V(n) & \text{if } n \neq 4m \\ G(n) + V(n) & \text{if } n = 4m \end{cases}. \tag{2.37}$$

Where $G(n)$ and $V(n)$ are the Fourier coefficients of grating encoder error $g(k)$ and rotary vibration $v(k)$ respectively and m is any integer.

However, the four head average cannot extract rotary vibration harmonics multiple 4-th order. For these harmonics, a rotary vibration prediction method is used.

Rotary vibration prediction

Ordinarily the error map harmonics at each spindle speed should remain constant. The majority of any variation in the error map harmonics was found to be caused by the rotary vibration component of the derived encoder error map. The measured rotary vibration $v(s)$, caused by a disturbance torque $M(s)$, can be predicted by considering the rigid body dynamics of the spindle.

$$\frac{v(s)}{M(s)} = \frac{1}{Js^2 + Bs}, \tag{2.38}$$

where J is rotary inertia and B is the damping coefficient. With precision air-bearings spindles the damping coefficient is small enough that it can be neglected, so the transfer function becomes

$$\frac{v(s)}{M(s)} = \frac{1}{Js^2}. \tag{2.39}$$

The disturbance torque generally depends only on rotary position, and its harmonic frequency will change with the spindle speed. Consequently, the induced rotary vibrating motion is smaller at high speeds than that at low speeds. The encoder error map components $g(k)$ and $r(k)$ are much more insensitive to spindle speeds, typically $r(k)$ changes only several thousandths of an arc-sec over 100 rpm. Based on this speed-dependent characteristic, $G(n)+V(n)$ of Equation 2.37 can be partitioned as:

$$G(n)+V(n)=G(n)+\frac{A_n}{\omega^2}. \tag{2.40}$$

From the calibration maps $p_{Hj}(k,\omega)$ taken over a wide speed range, the complex constants A_n can be identified and the complete rotary vibration Fourier coefficients can be completely defined as

$$V(n)=\begin{cases}\frac{P_{H1}(n)+P_{H2}(n)+P_{H3}(n)+P_{H4}(n)}{4} & \text{if } n\neq 4m\\ \frac{A_n}{\omega^2} & \text{if } n=4m\end{cases}. \tag{2.41}$$

The speed-dependent rotary vibration can be estimated with the inverse Fourier transform as

$$v(k,\omega)=\sum_{n=-20}^{20} V(n)\cdot e^{2\pi jkn/N}. \tag{2.42}$$

Here only the first 20 harmonics are included, as typically the vibration harmonics beyond 20 are negligible. The original calibration results can be compensated for rotary vibration and estimation of encoder angle measurement error for the j-th scanning unit is

$$q_{Hj}(k)=p_{Hj}(k)-v(k) \quad \text{j=1,2,3,4}. \tag{2.43}$$

2.1.3 Low-speed Calibration Accuracy Enhancement

In the TDR calibration method presented, there are three approximations: (a) spatial sampling events are treated as evenly spaced in Equation 2.10; (b) The average speed within one spatial count is used as the instantaneous speed ω_k in Equation 2.11; (c) The rotary vibration component of the calibration error map, $r(k)$, does not vary significantly between the two revolutions of time data in Equation 2.26. These approximations are necessary to carry out self-calibration when the encoder error is unknown. However, at low speeds, these approximations can introduce errors into the calibration results. Here we present an integration method to eliminate these errors.

Based on the calibrations results ($p(k)$ and $\overline{a}$ from Equation 2.28) derived from the two data sets, we can more accurately calculate ω_k and θ_k. The first approximation can be resolved by using the encoder error estimation from the previous calibration result $p(k)$. The spatial sampling events are more accurately found as $\theta_k=\theta_0+p(k)$ and the spindle speed at each sampling event can be approximated as

$$\omega_k=a\left(\frac{1}{\Delta_0}\left[k+p(k)\right]\right)+b\left(\frac{1}{\Delta_0}\left[k+p(k)\right]\right)^2. \tag{2.44}$$

The second approximation can be resolved by calculating the instantaneous spindle speed with the damping estimate from the previous calibration result $\overline{a}$. As shown in Figure 2.5, the spindle speed at time τ within one count $\theta_{k-1}<\theta<\theta_k$ can be expressed as

$$\omega(\tau)=\omega_k\cdot e^{c(T_k-\tau)} \tag{2.45}$$

where $c = \overline{a}/\Delta_0$.

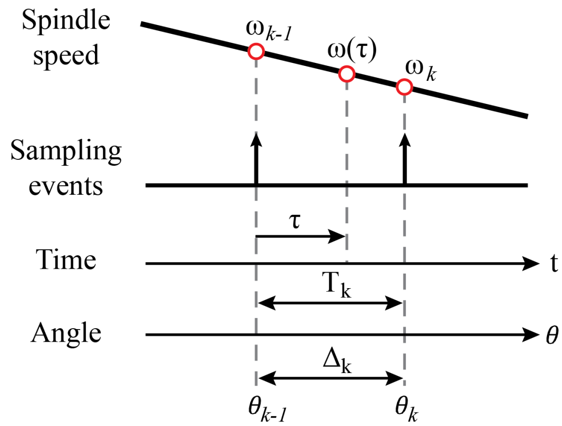

Figure 2.5: Spindle speed between count intervals.

By integration the spatial interval between counts can be more accurately found as

$$\Delta_k = \int_0^{T_k} \omega(\tau)\, d\tau = \omega_k \frac{e^{c \cdot T_k} - 1}{c}. \tag{2.46}$$

Consequently the instantaneous spindle speed is found

$$\omega_k = \Delta_k \frac{c}{e^{c \cdot T_k} - 1}. \tag{2.47}$$

The third approximation is resolved by including the change in rotary vibration between the two data sets using the rotary vibration result found in the previous calibration. The encoder error maps between each data set are assumed to cancel in Equation 2.25. At low speeds the rotary vibration component changes significantly even between sequential revolutions. To include this effect, the difference between rotary vibration derived from each data set is included and Equation 2.26 is rewritten as

$$\underbrace{\left(int \begin{bmatrix} \mathbf{U_1} & \mathbf{V_1} & -\mathbf{U_2} & -\mathbf{V_2} \end{bmatrix} \right)}_{\mathbf{W}} \begin{bmatrix} a_1 \\ b_1 \\ a_2 \\ b_2 \end{bmatrix} = int\left(\mathbf{m_1} - \mathbf{m_2}\right) - v_1(k) + v_2(k). \tag{2.48}$$

Replacing Equation 2.10 with Equation 2.44, Equation 2.11 with Equation 2.47 and Equation 2.26 with Equation 2.48 will result in a much more accurate calibration at low spindle speeds. This accuracy enhancement is an iterative process and multiple iterations are necessary to achieve the best results. Typical four iterations are necessary before the results converge. The procedure for enhanced calibration is shown in Figure 2.6.

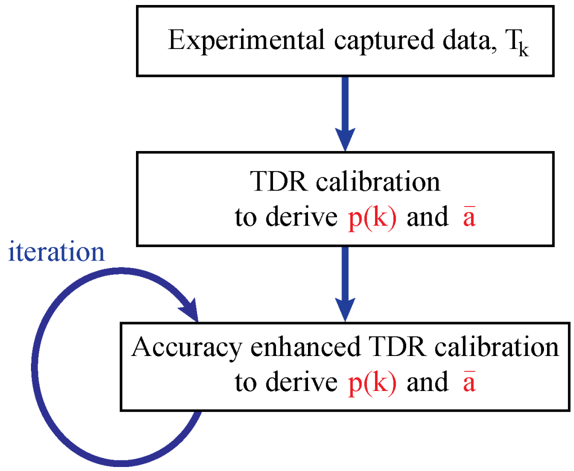

Figure 2.6: Iterative procedure for accuracy enhanced calibration.

2.2 Spindle Radial Error Motion Extraction

A new two-dimension method for analyzing spindle radial error motion has been recently developed [29–31], representing orthogonal x and y-direction spindle radial error motion as a complex Fourier series. This method finds application in encoder self-calibration, as a method to validate the accuracy of experimental calibration results. Normally, two orthogonal capacitance probe measurements are used, looking at a reference precision ball target. This standard capacitance probe measurement is compared to spindle radial error motion estimates obtained from the 4-head encoder setup to validate the accuracy of the calibration method. The analysis presented shows the extraction of the radial error motion components from the calibration results.

Following the procedure for removing rotary vibration from the raw calibration result, the error maps obtained from each scanning unit are composed solely of grating and radial error motion components.

$$\begin{array}{rccc} q_{H1}(k) = & g(k) & + & y(k)/R \\ q_{H2}(k) = & g(k-N/4) & - & x(k)/R \\ q_{H3}(k) = & g(k-N/2) & - & y(k)/R \\ q_{H4}(k) = & g(k-3N/4) & + & x(k)/R \end{array}. \tag{2.49}$$

The Fourier coefficients of each error map, $Q_{Hj}(n)$, can be written as

$$\begin{array}{rccc} Q_{H1}(n) = & G(n) & + & Y(n)/R \\ Q_{H2}(n) = & G(n)e^{-jn\pi/2} & - & X(n)/R \\ Q_{H3}(n) = & G(n)e^{-jn\pi} & - & Y(n)/R \\ Q_{H4}(n) = & G(n)e^{-jn3\pi/2} & + & X(n)/R \end{array}. \tag{2.50}$$

To obtain the spindle radial error motion components in the complex domain, $X+Yj$, the grating error components $G(n)$ need to be canceled between scanning unit measurements. The even grating error harmonics cancel between scanning units on opposite sides of the circular scale. The Y-direction spindle radial error motion can be obtained for even harmonics as

$$\frac{1}{2}\left(Q_{H1}-Q_{H3}\right)\begin{cases} G(n)+Y(n)/R & \text{if } n\neq 2m \\ Y(n)/R & \text{if } n=2m \end{cases} \tag{2.51}$$

and the X-direction spindle radial error motion also for even harmonics as

$$\frac{1}{2}\left(Q_{H2}-Q_{H4}\right)\begin{cases} G(n)e^{-in\pi/2}-X(n)/R & \text{if } n\neq 2m \\ -X(n)/R & \text{if } n=2m \end{cases} \tag{2.52}$$

where m is any integer. To obtain the two-dimensional representation of the spindle radial error motion, X and Y-direction error motion are added together as $X+Yj$, in the complex domain. The imaginary operator acts as an equivalent rotation for the grating error harmonics and allows them to cancel for odd harmonics. The rotated form of Equation 2.51

$$\frac{1}{2}\left(Q_{H1}-Q_{H3}\right)e^{in\pi/2}\begin{cases} G(n)e^{in\pi/2}+Y(n)e^{in\pi/2}/R & \text{if } n\neq 2m \\ Y(n)e^{in\pi/2}/R & \text{if } n=2m \end{cases} \tag{2.53}$$

where the grating harmonics of Equation 2.52 and Equation 2.53 now have equal but opposite phase. The final form of the two-dimensional spindle radial error motion is obtained for odd harmonics by combining Equation 2.52 and Equation 2.53.

$$\frac{1}{2}\left(Q_{H1}-Q_{H3}\right)e^{in\pi/2}+\frac{1}{2}\left(Q_{H2}-Q_{H4}\right)\begin{cases} Y(n)e^{in\pi/2}/R-X(n)/R & \text{if } n\neq 2m \\ 2G(n)e^{in\pi/2}+Y(n)e^{in\pi/2}/R-X(n)/R & \text{if } n=2m \end{cases} \tag{2.54}$$

The lower order spindle radial error motion harmonics will be most dominant in the experimental setup. Particularly the $[-1]$ component found from Equation 2.54 for $n=1$ will have the greatest magnitude.

This novel method of measuring spindle radial error motion, using four encoder scanning units, a circular scale and encoder calibration technique, yields harmonics of the spindle radial error motion that do not rely on the roundness of the target. The encoders are insensitive to motion that brings the circular scale closer or farther from the scanning unit and therefore do not sense roundness. This is an advantage to this radial error motion measurement, as it saves time with reversal methods necessary to cancel ball roundness measurements. Unfortunately not all the error motion harmonics can be found as they cannot be isolated from the grating error component.

2.3 Calibration Uncertainty

To improve the accuracy of the calibration method, uncertainties in the calibration technique and experimental setup should be addressed. Uncertainties exist in the experimental setup caused by air bearing supply pressure and ambient temperature fluctuations, mechanical floor vibration and electronic noise. These experimental uncertainties contribute to the repeatability of encoder spatial interval measurements used to obtain the calibration result. In addition, uncertainties due to the calibration method exist. Relying on time measurements to determine spatial intervals of the calibration technique, places importance on accurate time measurement, which can be influenced by limited timing resolution or clock jitter.

In this section, an analysis of how encoder signal repeatability and timing uncertainty effect the calibration results is presented and practical solutions are suggested to overcome them.

2.3.1 Marking Repeatability

The repeatability of spatial interval measurements is very important in this real-time application. Repeatability will affect the calibration results, but also during the manufacturing operation reliable measurements need to be made and compensated with calibration results to obtain an accurate rotational angular position measurement. This repeatability is influenced by variation of the encoder signal, independent of spindle rotation.

Consider an ideal analog voltage encoder signal,

$$V = M \cdot \sin(N \cdot \theta), \tag{2.55}$$

where M is the signal amplitude and N is the number of grating lines on the encoder circular scale. The change in angle measurement, $d\theta$, due to encoder signal variation, dV, at the zero crossing is found through the derivative of Equation 2.55 as

$$d\theta = \frac{dV}{M \cdot N} \tag{2.56}$$

and shown in Figure 2.7. The zero-crossing locations are specifically chosen due to low sensitivity of angle measurement for voltage noise. Equation 2.56 can be used to determine angular tolerances, but the

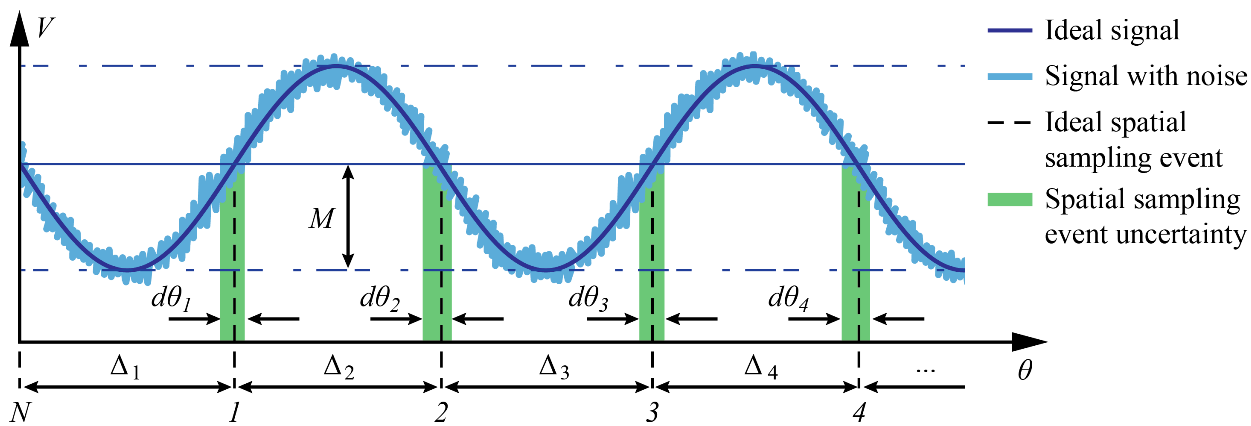

Figure 2.7: Demonstrated uncertainty in accurately determining spatial sampling events with encoder signal noise or variation, independent of spindle rotation.

application of writing patterns on a silicon wafer requires a linear tolerance. The linear manufacturing tolerance, dx, is shown in Figure 2.8 and given as

$$dx = d\theta \cdot R_w \tag{2.57}$$

where R is the writing radius that varies with rotational speed, n, as

$$R_w = R_i \cdot \frac{n_{min}}{n}, \tag{2.58}$$

and R_i is the inner writing radius of 0.5 m and n_{min} is the minimum writing speed of 180 rpm. An estimate

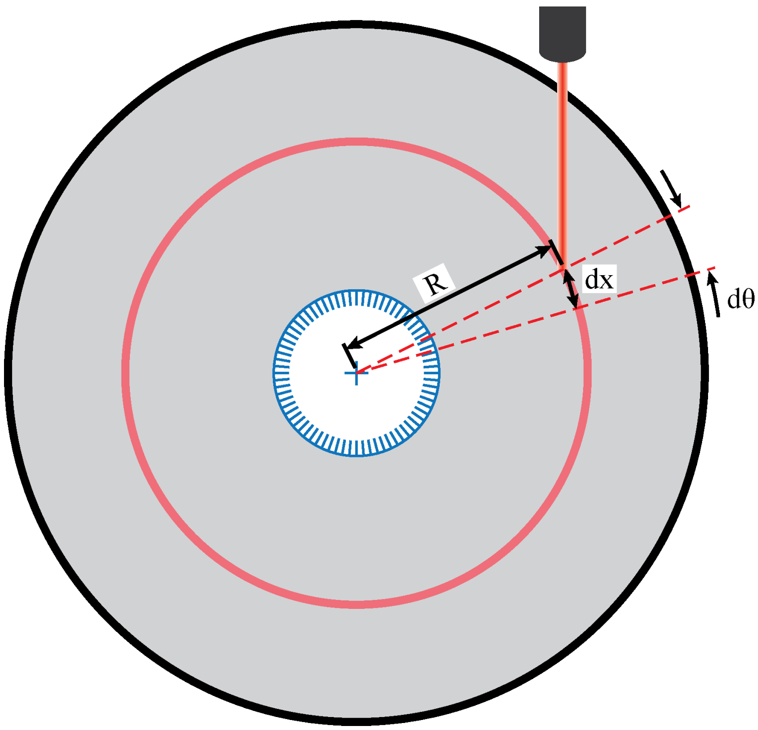

Figure 2.8: Linear manufacturing tolerance from encoder angular measurement accuracy for writing on a rotary table.

of the amount of signal variation due to noise, dV, can be obtained from measurement of the signal to noise ratio (SNR).

$$SNR = \frac{M_0}{dV}, \tag{2.59}$$

which can be re-written to find the encoder signal variation, dV, as

$$dV = \frac{M_0}{SNR}. \tag{2.60}$$

SNR can be improved by filtering the encoder signal to attenuate high frequency noise, discussed in Section 4.4.1. The exact relationship between SNR and the filter implemented is not determined, rather experimental measurements of the SNR for a certain filter implementation is used. The signal amplitude, M, will change with the frequency of the analog voltage signal due to sensor dynamics and signal post processing filters. The post processing filters improve SNR, but also attenuate the signal amplitude at higher frequencies. The amplitude attenuation can be modeled as a function of spindle rotation speed, n, as

$$M(n) = \underbrace{\frac{M_0}{\sqrt{1+(c_3\omega)^2}}}_{\text{sensor dynamics}} \cdot \underbrace{\frac{G}{\sqrt{(1-\omega^2 d_1)^2+(c_1\omega)^2}\sqrt{(1-\omega^2 d_2)^2+(c_2\omega)^2}}}_{\text{post processing filters}}, \tag{2.61}$$

where $\omega = 2\pi Nn/60$, coefficients of the post processing filters are c_1, d_1, c_2, d_2 and filter gain is G. Finally, substituting Equation 2.56, 2.58, 2.60 and 2.61 into Equation 2.57 gives the linear tolerance obtained as a function of speed, n, SNR and filter coefficients

$$dx = \frac{R_i \cdot n_{min}}{N \cdot SNR} \cdot \frac{\sqrt{1+(c_3\omega)^2}}{n} \cdot \frac{\sqrt{(1-\omega^2 d_1)^2+(c_1\omega)^2}\sqrt{(1-\omega^2 d_2)^2+(c_2\omega)^2}}{G}. \tag{2.62}$$

This analysis is used to determine the effectiveness of different post-processing filters and to set a goal for the SNR to achieve the 5 nm linear manufacturing tolerance. The SNR is experimentally measured by clamping the air bearing in place to stop any rotation. Experimental measurements show the initial SNR of the encoders is 145. Figure 2.9 shows the achievable linear tolerance from Equation 2.62, and Figure 2.10 shows the angular tolerance from Equation 2.56, with no post-processing filters and a base SNR of 145. Without post-processing filters to bring down the SNR, it is not feasible to achieve the 5 nm linear

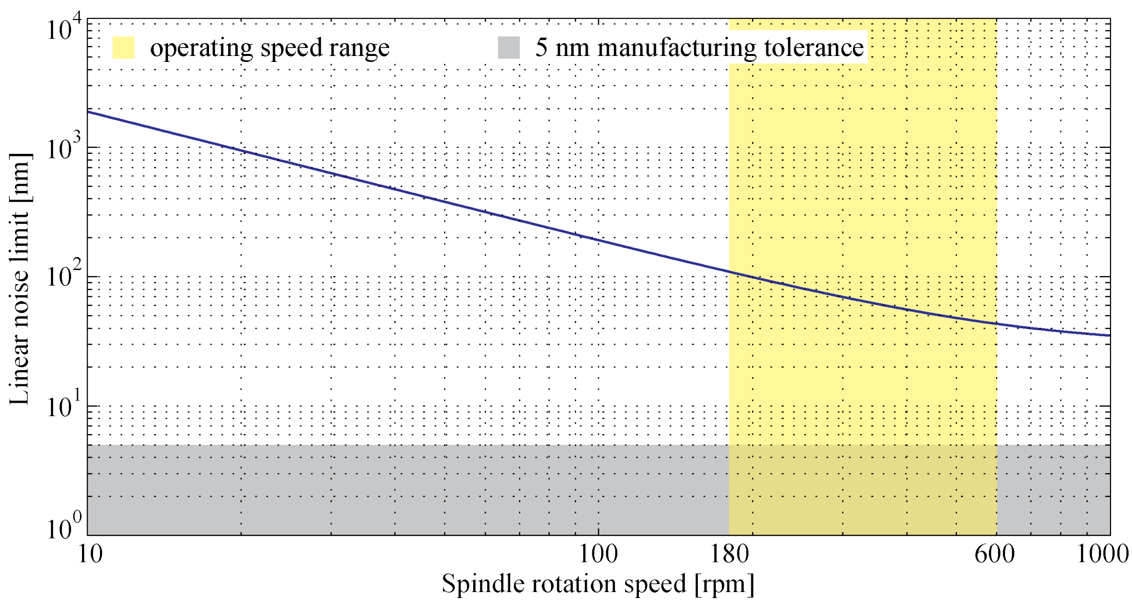

Figure 2.9: Predicted linear uncertainty in the position of spatial sampling events due to encoder signal variation, independent of spindle rotation. Uncertainties shown are found without post-processing filters and a base SNR of 145. Manufacturing speed range shown in yellow and constant 5 nm linear manufacturing tolerance shown in gray.

manufacturing tolerance. The SNR cannot be increased without filtering the encoder voltage signal which causes additional signal attenuation at higher frequencies, limiting the operating speed range.

By implementing different filter topologies, the marking repeatability can be shaped so that the manufacturing tolerance is met through the entire speed range. The shaping is performed by adjusting poles and zeros of the filter (c_1, d_1, c_2, d_2). It's found that a 4 pole Chebyshev filter with a bandwidth of 300kHz and minimum SNR of 3000 will meet the manufacturing tolerance for this application, Figure 2.11. With lower bandwidths the filters remove more noise from the encoder signals and will create a higher SNR, but will also adversely attenuate the encoder signal at higher frequencies increasing the uncertainty at higher speeds. With such an aggressive filter topology it is possible that the experimental results show a much higher SNR than 3000. The SNR of the encoder signals with signal processing filters is presented in Section 4.4.1.

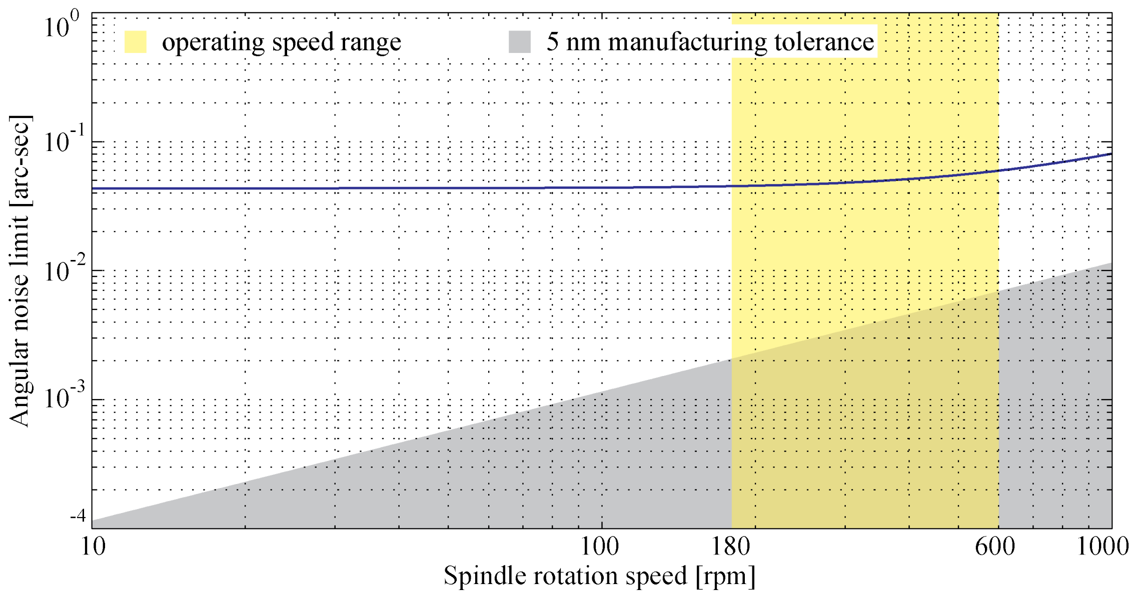

Figure 2.10: Predicted angular uncertainty in the position of spatial sampling events due to encoder signal variation, independent of spindle rotation. Uncertainties shown are found without post-processing filters and a base SNR of 145. Manufacturing speed range shown in yellow and constant 5 nm linear manufacturing tolerance shown in gray.

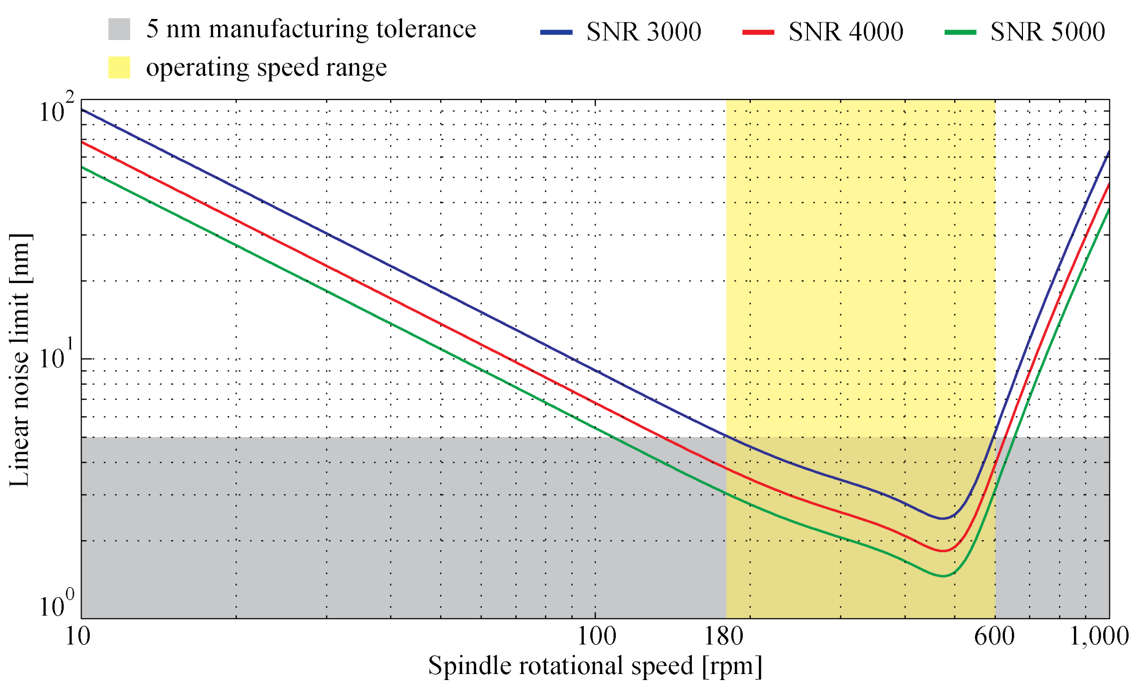

Figure 2.11: Predicted linear uncertainty in the position of spatial sampling events due to encoder signal variation, independent of spindle rotation. Uncertainty shown is found with 4 pole Chebyshev filter, 300kHz bandwidth and high SNR. Manufacturing speed range shown in yellow and constant 5 nm linear manufacturing tolerance shown in gray.

2.3.2 Timing Uncertainty

The TDR calibration method relies on accurate time measurements to determine the encoder error map. First the time measurements are used to estimate the dynamics of the spindle (inertia and damping coefficients), then the encoder error map is reconstructed from the time measurements. Finite time measurement resolution will cause uncertainty in the estimation of the encoder error map. Each time measurement, T_k, can be expressed as

$$T_k = \widehat{T}_k \pm \frac{1}{2 \cdot f_c} \tag{2.63}$$

where $\widehat{T}_k$ is the exact time interval width and f_c is the time measurement clock frequency. Figure 2.12 shows the uncertainty in time measurement due to finite time measurement resolution. The spatial interval

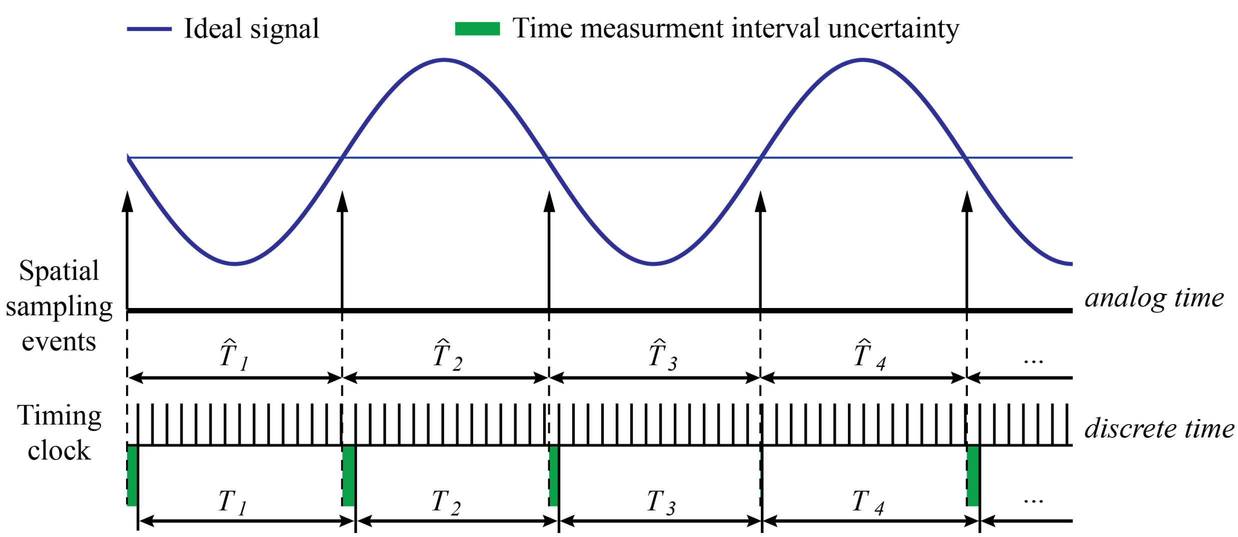

Figure 2.12: Demonstrated uncertainty in spatial sampling events due to timing measurement resolution.

is estimated based on a velocity assumption (Equation 2.11) as,

$$\Delta_k = \omega \cdot T_k \tag{2.64}$$

where the spindle speed is $\omega = 2\pi n/60$ and n is the spindle speed in rpm. Due to the uncertainty in the time measurement there will be a corresponding uncertainty in the spatial interval estimation,

$$\Delta_k = \widehat{\Delta}_k \pm \frac{\omega}{2 \cdot f_c} \tag{2.65}$$

where $\widehat{\Delta}_k$ is the exact spatial interval width. The angular uncertainty due to time measurement resolution is found as

$$d\theta = \frac{\omega}{2 \cdot f_c} \tag{2.66}$$

which can also be written as a linear tolerance from Equation 2.57 and the manufacturing writing radius Equation 2.58. Timing uncertainty gives the following constant linear manufacturing uncertainty

$$dx = \frac{R_i \cdot n_{min} \cdot \pi}{60 f_c}. \tag{2.67}$$

The linear manufacturing uncertainty caused by limited timing resolution is shown in Figure 2.13 and the angular manufacturing tolerance is shown in Figure 2.14. The minimum timing resolution required to meet the manufacturing tolerance is approximately 900 MHz.

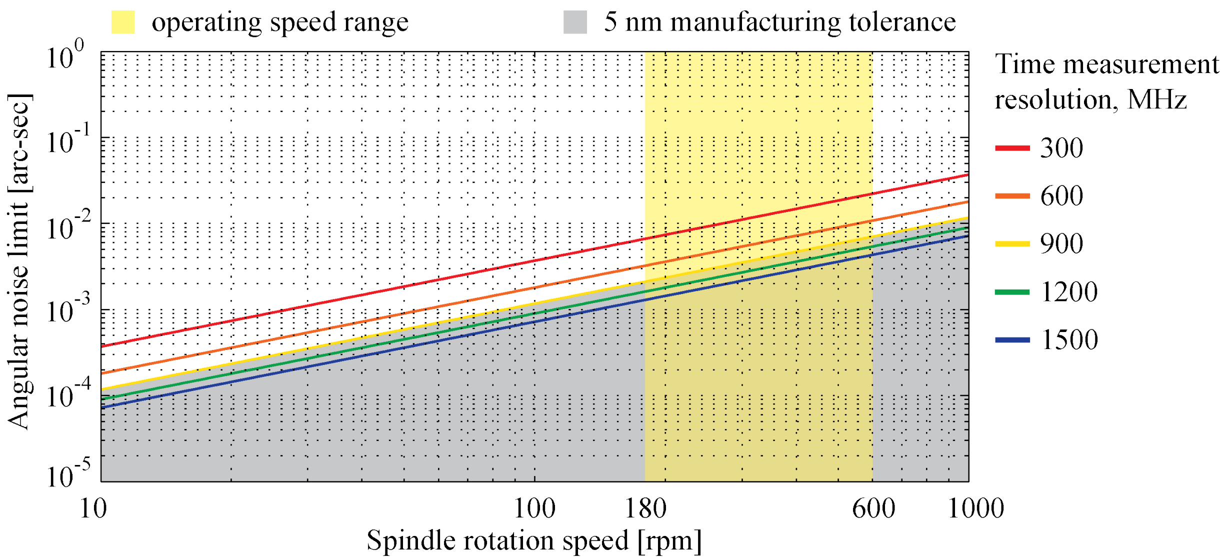

Figure 2.13: Predicted angular uncertainty in spatial sampling events due to finite time resolution.

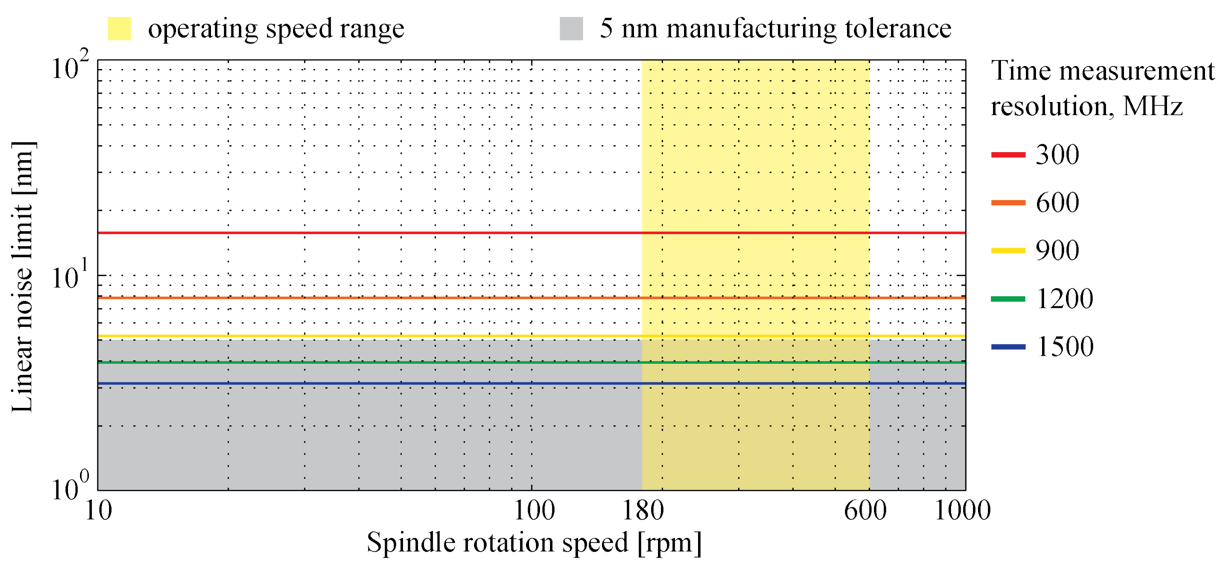

Figure 2.14: Predicted linear uncertainty in spatial sampling events due to finite time resolution.

2.3.3 Scanning Unit Alignment Uncertainty

In Section 2.1.2 two methods were introduced to completely isolate the rotary vibration component: harmonic cancellation and rotary vibration prediction. The harmonic cancellation method, used to determine all rotary vibration harmonics not a multiple of 4, relies on all scanning units to be evenly spaced around the encoder's circular scale (Equation 2.37). Accurate alignment of the scanning units is required to validate this assumption. A procedure has been developed to ensure accurate scanning unit alignment, as outlined in Section 4.5, but this section aims to determine the accuracy of alignment that is required to avoid significant calibration uncertainty.

To understand how misalignment results in incorrect rotary vibration isolation and consequently inaccurate error map calibration, the 4-head setup (Figure 2.4) is modified to include misalignment in Figure 2.15. In this situation, calibration results from each scanning unit differ from those in Equation 2.31 due to the

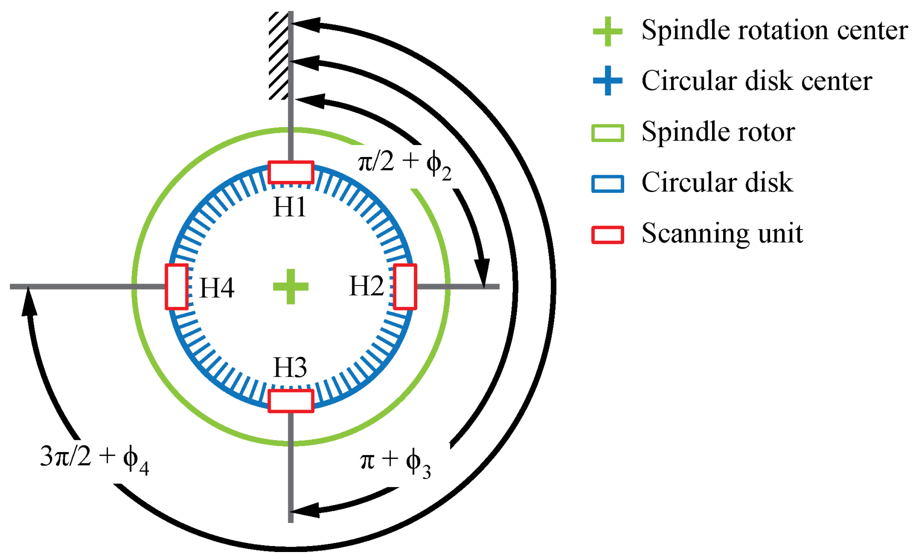

Figure 2.15: Relative alignment of each scanning unit, approximately evenly spaced around the circular scale with misalignment ϕ_j for j = 2,3,4 scanning units.

misalignment of each head ϕ_j.

$$\begin{array}{rcccccc} p_{H1}(k) = & g(k) & + & y(k)/R & + & v(k) \\ p_{H2}(k) = & g\left(k - N/4 - \phi_2 \frac{N}{2\pi}\right) & - & x(k)\cos\phi_2/R - y(k)\sin\phi_2/R & + & v(k) \\ p_{H3}(k) = & g\left(k - N/2 - \phi_3 \frac{N}{2\pi}\right) & + & x(k)\sin\phi_3/R - y(k)\cos\phi_3/R & + & v(k) \\ p_{H4}(k) = & g\left(k - 3N/4 - \phi_4 \frac{N}{2\pi}\right) & + & x(k)\cos\phi_4/R + y(k)\sin\phi_4/R & + & v(k) \end{array} . \tag{2.68}$$

The Fourier coefficients $P_{Hj}(n,\omega)$ of the derived encoder error map $p_{Hj}(k,\omega)$ for the j-th scanning unit are found as,

$$\begin{array}{rcccccc} P_{H1}(n,\omega) = & G(n,\omega) & + & Y(n,\omega)/R & + & V(n,\omega) \\ P_{H2}(n,\omega) = & G(n,\omega)\cdot e^{-jn(\pi/2+\phi_2)} & - & X(n,\omega)\cos\phi_2/R - Y(n,\omega)\sin\phi_2/R & + & V(n,\omega) \\ P_{H3}(n,\omega) = & G(n,\omega)\cdot e^{-jn(\pi+\phi_3)} & + & X(n,\omega)\sin\phi_3/R - Y(n,\omega)\cos\phi_3/R & + & V(n,\omega) \\ P_{H4}(n,\omega) = & G(n,\omega)\cdot e^{-jn(3\pi/2+\phi_4)} & + & X(n,\omega)\cos\phi_4/R + Y(n,\omega)\sin\phi_4/R & + & V(n,\omega) \end{array} . \tag{2.69}$$

The average of error map harmonics for all scanning units, used to extract rotary vibration, now includes residual grating error and spindle radial error motion components. These components no longer cancel between scanning units due to misalignment and alter the rotary vibration estimation.

$$\begin{aligned}\frac{P_{H1}(n)+P_{H2}(n)+P_{H3}(n)+P_{H4}(n)}{4} &= G(n)\frac{n}{4}\left[\phi_2\cdot e^{-jn(\pi+\phi_2/2)}+\phi_3\cdot e^{-jn(3\pi/2+\phi_3/2)}+\phi_4\cdot e^{-jn\phi_4/2}\right] \\ &+X(n,\omega)(-\cos n\phi_2+\sin n\phi_3+\cos n\phi_4)/4R+Y(n,\omega)(1-\sin n\phi_2-\cos n\phi_3+\sin n\phi_4)/4R+V(n) \\ &\text{for } n\neq 4m\end{aligned} \tag{2.70}$$

Residual grating error is most influential due to greater magnitudes compared with the spindle radial error motion component. Additionally, the much larger magnitude of the first order harmonic of grating error, dominated by encoder circular scale offset (Equation 1.1), will lead to the most residual grating error and cause the most inaccuracy in rotary vibration estimation. As a quick rule of thumb, the amplitude of residual grating error $|G(n)|$ when a single scanning unit is misaligned by ϕ_m is

$$|G_r(n)|=\frac{1}{4}|G(n)|\cdot n\phi_m \tag{2.71}$$

for a given harmonic n and amplitude of grating error $|G(n)|$. Higher harmonics will create more residual grating error as they have increased relative misalignment.

To include the effects of higher grating error harmonics a simulation was conducted. A grating error map is simulated for each scanning unit with only the first 20 harmonics not multiple of 4, the criteria for harmonic cancellation (Equation 2.37) and rotary vibration removal (Equation 2.42). The sum of grating error maps for the four scanning units should, without misalignment, cancel completely. With misalignment they do not cancel and give a measurement of the uncertainty. Figure 2.16 shows the simulated result with misalignment of 200 counts or (2,000 arc-sec). A rms uncertainty of 0.007 arc-sec is found, where

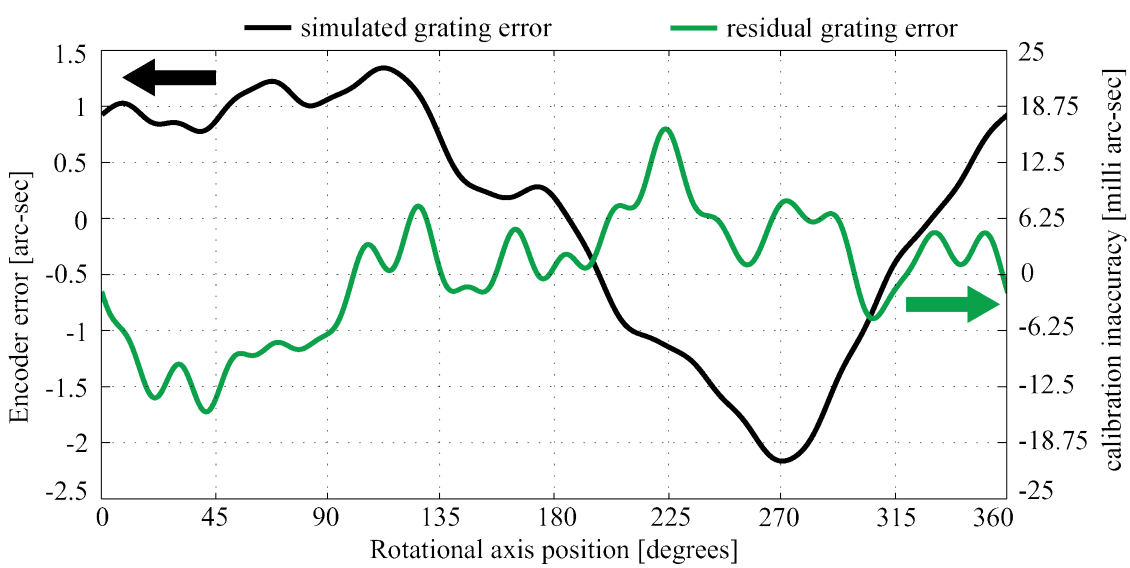

Figure 2.16: Inaccuracy of rotary vibration removal and calibration due to misalignment of scanning units in the 4-head setup. Simulated grating error shown in black (left hand scale) and residual grating error shown in green (right hand scale).

the prediction of Equation 2.71 estimates a residual grating error amplitude of 0.0025 arc-sec. Figure 2.17 shows the uncertainty over a range of misalignments from 1 count (10 arc-sec) to 200 counts (2,000 arc-sec), and displays the linear relationship to misalignment as predicted in Equation 2.71.

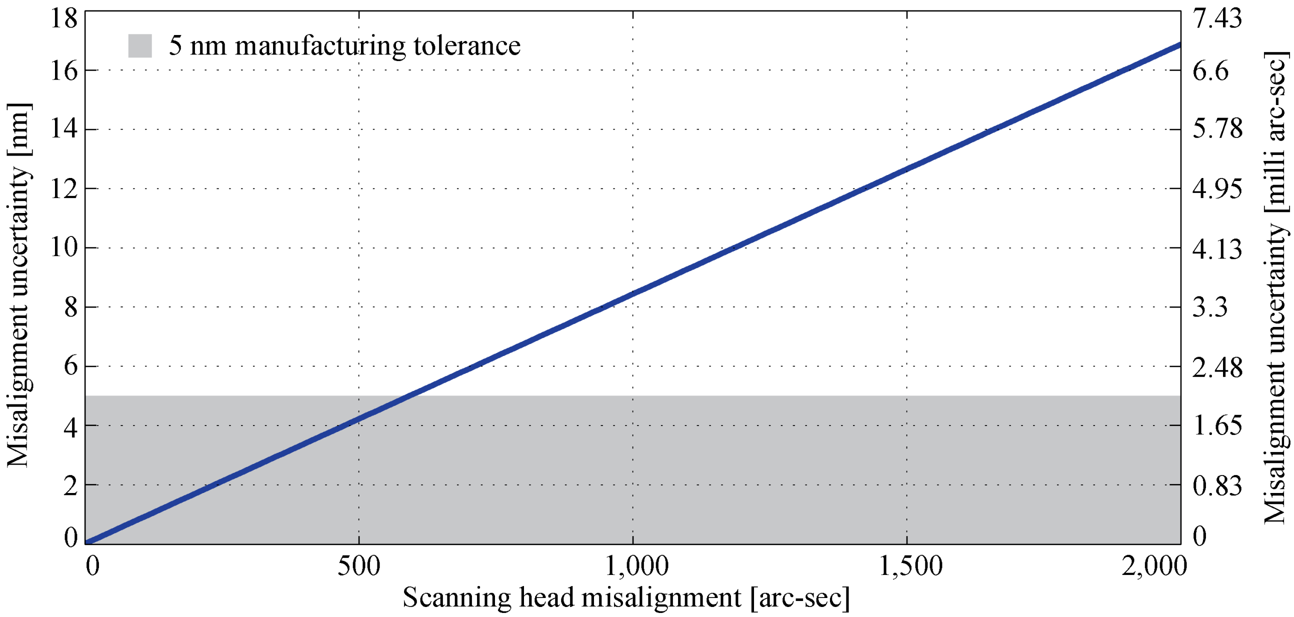

Figure 2.17: Inaccuracy of rotary vibration removal over a range of scanning unit misalignments.

2.4 Calibration Comparison

The EDA calibration method developed at the National Metrology of Japan (NMIJ) [8–10, 32] is known for having state of the art calibration accuracy. This method has been widely experimented on and in other national metrology institutes such as the Germany metrology institute PTB [11, 13]. The self-calibratable rotary encoder developed at NMIJ [26] and based on the calibration theory of the EDA method, has particular application in our four head setup. The EDA method does not rely on spindle dynamics and thus is insensitive to rotary vibration or torque disturbance. However, the EDA method cannot determine encoder error map harmonics that are multiples of the number of scanning units installed on the setup. This is due to relying on error map harmonic cancellation between the scanning units to determine the measurement errors. A comparison of the TDR and EDA methods can provide insight into the limitations of encoder calibration and help support the calibration accuracy of the TDR method.

The analysis and derivation of the EDA calibration method for a self-calibratable encoder [26] does not consider the measurement error contribution of spindle radial error motion. The authors assume scanning units mounted evenly around the circular scale measure identical error components. The theoretical derivation of the self-calibratable rotary encoder, including spindle radial error motion components, is provided to show the method still has application for a calibration comparison between the TDR method.

Figure 2.18 shows the cumulative angle measurement errors, $p_{Hi}(k)$, from each scanning unit mounted in the four head setup referenced by the ideal grating positions equally spaced apart by $\Delta_0 = 2\pi/N$. The measurement errors have both grating and spindle radial error motion components defined in Equation 2.49. The ideal circular scale grating positions are unknown during the measurement, so these errors can not be

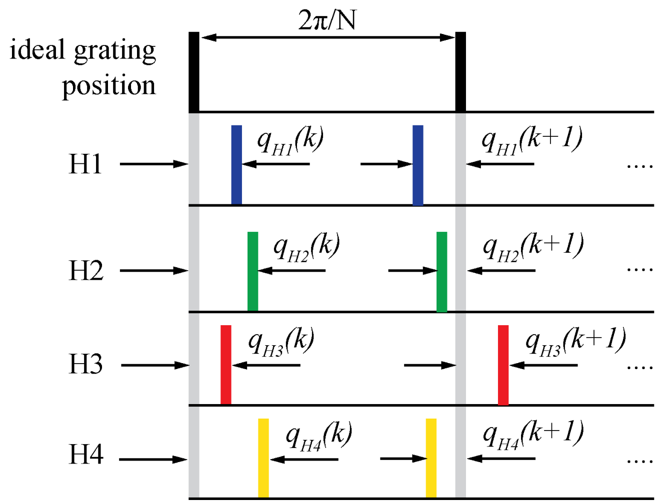

Figure 2.18: Cumulative angle measurement errors, referenced to the ideal grating positions evenly spaced around the circular scale.

directly found. Instead, the angle measurement differences, $d_{i,j}$, are used. The measurements are defined for each of the scanning units, j with respect to i-th scanning unit. This is shown in Figure 2.19 for measurement difference with respect to scanning unit H1. These relative errors can be determined through time

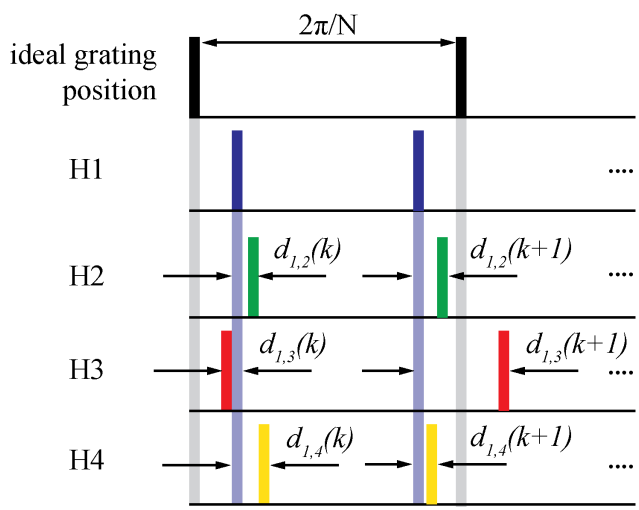

Figure 2.19: Angle measurement differences relative to scanning unit H1.

measurements when each spatial interval is detected for each scanning unit, $t_{k,Hj}$. In comparison the TDR method relies on time measurements between spatial intervals, T_k. The relative measurement differences are found as

$$d_{i,j}(k) = \frac{t_{k,Hi} - t_{k,Hj}}{t_{k+1,Hj} - t_{k,Hj}} \cdot \frac{2\pi}{N} \tag{2.72}$$

where $\frac{2\pi/N}{t_{k+1,Hj} - t_{k,Hj}}$ is an estimation of speed between consecutive spatial intervals. The speed between consecutive spatial intervals is assumed constant and because no assumption is made of the long term spindle free response profile, which can vary significantly, the method is insensitive to rotary vibration. The measurement differences of Equation 2.72 can also be written in the form of the encoder error maps, $q_{Hj}(k)$, as

$$d_{i,j}(k) = q_{Hi}(k) - q_{Hj}(k). \tag{2.73}$$

The average of the measurement differences for all scanning units yields an estimate of the encoder error map, $\overline{q}_{Hi}(k)$, as

$$\overline{q}_{Hi}(k) = \frac{1}{4}\sum_{j=1}^{4} d_{i,j}(k) = q_{Hi}(k) - [q_{H1}(k) + q_{H2}(k) + q_{H3}(k) + q_{H4}(k)]/4, \tag{2.74}$$

where $[q_{H1}(k) + q_{H2}(k) + q_{H3}(k) + q_{H4}(k)]/4$ is the average of error maps for each scanning unit. This is a harmonic cancellation term (Section 2.1.2), where all error map harmonics not multiple of four cancel.

The presence of radial error motion does not affect this result due to its cancellation between diametrically opposing scanning units. Only the grating error component is removed from the estimated error map

$$[q_{H1}(k) + q_{H2}(k) + q_{H3}(k) + q_{H4}(k)]/4 = [g(k) + g(k-N/4) + g(k-N/2) + g(k-3N/4)]/4. \tag{2.75}$$

The Fourier coefficients of the estimated error map, $\overline{Q}_{Hi}(n)$, from the EDA method are

$$\overline{Q}_{Hi}(n) = \begin{cases} Q_{Hi}(n) & \text{if } n \neq 4m \\ 0 & \text{if } n = 4m \end{cases}. \tag{2.76}$$

The error map estimation of Equation 2.74 is only a partial representation of the actual error map, without error map harmonics that are multiple of four.

This method estimates the encoder error map using measurements from all scanning units. This has an averaging effect so that uncertainties in the error map calibration are significantly less than the TDR method. Although this method provides calibration with reduced uncertainty, the method is limited in accuracy because it cannot determine the full harmonics of the measurement error.

Chapter 3

Simulation

Simulation is used to confirm the accuracy of the calibration method and determine any theoretical limitations to improve upon. The advantage of simulation being that the theoretical accuracy of the calibration method can be found without additional uncertainties introduced due to the mechanical setup or custom electronics. Experimental accuracy, on the other hand, cannot be so easily determined and we must rely on other benchmarks such as repeatability and calibration comparison methods to support experimental accuracy.

In this section the simulation method is presented, with the equations and parameters implemented. A simulation of a second-order damping spindle is presented and comparison of the calibration accuracy obtained from three calibration methods is presented. The methods investigated are the original TDR calibration method [28], TDR calibration with rotary vibration removal and TDR calibration with integration enhancement and rotary vibration removal. Each method shows the incremental improvement in calibration accuracy that has been developed. The set repeatability and accuracy of spindle radial error motion estimation is investigated for TDR calibration with rotary vibration removal and integration enhancement.

3.1 Simulation Method

The TDR self-calibration method is applied to a simulated spindle with 4 scanning units. The simulated model includes graduation error, spindle radial error motion and rotary vibration due to torque disturbance, Figure 3.1. The exact spatial interval positions for each scanning unit are first found, including the small spatial deviations due to graduation error and spindle radial error motion. The dynamics of the spindle, inertia and second-order damping, are simulated to determine the effective time measurements of each spatial interval using a modified version of Equation 2.4, that includes the effect of disturbance torque,

$$d\omega/dt + c\omega = M(\theta). \tag{3.1}$$

The time measurements are quantized, to include time uncertainty due to a finite time measurement resolution. This simulation is performed at various rotational speeds over the range of 100 rpm to 1,000 rpm. The time measurements are then put through the TDR self-calibration method and estimates of the spindle dynamics, encoder error map, spindle radial error motion and torque disturbance are found. A direct comparison of the estimated components with the input values is used to determine the theoretical calibration accuracy. This represents a realistic performance benchmark for our algorithm because the self-calibration method does not change with experimental measurements. Rather the simulated rotation axis is replaced

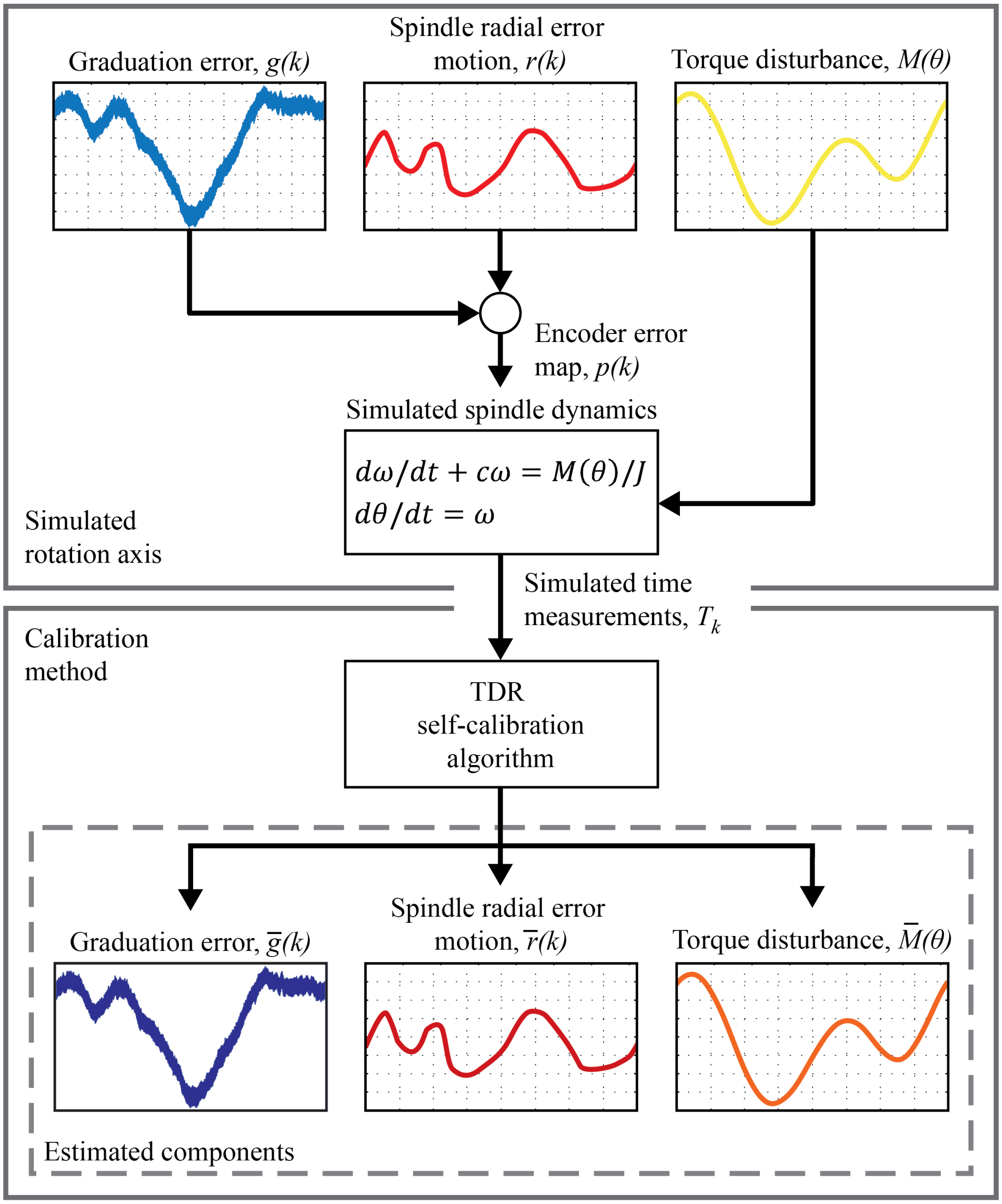

Figure 3.1: Simulation block diagram. Graduation error and spindle radial error motion are combined to determine spatial locations of sampling events. Modeled spindle dynamics and torque disturbance are used to simulate time measurements of the spatial sampling events. TDR calibration is performed and the results are compared with the inputs.

with the experimental setup.

3.2 Simulation Parameters

Experimental data was used to guide the selection of the parameters used in simulation. The spindle dynamics were simulated with a second-order damping model from Equation 2.6 with the inertia and normalized damping values given in Table 3.1.

Table 3.1: Coefficients of the simulated dynamics.

$J = 0.389\ kg \cdot m^2$	$c_0 = 7.72 \times 10^{-3}\ s^{-1}$	$c_1 = 1.35 \times 10^{-4}\ rad^{-1}$

Inertia was estimated using a solid model of the spindle rotor while damping coefficients were obtained from experimental calibration results. To effectively simulate the timing electronics, a timing resolution of 600 MHz frequency was simulated, which is readily available in experiment. The graduation error, $g(k)$, and torque disturbance, $M(\theta)$, were also found through experimental calibration results as shown in Figure 3.2 and Figure 3.3 respectively.

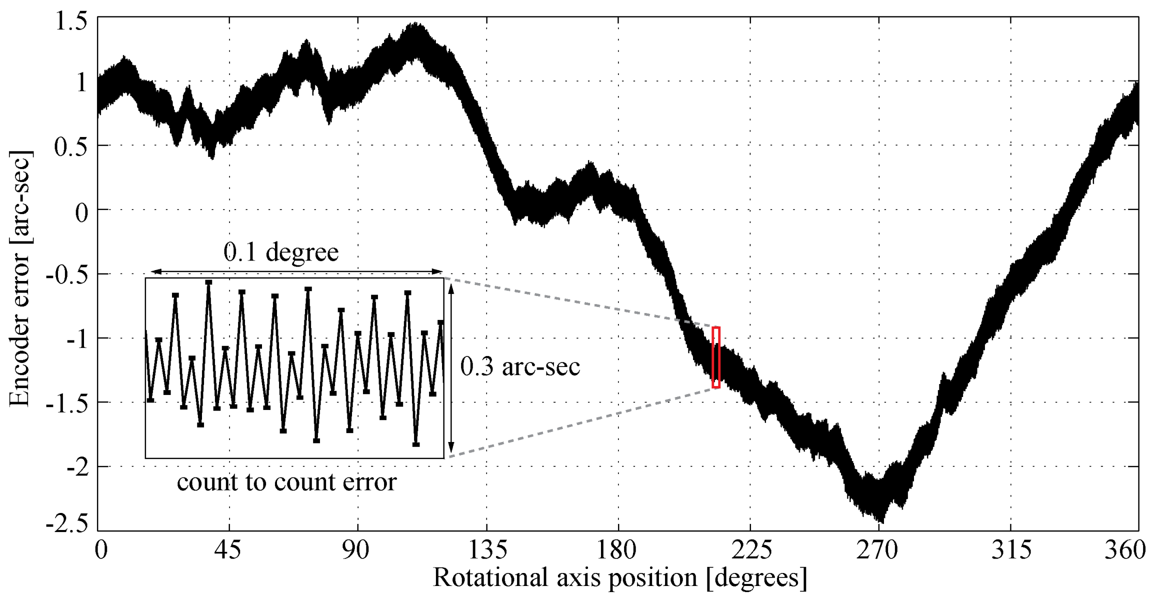

Figure 3.2: Graduation error input of simulation.

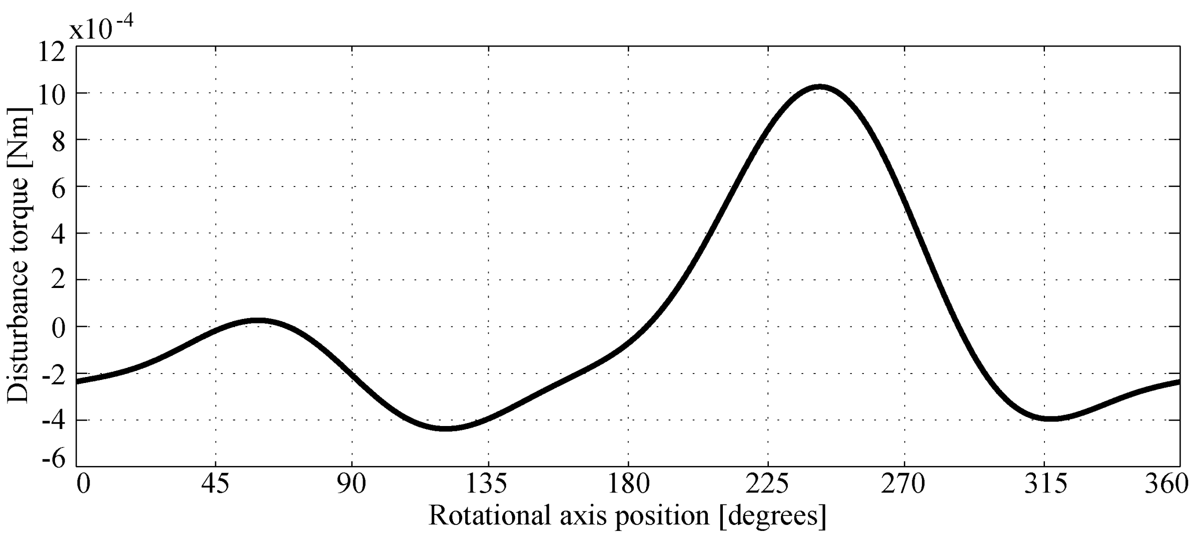

Figure 3.3: Torque disturbance input of simulation.

High frequency, count to count, graduation error was simulated to include the effect of quadrature decoding interpolation. Torque disturbance was constructed with 5 harmonics because only the first five disturbance torque harmonics could accurately be obtained from experiment. Subsequent harmonics were below the noise limit of the experimental calibration. The harmonic amplitudes of the disturbance torque are shown in Table 3.2. The input values of spindle radial error motion were found with capacitance probe

Table 3.2: Torque disturbance input harmonics.

Harmonic No.	1	2	3	4	5
Amplitude [Nm$\times 10^{-3}$]	0.192	0.213	0.057	0.053	0.011

measurements and ball roundness separation shown in Figure 3.4. A 2D representation of the spindle error motion [29–31] is used, with harmonic amplitudes given in Table 3.3. The spindle error motion harmonics are typically speed dependent, increasing at higher rotational speeds in experimental measurements. This speed variation was also included in the simulation, approximated as a 5% increase of the initial harmonic amplitudes, in Table 3.3, per 100 rpm change in speed.

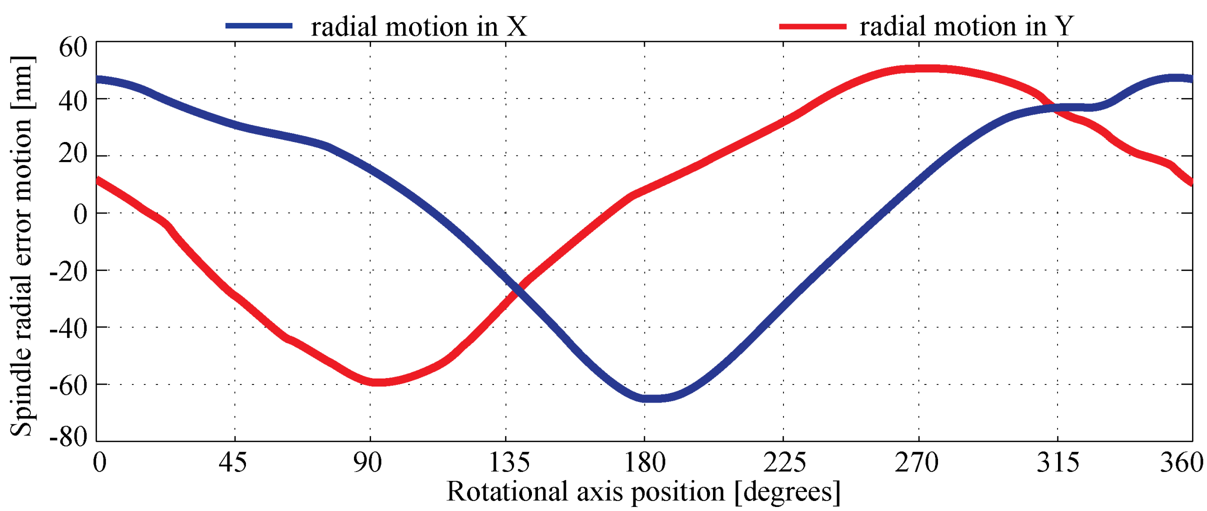

Figure 3.4: Spindle radial error motion input of simulation.

Table 3.3: Spindle radial error motion input harmonics.

Harmonic No.	-5	-4	-3	-2	-1	2	3	4	5
Amplitude [nm]	1.0	0.4	0.3	5.4	49.8	7.9	4.5	0.5	1.1

3.3 Simulation Results

Three calibration methods are applied to the simulated time measurements, T_k: (a) The original TDR calibration method in [28], without vibration removal or integration enhancement. (b) TDR calibration with rotary vibration removal but without integration enhancement. (c) TDR calibration with both rotary vibration removal and integration enhancement.

3.3.1 Calibration Inaccuracy

Calibration inaccuracy is investigated for the three methods. Calibration inaccuracy is defined as the difference between the true encoder error map, $g(k)+r(k)$ and the estimated encoder error map from the calibration method, $q(k)$ from Equation 2.43. Figure 3.5 shows the simulated result at a spindle rotation speed of 500 rpm. Without integration enhancement or rotary vibration removal, the rms inaccuracy is 0.0604 arc-sec

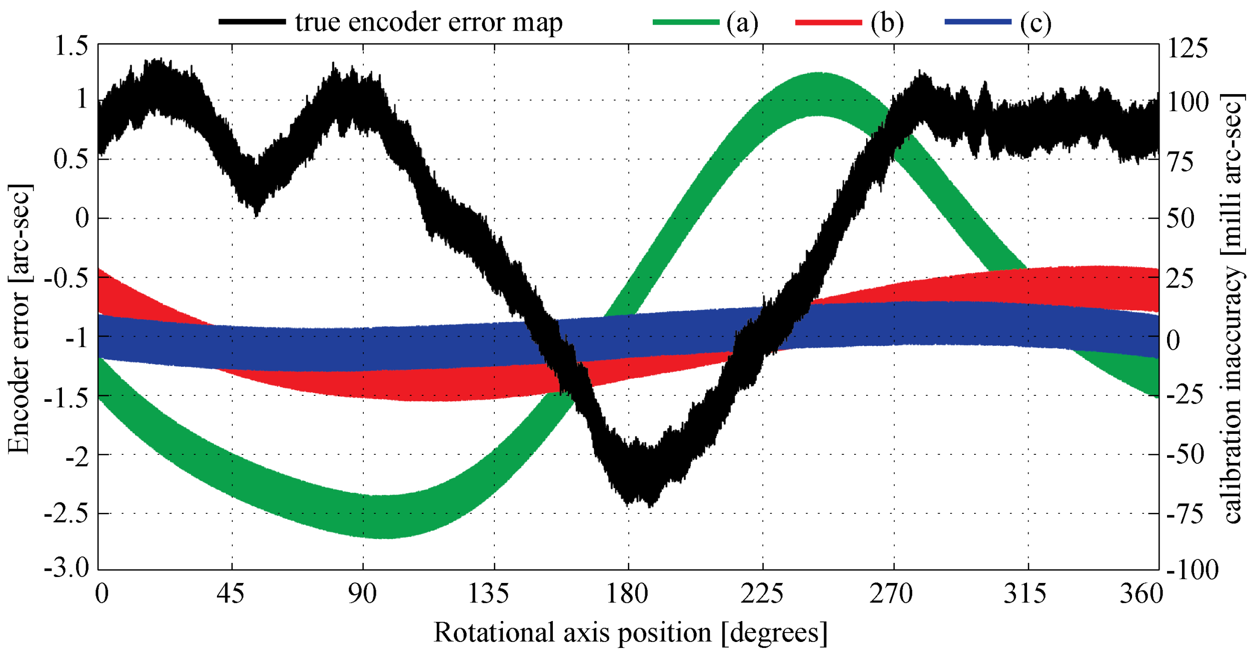

Figure 3.5: Simulated inaccuracy at spindle speed of 500 rpm. The true encoder error map is shown in black (left hand scale); the inaccuracy curves (right hand scale) of TDR calibration (a) without integration or vibration removal, (b) vibration removal only, and (c) with both integration enhancement and rotary vibration removal.

rms. With rotary vibration removal the inaccuracy is improved to 0.0149 arc-sec rms. Finally, with both rotary vibration and integration enhancement the inaccuracy is further improved to 0.0066 arc-sec rms. To further study calibration inaccuracy the simulation was conducted over a wide spindle rotation speed range. Figure 3.6 shows the rms inaccuracy of each method over the speed range of 1,000 rpm down to 100 rpm. It is confirmed that rotary vibration and integration enhancement greatly improve the TDR method accuracy close to the theoretical limit set by time-measurement quantization (Equation 2.66).

Two limitations in this calibration technique could exist. Erroneous damping estimation, the main working principle of our calibration method, could result in incorrect error map estimation. Alternatively the reconstruction of the error map from time measurements could cause a dominant inaccuracy. These two limitations are discussed in the following section.

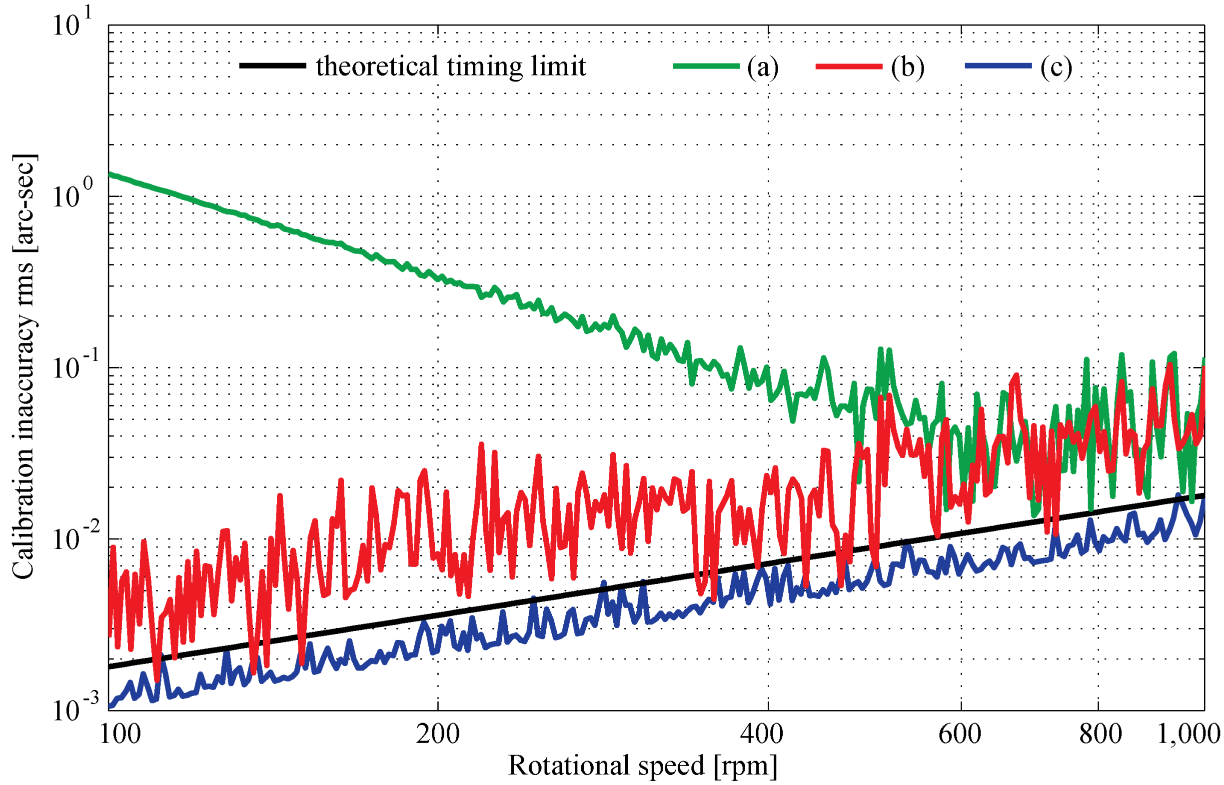

Figure 3.6: Simulated inaccuracy at spindle speeds. Time quantization accuracy limit shown in black; rms inaccuracy curves of TDR calibration (a) without integration or vibration removal, (b) vibration removal only, and (c) with both integration enhancement and rotary vibration removal.

3.3.2 Damping Estimation and Error Map Inaccuracy

The calibration technique relies on accurate damping estimation to remove the speed dependence of the time measurements and estimate the spatial distances between each encoder count. Thus, an incorrect damping estimation would result in an incorrect error map estimation.

The damping estimates from a calibration of simulated time measurements are compared for two experimentally applicable calibration methods: (b) TDR calibration with rotary vibration removal but without integration enhancement; (c) TDR calibration with both rotary vibration removal and integration enhancement. As shown in Figure 3.7 and Figure 3.8 there is a significant improvement in damping estimation with integration enhancement. Still, at high speeds the damping estimate deviates from the true damping coefficient as uncertainties in the time measurements make accurate damping estimation more difficult. The second-order damping coefficient, Figure 3.8, is especially sensitive to uncertainties and is sometimes estimated with a negative value. A negative damping coefficient has no physical meaning, and would imply damping is adding energy to the system instead of removing it. The negative result indicates the calibration algorithm is fitting uncertainty in the time measurements instead of physical encoder error.

The inaccuracy of calibration methods (b) and (c) were investigated in Section 3.3.1 and as seen in Figure 3.7 and Figure 3.8 there is significant damping estimation inaccuracy for these methods. To determine if the cause of error map inaccuracy is due to poor damping estimation, the best case calibration scenario with perfect damping coefficient estimation, is investigated. In this case, the error map estimation is then

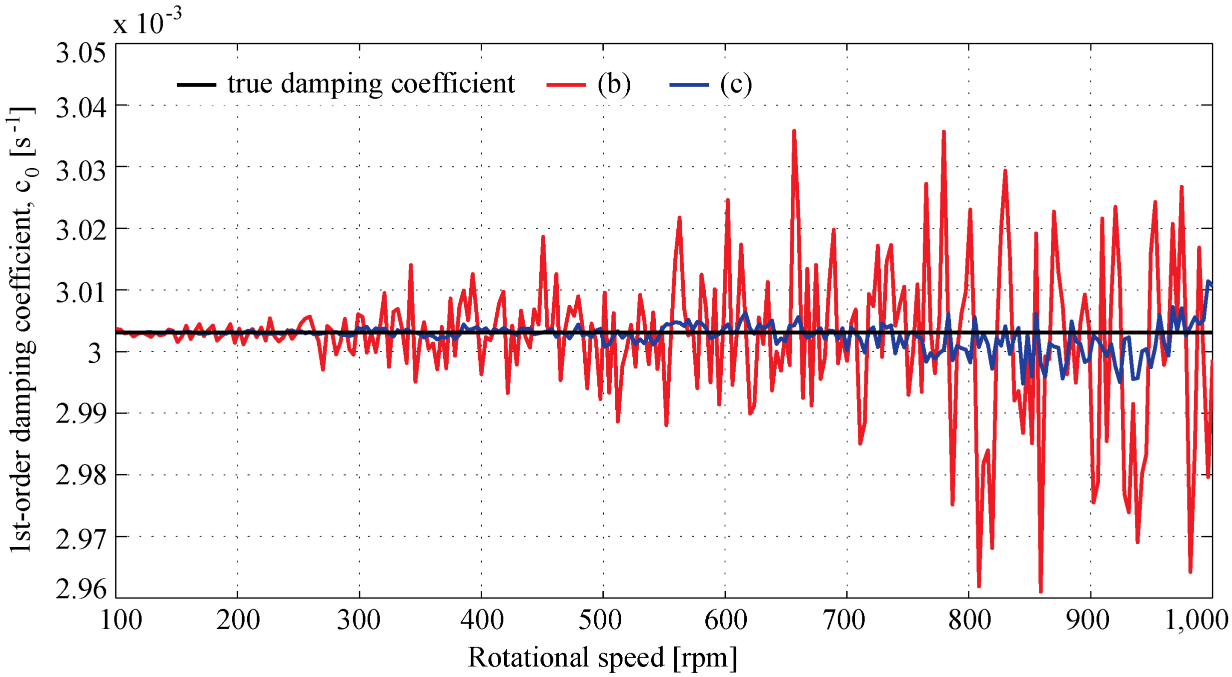

Figure 3.7: First-order damping coefficient simulation results. True damping coefficient shown in black and damping coefficients of TDR calibration with (b) vibration removal only and (c) both integration and rotary vibration removal.

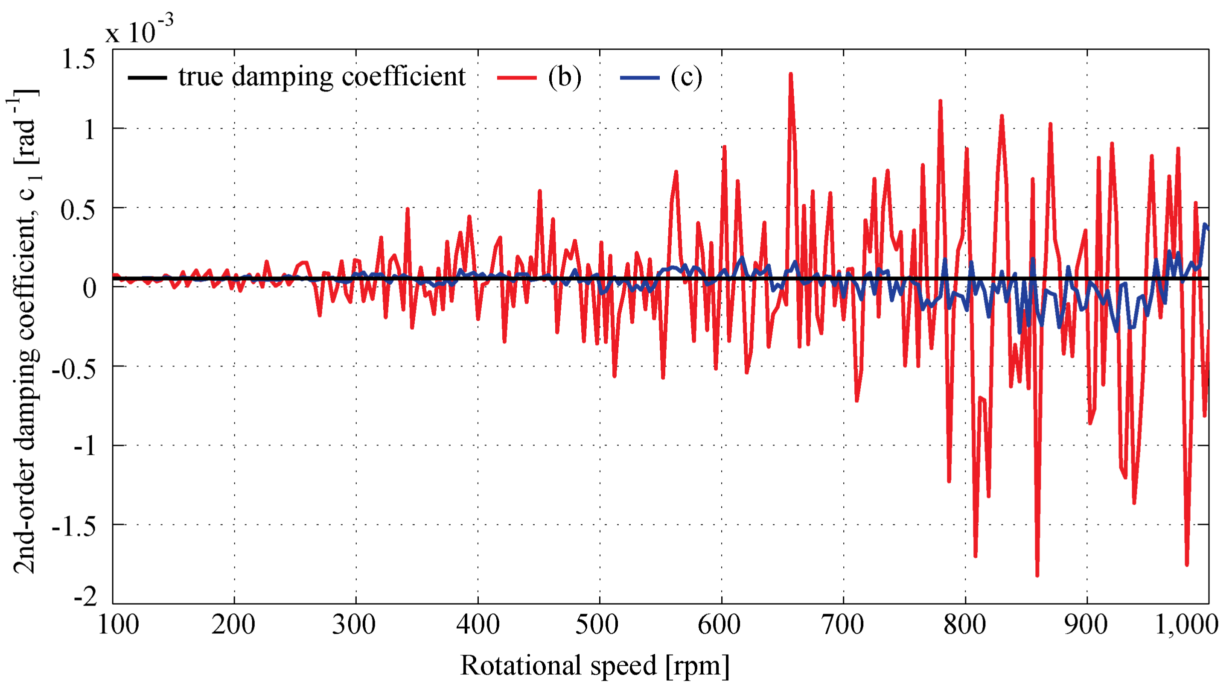

Figure 3.8: Second-order damping coefficient simulation results. True damping coefficient shown in black and damping coefficients of TDR calibration with (b) vibration removal only and (c) both integration and rotary vibration removal.

purely a function of time measurement uncertainties. Figure 3.9 shows the simulated calibration inaccuracy result at a spindle speed of 500 rpm. The rms inaccuracy with perfect damping estimation does not improve

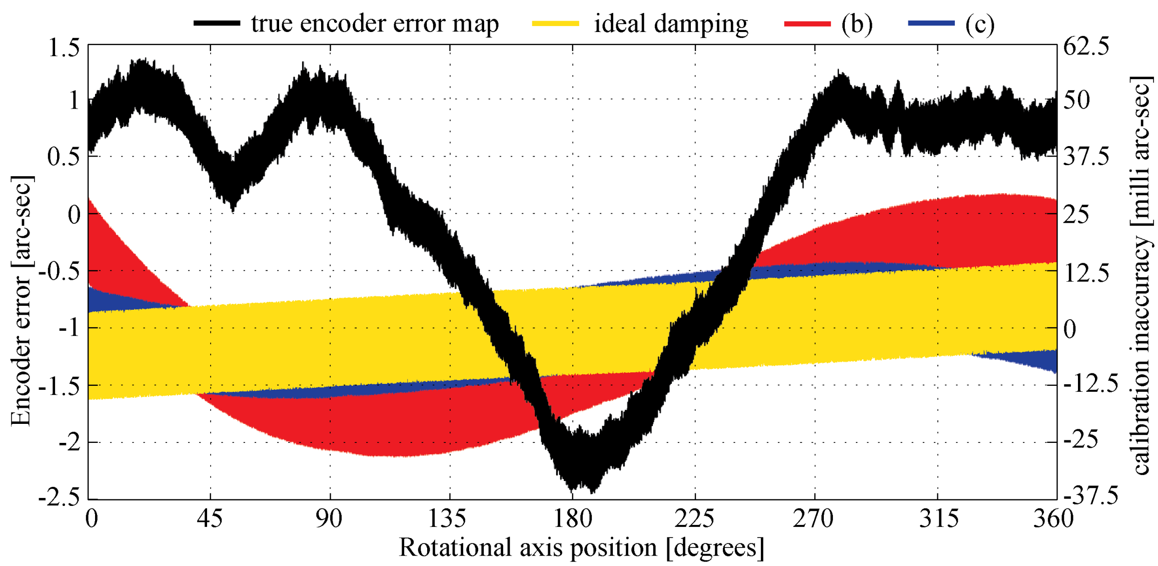

Figure 3.9: Simulated inaccuracy at spindle speed of 500 rpm. The true encoder error map is shown in black (left hand scale); the inaccuracy curves (right hand scale) of error map reconstruction with perfect damping estimate and TDR calibration with (b) vibration removal only, and (c) with both integration enhancement and rotary vibration removal.

significantly, found as 0.0062 arc-sec less than 0.4 thousandths of an arc-sec improvement. The simulation was also conducted over the speed range of 1,000 rpm down to 100 rpm shown in Figure 3.10. It is confirmed

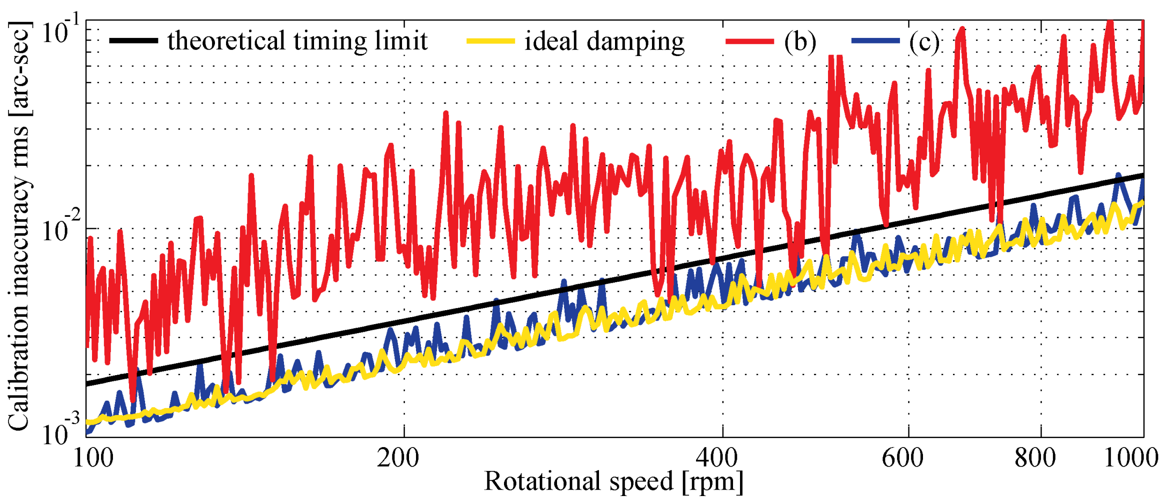

Figure 3.10: Simulated inaccuracy at spindle speeds. Time quantization accuracy limit shown in black; rms inaccuracy curves error map reconstruction with perfect damping estimate and TDR calibration with b) vibration removal only, c) with both integration enhancement and rotary vibration removal and with perfect damping estimate

that error map inaccuracy is a result of error map reconstruction and not a cause of poor damping estimation.

An improvement to the calibration method can be made to increase the accuracy and consistency of the damping estimation as presented in Appendix A, but this further effort would not improve the result. Time measurement uncertainty is the dominant cause of error map inaccuracy.

3.3.3 Experimental Calibration Inaccuracy Metrics

Calibration accuracy can only be determined in simulation and cannot be directly found in experiment. Instead, experimentally achievable metrics, set repeatability and spindle radial error motion estimation, are used to indirectly asses the accuracy of experimental results. Simulation is performed on TDR calibration with rotary vibration removal and integration enhancement, so that a conversion to approximate accuracy in experiment can be determined.

Calibration Set Repeatability

Due to dynamic reversal, two sets of data are required to perform estimation of the spindle dynamics. Thus two calibration error maps, $q_1(k)$ and $q_2(k)$, are obtained each calibration. It is assumed in the derivation that both error maps are identical, any difference in the error maps is a direct cause of calibration uncertainty. Set repeatability is defined as the difference between the two error maps obtained in one calibration, $q_1(k) - q_2(k)$, and can give a measure of error map estimation uncertainty. Figure 3.11 shows the simulated result at a spindle rotation speed of 500 rpm. The TDR calibration method with rotary vibration removal

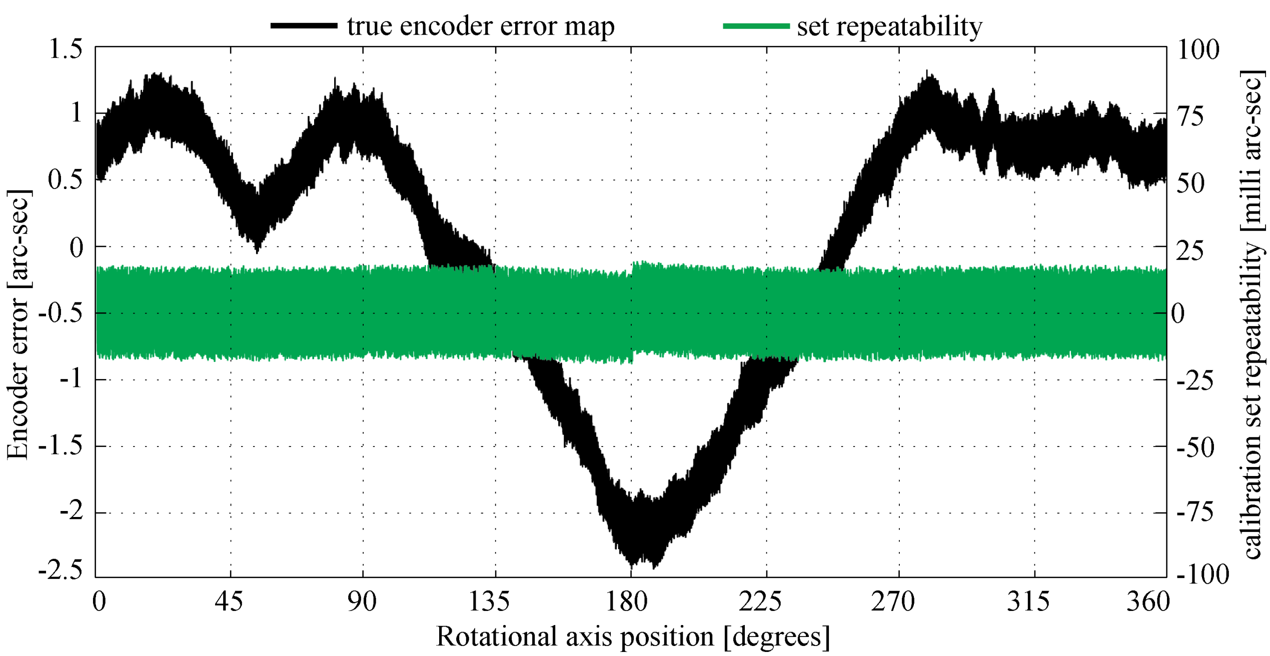

Figure 3.11: Simulated set repeatability at 500 rpm. The true encoder error map shown in black (left hand scale); set repeatability of TDR calibration with integration enhancement and vibration removal (right hand scale).

and integration enhancement shown, has a rms set repeatability of 0.0074 arc-sec. Figure 3.12 shows both calibration inaccuracy and set repeatability curves over a wide spindle rotation speed range. Similar to calibration inaccuracy set repeatability varies with speed due to time measurement quantization. Set repeatability is determined from the difference of two error maps, the uncertainty of each error map will be added as the root sum of squares and thus repeatability will be proportional to accuracy,

$$\text{rms set repeatability} = \sqrt{2} \cdot \text{rms inaccuracy}. \tag{3.2}$$

This predicted pattern is confirmed in simulation results. Set repeatability shows the trend of increasing inaccuracy with rotational speed and gives the best case inaccuracy that can be achieved. The set repeatability metric is more consistent, than the inaccuracy, which is believed to be caused by the calibration algorithm fitting the damping coefficients around uncertainties.

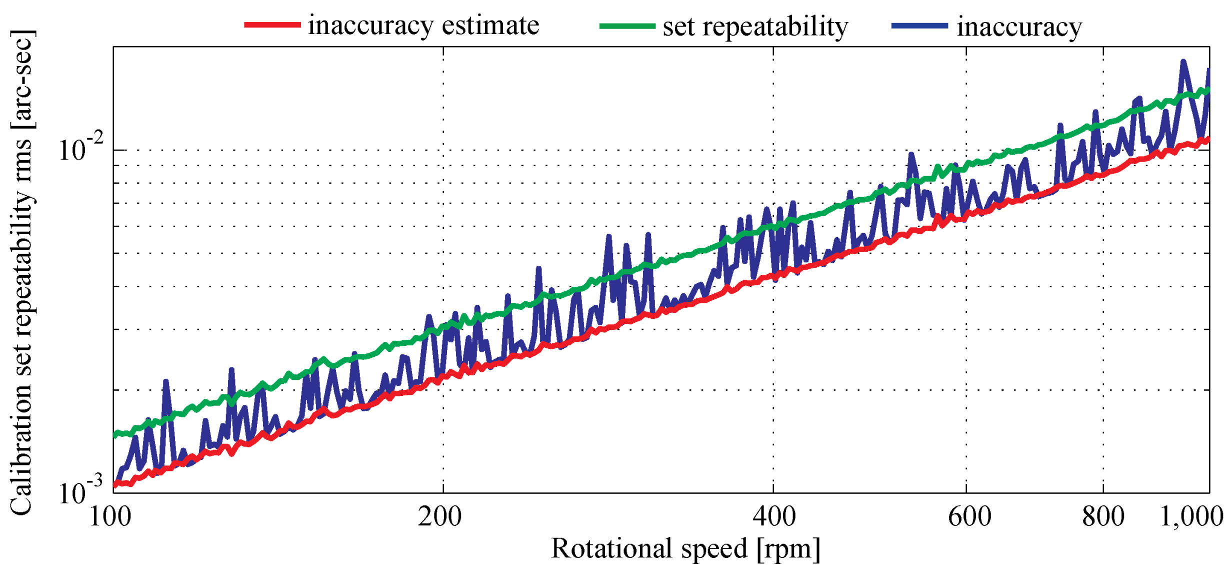

Figure 3.12: Simulated rms set repeatability at spindle speeds. rms inaccuracy of TDR calibration with both integration and rotary vibration removal shown in blue; rms set repeatability shown in green; and accuracy estimation of Equation 3.2, shown in red.

Spindle Radial Error Motion Estimation

Section 2.2 presented a method for extracting the spindle radial error motion from calibration results of four scanning units in the 4-head setup. This method was performed on the calibration results from simulated time measurements and compared to the error motion input, Figure 3.4 and Table 3.3.

Two-dimensional error motion harmonics, -1, +3 and -5 are extracted as shown in Figure 3.13, Figure 3.14 and Figure 3.15. The estimated spindle radial error motion follows the trend of increasing error motion with spindle speed. For the higher error motion harmonics, with smaller amplitudes, the uncertainty of the estimation increases. Although the introduced timing uncertainties are high frequency, effecting the results of individual spatial events, uncertainties are seen in the lower harmonics of the error map estimation. This is due to the reconstruction of the error map from each individual time measurement, so that the uncertainties are spread out across all harmonics of an error map. The inaccuracy of error motion estimation is shown in Figure 3.16. The higher magnitude of the -1 harmonic leads to increased amount of inaccuracy. The error motion measured by the scanning units is motion at the circumference of the circular scale, thus error motion inaccuracy is directly related to angular inaccuracy through the radius of the circular scale. Then inaccuracy of error motion estimation can be related to the inaccuracy of error map estimation

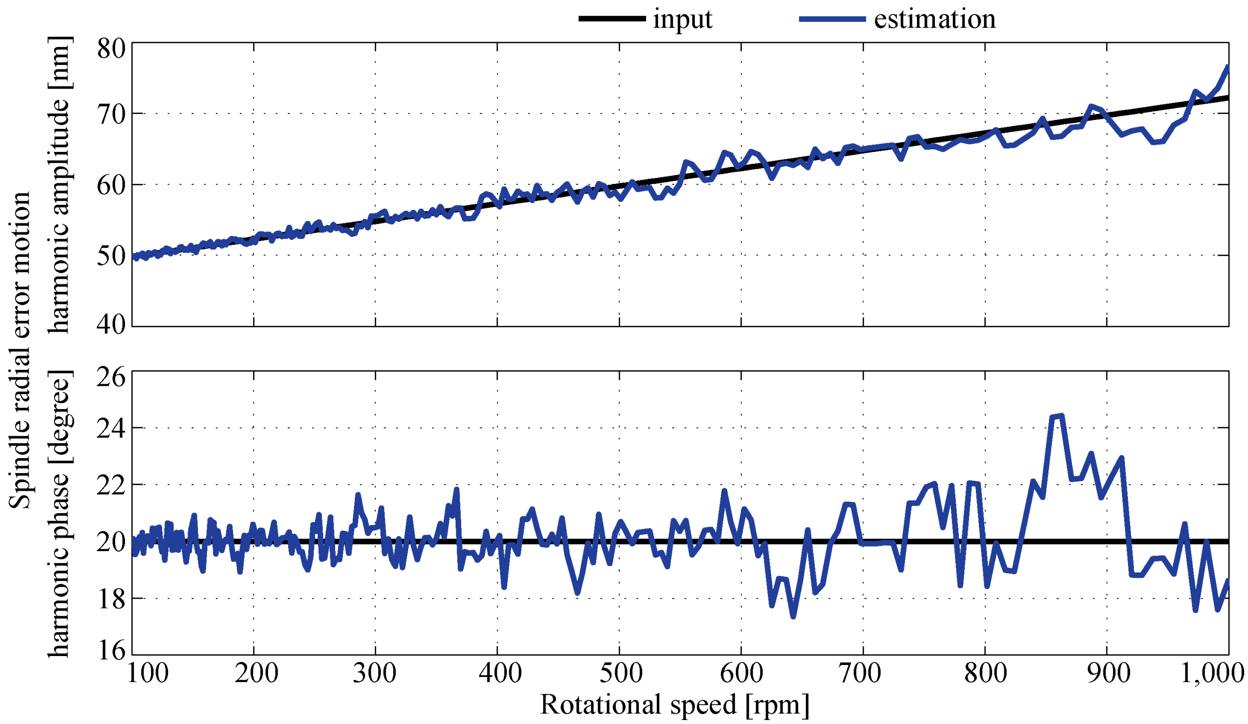

Figure 3.13: Simulation results of fundamental -1 spindle error motion harmonic. Input spindle radial error motion shown in black; spindle radial error motion estimation derived from encoder calibration error maps shown in blue.

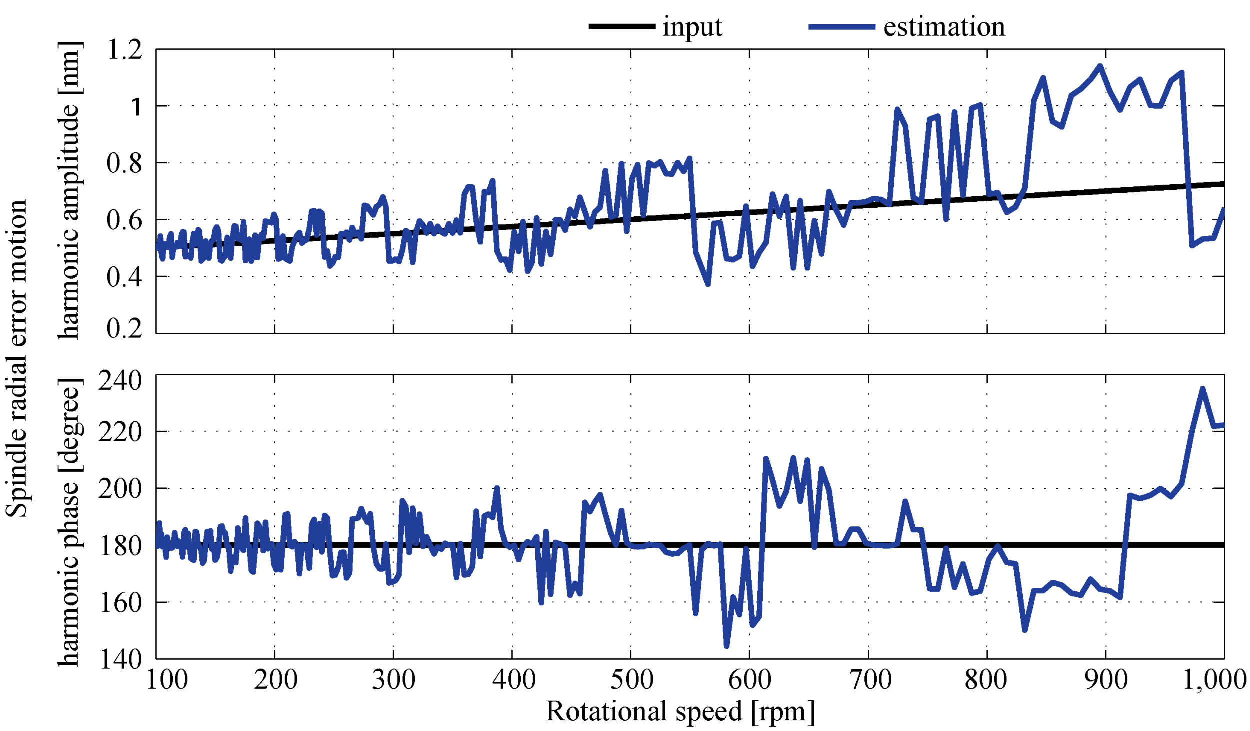

Figure 3.14: Simulation results of spindle error motion harmonic +3. Input spindle radial error motion shown in black; spindle radial error motion estimation derived from encoder calibration error maps shown in blue.

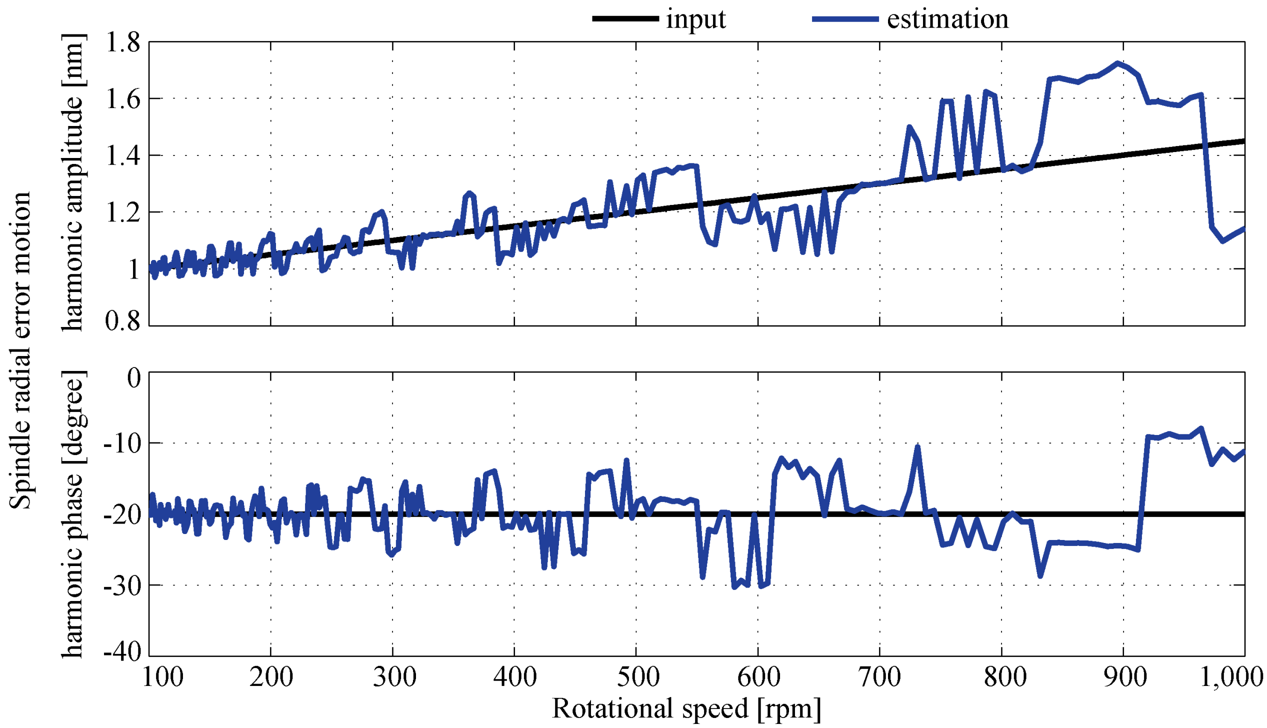

Figure 3.15: Simulation results of spindle error motion harmonic -5. Input spindle radial error motion shown in black; spindle radial error motion estimation derived from encoder calibration error maps shown in blue.

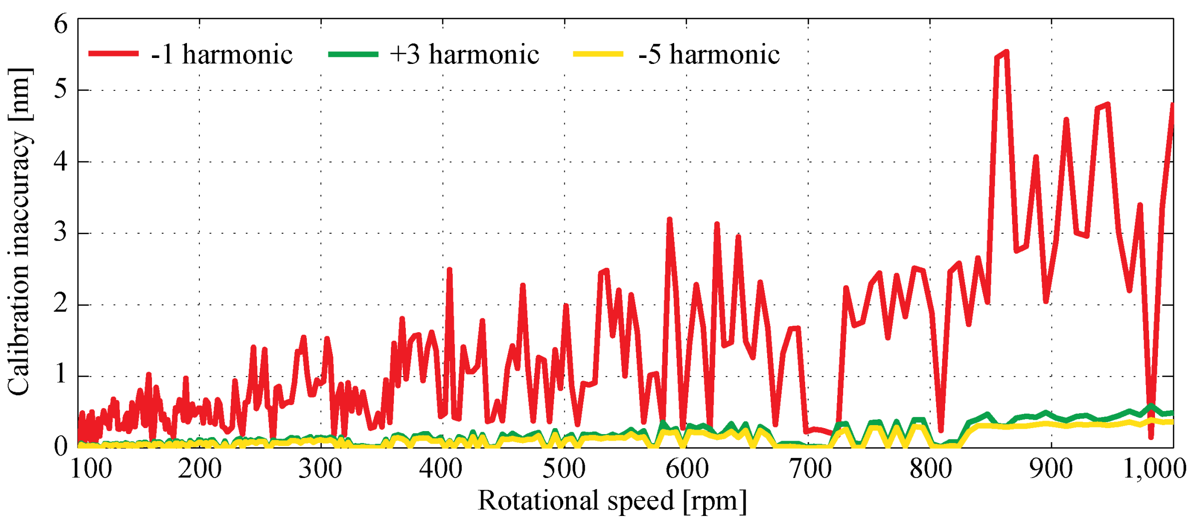

Figure 3.16: Simulated spindle error motion estimation inaccuracy for a range of speeds. Spindle radial error motion estimation of -1 (red), +3 (green) and -5 yellow.

as shown in Figure 3.17. The error map inaccuracy, which accounts for a range of frequency components, can be approximately related to -1 harmonic error motion inaccuracy as

$$[\text{-1}] \text{ error motion inaccuracy} = 3 \cdot \text{rms inaccuracy} \tag{3.3}$$

In experiment, spindle radial error motion measurements with capacitance probe sensors can be used to determine the spindles actual error motion.

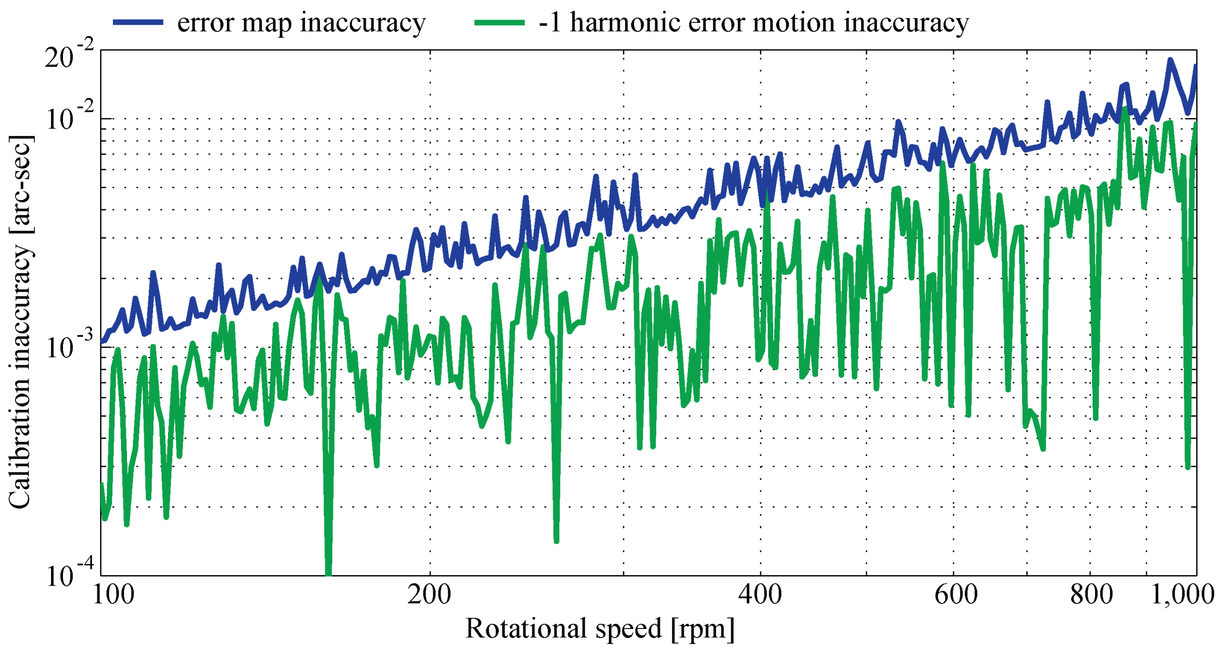

Figure 3.17: Comparison of error map inaccuracy to error motion inaccuracy

Chapter 4

Experimental Setup

A precision rotary table was designed and manufactured by Darya Amin-Shahidi [14] as a test bench of various encoder calibration techniques. Custom time measurement and encoder processing electronics were developed by Darya Amin-Shahidi [14], Kris Smeds [33], Arash Jamalian and Richard Graetz, with up to 1,500 MHz time measurement resolution, and active and passive signal filtering of multiple scanning unit encoder signals. Software and Hardware development by Kris Smeds, Xiaodong Lu and Richard Graetz, allows simultaneous time measurement of up six scanning unit's spatial intervals and transfer of the data through a TCP/IP protocol to a desktop computer to perform calibration. Figure 4.1 shows the flow of data in the experimental setup: from precision rotary table, to encoder signals, to custom electronics, to desktop computer and processed into calibration information.

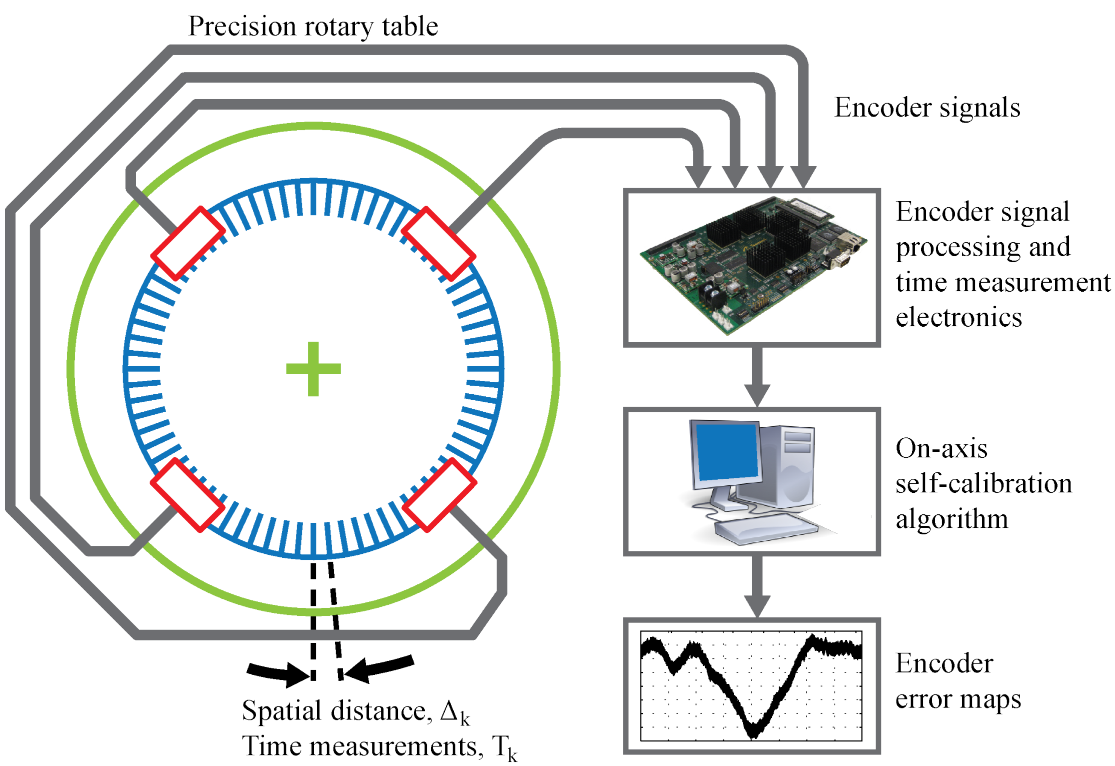

Figure 4.1: Flow of data int the experimental setup. block diagram.

4.1 Precision Rotary Table

The precision rotary table, Figure 4.2, was specifically designed by Darya Amin-Shahidi as a test bench for the TDR calibration method. The experimental setup consists of an aerostatic-bearing spindle (Professional

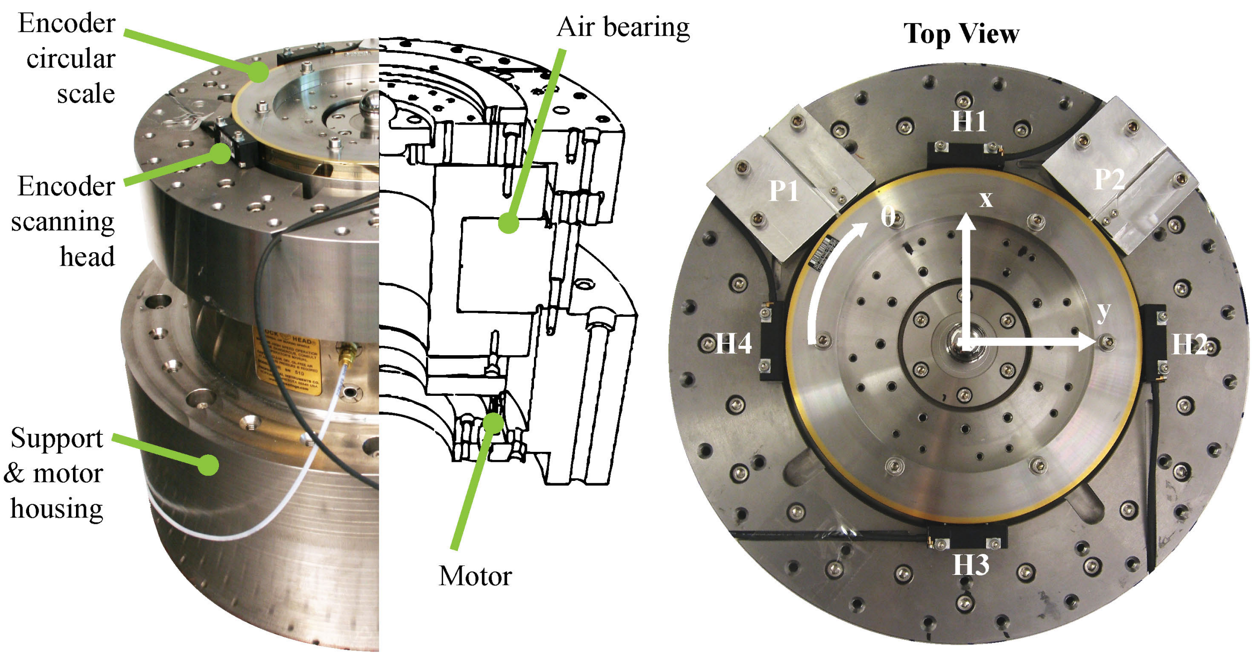

Figure 4.2: Encoder calibration experimental setup designed by Darya Amin-Shahidi [14].

Instruments 10R blockhead) that provides very smooth and repeatable rotational dynamics necessary for the dynamics reliant TDR calibration technique. A bearing-less incremental angle encoder (Heidenhain ERA4282c [2]) is installed to measure the rotational angular position of the spindle rotor. The circular scale with 32,768 (2^{15}) grating lines, is installed on the spindle rotor and four scanning units are installed equally spaced around the circular scale on the spindle stator. An error map correlation method, described in Section 4.5, is performed to confirm the alignment of each head to less than 10 arc-sec (1 count) of being equally spaced around the circular scale. A capacitance probe distance sensor is used to center all the mating parts on the spindle rotor to within $1\mu m$. More effort is made in centering the circular scale, to avoid angle measurement errors from eccentric mounting, and a centering of $0.3\mu m$ is achieved. Each scanning unit can generate $N = 131,072$ zero-crossings per revolution using quadrature interpolation of phase A and B signals output from the encoder electronics.

The encoder [2] is guaranteed with a grating accuracy of within ± 1.9 arc-sec and system accuracy of within ± 2.5 arc-sec. Provided with the encoder is a calibrated error map, Figure 4.3. The error map was measured at only 6,400 points and does not include high error frequency harmonics, but shows the encoder is within the accuracy tolerance, with ± 1 arc-sec accuracy. This error map cannot be used to compensate angle measurement errors because of the missing error harmonics and due to missing error components tied to installation and performance of the application axis.

The calibration facility is located on the second story where floor vibrations are significant enough to affect calibration results. To solve this issue the precision rotary table was installed on an optical table that provides passive vibration isolation. To calibrate at 600 rpm and higher speeds the spindle is motorized by a

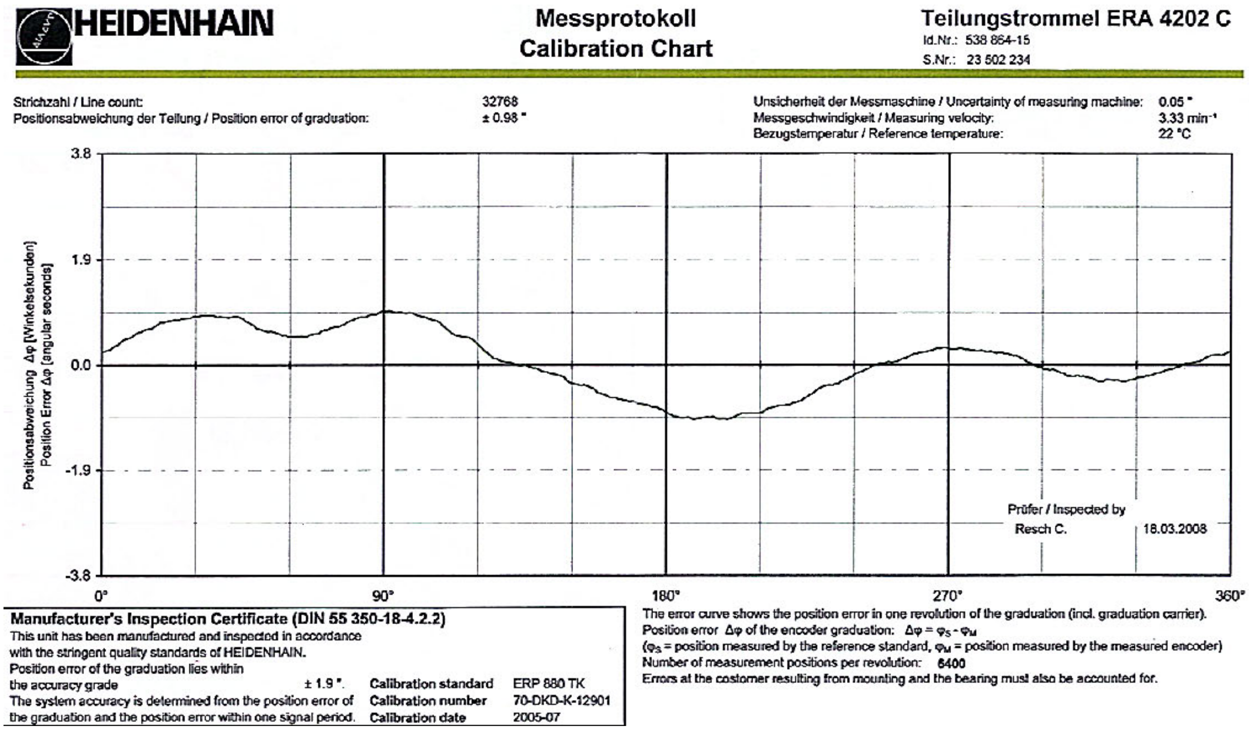

Figure 4.3: Heidenhain's calibrated error map for the ERA4282c angle encoder.

brushless motor (ThinGap TG8263) that exhibits exceptional low torque ripple characteristics. In addition, two capacitance probes P1 and P2 (Figure 4.2 right) are installed on the stator, reading against the circular scale, to measure spindle radial error motion. This measurement is used for the error motion comparison method as described in Section 2.2.

The incremental encoder used in the setup, Heidenhain's ERA4282c, is the most important device in the calibration setup. An in depth analysis of the encoder, it's operating principle and operation characteristics and discussed in the next section.

4.2 Heidenhain's ERA4282c Incremental Angle Encoder

The ERA4282c angle encoder, commercially produced by Heidenhain GmbH, has a circular scale with 32,768 grating periods written on the circumference of the scale with a period λ_s of $20\mu m$. The operation of this angle encoder is based on the image scanning principle of Section 1.3.1 and shown in Figure 4.4.

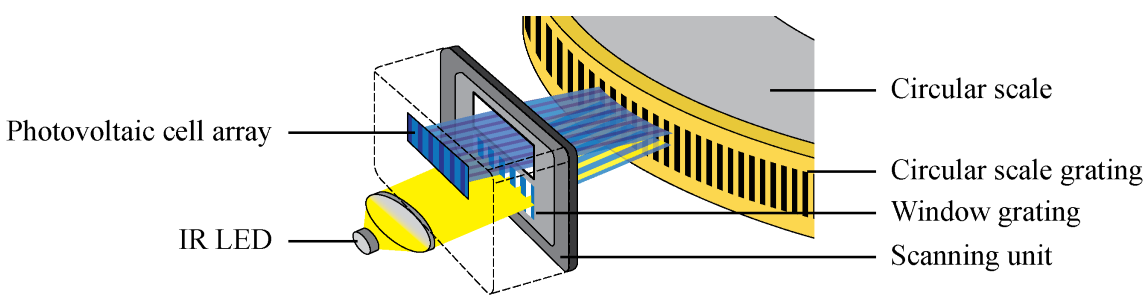

Figure 4.4: Single field imaging scanning principle of Heidenhain's ERA4282c angle encoder.

Infrared light passes out of the scanning unit through a window grating, reflects off the circular scale and back into the scanning unit and onto a photocell. An optical beat is created in the light due to interference of the patterns on the window grating and circular scale. Relative movement of the circular scale causes a change in the light intensity that falls on the photocell, producing the electrical encoder signals. The photovoltaic cell is structured with 56 separate cells for generating four 90° electrically phase shifted scanning signals, Figure 4.5. Shown in Figure 4.6 a repeating pattern of 0°, 90°, 180°, then 270° cells, each 200μm

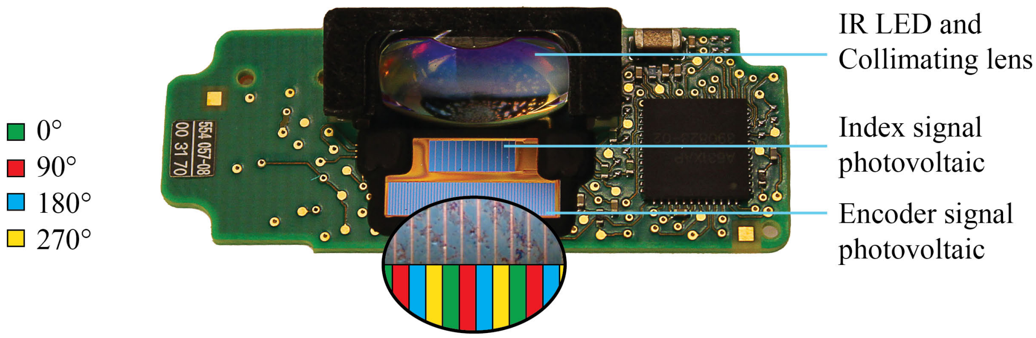

Figure 4.5: Inside the ERA4282c scanning unit.

wide, repeats 14 times along the entire length of the photovoltaic cell array. Each pair of 180° electrically

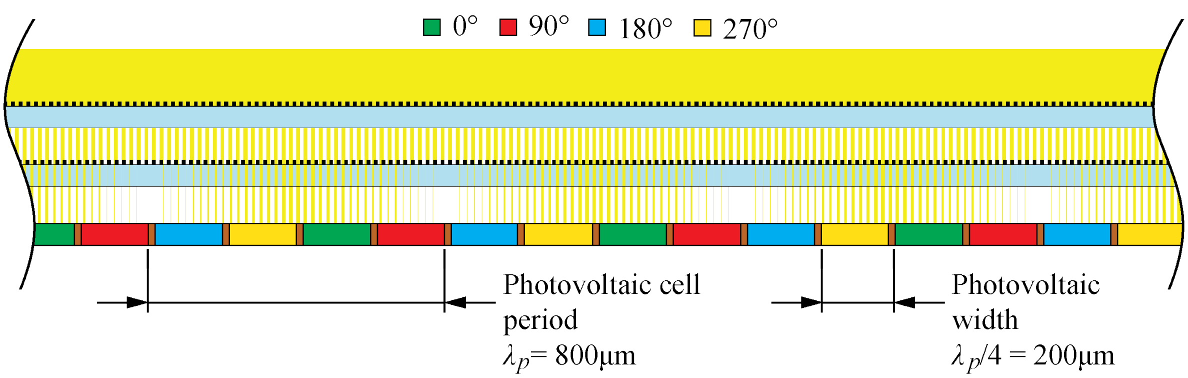

Figure 4.6: Photovoltaic cell array structure of the ERA4282c encoder with individual cells that produce the 0°, 90°, 180°, and 270° electrical encoder signals.

phase offset signals are differentially combined into the two encoder signals, Figure 4.7, which are then used to determine the spatial sampling widths, Δ_k. Due to the 200μm spatial delay of each individual photovoltaic

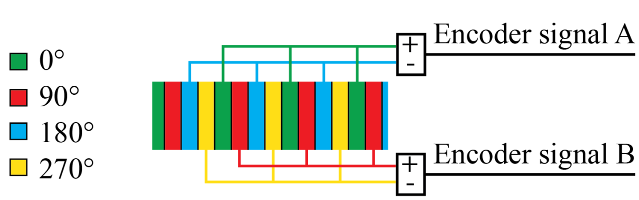

Figure 4.7: Differential combination of photovoltaic cell signals.

cell, the encoder signals are themselves delayed, i.e. encoder signal B is a response to grating lines delayed by $200\mu m$ or 10 grating lines compared to encoder signal A. Although there are many practical manufacturing justifications for this design it is shown that this delay causes additional encoder error, discussed in Section 4.2.2.

4.2.1 Theoretical Operation and Design

The differing grating periods on the window and circular scale are designed so that the optical beat has a dominant low frequency component whose period matches the period of the photovoltaic cell, λ_p, measured as $800\mu m$. The light that lands on the photovoltaic cell can be modeled by considering the regions on the window grating where light passes through, L_w, and regions on the circular scale where light is reflected off, L_s. For simplicity these regions are modeled as offset single frequency harmonics,

$$\begin{aligned} L_w &= 1 + \sin(f_w x), \\ L_s &= 1 + \sin(f_s x - N\theta) \end{aligned} \tag{4.1}$$

where the frequency harmonic of the window is $f_w = 2\pi/\lambda_w$ and of the circular scale is $f_s = 2\pi/\lambda_s$. Local position is defined as x and the phase of the circular scale reflection is controlled by the spindle rotational angular position given by θ, Figure 4.8. The modulation of the two functions in Equation 4.1, as the light

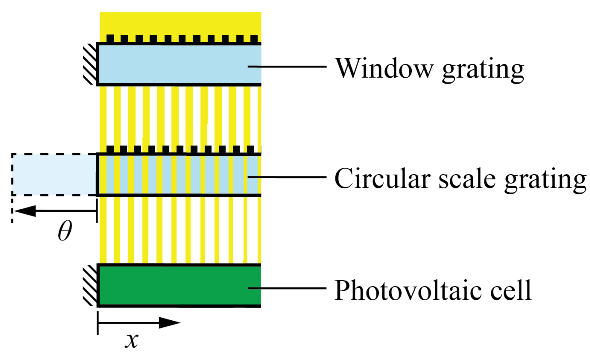

Figure 4.8: Definition of coordinates; Local position on window grating, circular scale grating and photovoltaic cell given as x. Absolute position of circular scale, controlled by spindle rotation given as θ.

passes through the window grating and then reflects off the circular scale creates an optical beat in the light that then falls on the photovoltaic cell. This optical beat is found as,

$$\begin{aligned} L_w \cdot L_s =& 1 + \sin(f_w x) \\ &+ \cos(N\theta)\left[\sin(f_s x) + \frac{1}{2}\cos[(f_s - f_w)x] - \frac{1}{2}\cos((f_s + f_w)x)\right] \\ &- \sin(N\theta)\left[\cos(f_s x) - \frac{1}{2}\sin[(f_s - f_w)x] + \frac{1}{2}\sin((f_s + f_w)x)\right]. \end{aligned} \tag{4.2}$$

To maximize sensitivity of the light to spindle rotation, the lowest frequency harmonic, $f_s - f_w$, is chosen to be periodic over the photovoltaic cell array, λ_p. This ensures that the signal does not cancel between differential pairs or between the photovoltaic cells of the same 90° phase shift. Based on this criteria, the window grating should be designed as

$$\lambda_w = \frac{1}{(1/\lambda_s \pm 1/\lambda_p)}. \tag{4.3}$$

The other frequency components, f_s and $f_s + f_w$ do not have a significant effect on sensitivity, but do affect alignment between the quadrature signals. To determine the shape of the encoder signals A and B, the cumulative light that falls on each photovoltaic must be found through integration of Equation 4.2 over each individual photocell,

$$\begin{aligned}\int_{x_{start}}^{x_{end}} (L_w \cdot L_s)\,dx = &\left[x - \frac{1}{f_w}\cos(f_w x)\right]\Bigg|_{x_{start}}^{x_{end}} \\ &+ \cos(N\theta)\left[-\frac{1}{f_s}\cos(f_s x) + \frac{1}{2(f_s - f_w)}\sin[(f_s - f_w)x] - \frac{1}{2(f_s + f_w)}\sin((f_s + f_w)x)\right]\Bigg|_{x_{start}}^{x_{end}} \\ &- \sin(N\theta)\left[\frac{1}{f_s}\sin(f_s x) + \frac{1}{2(f_s - f_w)}\cos[(f_s - f_w)x] - \frac{1}{2(f_s + f_w)}\cos((f_s + f_w)x)\right]\Bigg|_{x_{start}}^{x_{end}}.\end{aligned} \tag{4.4}$$

Each harmonic in Equation 4.4 is periodic over λ_p thus only one photovoltaic cell period of the entire photovoltaic cell needs to be integrated to determine the shape of the encoder signals A and B.

$$\text{encoder signal A} = \int_{x_{start}=0\mu m}^{x_{end}=200\mu m} (L_w \cdot L_s)\,dx - \int_{x_{start}=400\mu m}^{x_{end}=600\mu m} (L_w \cdot L_s)\,dx$$

$$\text{encoder signal B} = \int_{x_{start}=200\mu m}^{x_{end}=400\mu m} (L_w \cdot L_s)\,dx - \int_{x_{start}=600\mu m}^{x_{end}=800\mu m} (L_w \cdot L_s)\,dx. \tag{4.5}$$

In-depth derivation of the encoder signals is left for Appendix B, the result being the encoder signals found as

$$\begin{aligned}\text{encoder signal A} &= \frac{2}{f_w} + M_A \sin(N\theta + \phi_A) = 6.2 - 180\sin(N\theta - 45.73^\circ) \\ \text{encoder signal B} &= \frac{2}{f_w} + M_B \sin(N\theta + \phi_B) = 6.2 - 180\sin(N\theta + 45.73^\circ)\end{aligned} \tag{4.6}$$

where M_A and M_B the amplitude of the encoder signals is $-\frac{2\sqrt{f_s^2+f_w^2}}{f_s^2-f_w^2}$ and the phase of the encoder signals $\phi_A = -\tan^{-1}\frac{f_s}{f_w}$ and $\phi_B = \tan^{-1}\frac{f_s}{f_w}$. The units of the signal amplitude and offset voltage are derived from grating and window period in μm and have no physical meaning. However, the ratio of offset voltage to amplitude is indicative of the amount that can be created with the image scanning principle operation as can be used to estimate high frequency encoder error.

The high frequency optical beat $f_s + f_w$, causes a misalignment between the encoders signals where ideally the encoder signals should be separated by 90° electrical angle. This misalignment will cause additional high frequency encoder error when using both signals in quadrature decoding interpolation. The delay can be removed by changing the structure of the photovoltaic cell array (changing the integration limits in Equation 4.5) or signal processing by combining a ratio of phase A and B together to correct for the misalignment

$$\text{corrected encoder signal B} = 0.0253 \cdot \text{encoder signal A} + 0.9997 \cdot \text{encoder signal B}. \tag{4.7}$$

These methods can only be speculated upon due to the proprietary design of the angle encoder and no means to experimental validate the hypothesis, but they would be used to correct for a constant amount of misalignment. In practice these ideal conditions for the image scanning principle may not exist, so that any constant compensation of unbalance or misalignment would differ from their actual values. Installation of the scanning unit, such as tilt and yaw orientation, can affect the signal amplitude, unbalance and phase alignment by changing the apparent period of the window grating.

This theoretical analysis of the encoder gives insight into potential problems of the encoder operation. In following section photovoltaic cell delay, sinusoidal signal offset and phase misalignment are discussed as causes of high frequency encoder error.

4.2.2 High Frequency Encoder Error

As discussed in Section 4.2.1, high frequency encoder error can exist and has been identified as a result of specific encoder operating characteristics and quadrature decoding interpolation, Figure 4.9.

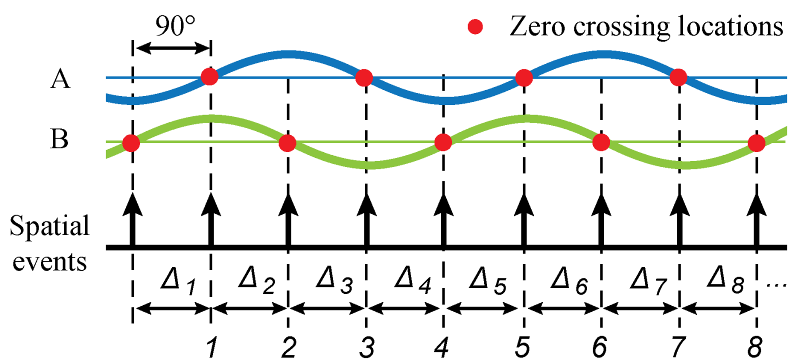

Figure 4.9: Ideal sinusoidal encoder signals, phase A and B signals with relative 90° phase-shift and no signal unbalance.

This section will explain how the high frequency harmonic is produced and aims to estimate the amount of high frequency error created from each of the identified causes.

Photovoltaic cell spatial offset

The physical layout of the photovoltaic cell in the ERA4282c is found to have a 200μm offset between phase A and phase B photocells which will cause a delay of 10 lines between each signal. The result is encoder signal B shows a response to grating lines that have already been seen on encoder signal A. Similarly any encoder error due to installation, graduation or spindle motion error will be delayed between the two signals. Since the encoder signals are used together to increase the rotation angle resolution of the encoder, a high frequency harmonic error, between each count on the encoder, is produced due to the delay.

A estimation of this high frequency error can made by considering the dominant 1 cpr error component due to installation eccentricity. The measurement error calibrated from the rising and falling edges of only encoder signal phase A is approximately

$$q_A(k) = A_1 \sin\left(\frac{2\pi}{N/2}k\right) \tag{4.8}$$

where A_1 is the harmonic amplitude of the 1cpr encoder error harmonic and $k = 1,2,3...N/2$. The error seen on encoder signal phase B assuming the sensors are symmetric in every way except for a delay of 10 gratings lines (20 rising and falling edges), is

$$q_B(k) = q_A(k-20) = A_1 \sin\left(\frac{2\pi}{N/2}[k-20]\right). \tag{4.9}$$

The amplitude of the high frequency error from count to count is given as the difference between the error seen on phase A and phase B

$$q_A(k) - q_B(k) = A_1 \sin\left(\frac{2\pi}{N/2}20\right) \cos\left(\frac{2\pi}{N/2}k\right). \tag{4.10}$$

The delay of the photocell will cause a high frequency error proportional to approximately 0.2% of the amplitude of the first order error harmonic. Realistically this could cause encoder error of a few thousandths of an arc-sec with precise installation, negligible when compared with the other high frequency error sources.

The photocell delay will have a cumulative effect for higher order error harmonics. The high harmonics have a lower harmonic amplitude but the delay has a greater effect therefore an experimental error analysis should be conducted.

Signal unbalance

Signal unbalance or voltage offset in either of the encoder phase signals will cause a repeatable pattern of uneven spacing between intervals. An offset voltage could be caused by electrical noise in the real world circuit or as discussed in Section 4.2.1 a mismatch of grating periods due to installation. As shown in Figure 4.10, a voltage offset in sinusoidal encoder signal phase A, produces a repeating pattern of two short spatial intervals and then two long intervals. The magnitude of error caused by an offset in the encoder

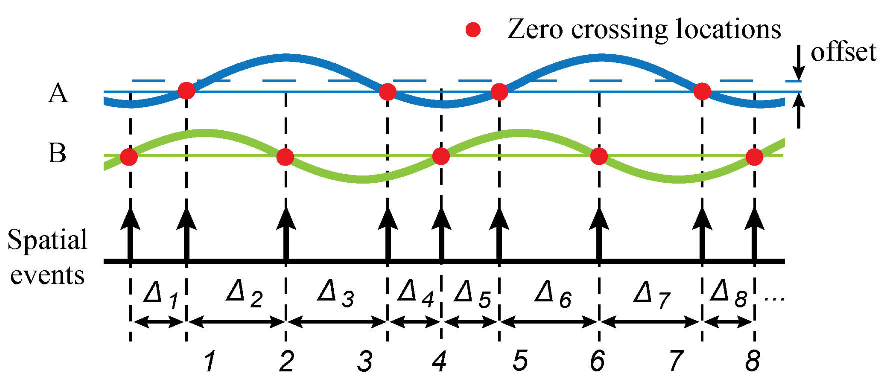

Figure 4.10: Unbalance of sinusoidal encoder signal phase A as cause of high frequency encoder error.

signal can be estimated as

$$\text{offset encoder error} = \frac{1}{N}\sin^{-1}\left(\frac{V_{\text{offset}}}{M}\right). \tag{4.11}$$

An offset voltage of 3% or $6/180$ as found in the theoretical derivation would cause 0.19 arc-sec of angle measurement error.

Signal phase misalignment

In reality and as shown in the theoretical derivation Section 4.2.1, there could exist a phase misalignment between the two encoder signals. Phase misalignment between the two encoder signals will cause a repeatable pattern of spatial interval widths, odd counts being closer together than the average and even counts being farther apart, Figure 4.11 or vice versa. The amount of encoder error caused by a phase misalignment

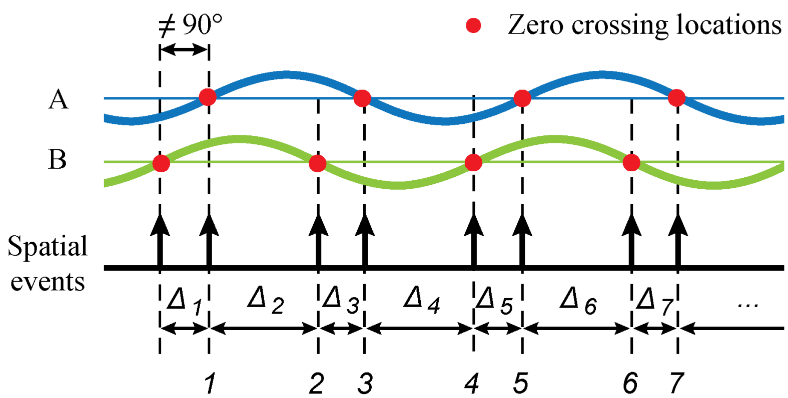

Figure 4.11: Phase misalignment of sinusoidal encoder signals, phase A and phase B as cause of high frequency encoder error.

can be found with the following equation

$$\text{phase misalignment error} = \phi_{\text{misalignment}}\frac{4}{N}3600. \tag{4.12}$$

The theoretical derivation of Section 4.2.1 predicts a phase misalignment of 1.45°, which will cause count to count high frequency error of 0.16 arc-sec.

It has been shown that the high frequency encoder error harmonics exist and can be caused by the basic operating principle of the encoder and quadrature decoding interpolation. In addition, high frequency error harmonics exist due to placement of the grating lines of the circular scale. To improve the accuracy of an incremental angle encoders, all the repeatable errors in the measurement should be removed through calibration. A high accuracy calibration method needs to capture both the low frequency harmonic errors and high frequency error from count to count.

4.3 Motor Control and Ripple Compensation

Rotational speed control was implemented with feedback from the rotary encoder, allowing the calibration method to be investigated at high rotational speeds. As a side application of encoder calibration the controller was developed to achieve very smooth rotational speed, with motor torque ripple and encoder error compensation.

A TG8263 DC brushless motor, commercially produced by ThinGap LLC, is installed on the air bearing spindle Figure 4.12. This DC brushless motor exhibits very low motor torque ripple and is ideal for designing a smooth velocity servo. Spindle speed control was performed using a dSPACE control system,

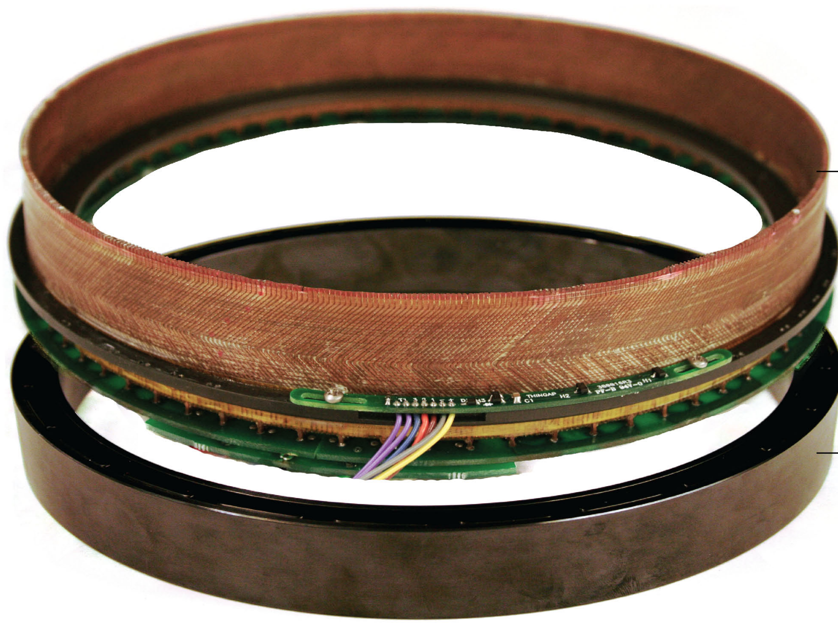

Figure 4.12: ThinGAP TG8263 DC brushless motor installed on the air bearing spindle.

providing Analog to Digital Converter (ADC) input, for encoder signal feedback and Digital to Analog Converter (DAC) output, interfacing with the servo amplifier. Based on experimental frequency response measurements a lead lag controller with a bandwidth of $20Hz$ and phase margin of $55°$ was designed using loop shaping techniques.

To improve the performance of the controller, the characteristic torque ripple of the motor was calibrated. Inconsistency in the magnetic field of the motor rotor is a main cause of torque ripple. The sinusoidal magnetic field in the motor rotor is produced by 12 pole pair permanent magnets. The theoretical torque produced by the motor M can be found through Lorentz force; proportional to strength of the magnetic field B, current in the motor coils I, length of the coil in the field L and radius of the motor R.

$$M = B \cdot L \cdot I \cdot R \tag{4.13}$$

The commutation law, using feedback from the angle encoder, gives a sinusoidal current in each phase of the coils which is modulated with the magnetic field creating a DC torque. Torque ripple can additionally be caused by error in the commutation law due to encoder and measurement error.

Several techniques have been used in the motor design to minimize torque ripple caused by magnetic field variations. The coils of the motor are slanted, forming a diamond pattern on the return path, averaging the magnetic field seen by a single coil over a larger area. In addition 8 consecutive coils of the same phase are placed side by side further averaging the magnetic field Figure 4.13. Both these techniques act as spatial

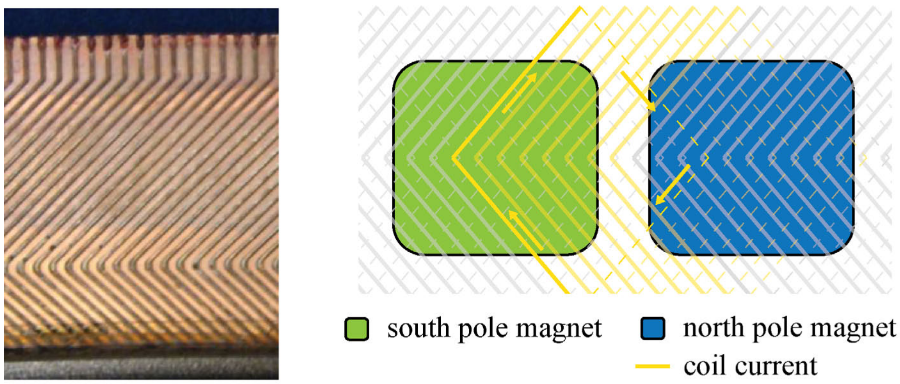

Figure 4.13: Slanted profile of the motor coils, designed to reduce motor torque ripple.

filters, attenuating any high harmonics in the magnetic field. Further torque ripple is attenuated with three phase modulation. The coils are configured for as shown in Figure 4.14 for each coil phase. This acts similarly to harmonic cancellation where any torque ripple harmonic not multiple of three (the number of current phases) is canceled. Although the design has been optimized to reduce torque ripple ripple still,

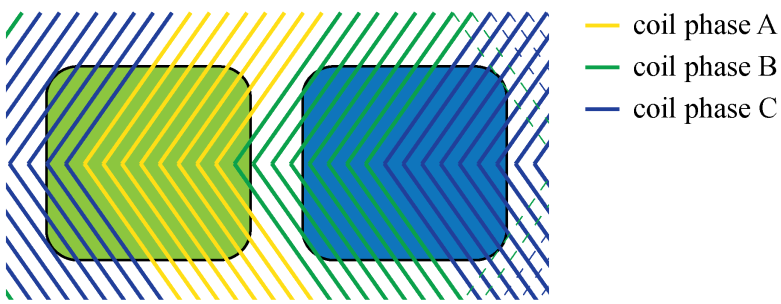

Figure 4.14: Three phase coil configuration cancels harmonic in the magnetic field.

some still exists and is the dominant factor limiting smooth rotation. The amount of torque ripple can be found experimentally by measuring the back EMF or voltage across the coils given by

$$V_{emf} = \omega \cdot B \cdot L \cdot R. \tag{4.14}$$

The angle encoder allows an accurate estimation of the spindle speed, ω, so that the motor torque constant, $K_T = T/R$, can be found through Equation 4.13 and Equation 4.14 as

$$K_T = \left[V_{emfA} \cdot \sin(\theta) + V_{emfB} \cdot \sin(\theta - 2\pi/3) + V_{emfC} \cdot \sin(\theta - 4\pi/3)\right]/\omega. \tag{4.15}$$

Where the Electromotive Force (EMF) voltage measured across the i-th phase is given as V_{emfi}. The experimental motor torque constant, is shown in Figure 4.15. The torque constant is found through experimental EMF voltage measurements and Equation 4.15 is found with mean of 0.4565 Nm/A and less than 0.11%

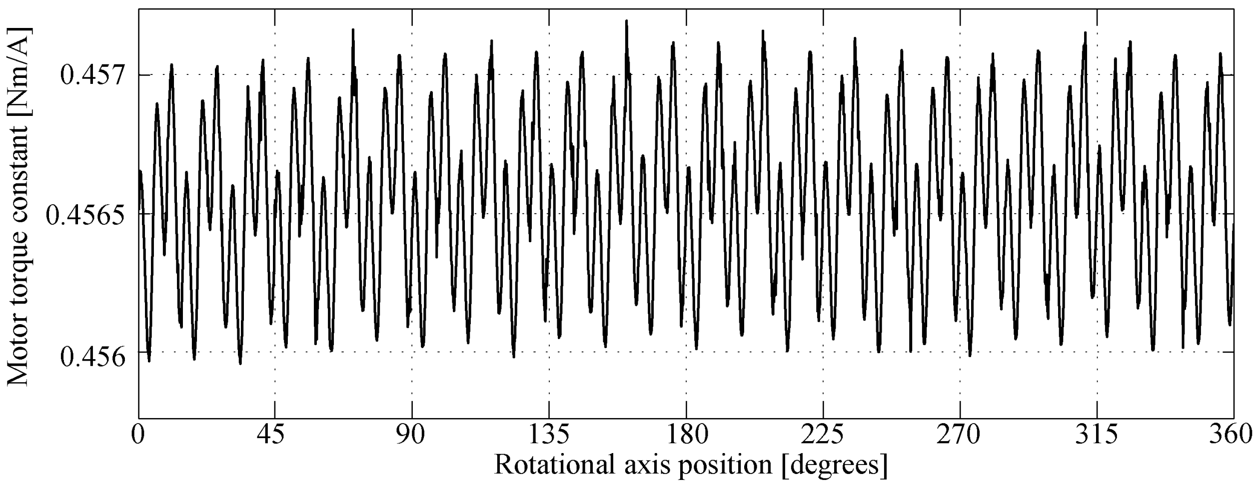

Figure 4.15: Experimentally measured motor torque constant.

ripple. The ripple component is due to 12, 24 and 72 cpr harmonics with the amplitudes in Table 4.1. Although the higher harmonics have greater amplitude the lower harmonics will have a greater effect on

Table 4.1: Motor torque constant ripple harmonics.

Harmonic No.	12	24	72
Harmonic amplitude [Nm/A]	2.2×10^{-5}	2.6×10^{-4}	3.4×10^{-4}

velocity ripple due to the inertia of the air bearing spindle filtering out higher order harmonics. The torque ripple is compensated by using the experimental measurement as a look up table to compensate for torque variations real time in the controller. With torque ripple compensation, the velocity ripple is dominated by error in the commutation law caused by encoder angle measurement errors. Given a constant velocity command for the control system implemented in Figure 4.16, the position error was experimentally measured as shown in Figure 4.17. A later experimental calibration showed the correlation between the position error in

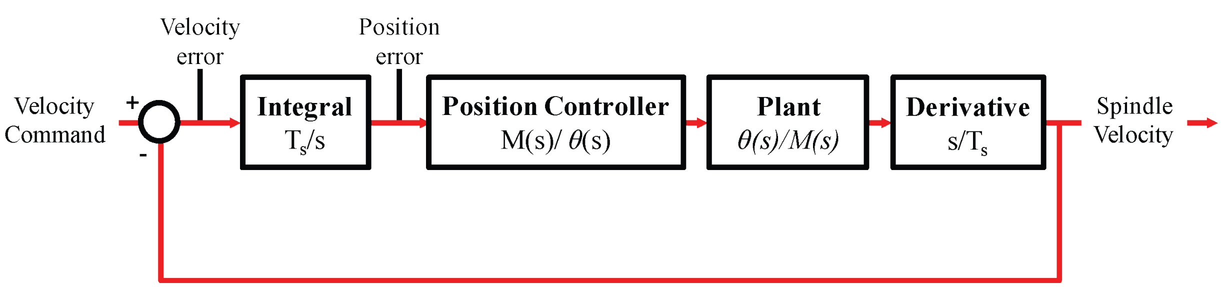

Figure 4.16: Spindle velocity control system.

the velocity control and the encoder angle measurement error. Using a lookup table, the angle measurement error was corrected with the calibrated error map and the position error in velocity control was brought down to 0.2 arc-sec which is purely due to encoder signal quantization (Figure 4.18).

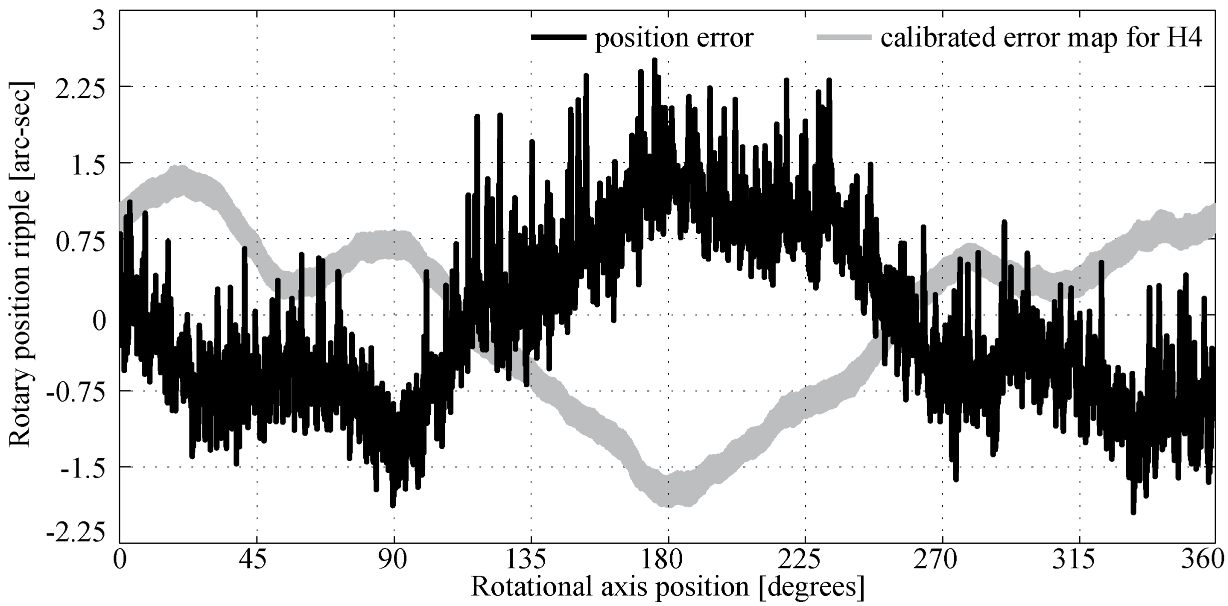

Figure 4.17: Position ripple for constant constant velocity control dominated by commutation error.

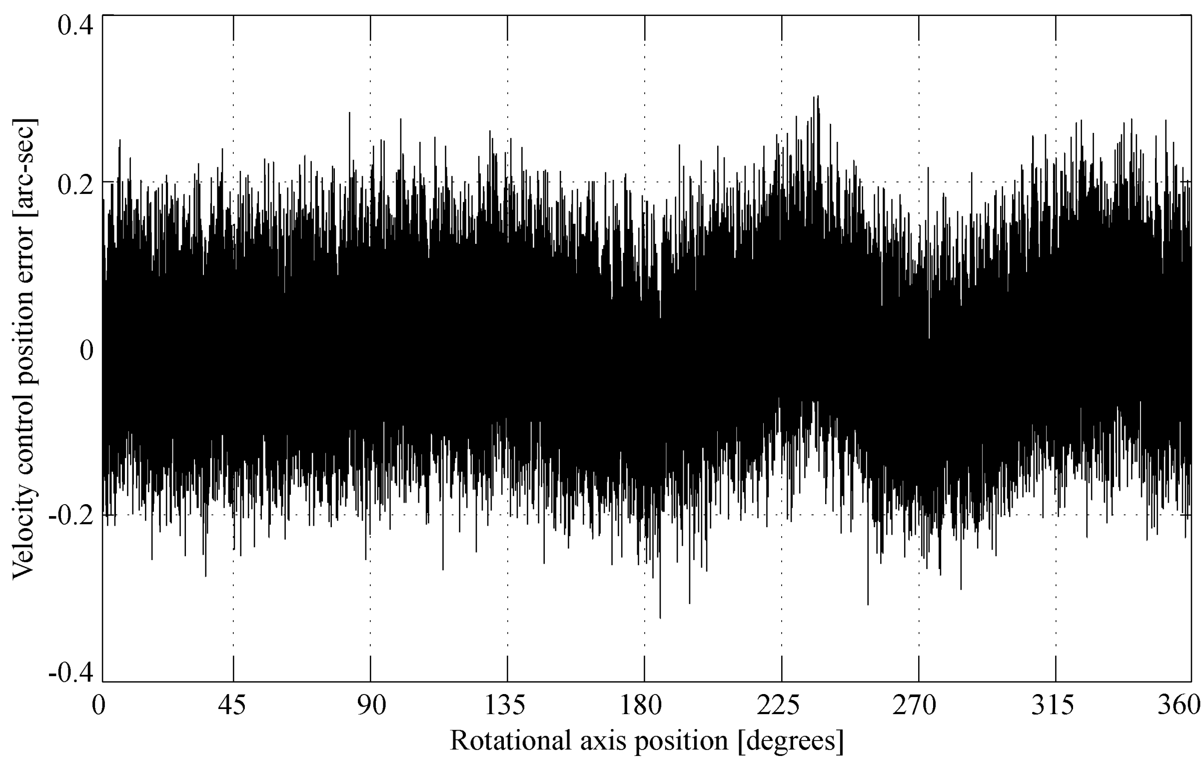

Figure 4.18: Position ripple for constant constant velocity control dominated by encoder signal quantization error.

4.4 Custom Electronics

Accurate time measurements of encoder spatial intervals are necessary for accurate rotational angular position measurement and accurate calibration. These uncertainties are minimized by improving the SNR on the encoder signals (Section 2.3.1) and the time measurement resolution (Section 2.3.2). To achieve these results, custom time measurement and encoder processing electronics have been developed by Darya Amin-Shahidi [14], Kris Smeds [33] and Richard Graetz.

The final revision of the time measurement electronics is based on a multi-rate multiprocessor control platform designed specifically for high-speed precision motion control [33]. The platform, nicknamed Tsunami, is built around the Virtex 5 FPGA and four Tigershark Digital Signal Processor (DSP)s. The full capability of the platform is not utilized in this application, but the high speed FPGA allows fast digital signal processing and time measurement, with a resolution of 1,500 MHz (0.667 ps). Due to limited RAM on the Tsunami platform 256*mb* of time measurement data can be stored for calibration. This allows continuous simultaneous time measurement of four scanning units over a range of 100 rpm. The Tsunami platform with encoder signal processing board is shown in Figure 4.19.

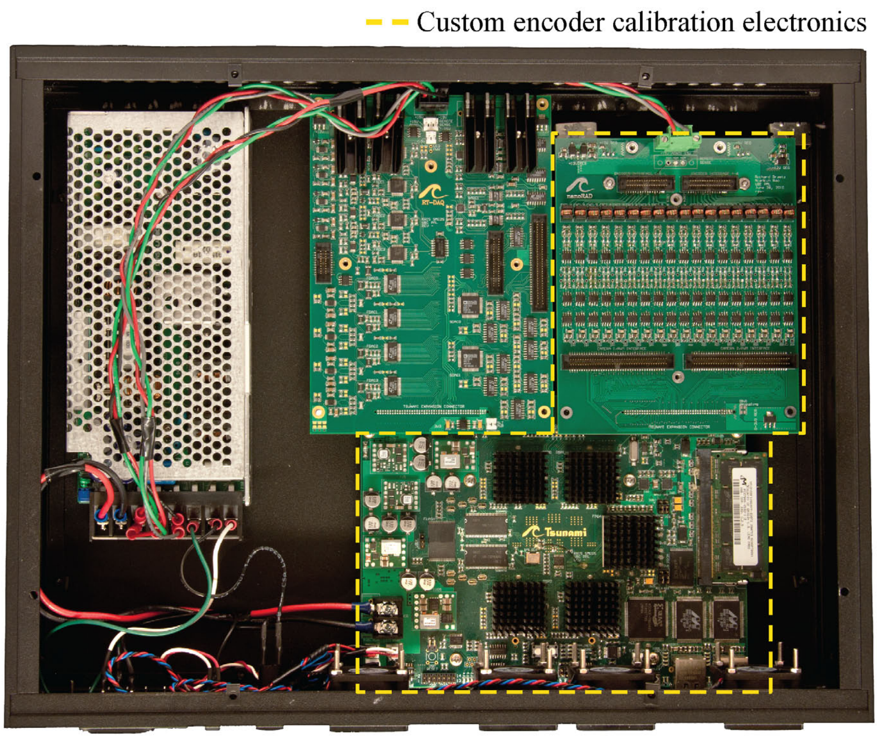

Figure 4.19: Tsunami, multi-rate multiprocessor control platform developed by Kris Smeds.

4.4.1 Tsunami Daughter Board Detailed Design

The Tsunami daughter board, nicknamed NanoRAD, was designed to perform application specific analog signal processing, buffering, and digital conversion. Several generations of the daughter board were developed (Figure 4.20) to investigate various signal processing topologies and calibration techniques such as analog encoder signal averaging and simultaneous signal measurement of multiple scanning units.

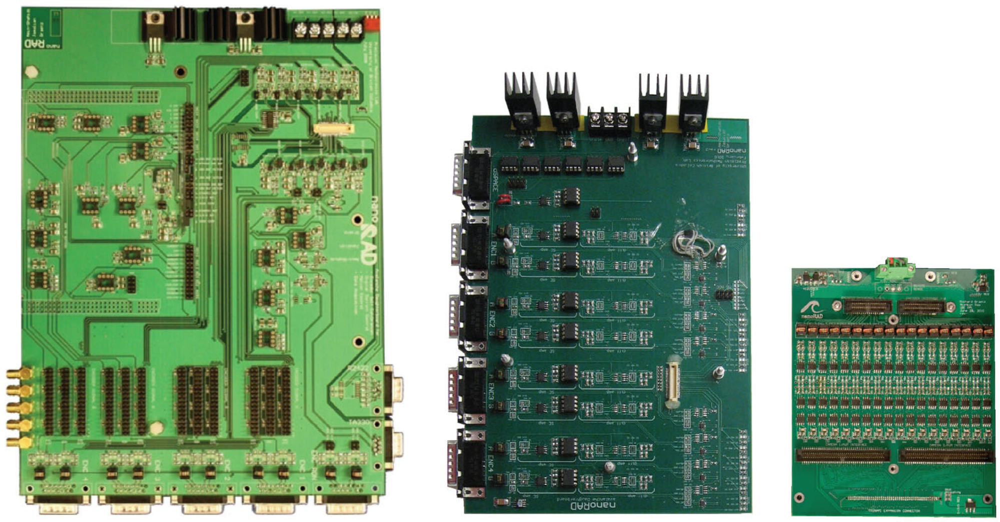

Figure 4.20: Three generations of the NanoRAD daughter board developed by Darya Amin-Shahidi, Arash Jamalian and Richard Graetz. From left to right, earliest to current design.

The analog encoder signals are processed to improved repeatability and minimize electrical noise. Differential pairs of each encoder signal are first sent through a common mode choke, designed to pass the differential signals but block electromagnetic interference (EMI) on the signal lines. Differential pairs then pass through several active filter stages, utilizing a multiple feedback (MFB) topology filter built around a fully differential amplifier. The final processing stage converts the analog signal to a digital 3.3V CMOS/TTL compatible digital signal that can be accessed by the FPGA on the Tsunami platform. All three encoder signals (phase A and B and index) are processed identically to avoid delay and phase shift between signals. The marking repeatability of the index signal does not have a huge effect on calibration uncertainty as it's repeatability is only required to be within 10 arc-sec (1 count) to determine the start of the next revolution. The index signal is filtered to prevent phase shift between it and the other phase signals which would result in incorrect identification of the start of the next revolution. The schematic design of the signal processing circuit is shown in Figure 4.21. The custom electronics are designed to provide real time access to encoder

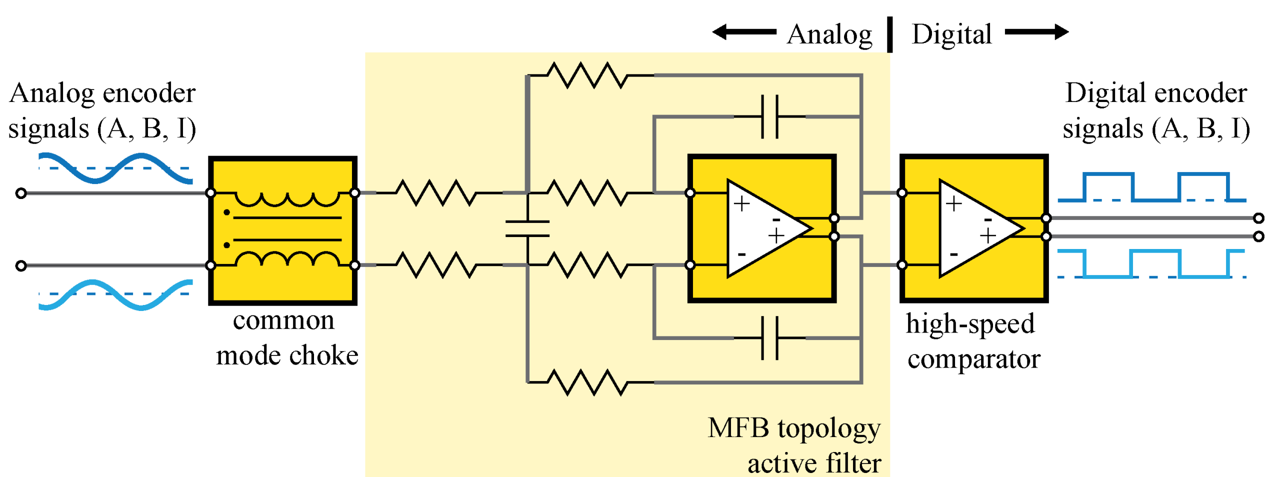

Figure 4.21: Analog encoder signal processing on the NanoRAD daughter board.

angle measurements necessary in a real time manufacturing application. The delay of the encoder signal and interpretation of angle is minimized so that in the manufacturing operation, encoder angle measurements can be obtained and compensated in real time. If instead the encoder signals were sampled with a ADC, more accurate measurements could be obtained but the real time application would be lost. Digital filtering could be used to remove signal noise and signal interpolation could accurately determine the exact zero-crossing location independent of time measurement resolution, but the extra processing would significantly delay the angle measurement. MFB or Sallen-key topologies allow complex root/pole analog filters, such as Bessel, Butterworth, and Chebyshev to be implemented. Of these filters the Chebyshev filter gives the most high frequency attenuation, improving the encoder signal SNR the most for this application. The MFB topology is used over Sallen-key because it is ideal for filters with high gain and quality factor. Increasing the signal gain allows for faster response from the high-speed comparator and minimizes the influence of additional noise added to the signal after amplification.

As determined in Section 2.3.1 a filter bandwidth of 300 kHz will give the best linear manufacturing tolerance results between 180 and 600 rpm. A four pole Chebyshev filter with 0.5dB passband, 300 kHz bandwidth and 6 times gain was implemented.

PCB design

The NanoRAD's design was implemented on a 4-layer printed circuit board (PCB), Figure 4.22. The daughter board contains both analog and digital encoder signals. The analog components are isolated from digital components, so that the analog signals are not influenced by switching noise inherent to all digital electronics. This is done by isolating the power planes for the analog and digital components. However the two cannot be entirely isolated and a common ground connection must be made, to keep the reference level for both sides the same. A single point connection will enforce a single controlled current return path, which has the effect of increasing the inductance of the path for digital currents and limiting high frequency noise on the shared ground plane, while providing a common reference level.

The daughter board takes in $\pm$15V from an external power supply and then creates all the required voltages levels for encoder supply, signal processing and digital conversion. Linear regulators are used for this purpose and they provide excellent common mode rejection of EMI on the power levels. In a previous iteration of the NanoRAD, all the required voltage levels were supplied by an external power supply. It was found that EMI and noise on the voltage levels was increasing the calibration uncertainty through deterioration of marking repeatability. Using several ferrite core inductors wrapped around the voltage supply lines reduces this effect.

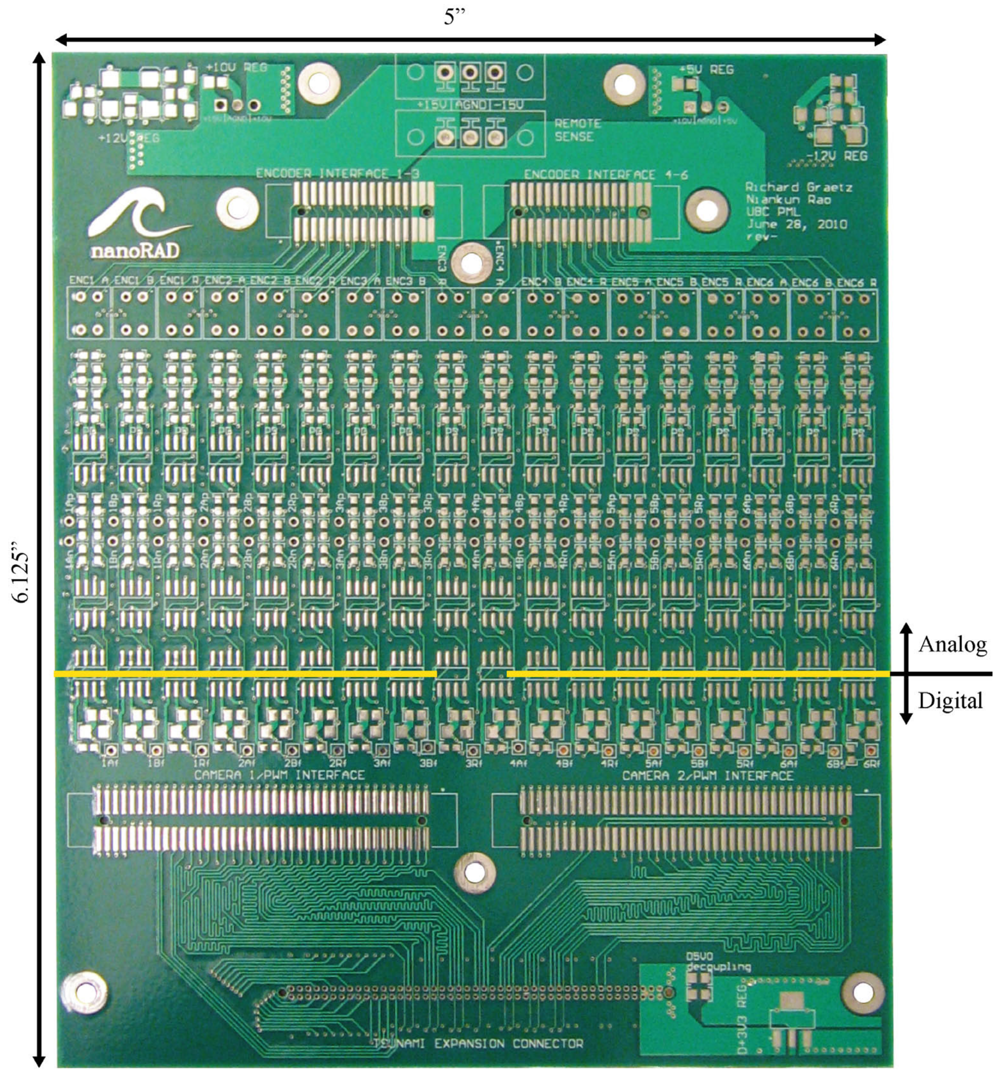

Figure 4.22: PCB design of NanoRAD.

4.5 Scanning Unit Alignment

As discussed in Section 2.3.3, scanning unit misalignment can cause error in the estimation of rotary vibration harmonics. Due to tolerances in the mounting bolts, each scanning unit can be positioned to 4,000 arc-sec (400 counts) from their nominal position. Misalignment of this magnitude could cause 0.014 arc-sec of error map inaccuracy due to incorrect estimation of rotary vibration. To minimize this error, great effort has been spent to accurately align each scanning unit to be evenly spaced around the circular scale. Error map cross-correlation and analog signal phase alignment are used together to accurately align each scanning unit.

Only relative alignment of each scanning unit is necessary. The position of scanning unit H1 is chosen as the absolute position and scanning units H2, H3 and H4 are positioned relative to this head at 90° intervals, Figure 4.23. First the scanning units are installed on the spindle stator at approximately the correct positions. Encoder calibration is performed for each scanning unit and their error maps obtained (Equation 2.43). Spatial intervals, Δ_{Hj}, are computed from each error map and cross-correlation is performed between calibrated

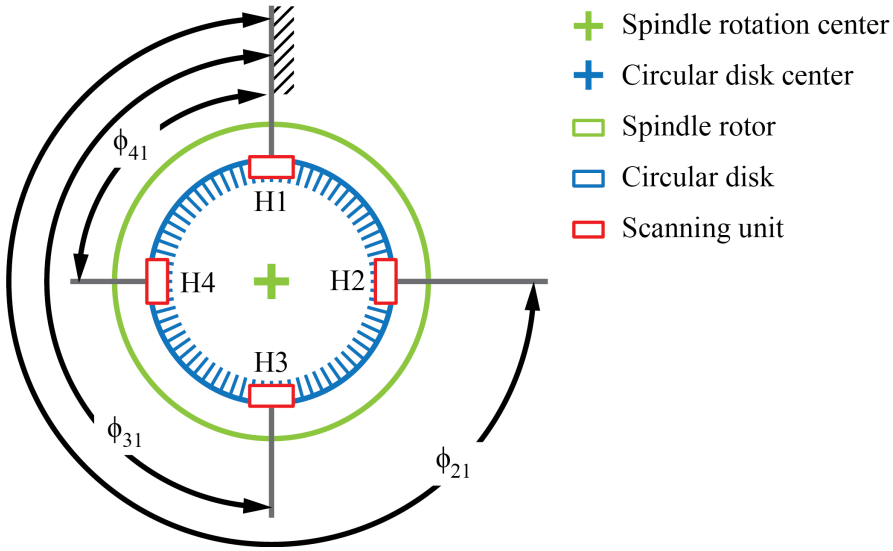

Figure 4.23: Relative alignment of each scanning unit to be evenly spaced around the circular scale.

spatial intervals of each scanning unit and scanning unit H1.

$$(\Delta_{H1} \star \Delta_{Hj})[n] = \sum_{k=1}^{N} \Delta_{H1}[k] \cdot \Delta_{Hj}[k+n] \tag{4.16}$$

where the head number is $j = 2,3,4$. Cross-correlation can be used to find how much the calibrated spatial intervals of the j-th scanning unit Δ_{Hj}, must be shifted to make it them the most similar to the spatial intervals of scanning unit H1 Δ_{H1}. Δ_{Hj} slides along the x-axis, calculating the integral of their product at each position, n. When the functions match, the value is maximized, indicating the rough relative alignment of the j-th scanning unit to scanning unit H1, ϕ_{j1}, within 1 grating line.

It was found that cross-correlation of the spatial intervals was much more sensitive to head alignment, compared with cross-correlation of error maps. The spatial intervals are dominated by high frequency, thus any small change in alignment would result in a large change of cross-correlation. Figure 4.24 shows the normalized cross-correlation of the spatial intervals between H1 and H2 with a very noticeable maximum correlation peak. In comparison the error map has dominant low frequency harmonics that make estimation of the alignment to within a grating line more difficult. Figure 4.25 shows the normalized cross-correlation of the error maps of H1 and H2 with no noticeable maximum correlation peak.

The scanning units are repositioned based on the cross-correlation maximum and the calibration procedure is repeated until all heads are within 1 grating line of their ideal position.

Fine alignment of each scanning unit is achieved using the analog signals of each scanning unit. Each scanning unit is repositioned until their phases align, ensuring scanning unit alignment to less than 1 grating line. Misalignment of 1 grating line (40 arc-sec) would cause a negligible calibration error of 0.1 thousandths of an arc-sec and result in 0.33nm linear tolerance error.

In addition to positioning the scanning units evenly around the circular scale, their radial position must also be controlled. The radial distance of each scanning unit from the circular scale was found to affect the amplitude of the voltage signals. Moving a scanning unit closer to the scale resulted in higher signal

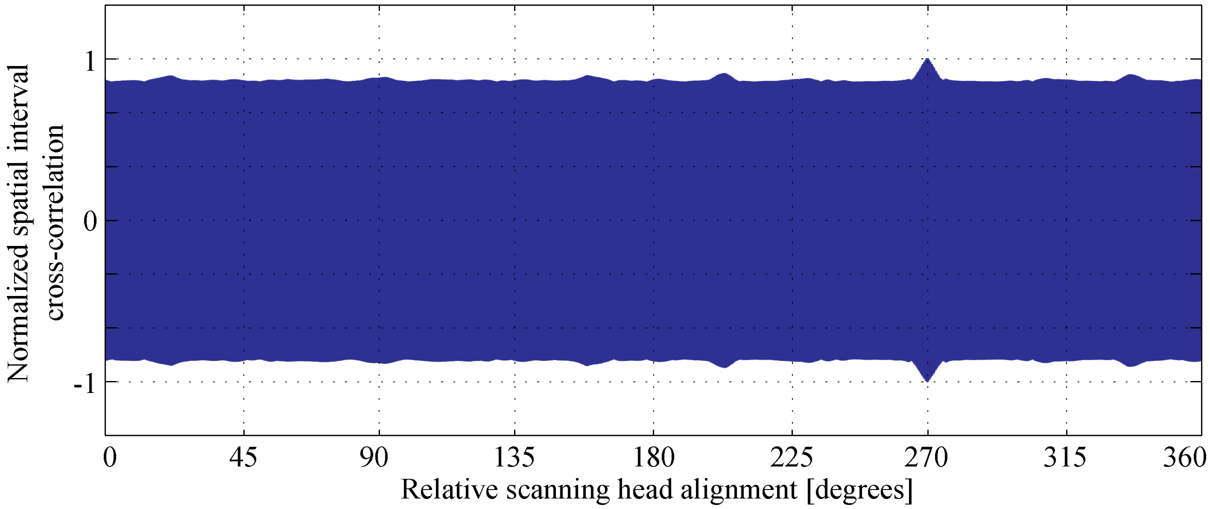

Figure 4.24: Normalized cross-correlation of spatial intervals, Δ_{Hj}, calibrated from scanning units H1 and H2.

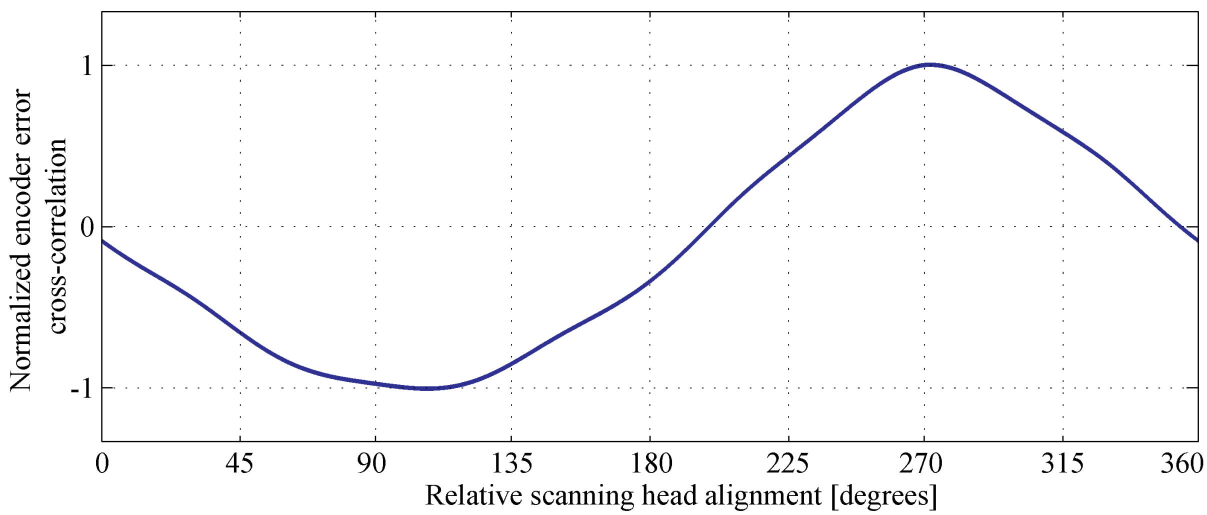

Figure 4.25: Normalized cross-correlation of angle measurement error, q_{Hj}, calibrated from scanning units H1 and H2.

amplitudes and also more repeatable calibration results. As the scanning unit is brought closer to the circular scale the imaging height is shifted down and the light reflected back into the scanning unit enters at a lower height. The improvement in encoder signal could be due to more light being able to enter the scanning unit but could also be related to the manufacture of parts that the encoder parts are mounted to. A nominal spacing of $150\mu m$ between scanning unit and circular scale was used, as specified by the manufacturer [2]. A closer spacing was avoided to prevent scratching the circular scale in case of thermal expansion of the setup bringing the scanning unit and circular scale in contact.

Chapter 5

Experimental Results

Encoder signal time measurements were captured from the precision rotary table setup from spindle speeds of 300 rpm down to 200 rpm. Time measurements for 131,072 spatial intervals each spindle revolution were captured simultaneously for the four scanning units with a time measurement resolution of 1,500 MHz.

Figure 5.1 shows an experimentally measured spindle free response, where the apparent speed is the ratio of the nominal spatial interval, Δ_0, and time measurement between spatial intervals T_k. The ripple in speed is repeatable, caused by encoder angle measurement error and the overall pattern fits Equation 2.5 for a first-order damping model.

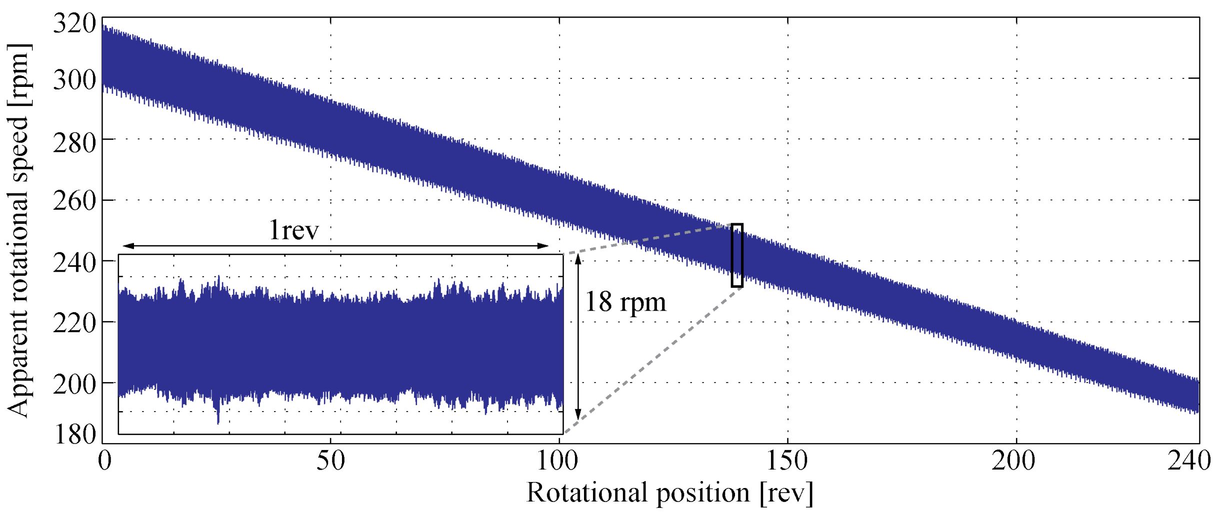

Figure 5.1: Experimentally measured spindle free response.

The time measurement data for each scanning unit was used to investigate encoder calibration of the TDR method calibration method. Estimation of the spindle dynamic coefficients, inertia and damping and presented.

5.1 Damping Estimation

The TDR calibration method relies on estimation of the spindle dynamics to determine the encoder error map. A second-order damping model for the spindle is assumed based on Equation 2.6.

Figure 5.2 and Figure 5.3 show the constant (c_0) and spindle speed dependent (c_1) normalized damping coefficients estimated during calibration. The constant damping coefficient shows a trend of increasing

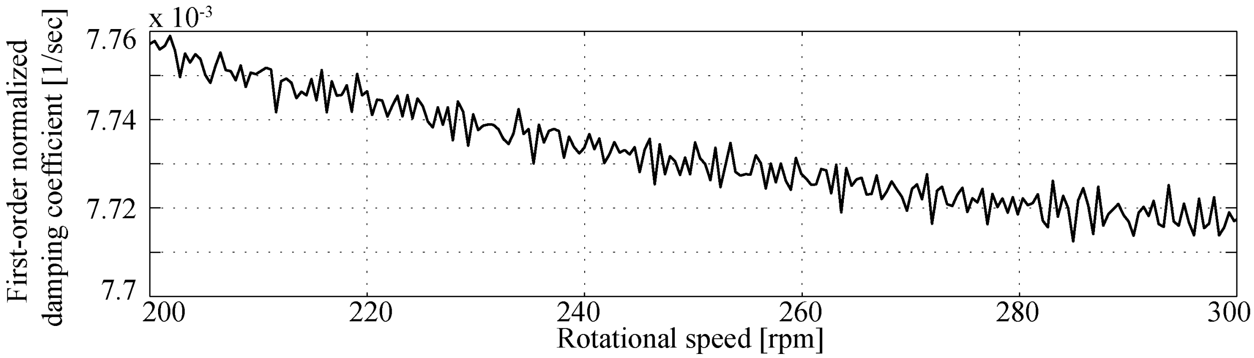

Figure 5.2: Experimental constant normalized damping coefficient estimation of TDR calibration method, c_0.

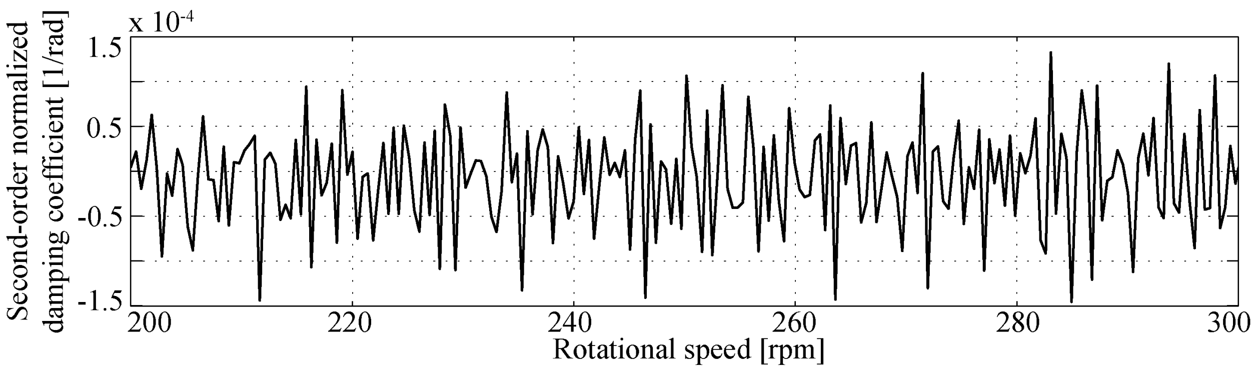

Figure 5.3: Experimental spindle speed dependent normalized damping coefficient estimation of TDR calibration method, c_1.

damping coefficient at lower spindle speeds, approximately 0.5% over 100 rpm. Spindle dynamics are expected to change due to uncontrolled ambient room temperature and air bearing supply pressure fluctuations due to air compressor on/off cycles. In addition heating generated by the viscous friction of the air bearing has been observed and could lead to varitations in the spindle dynamics. However, the spindle speed dependent damping coefficient fluctuations cannot be physical as the damping coefficient is sometimes estimated with a negative value. The negative result implies damping is adding energy to the system and instead causing the spindle speed to increase. The negative damping estimation is caused by the calibration algorithm, fitting the damping coefficient to uncertanties in the measurements. The measurement uncertainties need to be further eliminated before the second-order damping model is applicable.

For the remainder of the experimental results presented for this air bearing spindle, a first-order damping model is used in calibration.

5.2 Calibration Before Rotary Vibration Removal

Figure 5.4 shows the typical TDR calibration results for all four scanning units before rotary vibration removal (Equation 2.28). This initial encoder error estimation result shows how rotary vibration distorts each error map, so error maps between scanning units significantly differ from one another. The full error map harmonics are captured with the TDR method, including high frequency error show as the 0.3 arc-sec band on the signal. This high frequency error indicates significant phase misalignment and signal unbalance in the encoder signals. Figure 5.5 shows the raw calibration result with only the first 500cpr harmonics of

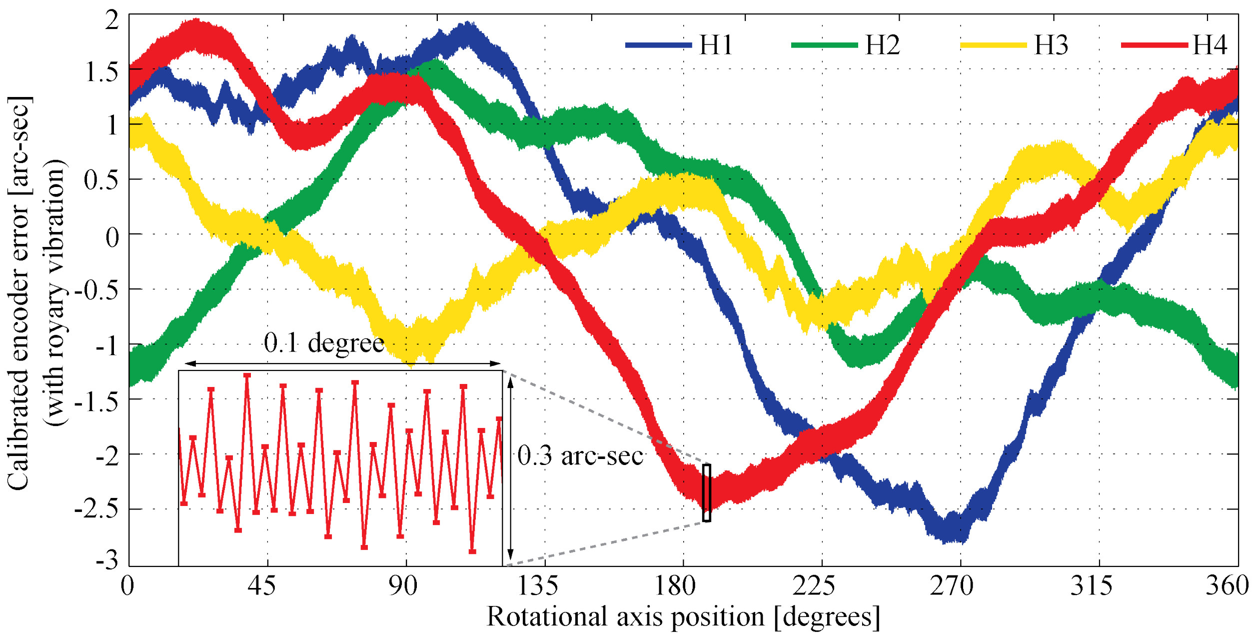

Figure 5.4: Calibrated error maps with rotary vibration, at 200 rpm.

each error map included. This 500cpr error map allows a better visualization of the distortion caused by rotary vibration, that only affects low frequency error harmonics. The initial cause of the extreme error map

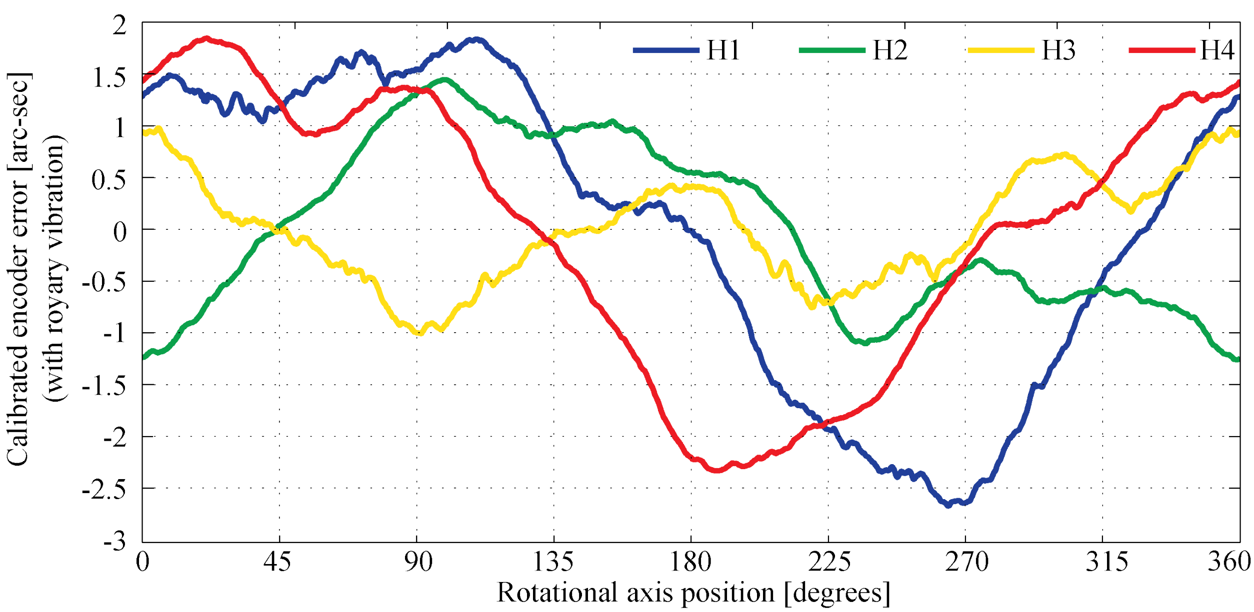

Figure 5.5: Calibrated error maps with rotary vibration, showing only the first 500 cpr harmonics.

differences between scanning units was unknown.

The first clue to understanding the cause was found by comparing a single scanning unit's calibrated error map at different spindle rotational speeds. Figure 5.6 shows the raw calibrated error map of scanning unit H1 at various speeds. As the spindle freely slows down from 300 rpm to 200 rpm, the raw calibrated error map is observed to grow in magnitude. Similarly for the calibrated error maps of scanning units H2 (Figure 5.7) and H4 (Figure 5.8) the change in speed causes growth of the magnitude of the error map.

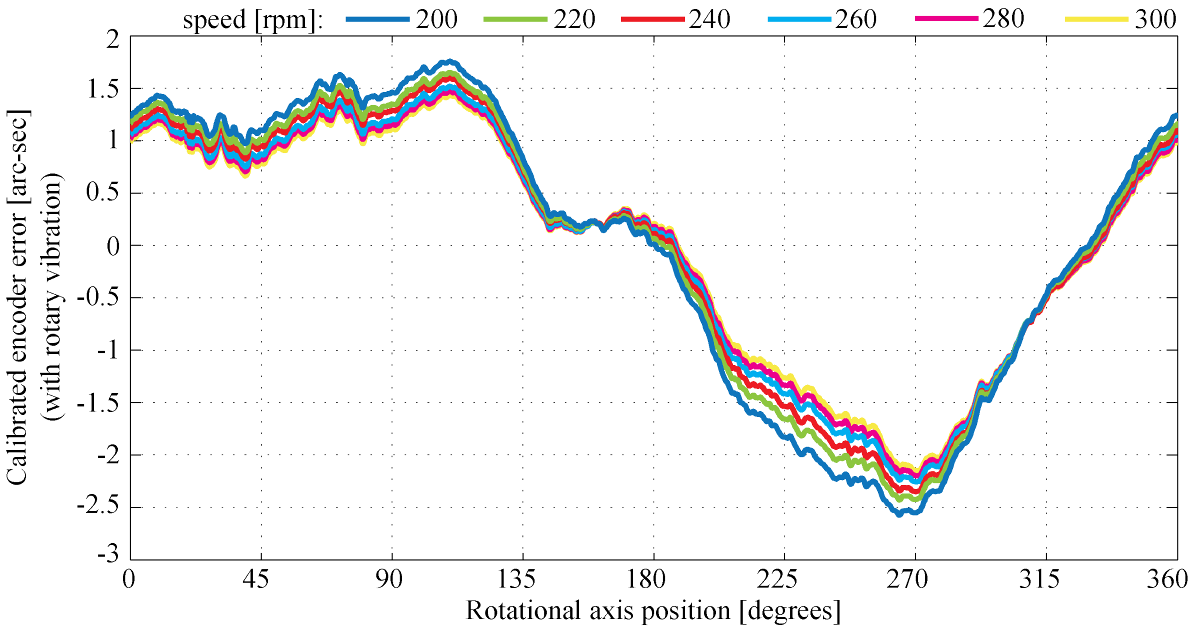

Figure 5.6: Calibrated error maps for H1, at spindle rotation speeds between 300 rpm and 200 rpm.

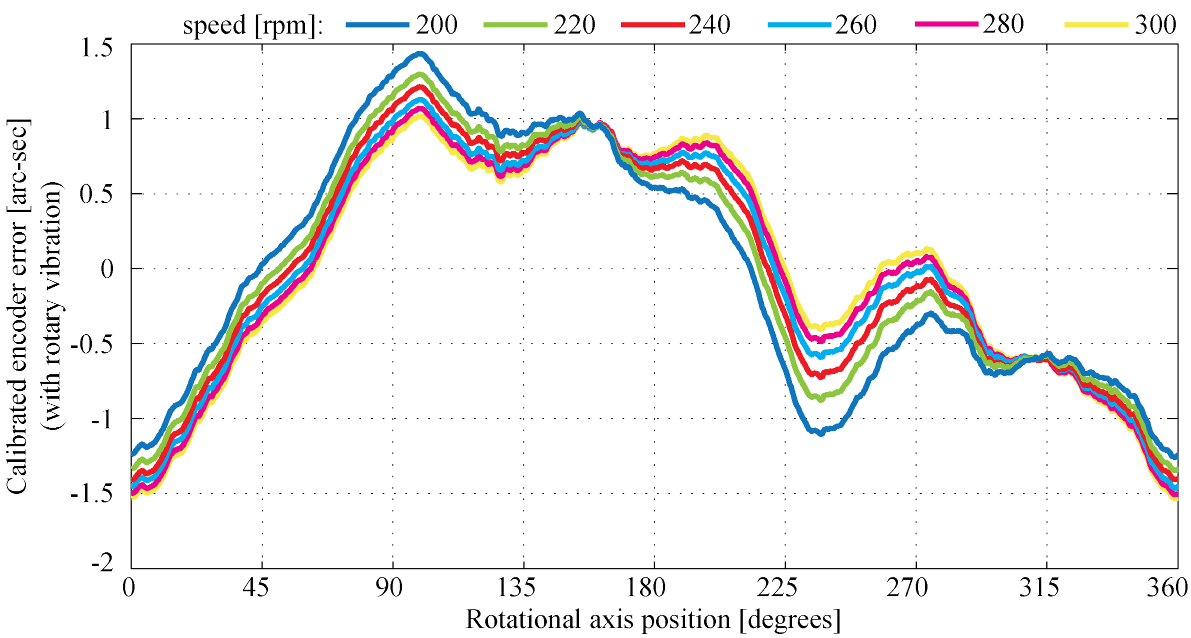

Figure 5.7: Calibrated error maps for H2, at spindle rotation speeds between 300 rpm and 200 rpm.

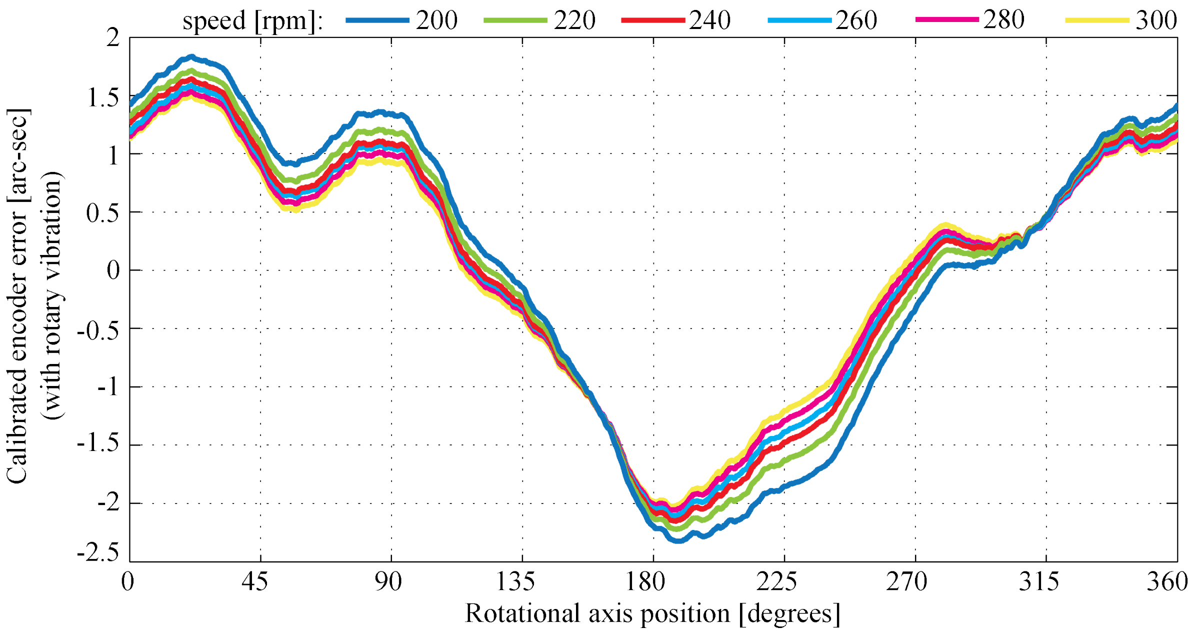

Figure 5.8: Calibrated error maps for H4, at spindle rotation speeds between 300 rpm and 200 rpm.

However the error map for scanning unit H3 (Figure 5.9) decreases in magnitude with the change in speed, which is a result of the calibration disturbance being out of phase with the actual error, causing a destructive interference. This result lead to a theory that the calibration disturbance was position dependent, due to different results on each error map from each scanning unit located at different positions on the spindle stator.

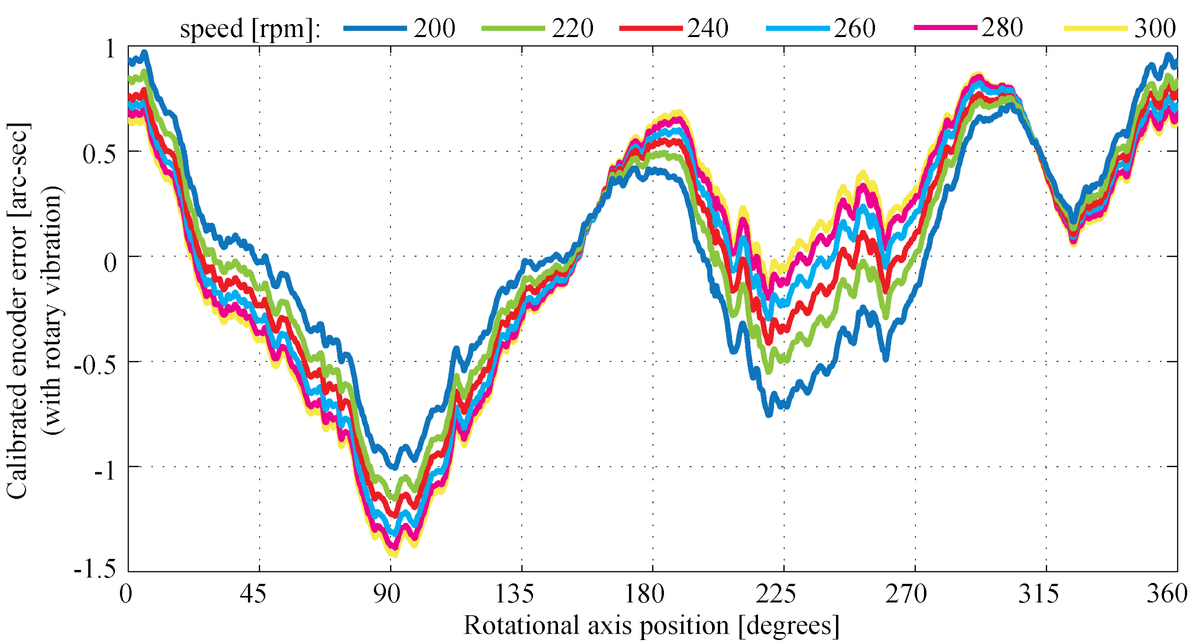

Figure 5.9: Calibrated error maps for H3, at spindle rotation speeds between 300 rpm and 200 rpm.

The second clue was found by looking at the variation of each error map harmonic over the range of speed. The double sided amplitude and phase of the Fourier coefficients of error maps calibrated at each spindle speed are show for scanning unit H1, H2, H3 and H4 in Figure 5.10, Figure 5.11, Figure 5.12 and Figure 5.13 respectively. The distortion of the error maps over the speed range can be seen. The most obvious effect is that the calibration disturbance is affecting the lower frequency harmonics the most. The variation in the first and second harmonics can easily be seen while the higher harmonics are constant with rotational speed.

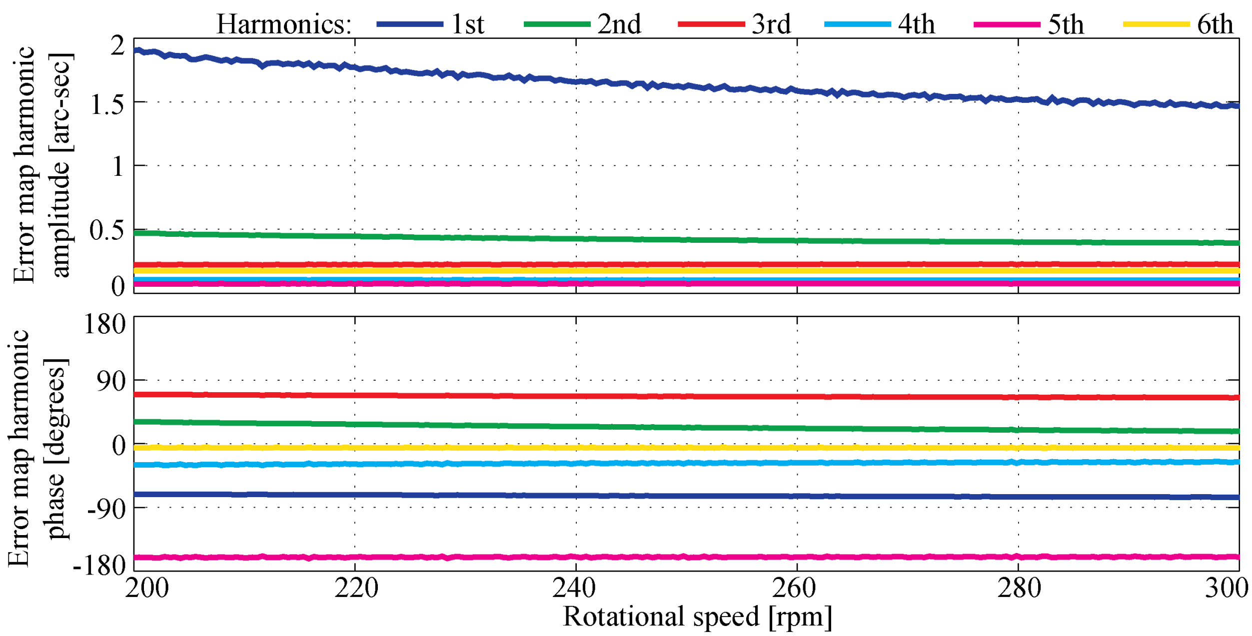

Figure 5.10: Amplitude and phase for calibrated error maps of scanning unit H1.

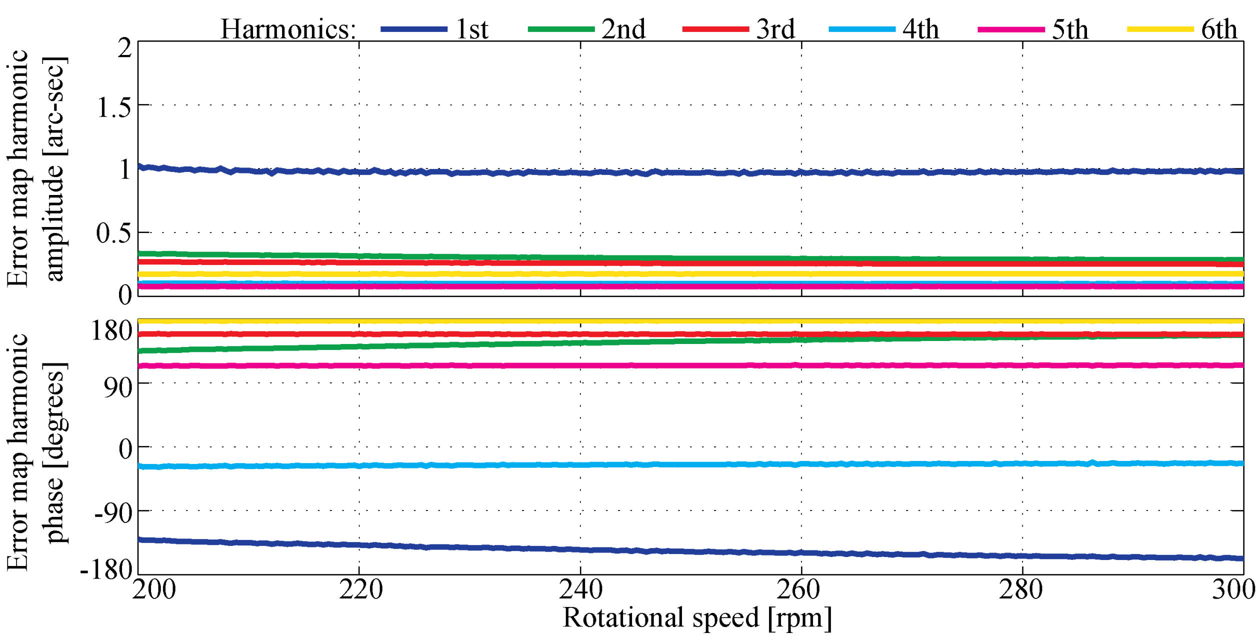

Figure 5.11: Amplitude and phase for calibrated error maps of scanning unit H2.

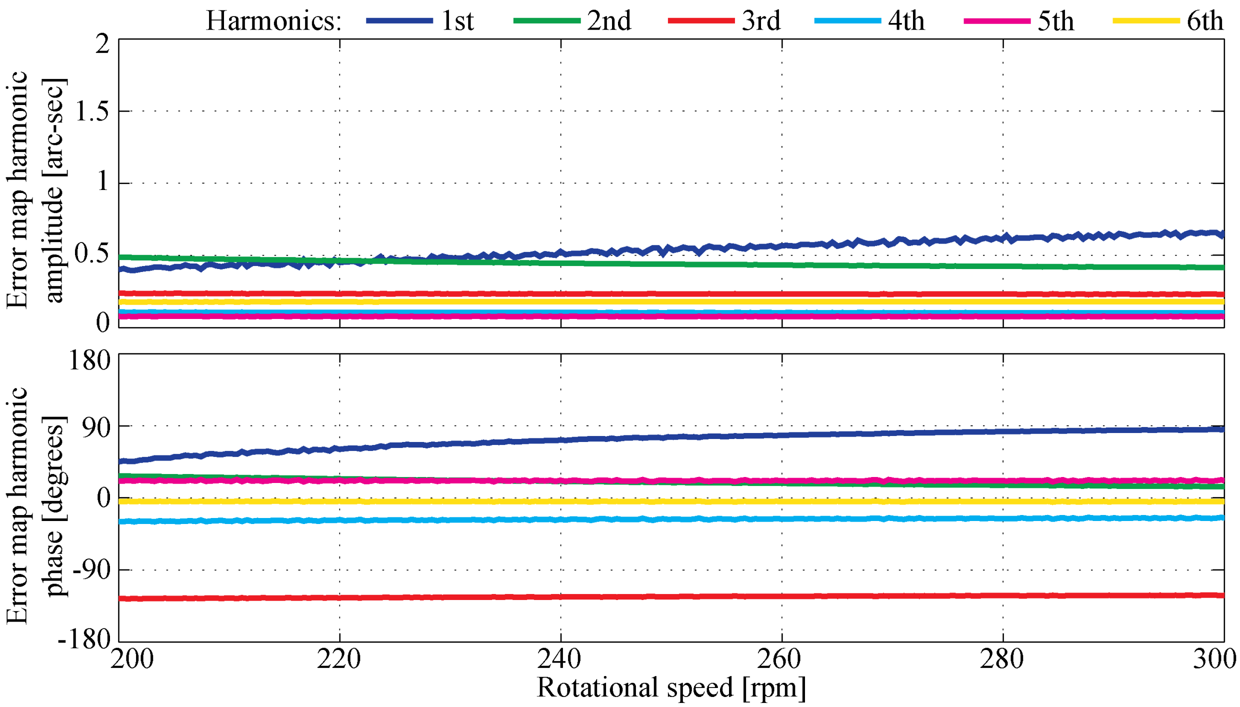

Figure 5.12: Amplitude and phase for calibrated error maps of scanning unit H3.

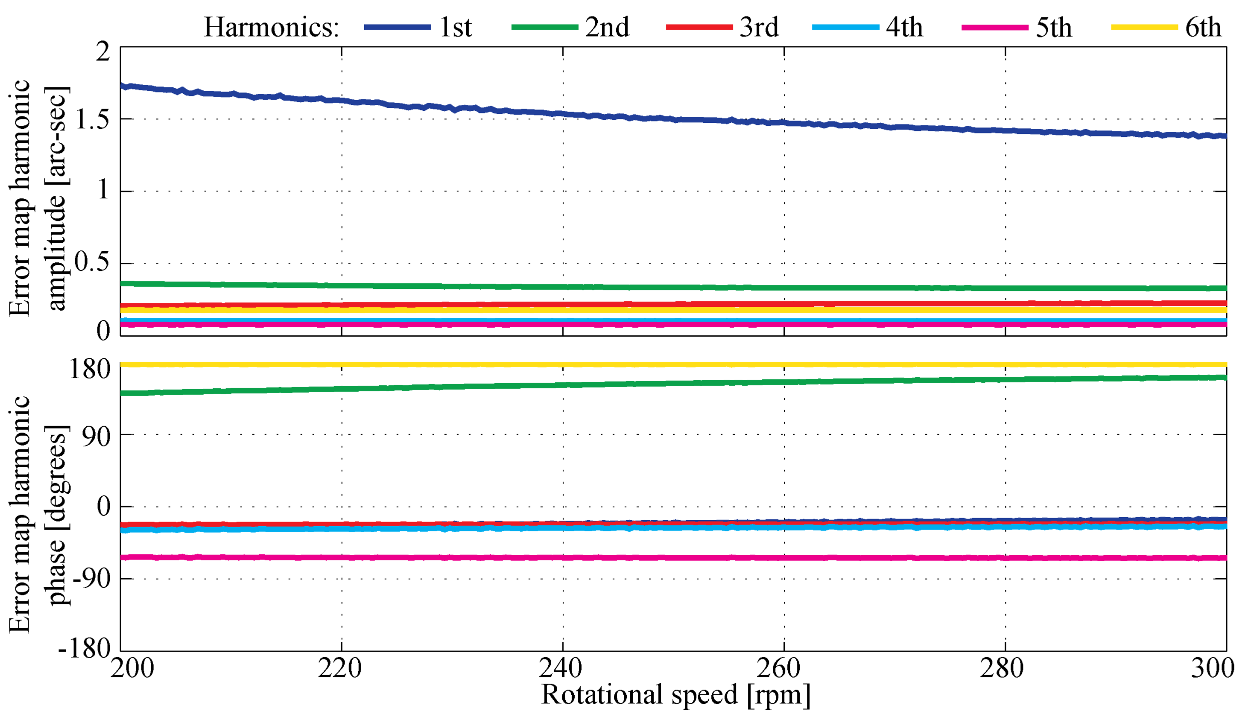

Figure 5.13: Amplitude and phase for calibrated error maps of scanning unit H4.

5.3 Rotary Vibration Removal

At this point the theory of the calibration result (Equation 2.31) was developed and the calibration disturbance identified as rotary vibration. The rotary vibration disturbance can be completely removed with harmonic cancellation and prediction methods of Section 2.1.2. Figure 5.14 shows the double sided amplitude of the rotary vibration harmonics (Equation 2.41) across the calibrated speed range. Although the

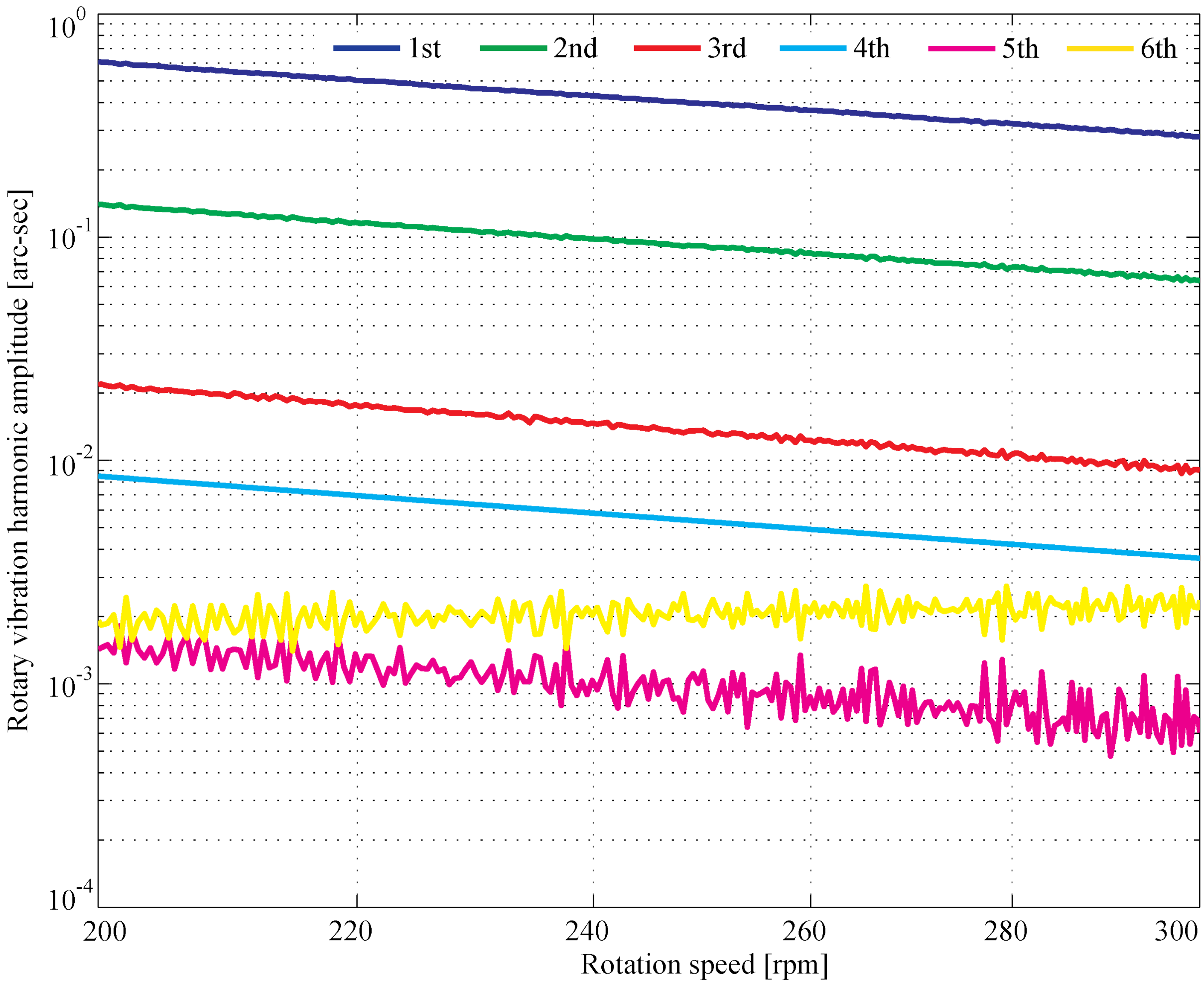

Figure 5.14: Rotary vibration amplitude spectrum for the first six harmonics, extracted during freely slowing down spindle response.

rotary vibration removal is performed for all harmonics up to the 20-th (Equation 2.42) the experimental results show that rotary vibration harmonics above the sixth harmonic are negligible. Each rotary vibration harmonic, except for the sixth, follows the trend of decreasing amplitude at high rotational speeds with a $-40 decibels/decade$ slope. Contrary to theory, the sixth rotary vibration harmonic does not follow the prediction and represents a constant rotary vibration harmonic. The rotary vibration prediction method cannot identify these components while the harmonic cancellation method still can. This is discussed further Section 5.3.1.

The rotary vibration is then reconstructed in the spatial domain for each spindle speed as shown in Figure 5.15 and removed from the calibration result. The speed independent, rotary position dependent

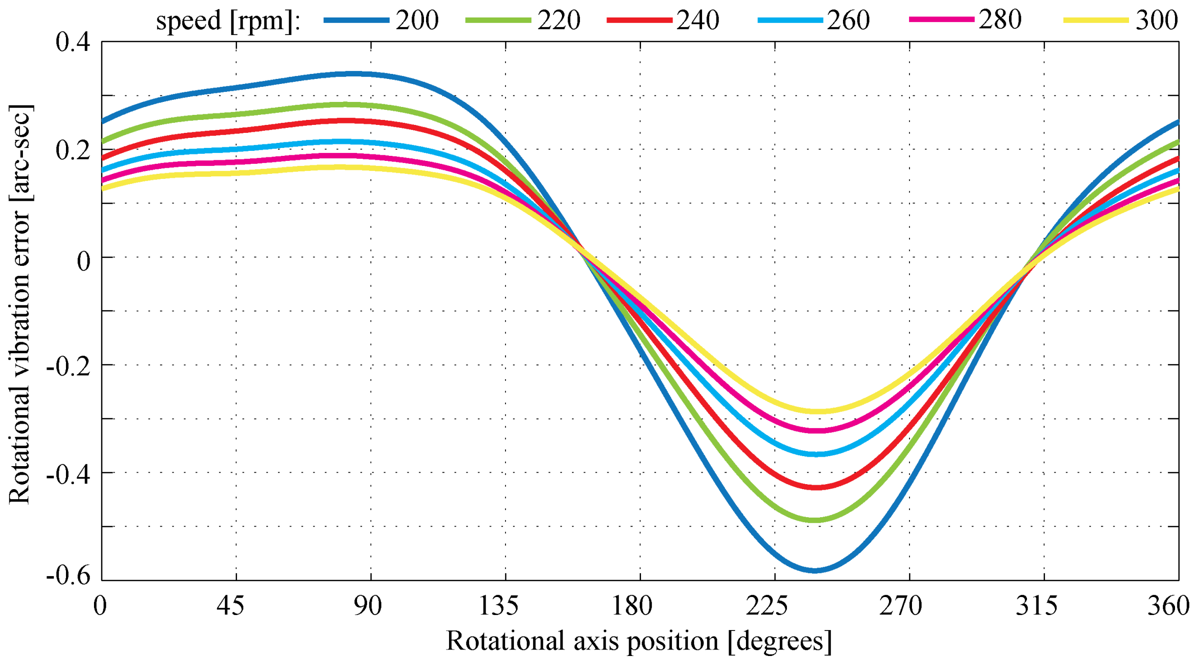

Figure 5.15: Rotary vibration component removed from calibration results.

disturbance torque can be estimated with Equation 2.39. Figure 5.16 shows the estimated disturbance torque of the air bearing spindle, on the order of 0.0015 Nm amplitude.

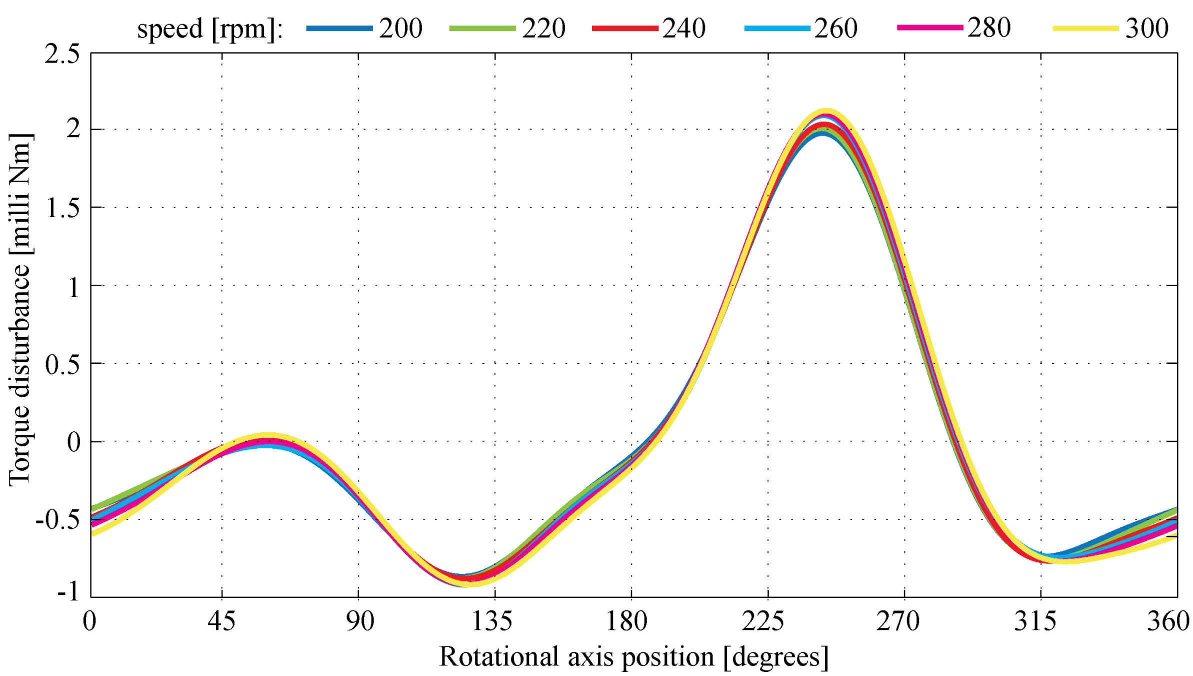

Figure 5.16: Estimated speed independent, rotary position dependent disturbance torque.

5.3.1 Harmonic Cancellation vs. Prediction

Two methods for rotary vibration removal are presented Section 2.1.2, harmonic cancellation and rotary vibration prediction. A combination of the methods was chosen to extract the complete rotary vibration component from the calibrated error map, while the harmonic cancellation method can not identify rotary vibration harmonics multiple of the number of scanning units installed. Theoretically the rotary vibration method can predict all the rotary vibration harmonics but the prediction requires an assumption of the spindle dynamics. It is found that experimental rotary vibration does not follow the prediction of, Equation 2.39 exactly. Instead the experimental results show there exists a rotary vibration component that is speed independent.

Figure 5.17 shows a comparison of the first harmonic of rotary vibration extracted with the harmonic cancellation and rotary vibration prediction methods. For the predicted methods a single scanning unit's calibration result is used to make the prediction, show for all four scanning units in the setup. At low rotational speeds, the speed dependent rotary vibration dominates and both methods converge. At high rotational speeds, the constant rotary vibration component starts to dominate and the results diverge. Similar

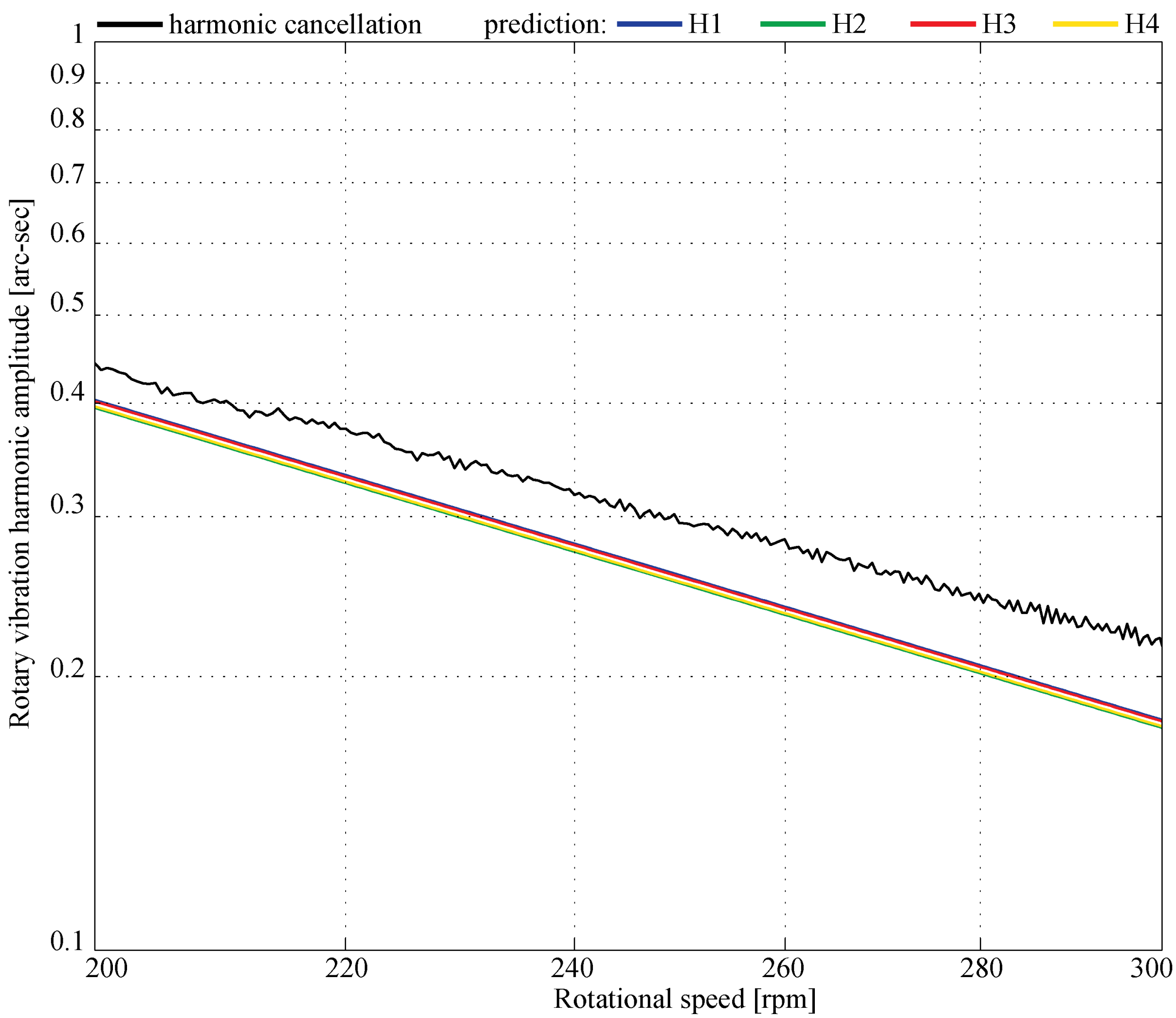

Figure 5.17: Comparison of the first harmonic of rotary vibration extracted by harmonic cancellation and prediction methods.

patterns are seen for rotary vibration extraction of the second and third order harmonics, Figure 5.18 and Figure 5.19 respectively. The constant rotary vibration component contributes 0.046 arc-sec, 0.1 arc-sec and 0.001 arc-sec for the first, second and third order harmonics. Due to the steadily decreasing harmonic amplitude of each rotary vibration component the constant rotary vibration component for the fourth order harmonic will be negligible.

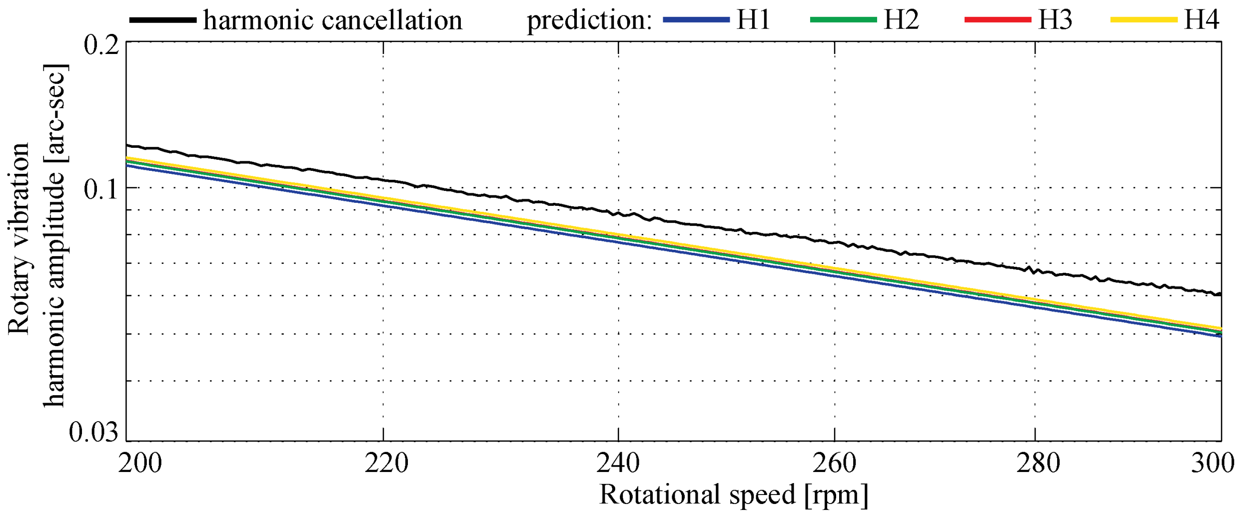

Figure 5.18: Comparison of the second harmonic of rotary vibration extracted by harmonic cancellation and prediction methods.

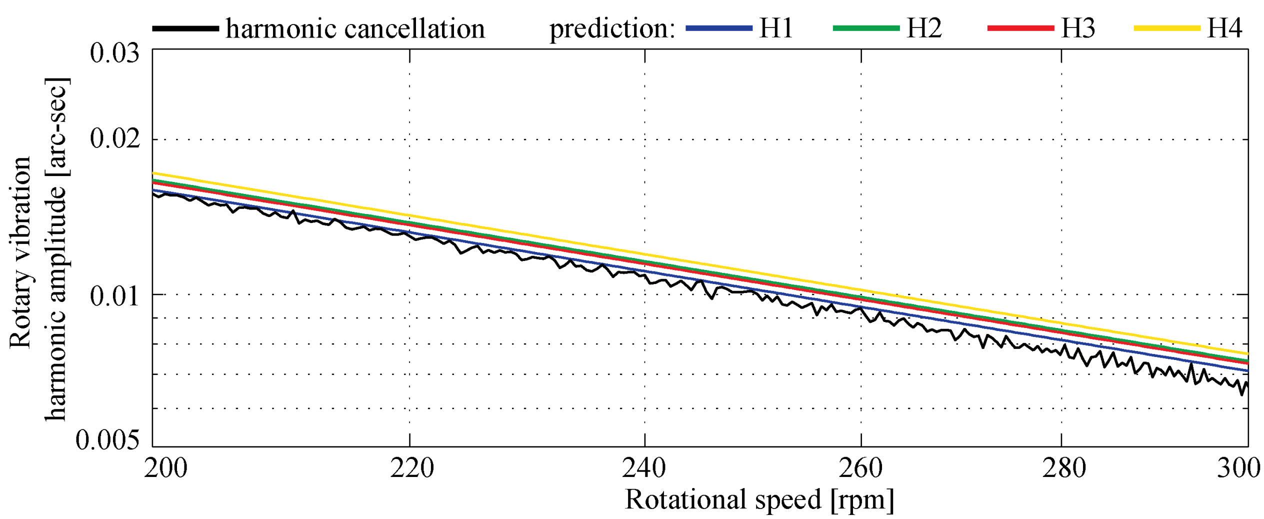

Figure 5.19: Comparison of the third harmonic of rotary vibration extracted by harmonic cancellation and prediction methods.

Several theories for the cause of rotary vibration exist as discussed in the following section.

5.3.2 Possible Causes of Rotary Vibration

Although the actual cause for the measured rotary vibration is un-verified, here several possible causes are discussed. Two theories have been developed as a cause of the position dependent torque disturbance to explain the dominant first and second order harmonics. The other harmonic components do exist but on much lower order of magnitude. Both theories deal with the deformation of the air bearing rotor and stator, highlighted in the experimental setup in Figure 5.20.

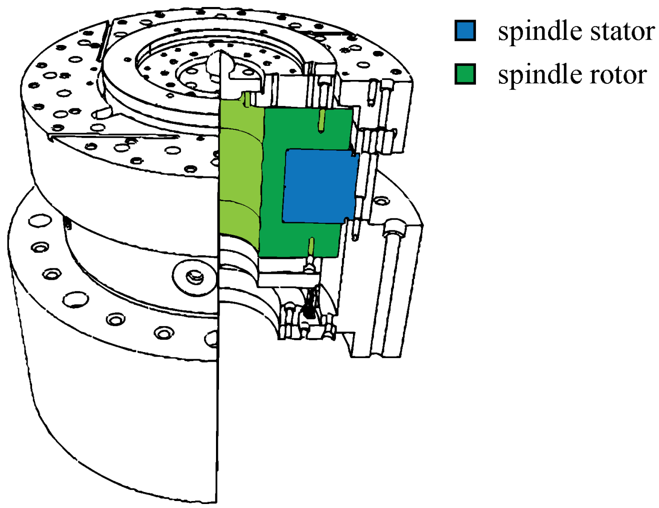

Figure 5.20: Experimental setup with air bearing rotor and stator highlighted.

The low damping coefficient of the air bearing is created due to an air gap, on the order of a few μm, between the spindle stator and rotor. Due to the small size of the air gap any small deformation of the air bearing can have a large effect on performance. Deformations can be caused by mounting non-circular or non-flat surfaces to the air bearing.

If the mating parts of the air bearing spindle cause an out parallelism tolerance issue between the top of bottom surfaces of the air bearing stator a 1cpr harmonic torque disturbance can exist as depicted in Figure 5.21. At one rotational angular position the spindle rotor and stator will match the most, $\theta = 0°$ Figure 5.21b. In this position the potential energy stored in deformation of the spindle rotor is a minimum. As the spindle rotates, kinetic energy of rotational speed is transferred into potential energy that deforms the spindle rotor, causing the spindle to slow down. At $\theta = 180°$ the spindle rotor is deformed the most and will have the least kinetic energy Figure 5.21c. This deformation would result in a dominant 1 cpr disturbance torque.

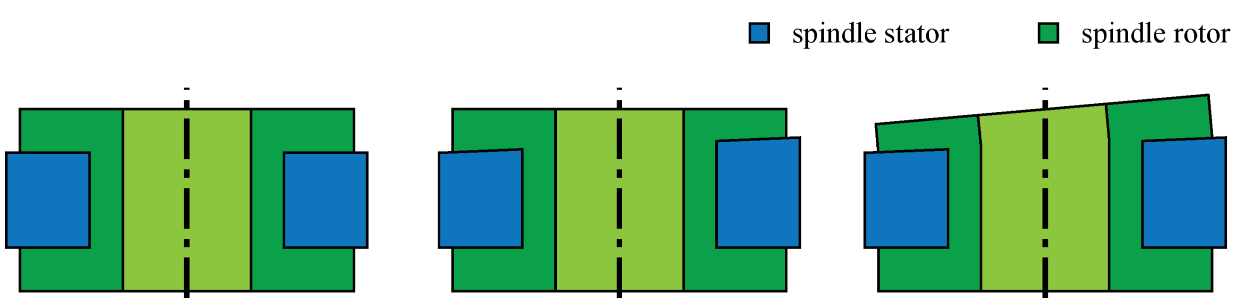

(a) Ideal case

(b) Deformed bearing, 0° rotation

(c) Deformed bearing, 180° rotation

Figure 5.21: Out of parallel deformation of spindle rotor causing 1cpr rotary vibration harmonic.

If the mating parts are non-circular and cause an elliptic deformation of the air bearing stator and rotor a $2cpr$ harmonic torque disturbance can exist as depicted in Figure 5.22. At one rotation position the spindle rotor and stator will match the most, $\theta = 0°$ Figure 5.22b. Similar to the theory proposed for the 1cpr harmonic, the transfer of kinetic and potential energy as the spindle rotates and the rotor/stator deform is the cause of disturbance torque. However the disturbance occurs twice per revolution due to the elliptic shape. At $\theta = 90°$ the spindle is deformed the most and will have the least kinetic energy Figure 5.22c.

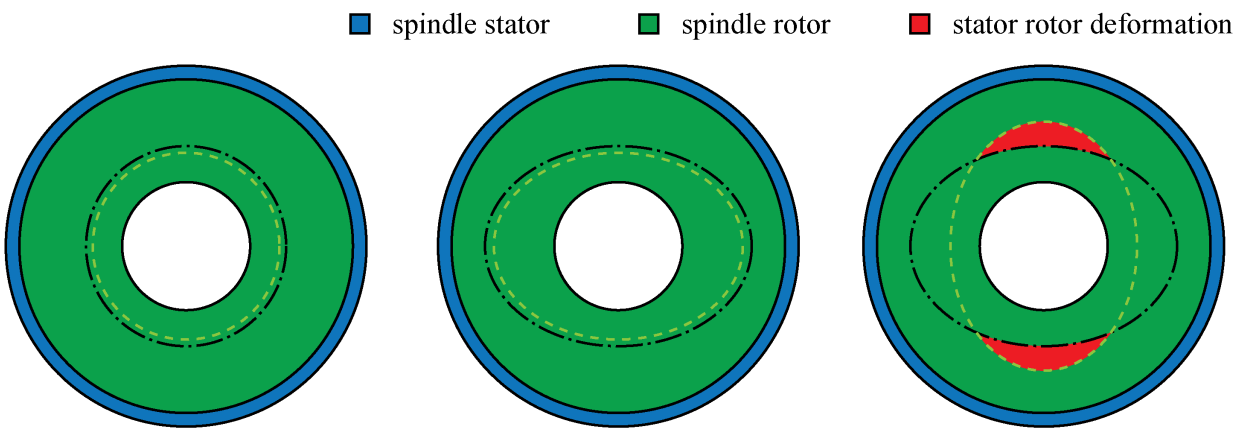

(a) Ideal case (b) Deformed bearing, 0° rotation (c) Deformed bearing, 90° rotation

Figure 5.22: Elliptic deformation of spindle rotor causing 2cpr rotary vibration harmonic.

An experiment was devised to support the theory of a $2cpr$ torque disturbance being caused by stator expansion. The expansion of the stator due to spindle rotation was directly measured with a capacitance probe distance sensor shown in Figure 5.23. Figure 5.24 shows the stator expansion measured across the

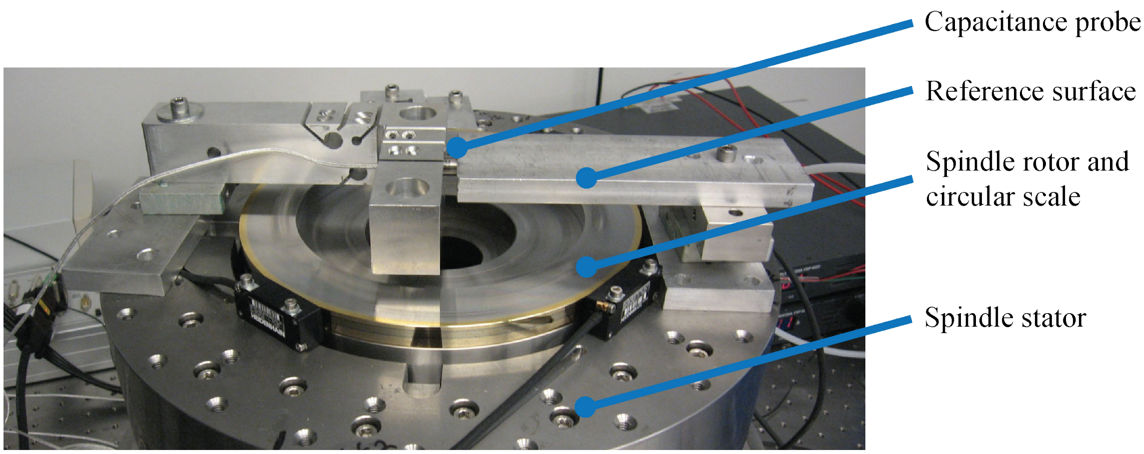

Figure 5.23: Experimental setup for measuring stator expansion.

diameter of the air bearing. Although the measurement shows expansion with an amplitude of $6nm$, the result is not significant enough to add solid proof as the cause of rotary vibration.

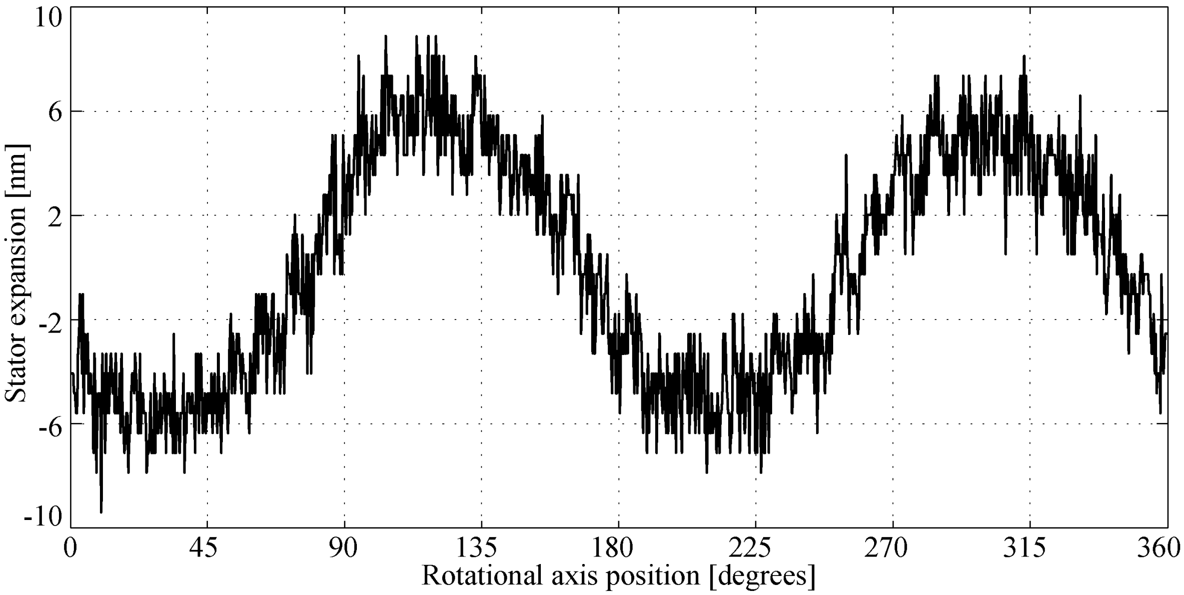

Figure 5.24: Experimentally measured stator expansion, measured across the diameter of the spindle stator.

Another possibility is that the air bearing spindle is damaged, either in manufacture, shipment or in its operation over the last three years. To eliminate this possibility the spindle should be disassembled and the bearing surfaces should be inspected to ensure flatness. This collaboration with the spindle manufacturer is on going to study this possibility.

Further investigation must be done to confirm the causes of torque disturbance in the experimental setup. In addition a theory explaining the constant rotary vibration component has not been developed. Both these aspects are left for future work.

5.4 Calibration After Rotary Vibration Removal

The rotary vibration component is removed form the raw calibration results and the actual encoder error map composed solely of grating and spindle radial error motion components is obtained. This error map can be used to correct the angle measurements of each scanning head to increase angle measurement accuracy.

After removing the rotary vibration component, the encoder error maps for each scanning unit become very similar to one another except for a 90° phase shift between them, Figure 5.25. The differences between encoder error maps are due to each scanning unit being sensitive to different spindle error motion directions and components.

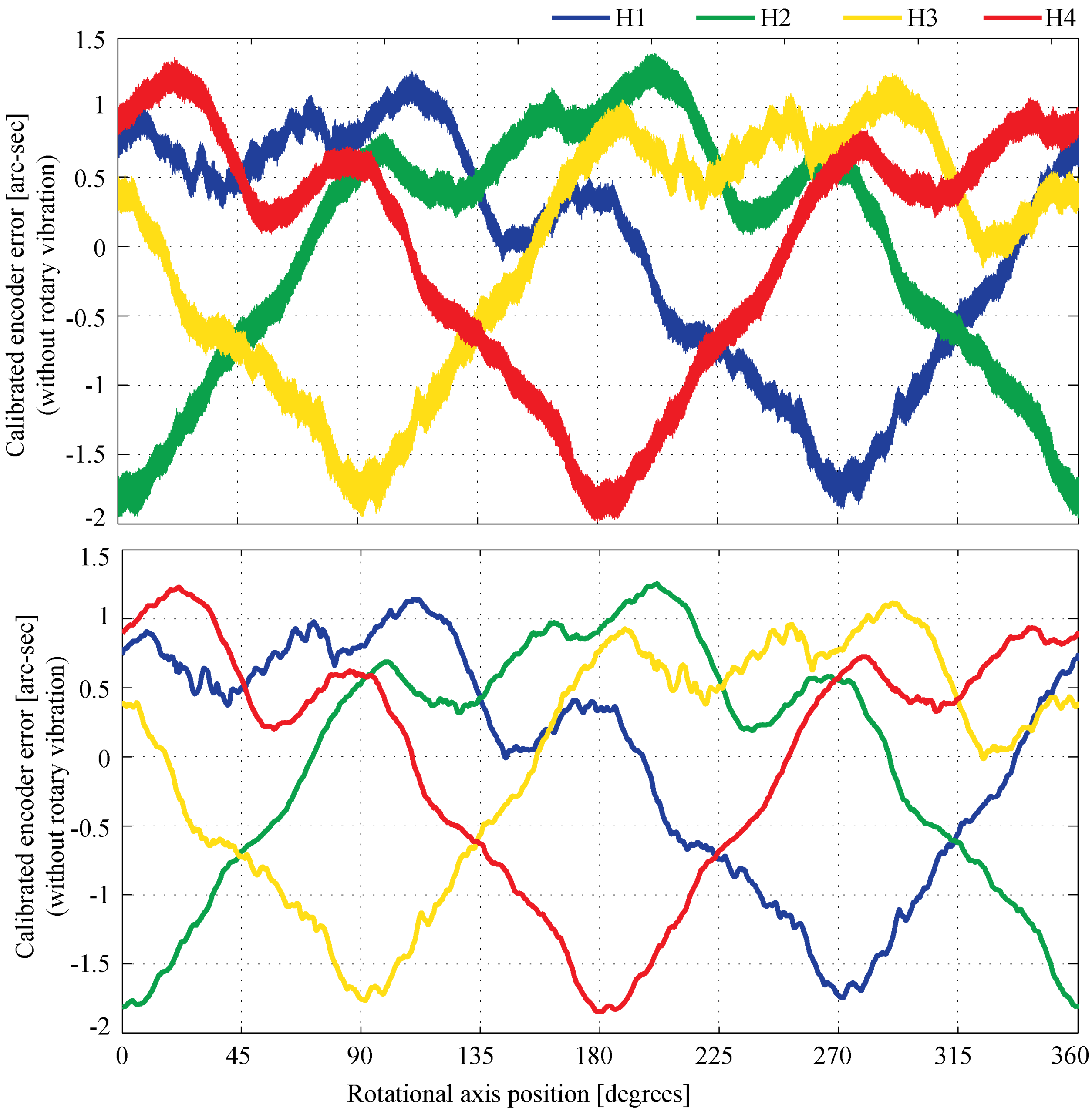

Figure 5.25: Calibrated error maps without rotary vibration at 200 rpm for full harmonics (top) and for the first 500 cpr harmonics (bottom).

The rotary vibration component causes the large differences in the error maps over the spindle speed calibration range. Without rotary vibration, the error maps at various calibration speeds are very consistent and do not change in magnitude. Figure 5.26, Figure 5.27, Figure 5.28 and Figure 5.29 show the now consistent calibrated error maps without rotary vibration for scanning units H1, H2, H3 and H4 respectively.

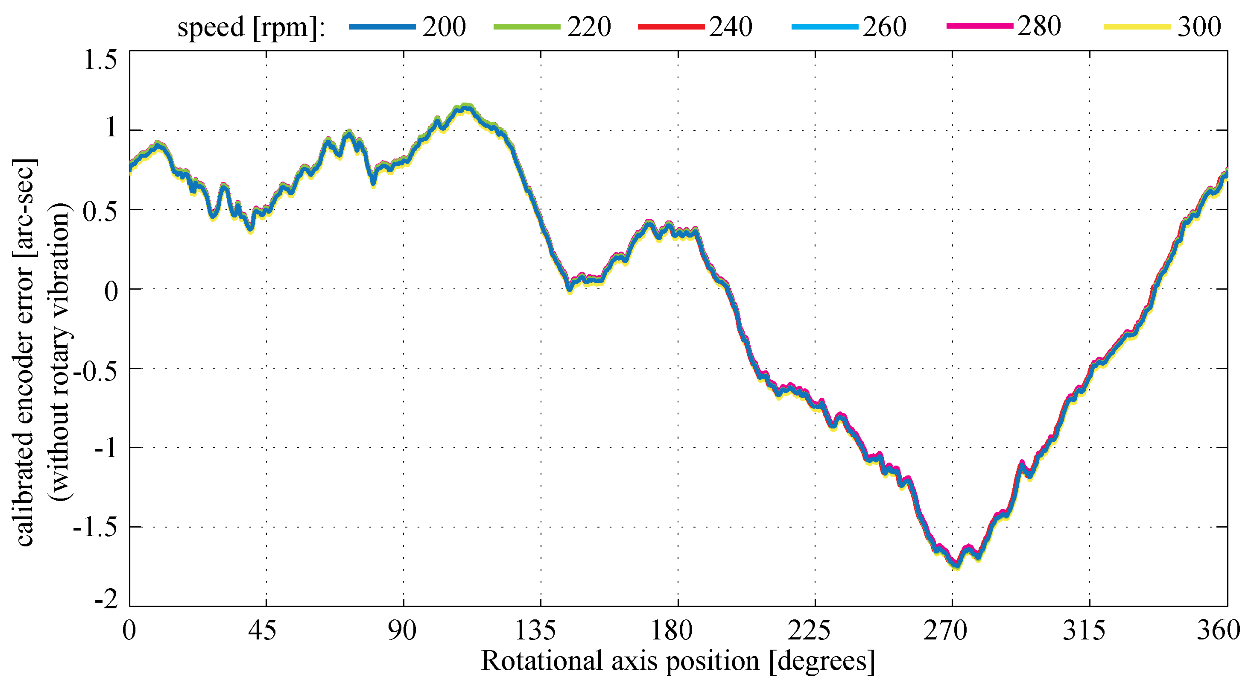

Figure 5.26: Calibrated error maps for H1, at spindle rotation speeds between 300 rpm and 200 rpm.

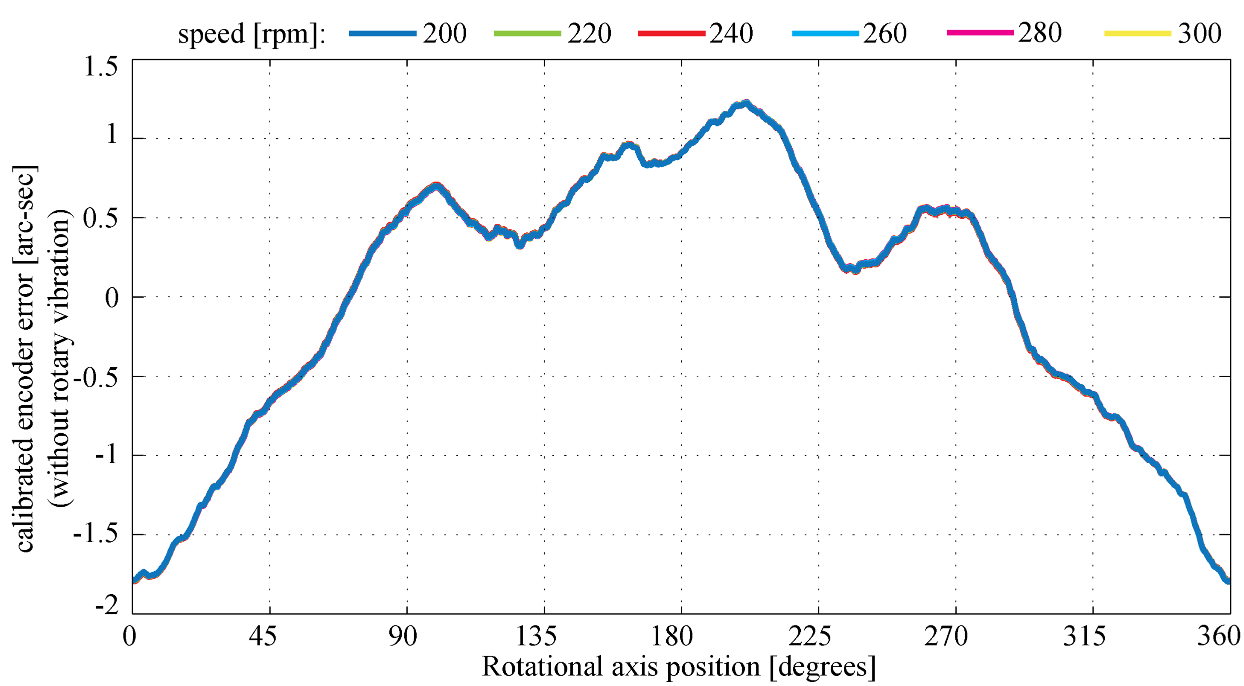

Figure 5.27: Calibrated error maps for H2, at spindle rotation speeds between 300 rpm and 200 rpm.

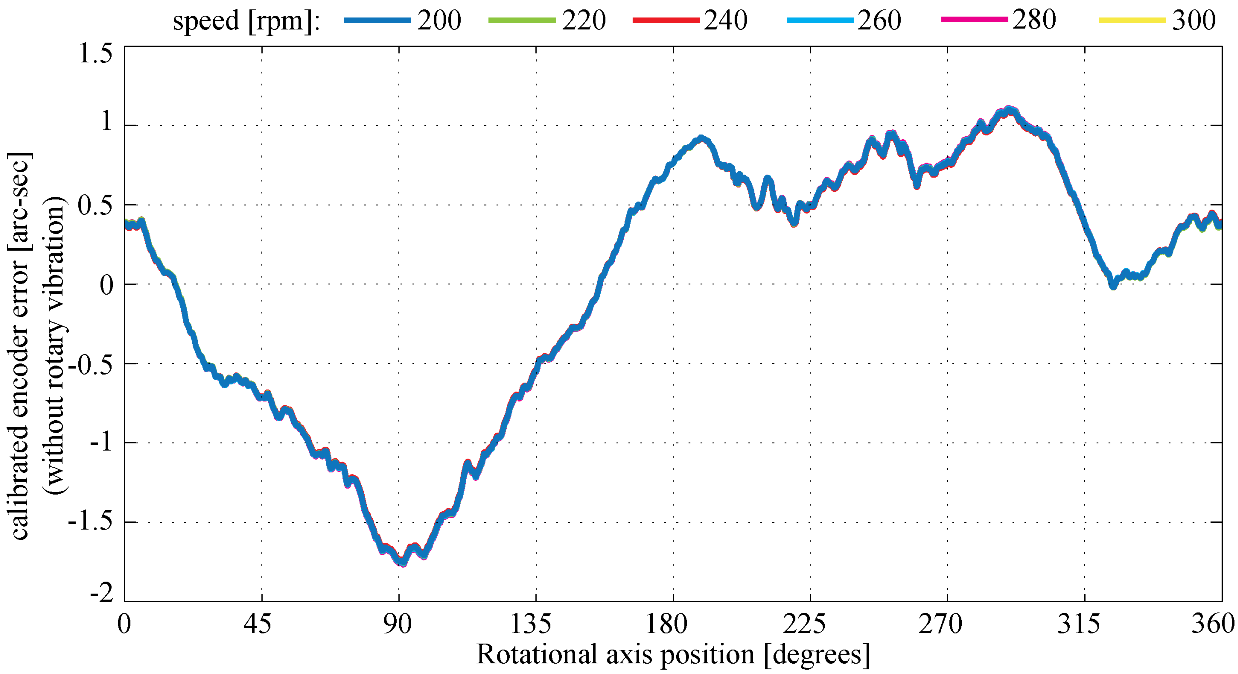

Figure 5.28: Calibrated error maps for H3, at spindle rotation speeds between 300 rpm and 200 rpm.

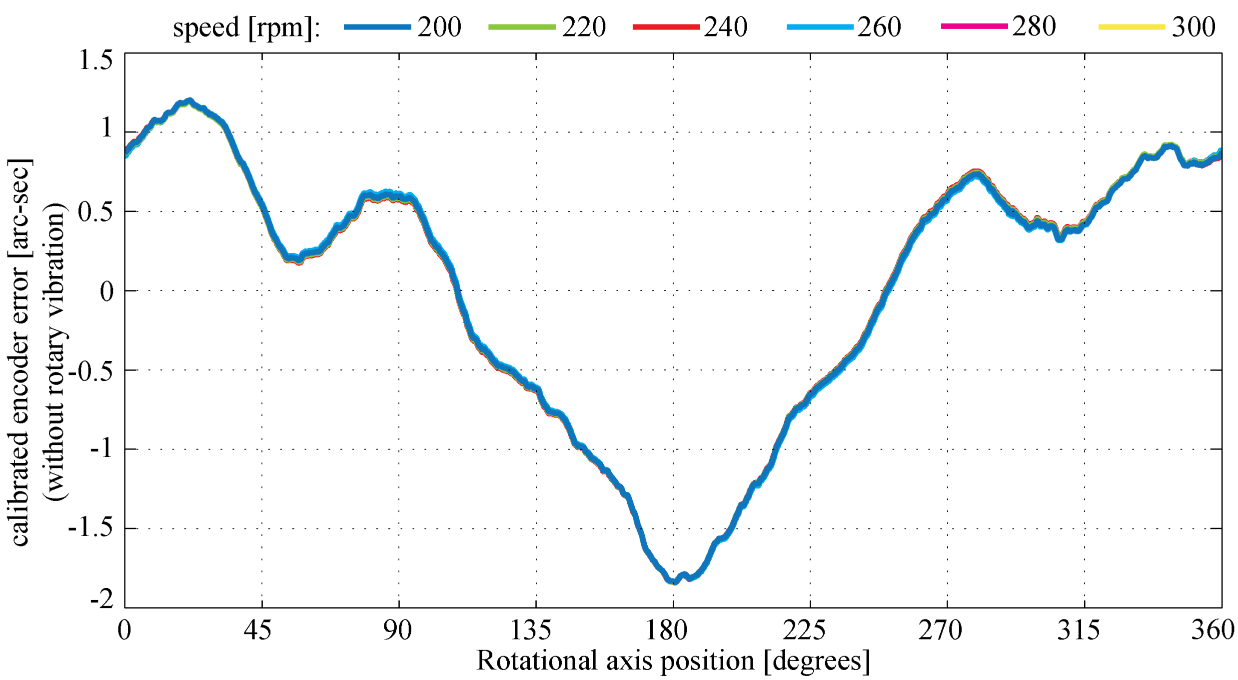

Figure 5.29: Calibrated error maps for H4, at spindle rotation speeds between 300 rpm and 200 rpm.

The consistency of the error maps without rotary vibration can be better seen in the frequency domain. Figure 5.30, Figure 5.31, Figure 5.32 and Figure 5.33 show the now stable lower harmonics of each error map over the range of speed. This shows the rotary vibration component has been entirely removed from each error maps.

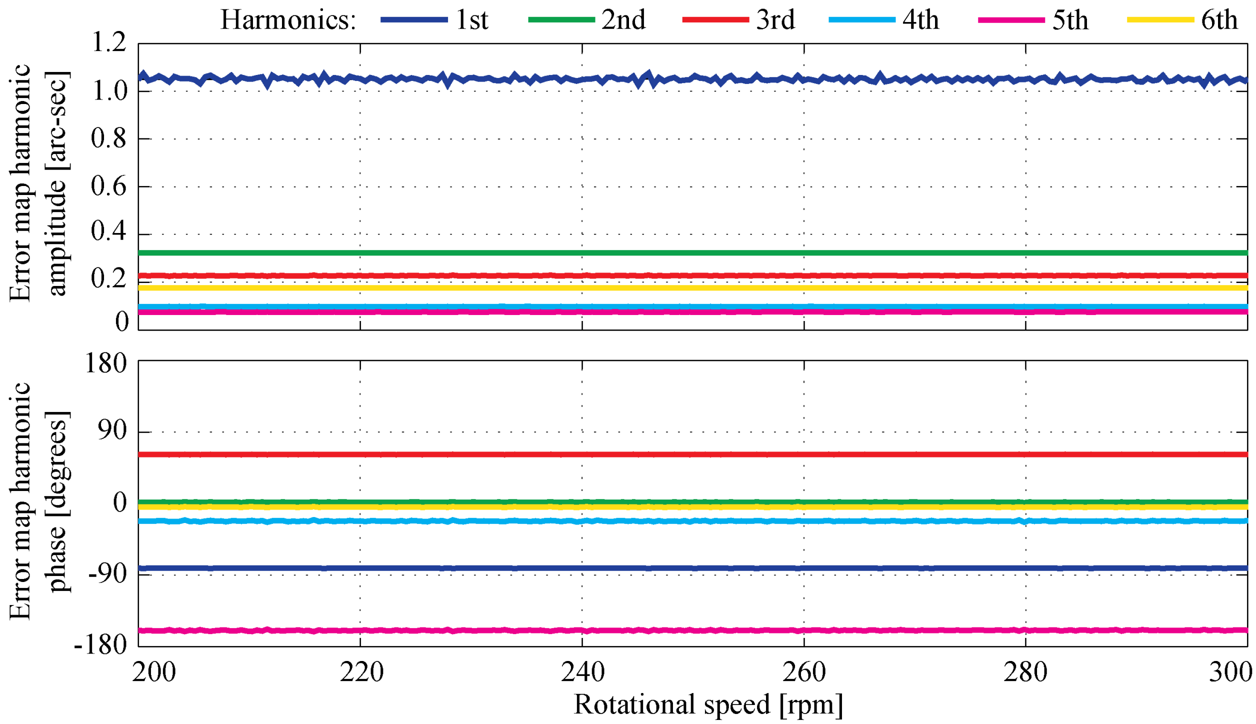

Figure 5.30: Calibrated error maps for H1, at spindle rotation speeds between 300 rpm and 200 rpm.

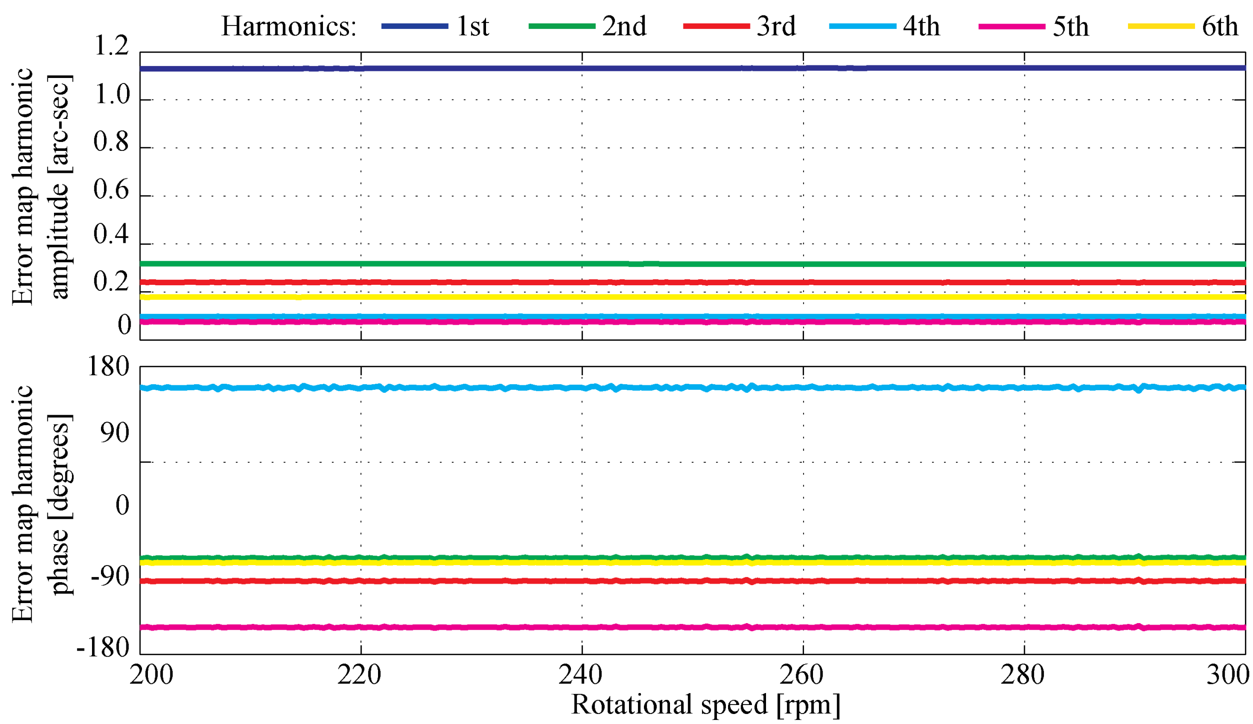

Figure 5.31: Calibrated error maps for H2, at spindle rotation speeds between 300 rpm and 200 rpm.

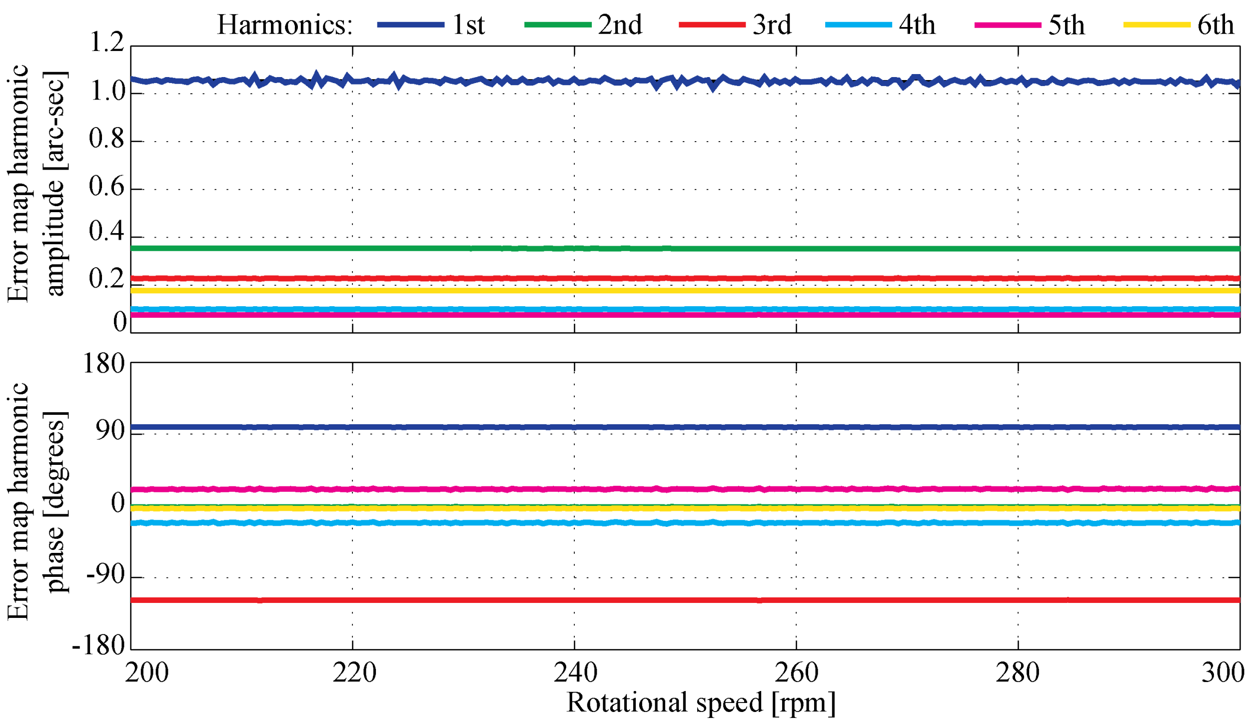

Figure 5.32: Calibrated error maps for H3, at spindle rotation speeds between 300 rpm and 200 rpm.

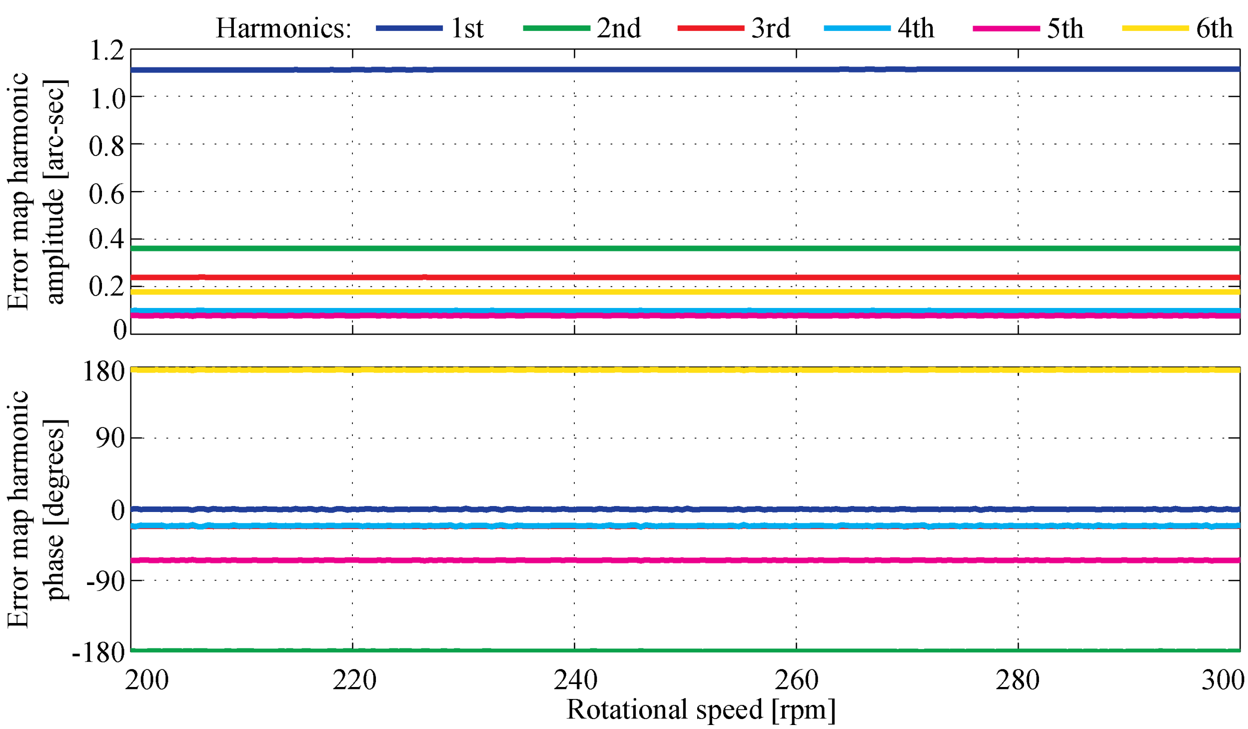

Figure 5.33: Calibrated error maps for H4, at spindle rotation speeds between 300 rpm and 200 rpm.

The dominant first order harmonic of encoder error has an amplitude of 1.1 arc-sec, which could be caused by an installation eccentricity of 0.55μm. The eccentricity of the circular scale was tightly controlled during installation using a capacitance probe displacement sensor. An eccentricity of $0.3\mu m$ was achieved which contributes only 0.6 arc-sec of first harmonic amplitude error. The remainder of the first order error harmonic must come from the pattern of lines printed on the circular scale.

The noise floor of the experimental calibration can be seen from the Fourier amplitude coefficients of the error map, Figure 5.34. The noise floor is shown at 1.5×10^{-4} arc-sec amplitude which affects most error map harmonics above the 700 cpr harmonic. The noise floor is caused by uncertainty in the encoder measurements due to marking or time uncertainties. The calibration uncertainty can be decreased by averaging multiple error maps but the encoder measurement uncertainty still exists. Both measurement and error map need to be improved to further increase the accuracy of the angle measurement. Improving one without the other would result in only a limited benefit.

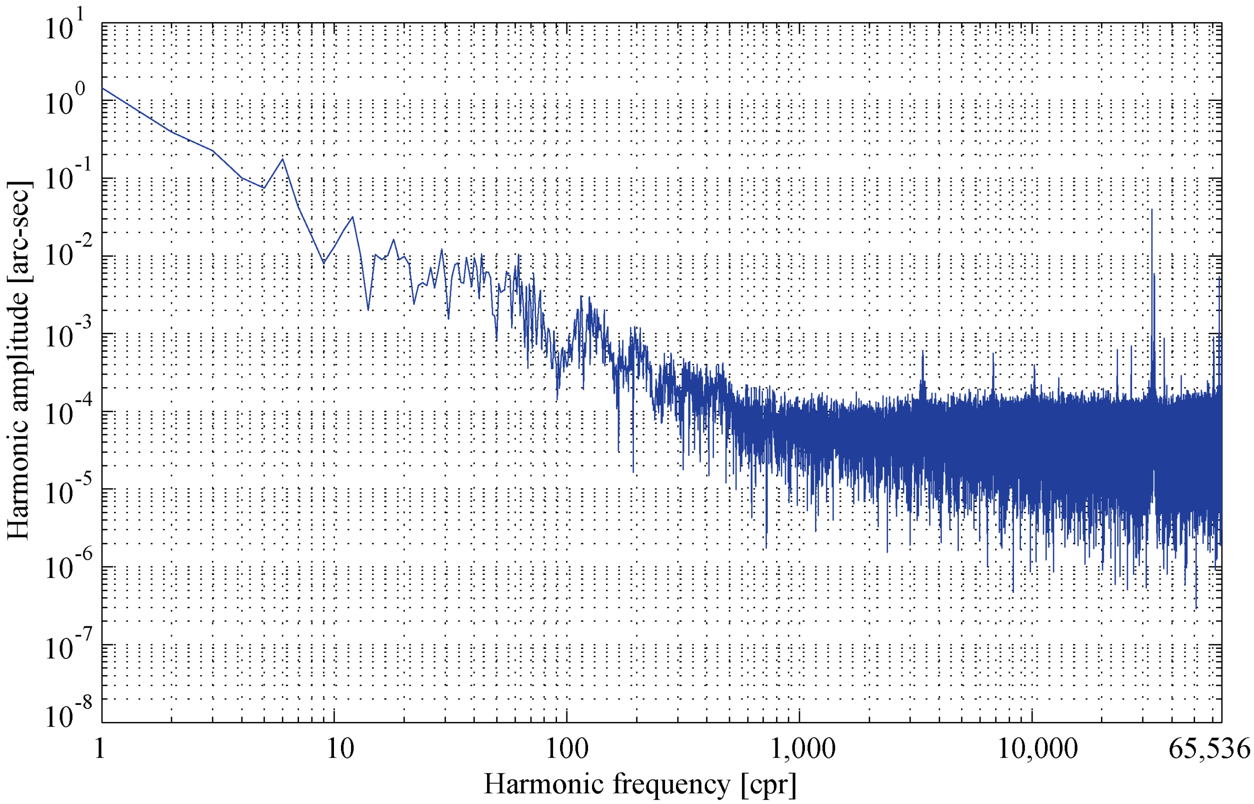

Figure 5.34: Fourier amplitude spectrum of calibrated encoder error map H1 without rotary vibration, at 200 rpm.

Figure 5.35 shows a comparison of Fourier amplitude coefficients for a typical calibrated error map and an average of 10 error maps. The noise floor is significantly reduced to 5×10^{-5} arc-sec which affects most error map harmonics above the 1,000 cpr harmonic. The average error is useful in that it allows the identification of harmonics with large amplitudes which may have previously been covered up by noise. Multiple peaks in the error map are identified given in Table 5.1.

The spikes in error map harmonics are abnormal but they can be explained as result of the fundamental operating principle of the incremental angle encoder. An analysis of the high frequency errors causing the thick band in the encoder error map is presented.

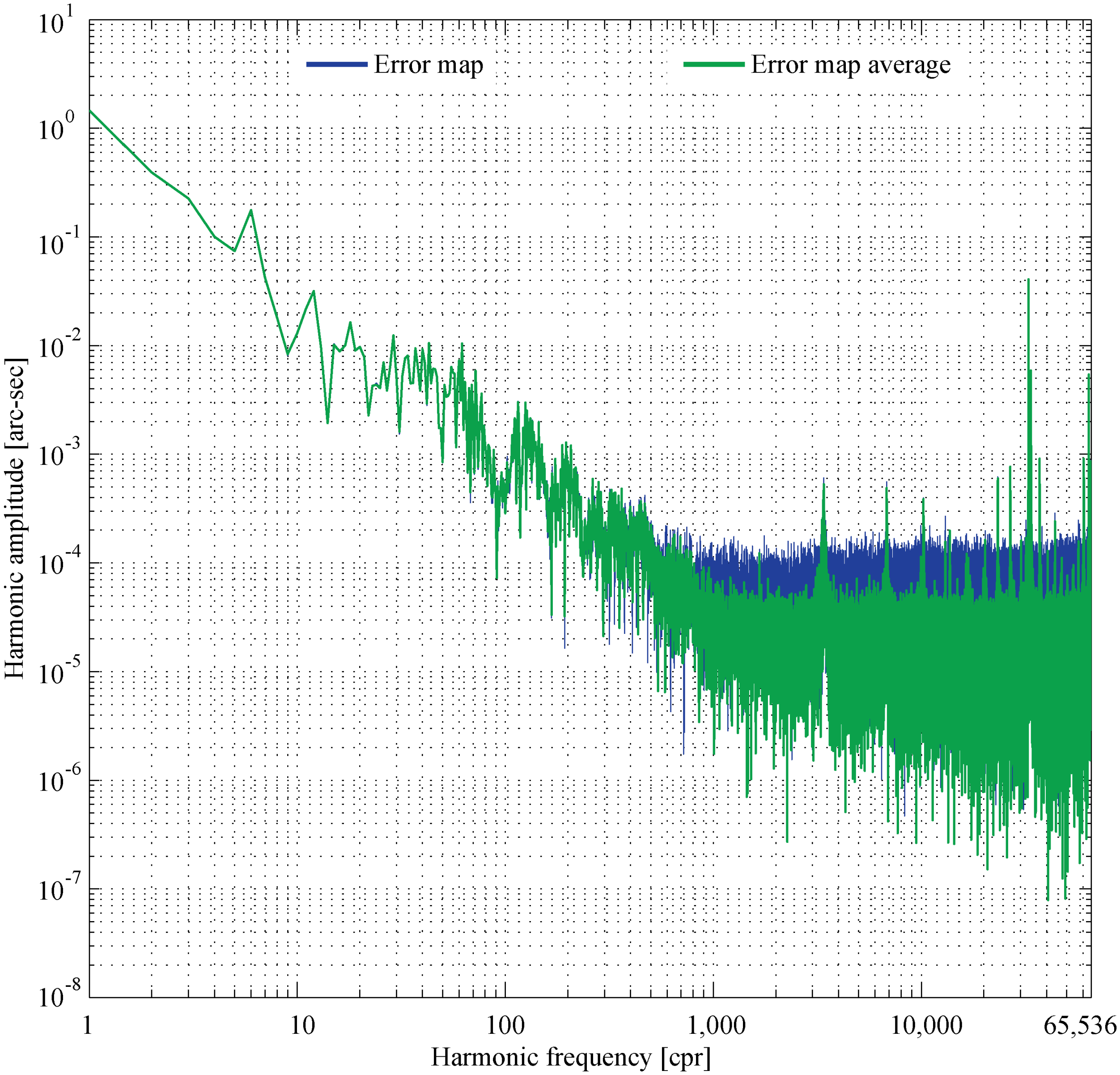

Figure 5.35: Comparison of the Fourier amplitude spectrum of calibrated encoder error maps with rotary vibration removal, at 200 rpm. Typical calibration result shown in blue, average of 10 error maps shown in green.

Table 5.1: Error map harmonics peak locations and amplitudes.

Harmonic No.	3,397	6,844	10,246	23,353	26,775	32,768
Amplitude [milli arc-sec]	0.5288	0.384	0.2719	0.599	0.7687	40.73

Harmonic No.	33,611	37,055	43,901	60,417	63,872	65,536
Amplitude [milli arc-sec]	5.894	0.912	0.1435	0.9098	5.433	142.2

5.4.1 High Frequency Error Components Analysis

The high frequency component makes up a significant portion of the encoder error map, contributing as much as 0.3 arc-sec of error, Figure 5.36. High frequency encoder error will exist based on the placement of

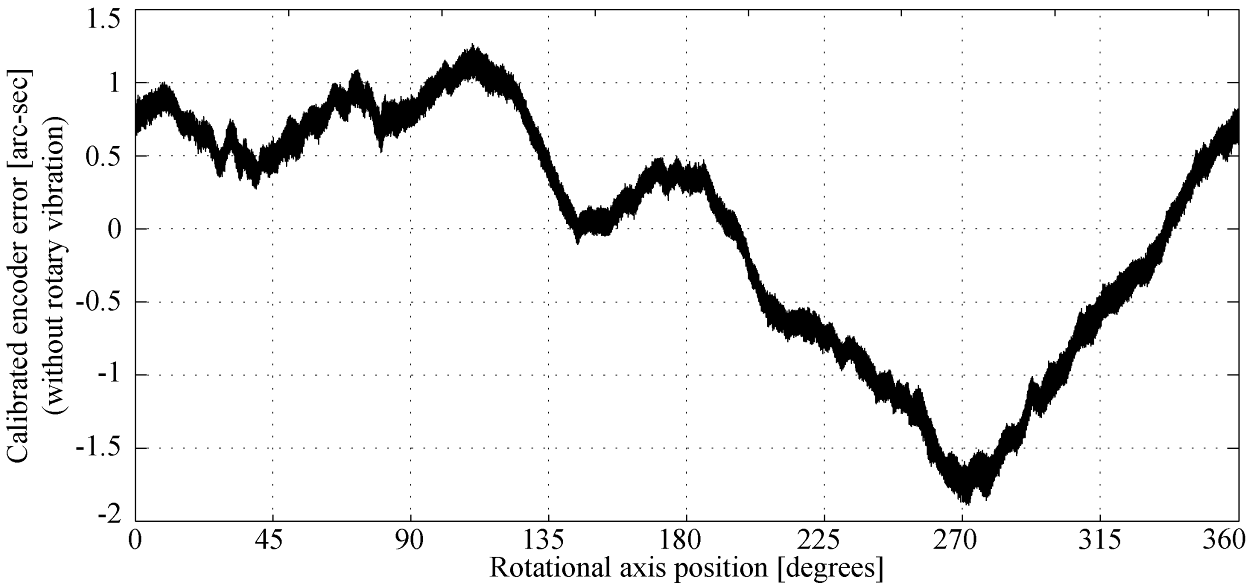

Figure 5.36: Typical calibrated encoder error map with rotary vibration removal, at 200 rpm.

the physical grating lines on the circular scale. Additional sources of the high frequency error are considered in Section 4.2.2, due to the operating characteristics of the encoder and quadrature decoding interpolation. These sources significantly increase the magnitude of high frequency error and make it a very important harmonic to capture. Encoder signal phase misalignment, signal unbalance and photocell spatial delay have been identified as causes. The error component caused by each of these sources can be determined by analyzing the deviations of each spatial interval from the nominal spacing, $\Delta_k - \Delta_0$. Figure 5.37 shows the count deviations, derived from the calibrated error map of scanning unit H1.

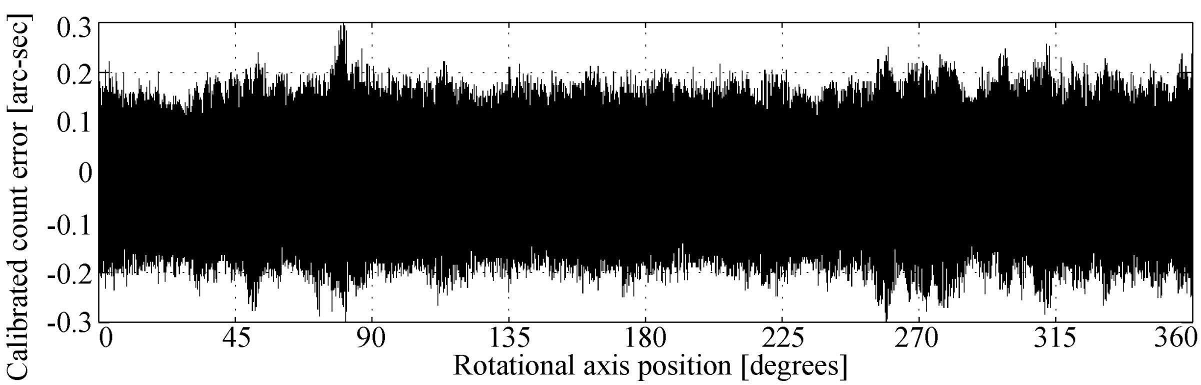

Figure 5.37: Deviations of each spatial interval from the nominal spacing on scanning unit H1.

Experimental signal phase misalignment

Encoder signals for phase A and phase B are assumed to be separated 90°. The alignment of phase A and B could differ from the nominal 90° due to the characteristic operation of the encoder and imperfect scanning unit installation Section 4.2.

A phase misalignment of greater than 90° can be found if the odd count deviations are consistently larger than the even count deviations. Conversely, a phase misalignment of less than 90° can be found if the odd count deviations are consistently smaller than the even count deviations (Figure 4.11). Figure 5.38 shows the count deviations with odd and even deviations highlighted.

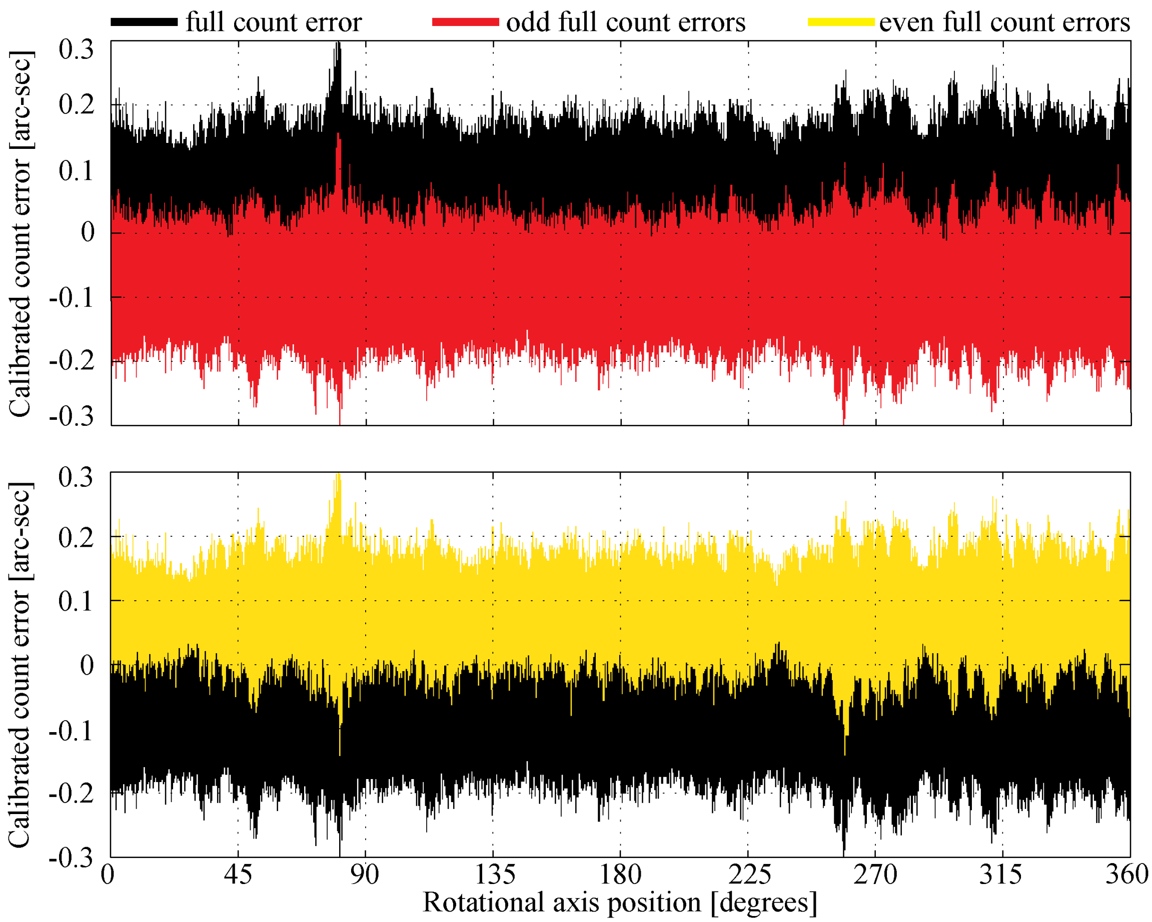

Figure 5.38: Offset between odd and even count deviations showing phase misalignment between the encoder signals.

The odd count deviations are found to be consistently smaller than the even count deviations, by 0.2 arc-sec. The difference is caused by a phase misalignment between encoder signal A and signal B of 1.8° smaller than the nominal 90°. Phase misalignment error is responsible for the highest harmonic error component at 65,536 cpr. This component can be removed from the calibration result by reconstructing the error map form the odd and even count errors without their mean values. As shown in Figure 5.39 the angle measurement error without the phase misalignment error component still has a significant high frequency component due to signal unbalance.

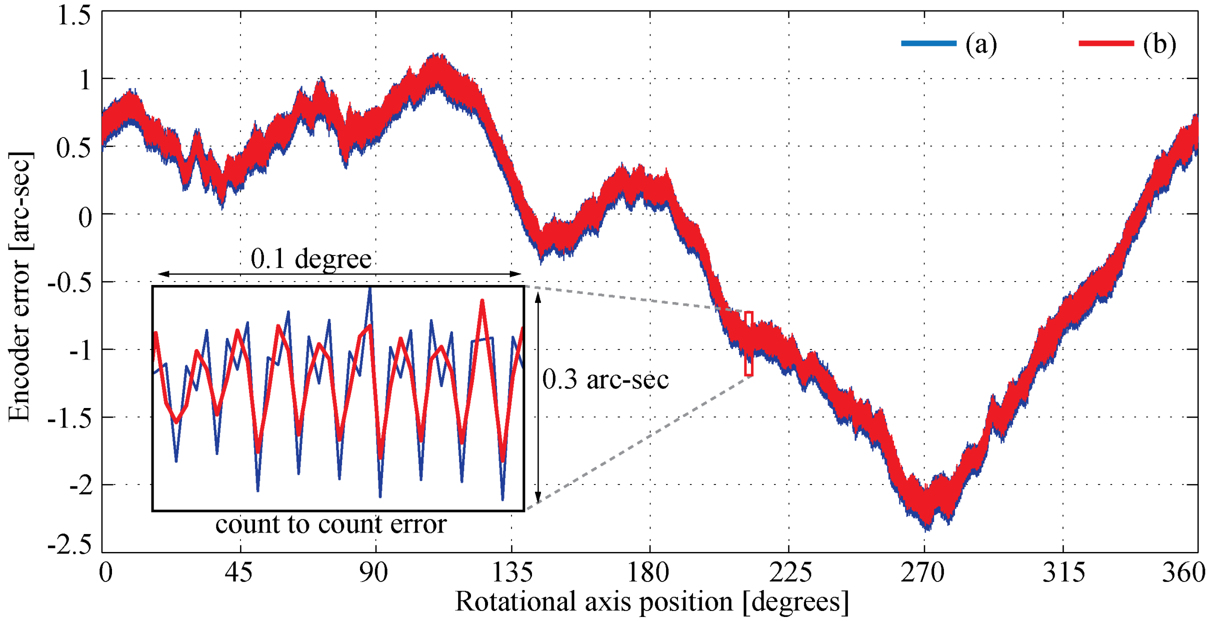

Figure 5.39: Comparison of error map (a) with and (b) without high frequency error caused by misalignment of encoder signal phase A and phase B.

Experimental signal unbalance

The zero-crossing locations of the encoder signal are used to determine spatial events. Signal unbalance shifts the encoder signal away from its' zero value and can be caused by the characteristic operation of the encoder, imperfect scanning unit installation and a voltage offset introduced in the electronics.

To determine phase signal unbalance the count deviations for signal A and B individually are determined, representing the spatial errors of a single encoder phase. The deviations can be found by calibrating the time measurements from only one of the encoder signal phases, A or B. Figure 5.40 and Figure 5.41 show the count deviations for encoder signal A and signal B respectively.

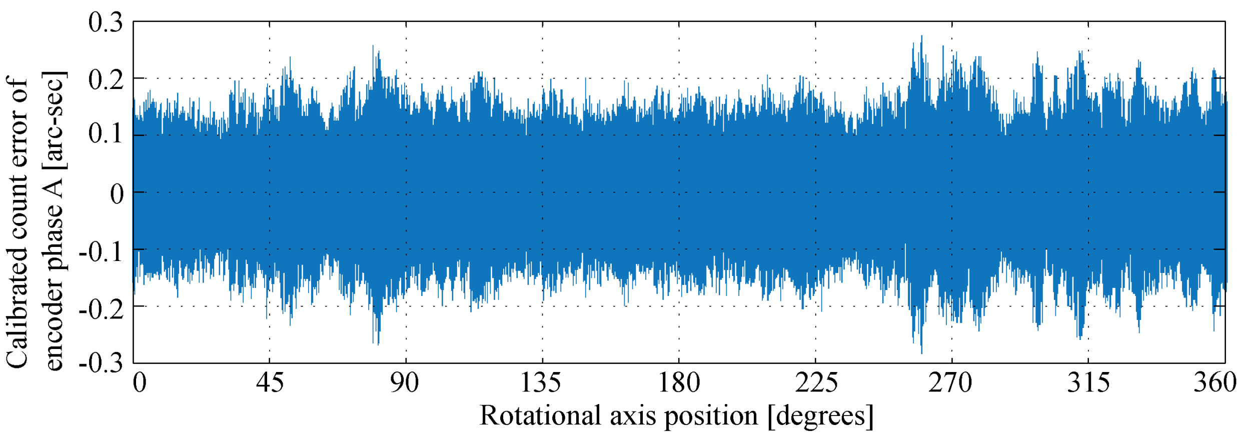

Figure 5.40: Count deviations of encoder signal phase A. Rising to falling edge of encoder signal A.

A positive voltage phase signal unbalance can be found if the odd count deviations of the signal are consistently smaller than the even count deviations. Conversely, a negative voltage phase signal unbalance

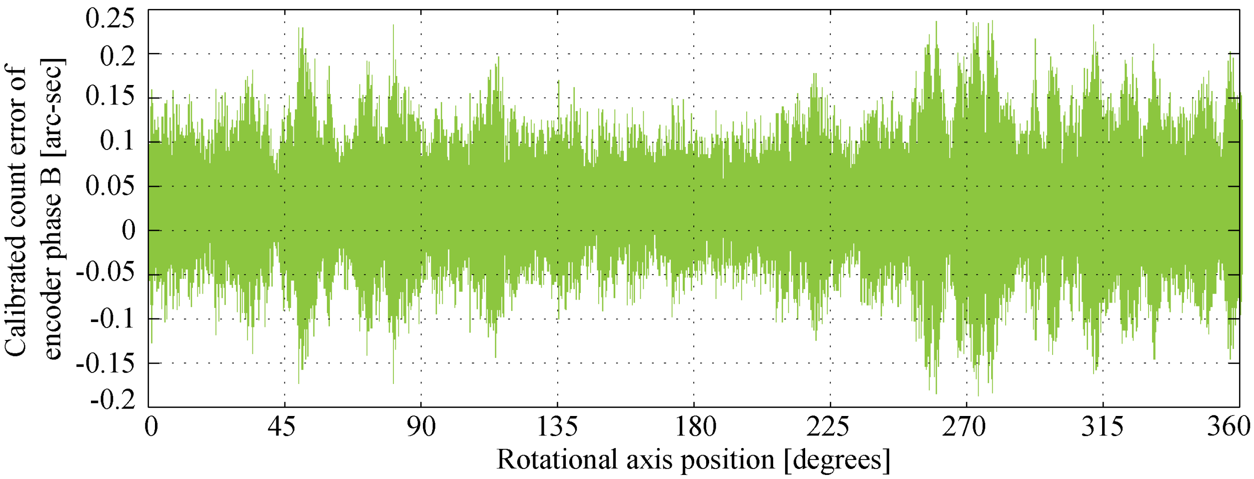

Figure 5.41: Count deviations of encoder signal phase B. Rising to falling edge of encoder signal B.

can be found if the odd count deviations of the signal are consistently larger than the even count deviations (Figure 4.10). Figure 5.42 and Figure 5.43 shows the count deviations for signal A and B, respectively, with the odd and even count deviations highlighted.

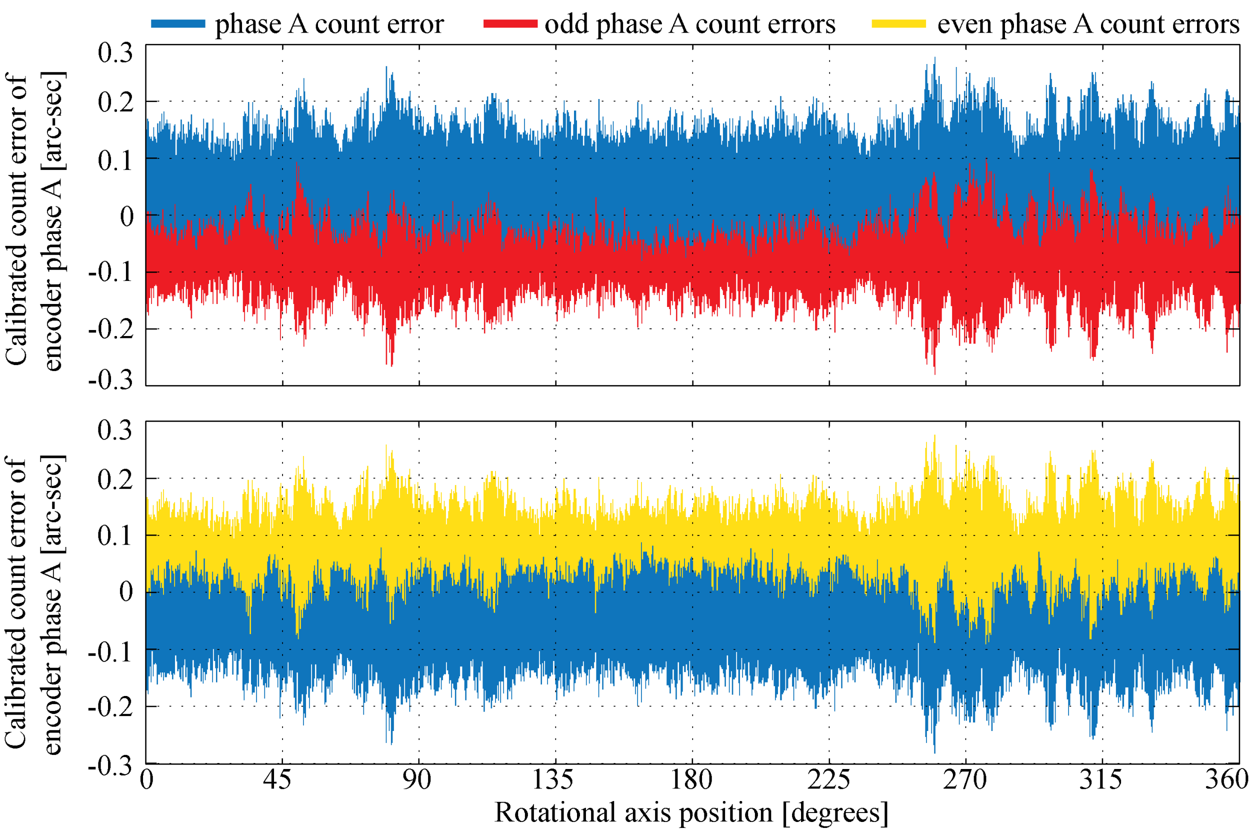

Figure 5.42: between odd and even count deviations of encoder signal A, showing phase unbalance.

Encoder signal A shows a signal unbalance of 0.19 arc-sec which is found as approximately 24 mV offset voltage (Equation 2.56). Encoder signal B shows a signal unbalance of 0.09 arc-sec which is found

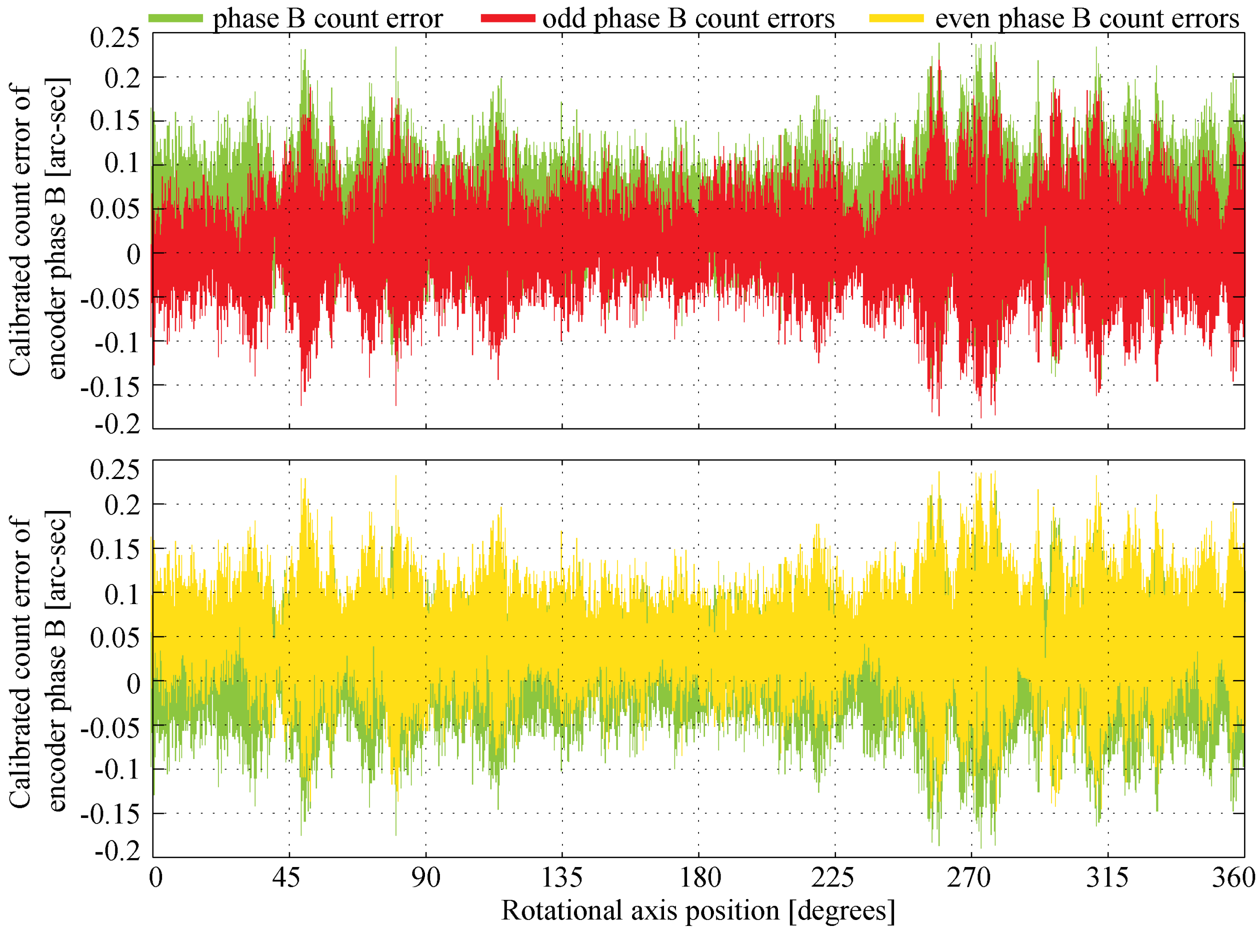

Figure 5.43: between odd and even count deviations of encoder signal B, showing phase unbalance.

as approximately 11 mV offset voltage. Signal unbalance is responsible for the harmonic error components around 32,768 cpr.

Both phase misalignment and signal unbalance can be removed from the calibration result by again reconstructing the error map from the odd and even count errors of signal phase A without mean values and from signal phase B without mean values. As shown in Figure 5.44 the high frequency error band is significantly reduced without phase misalignment and signal unbalance errors.

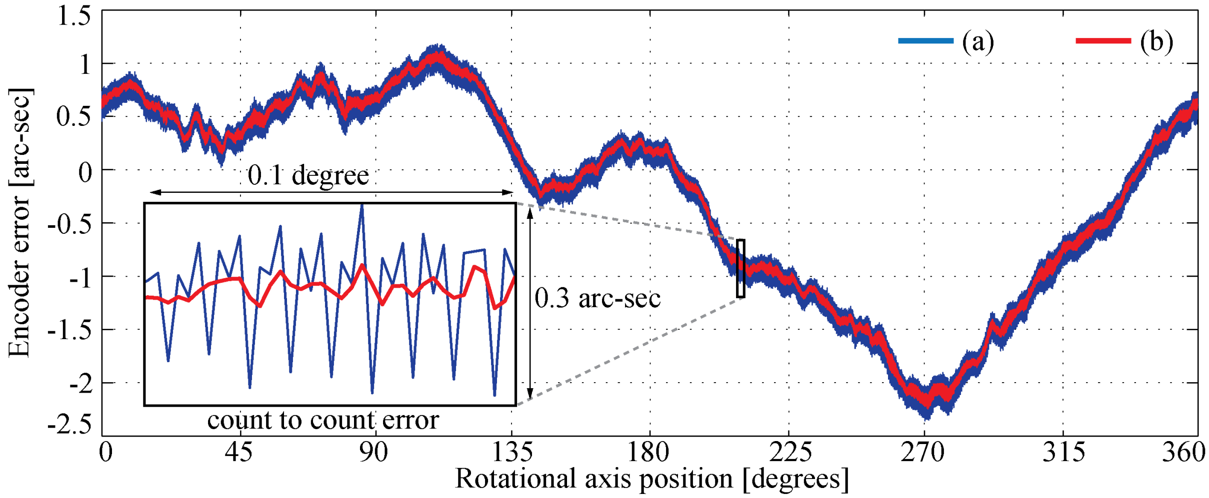

Figure 5.44: Comparison of error map (a) with and (b) without high frequency error caused by misalignment of encoder signal phase A and phase B and signal unbalance.

5.4.2 Experimental Photocell Spatial Offset

Due to a spatial delay in the photocell detectors used for phase A and B individually, a high frequency error component can be created.

Cross-correlation of the count deviations for phase A and phase B shows the $200\mu m$ (10 line) delay due to the physical layout of the photocell array, Section 4.2. By shifting the count deviations of signal phase B the similarity of the error between phase A and B can be seen. Figure 5.45 shows the difference of count deviations for signal phase A and phase B with and without the delay. Due to non-symmetries of the detectors, there is a difference in calibration results from each phase on the order of 0.01 arc-sec. The contribution of photocell delay to the high frequency error is negligible and no visible improvement is seen in the error map without the delay component.

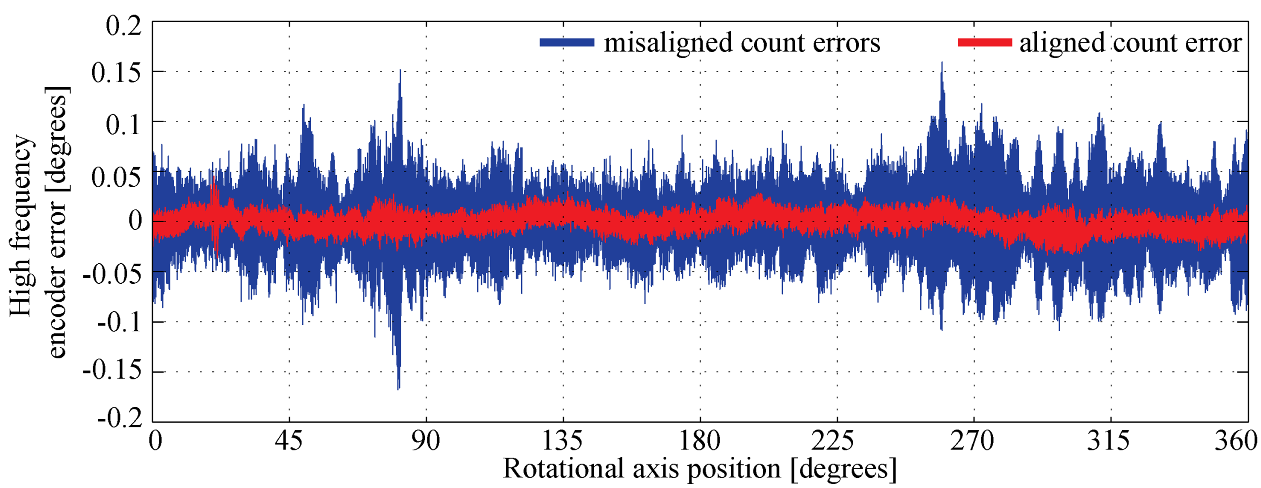

Figure 5.45: Difference of count deviations between encoder signal phase A and phase B, indicating photocell detector offset and detector non-symmetries.

5.5 Calibration Performance

Proving that a calibration method can improve measurement accuracy down to a few thousandths of an arc-sec is very challenging. The inaccuracy and repeatability of the calibration result must be observed. In addition the uncertainty of the experimental setup must be on the same order to ensure calibration results can be used without repetitive re-calibration.

Several techniques for determining inaccuracy have been proposed. Through simulation results, rms set repeatability and spindle error motion estimation were related to error map inaccuracy. These performance metrics can be used to estimate the experimental inaccuracy based on Equation 3.2 and Equation 3.3. The already established EDA calibration technique has the advantage of being insensitive to rotary vibration. A comparison of TDR and EDA calibration results can be used to determine the accuracy of rotary vibration removal and other calibration uncertainties.

5.5.1 Inaccuracy from RMS Set Repeatability

Numerous improvements in the experimental setup were made to achieve the most repeatable calibration results. Figure 5.46 shows the steady improvement in calibration set repeatability from developments made in the experimental setup. The initial rms set repeatability result was obtained without any filtering on the analog signals shown as (a). The following improvements were made to the experimental setup: (b) passive filtering of the analog encoder signals (c) using ferrite cores on the analog voltage supply cables to remove EMI (d) installing the setup on an optical table, providing passive vibration isolation from floor vibrations (e) implementing active filters to further remove common mode noise and combine differential encoder signals and (f) increasing active filter gain, lessening the effect of noise added to the signal after processing.

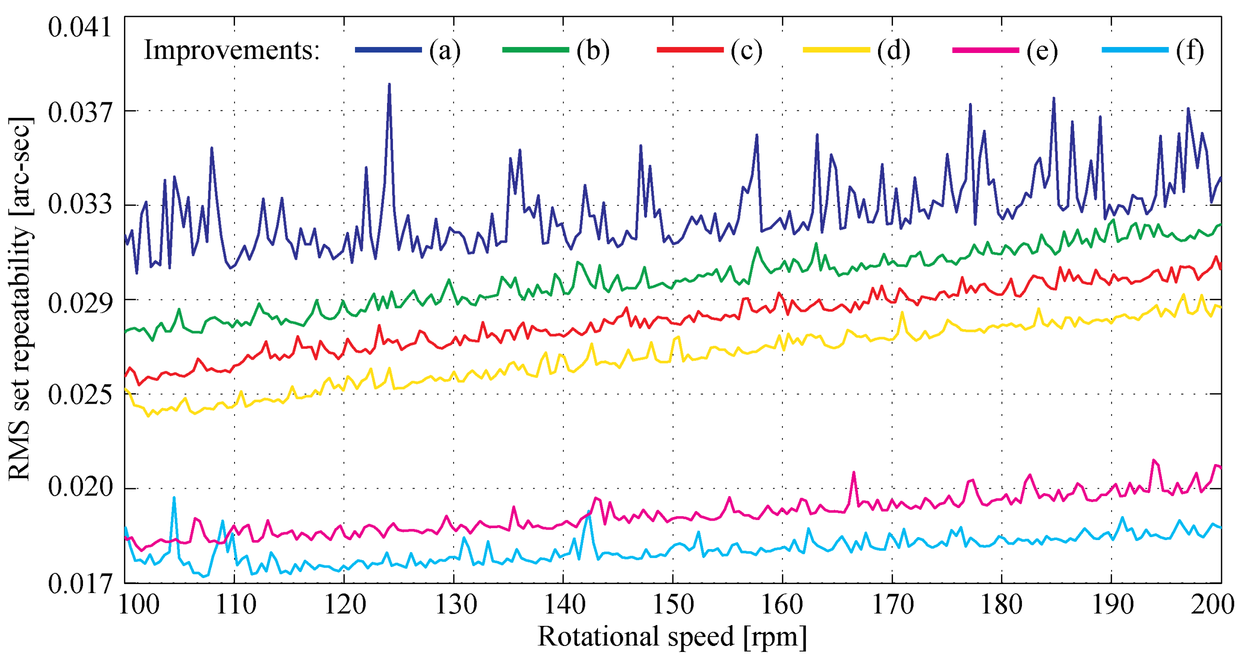

Figure 5.46: Steady improvements in calibration repeatability due to development of the experimental setup. (a) initial results (b) passive signal filtering (c) ferrite cores added on voltage supply cables (d) installed on optical table (e) active signal filtering (f) increased active filter gain.

Figure 5.47 shows the rms set repeatability obtained in the final setup with 1,500 MHz time measurement resolution on the Tsunami platform and aggressive 300kHz bandwidth Chebyshev active filters. The

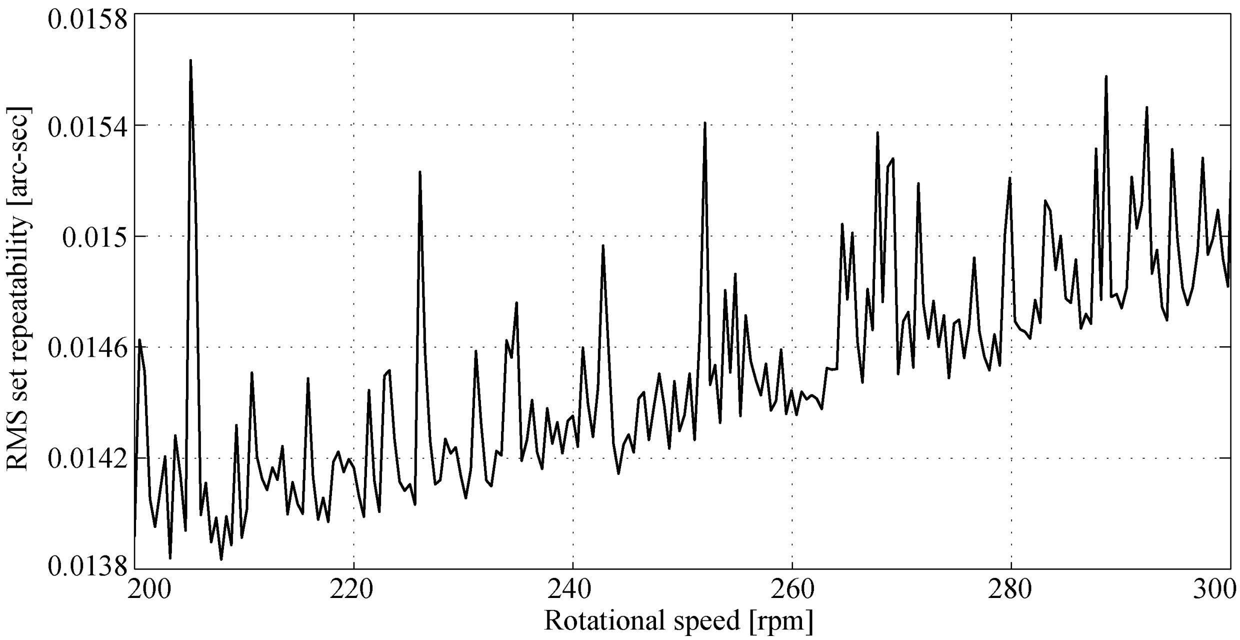

Figure 5.47: RMS set repeatability in the final experimental setup.

final result shows a rms set repeatability of 14 thousandths of an arc-sec at 200 rpm, which indicates the calibration accuracy is on the order of 10 thousandths of an arc-sec, Equation 3.2. The trend of increasing set repeatability with spindle speed is due to aggressive filtering and not from increased time measurement uncertainty. The time measurement uncertainty only contributes 0.0022 arc-sec at 300 rpm. As the spindle speed approaches the bandwidth of the filters, the signal amplitude is attenuated, increasing marking uncertainty.

To validate the accuracy predicted through set repeatability a comparison of spindle radial error motion measurements (Section 2.2) was made.

5.5.2 Inaccuracy from Error Motion Estimation

Encoder calibration time measurements and capacitance probe displacement measurements were captured simultaneously over a range of speed. The fundamental [-1] component of spindle radial error motion was extracted for both results shown in Figure 5.48. The error motion found through encoder calibration matches the measurement obtained from capacitance probe measurements but with higher uncertainty. Variations in the calibration results are caused by uncertainties in the encoder angle measurements, that are then reflected to harmonics of the error map. The rms inaccuracy of error motion estimation is on the order of 1nm or 0.002 arc-sec for the first harmonic. Based on the simulation result, this can be related to error map inaccuracy Equation 3.3. This predicts a calibration inaccuracy of 6 thousandths of arc-sec for the full calibration harmonic range.

Improvements in the experimental setup were also made to make this result as accurate as possible. Due to fluctuations in ambient temperature and air bearing supply pressure, the spindle error motion changes. A

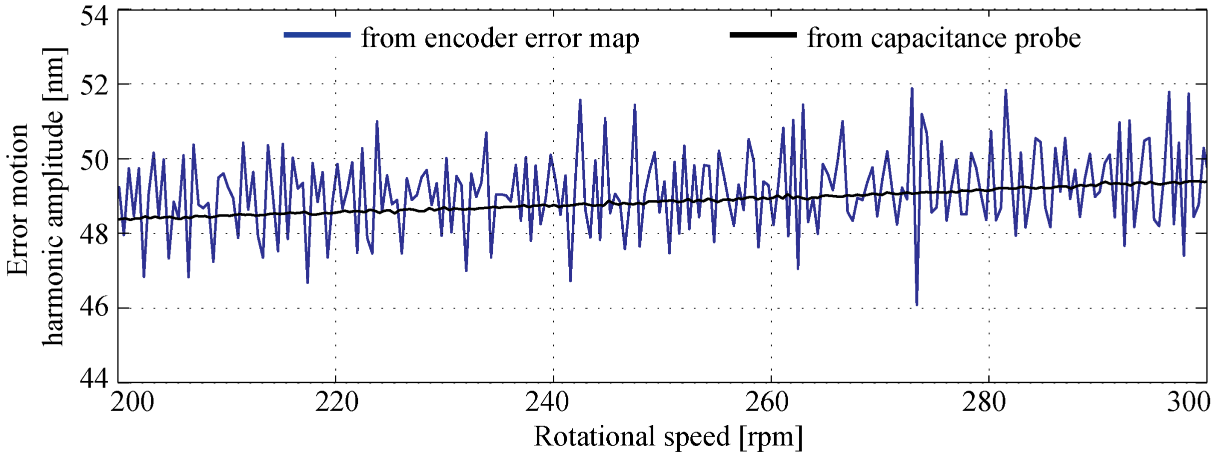

Figure 5.48: Spindle radial error motion measurement results using traditional capacitance probe and novel encoder calibration methods.

simultaneous scanning unit measurement is necessary to accurately predict the spindle radial error motion and not capture false error motion fluctuations caused by changing spindle dynamics. The importance of simultaneous scanning unit measurements can be seen from Figure 5.49.

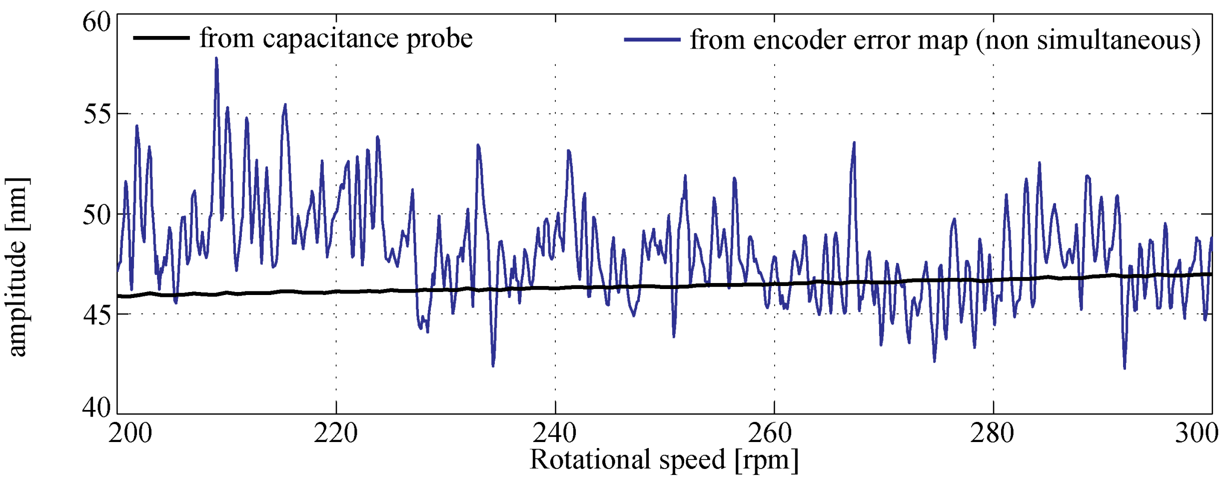

Figure 5.49: Spindle radial error motion measurement through encoder calibration without simultaneous encoder measurements.

5.5.3 Calibration Comparison

The EDA method, presented in Section 2.4, has already been established as a very repeatable encoder calibration method. This method is insensitive to rotary vibration but cannot calibrate the entire error map harmonics. A comparison of experimental calibration results using the TDR and EDA calibration methods gives insight into the uncertainties of both methods.

Calibration with the EDA and TDR methods was performed using the same experimental time measurements from the four head setup. Figure 5.50 shows a comparison of results from both methods, calibrated encoder error maps at 200 rpm with only the first 500 cpr harmonics included.

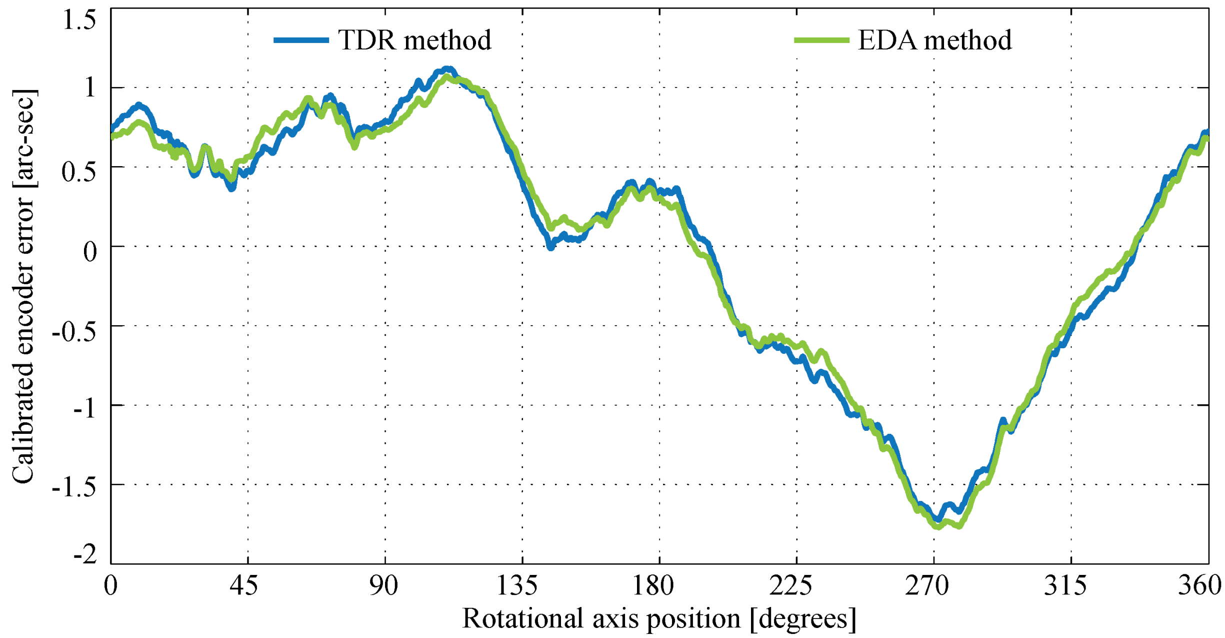

Figure 5.50: TDR and EDA calibration results, from identical time measurements from scanning unit H1 at spindle speed of 200 rpm. Showing the first 500 cpr harmonics.

The difference between the two calibration results is due to the missing $4k$ harmonics that cannot be determined by the EDA calibration method. Figure 5.51 shows the difference of the two calibration results, dominated by fourth order multiple harmonics.

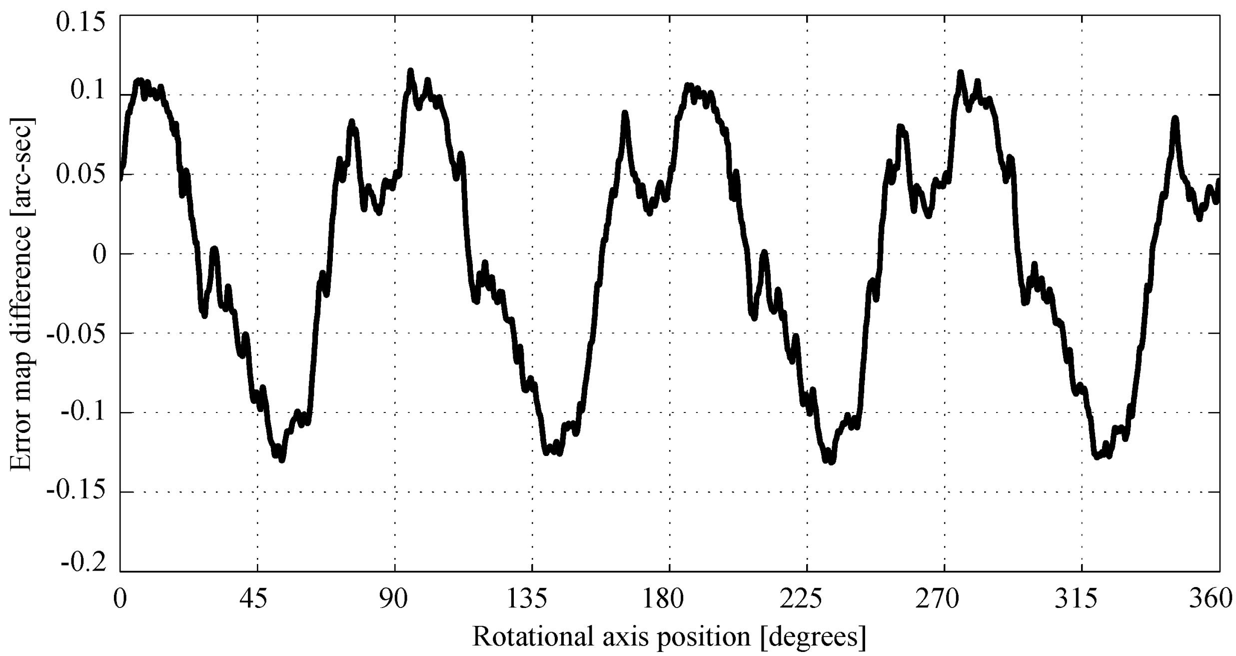

Figure 5.51: TDR and EDA calibration result difference, from identical time measurements from scanning unit H1 at spindle speed of 200 rpm. Showing the first 500 cpr harmonics.

High frequency error map harmonics are a large component of the calibration result. Most high frequency information is missed by the EDA method due to its' limitation of missing $4k$ harmonics. Figure 5.52 shows a comparison of error map results from both methods, calibrated at 200 rpm. The difference between

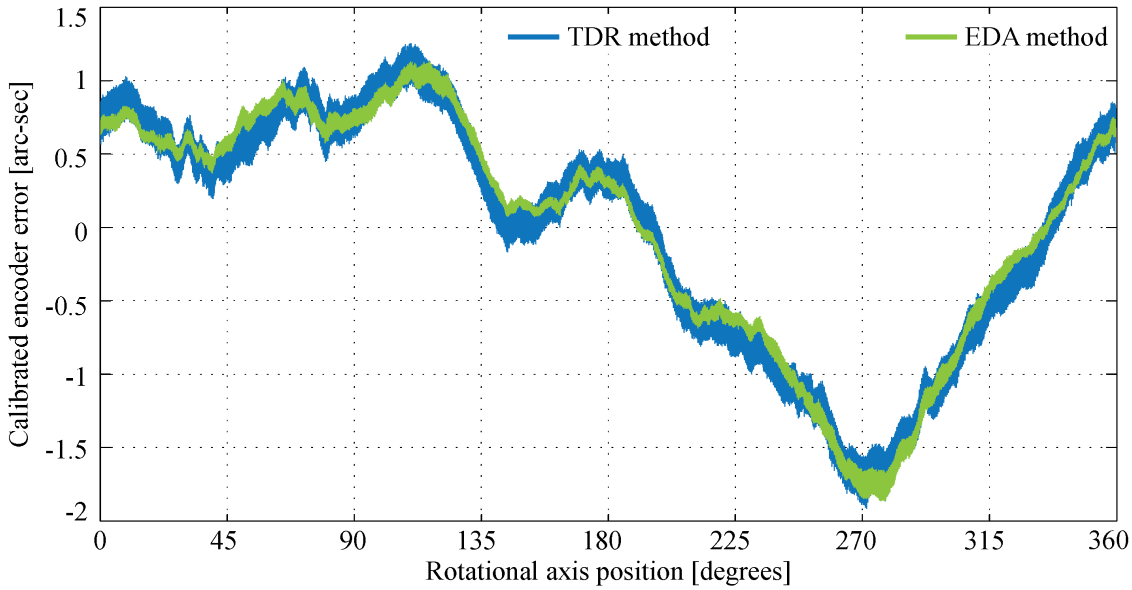

Figure 5.52: TDR and EDA calibration results, from identical time measurements from scanning unit H1 at spindle speed of 200 rpm.

the two calibration results shows dominant high frequency components at 32,768 cpr and 65,536 cpr due to phase misalignment and signal unbalance. This shows the advantage of the TDR method, where it can

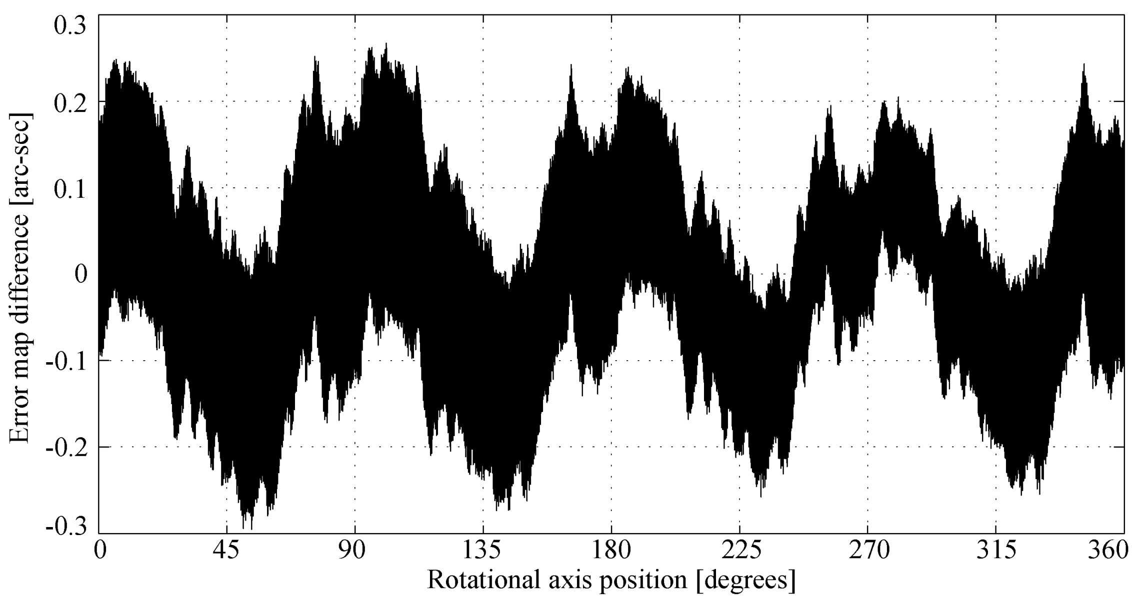

Figure 5.53: TDR and EDA calibration result difference, from identical time measurements from scanning unit H1 at spindle speed of 200 rpm.

capture all error map harmonics even the $4k$ harmonics missed by calibration with the EDA method. There is a fundamental limitation of the EDA method because it cannot capture the full error map harmonics.

Performing a calibration on a manufacturing axis with the EDA method would result in inaccuracies on the order of 0.3 arc-sec.

For error map harmonics not a multiple of four, the agreement between EDA and TDR methods is within 0.005 arc-sec for calibration at 200rpm. Figure 5.54 shows a comparison of the amplitudes of each harmonic of the error map for low frequency, and shown in Figure 5.55 for higher frequencies. Table 5.2

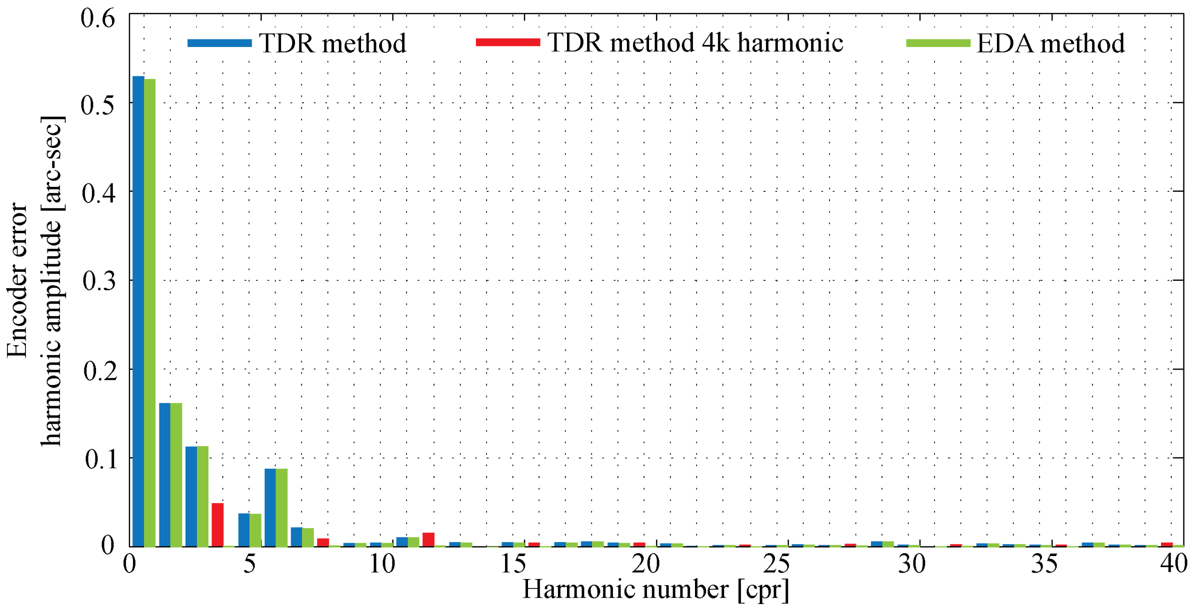

Figure 5.54: Low frequency error map harmonic amplitudes for TDR and EDA calibration methods.

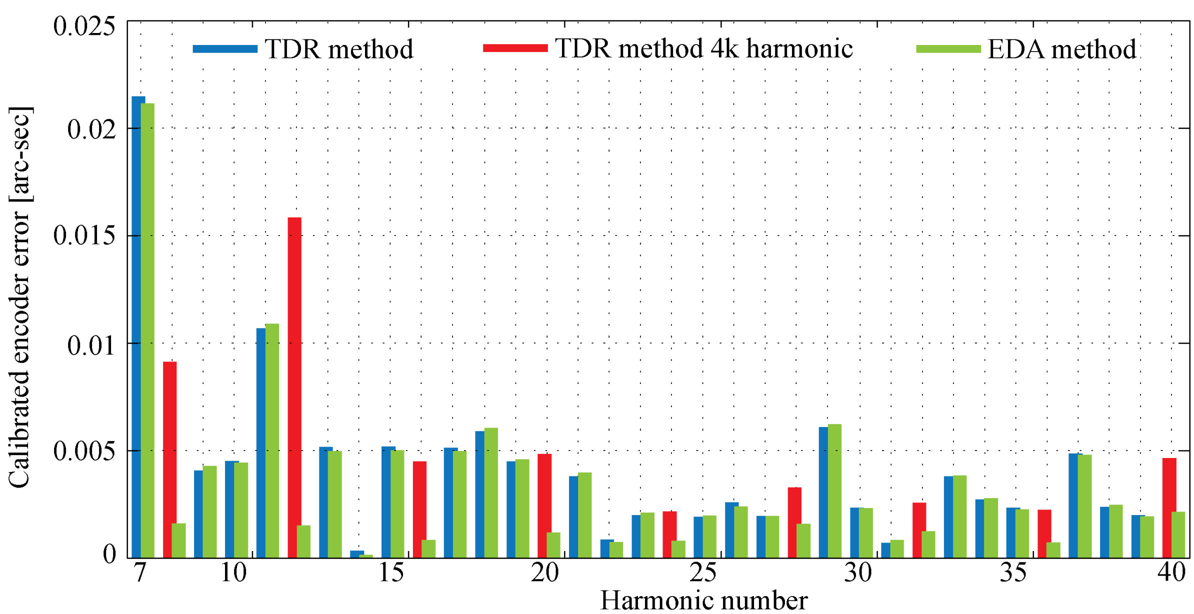

Figure 5.55: High frequency error map harmonic amplitudes for TDR and EDA calibration methods.

shows the quantitative comparison of harmonic amplitudes for encoder error maps obtained from TDR and EDA calibration methods.

Table 5.2: Error map harmonic amplitudes for TDR and EDA calibration methods.

Harmonic no.	*1*	*2*	*3*	*4*	*5*	*6*	*7*	*8*	*9*
TDR	*0.5251*	*0.1619*	*0.1141*	*0.0487*	*0.0370*	*0.0877*	*0.0208*	*0.0093*	*0.0045*
EDA	*0.5268*	*0.1619*	*0.1134*	*0.0010*	*0.0371*	*0.0878*	*0.0211*	*0.0016*	*0.0043*

Harmonic no.	*10*	*11*	*12*	*13*	*14*	*15*	*16*	*17*	*18*
TDR	*0.0044*	*0.0111*	*0.0156*	*0.0048*	*0.0001*	*0.0048*	*0.0043*	*0.0048*	*0.0060*
EDA	*0.0044*	*0.0109*	*0.0015*	*0.0050*	*0.0002*	*0.0050*	*0.0008*	*0.0050*	*0.0059*

The main advantage of the EDA method is seen in a comparison of the error map harmonics over the range of speed. Due to the harmonic cancellation and averaging between four scanning units, the calibration results for the EDA are very consistent. In comparison, the TDR method relies on only the results from a single encoder and is much more susceptible to measurement uncertainties. Figure 5.56 shows the amplitude and phase of the first error map harmonic over 300 rpm down to 200 rpm. The consistency of the EDA method is seen, where the TDR method fluctuates with ± 0.02 arc-sec. This fluctuation is caused by high frequency time measurement uncertainties that are spread over the entire harmonic spectrum, even to very low frequency, during the error map reconstruction.

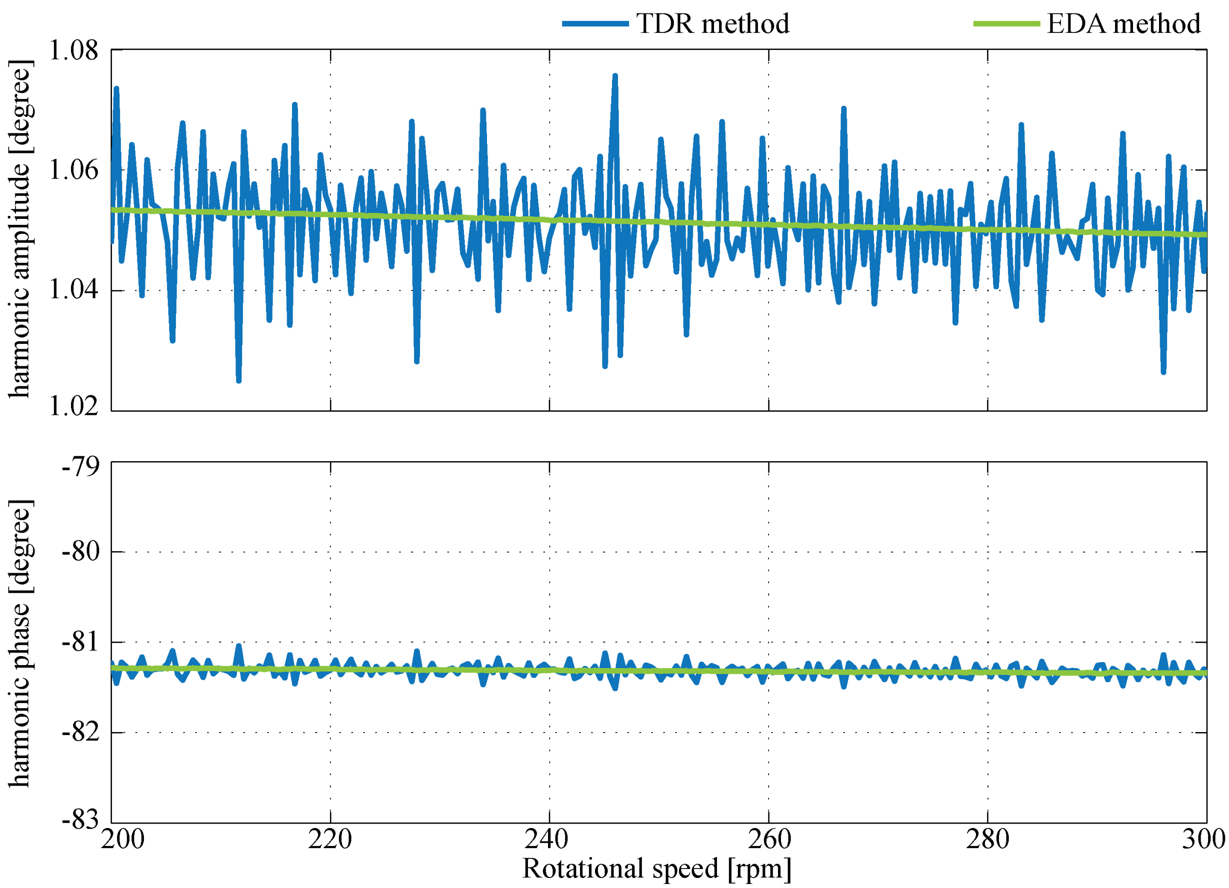

Figure 5.56: First encoder error harmonic for scanning unit H1 obtained from TDR and EDA calibration methods.

The mean trend of the harmonics is followed by both methods. This suggests rotary vibration has been successfully eliminated in TDR calibration. Error map averaging of the TDR calibration results would result in improved repeatability and accuracy for the TDR method.

This result is similarly seen for scanning units H2, H3 and H4 in Figure 5.57, Figure 5.58 and Figure 5.59 respectively. Alternatively for scanning unit H2, the amplitude spectrum is much more consistent than the result obtained from scanning unit H1. Instead, the uncertainty is seen in much larger fluctuations of the phase spectrum of $\pm 1°$.

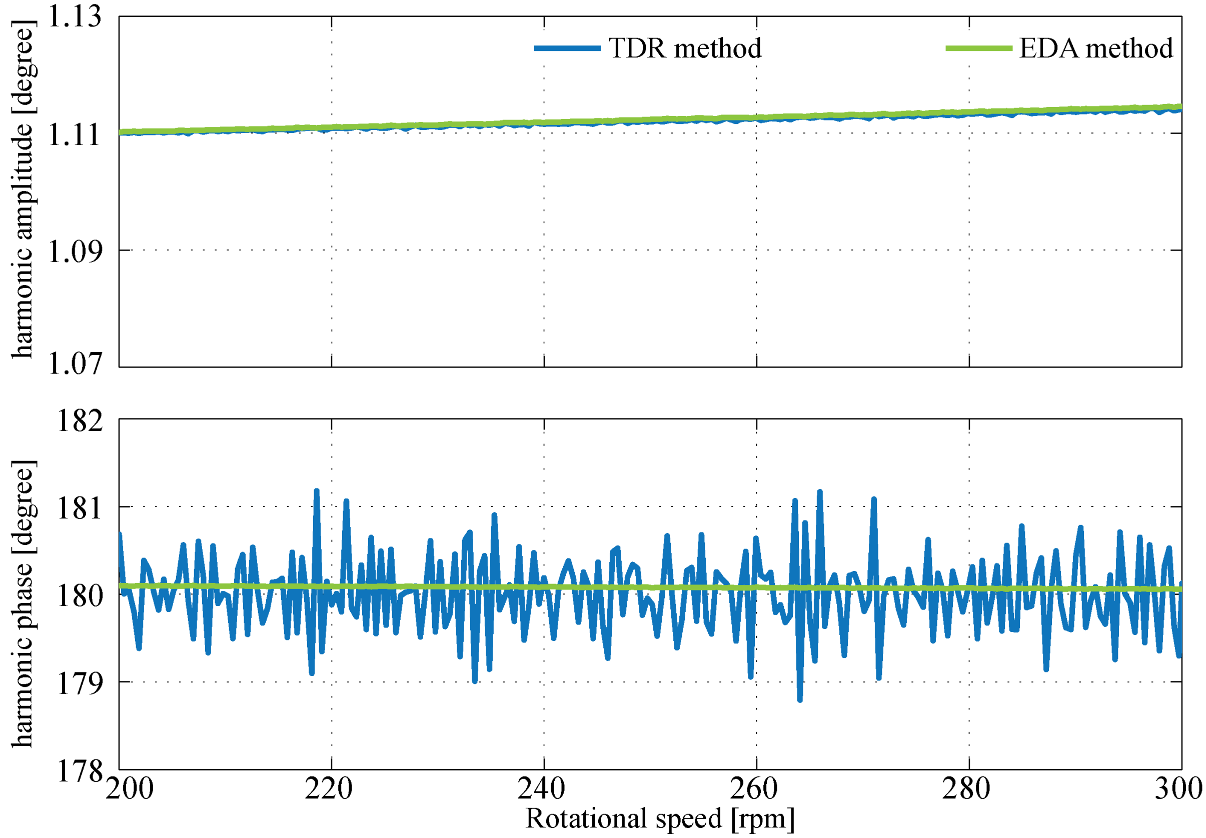

Figure 5.57: First encoder error harmonic for scanning unit H2 obtained from TDR and EDA calibration methods.

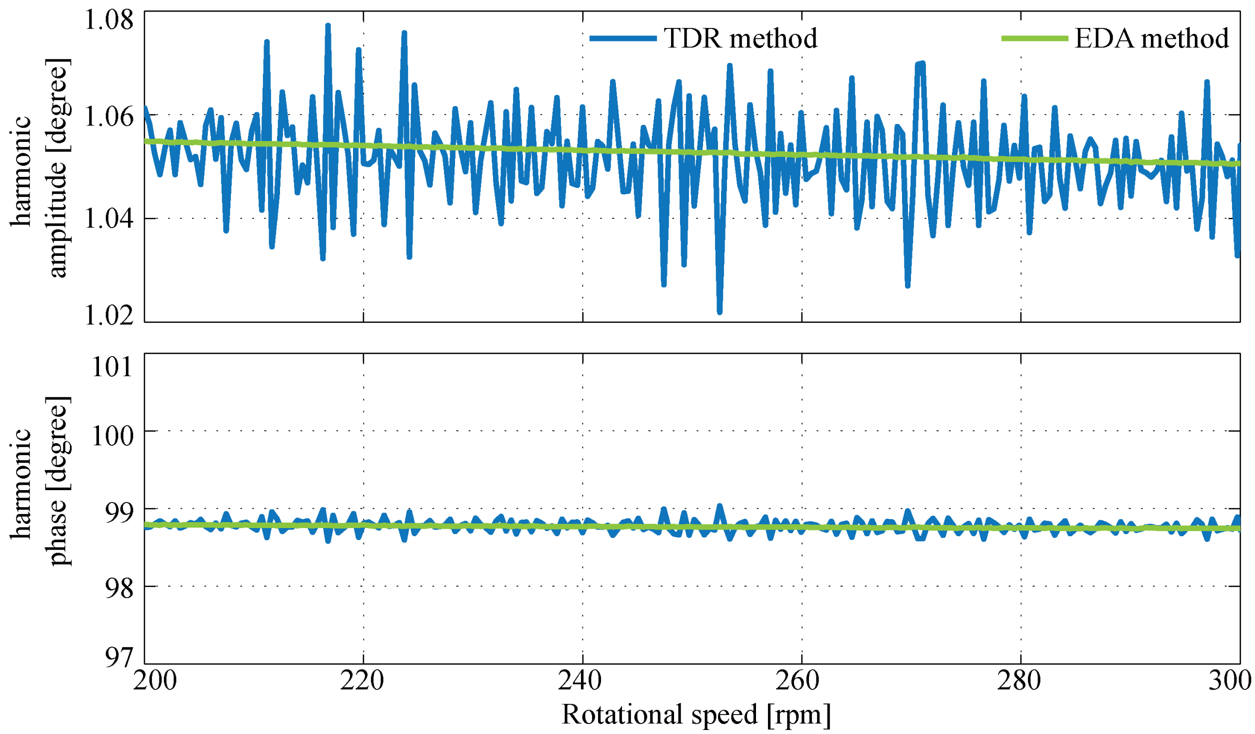

Figure 5.58: First encoder error harmonic for scanning unit H3 obtained from TDR and EDA calibration methods.

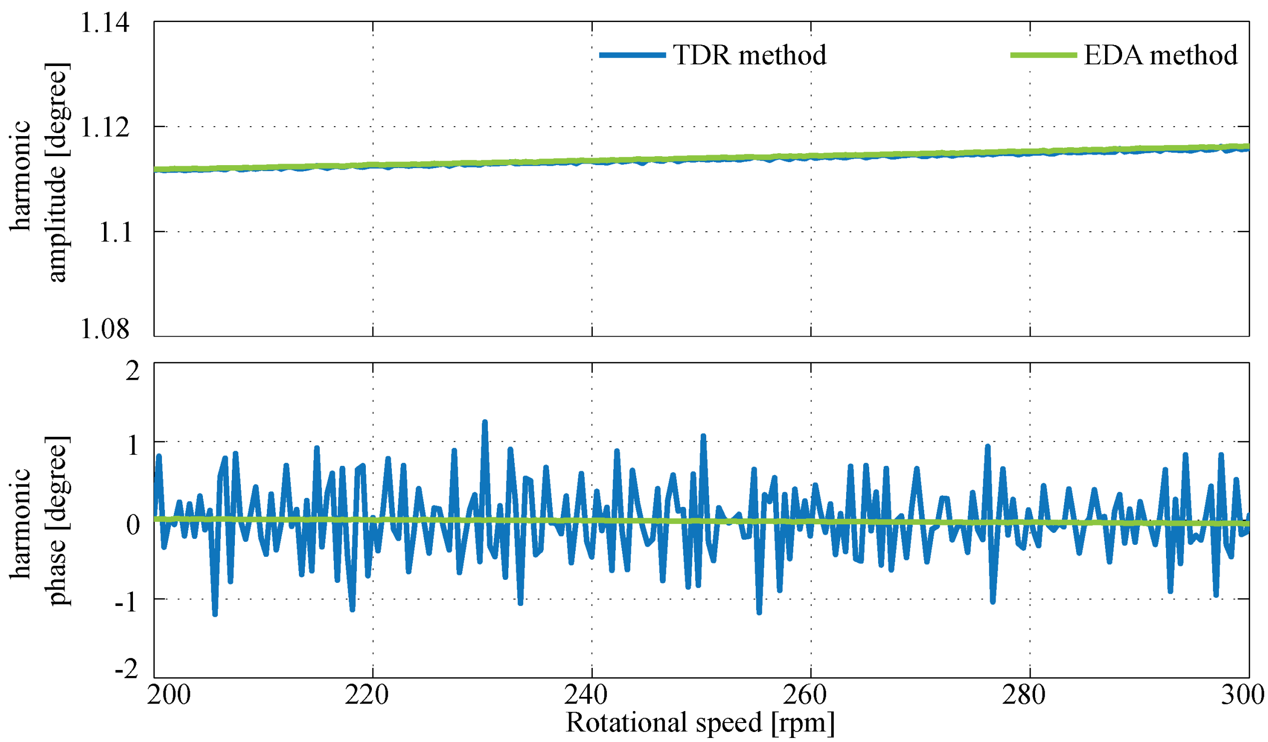

Figure 5.59: First encoder error harmonic for scanning unit H4 obtained from TDR and EDA calibration methods.

5.5.4 Experimental Setup Uncertainty

To improve angle measurements with the calibrated encoder error the experimental setup must be in a stable condition, where the encoder error does not change significantly from the past calibrated result. This will minimize tedious recalibration of the encoder error. The current experimental facility is located on the second floor and shares an air compressor supply with many pieces equipment. Consequently the facility is far from precise and there is a lot that can be improved to achieve better experimental setup uncertainties.

The uncertainty of the experimental setup due to environmental variations is evaluated by comparing error maps from many experimental tests at the same calibration speed. Variance is used as a metric to determine experiment uncertainty. The variance of a calibrated error map is found as the rms difference of each error maps from multiple experiments at 200rpm compared to a mean.

$$\sigma = \sqrt{\frac{1}{10}\sum_{i=1}^{10}\frac{1}{N}\sum_{k=1}^{N}\left[q_i(k) - q_0(k)\right]} \tag{5.1}$$

where $q_i(k)$ is the error map from the i-th calibration experiment and $q_0(k)$ is the average error map of all the experiments found as

$$q_0(k) = \frac{1}{10}\sum_{i=1}^{10} q_i(k) \tag{5.2}$$

The calibration uncertainty, 2σ, gives us a measurement of how much the calibration results change between experiments.

Encoder signal time measurements were captured from 300 rpm down to 200 rpm and then repeated 10 times for each calibration experiment. Each calibration measurement takes approximately 5 minutes to perform. Within the 50 minute experiment window, the spindle dynamics change significantly due to uncontrolled pressure and ambient temperature fluctuations. Figure 5.60 shows the calibrated error map for each calibration experiment.

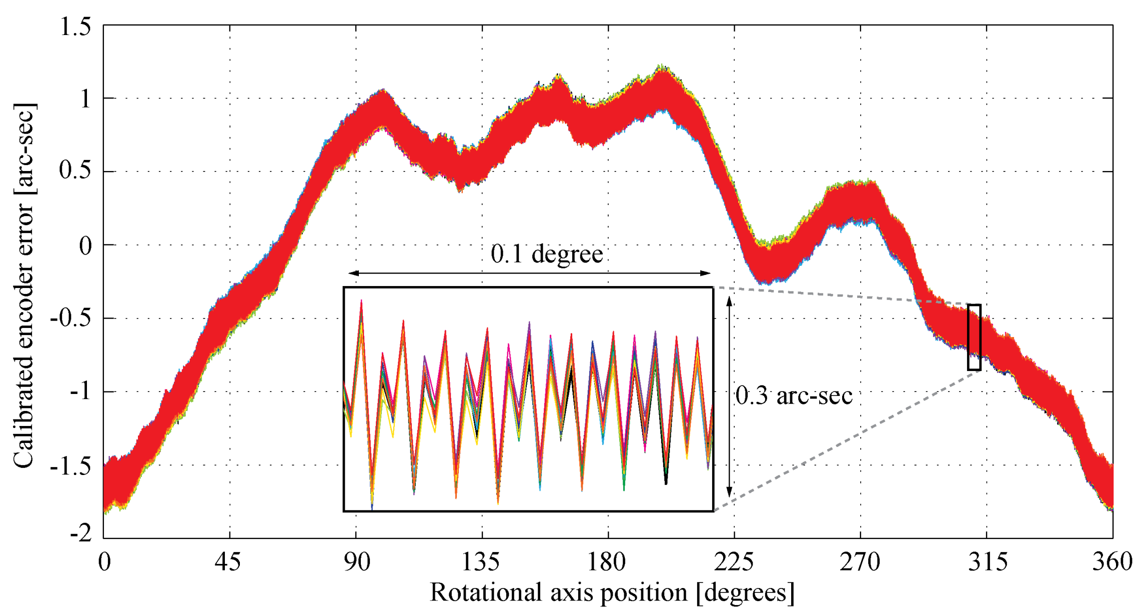

Figure 5.60: Calibrated error maps from uncertainty experiment.

The uncertainties in high frequency error map harmonic estimation are on the same order as the uncertainties in the low frequency harmonics. Figure 5.61 shows the error maps with only the 500cpr harmonics included, to highlight error map variation of low frequency harmonics.

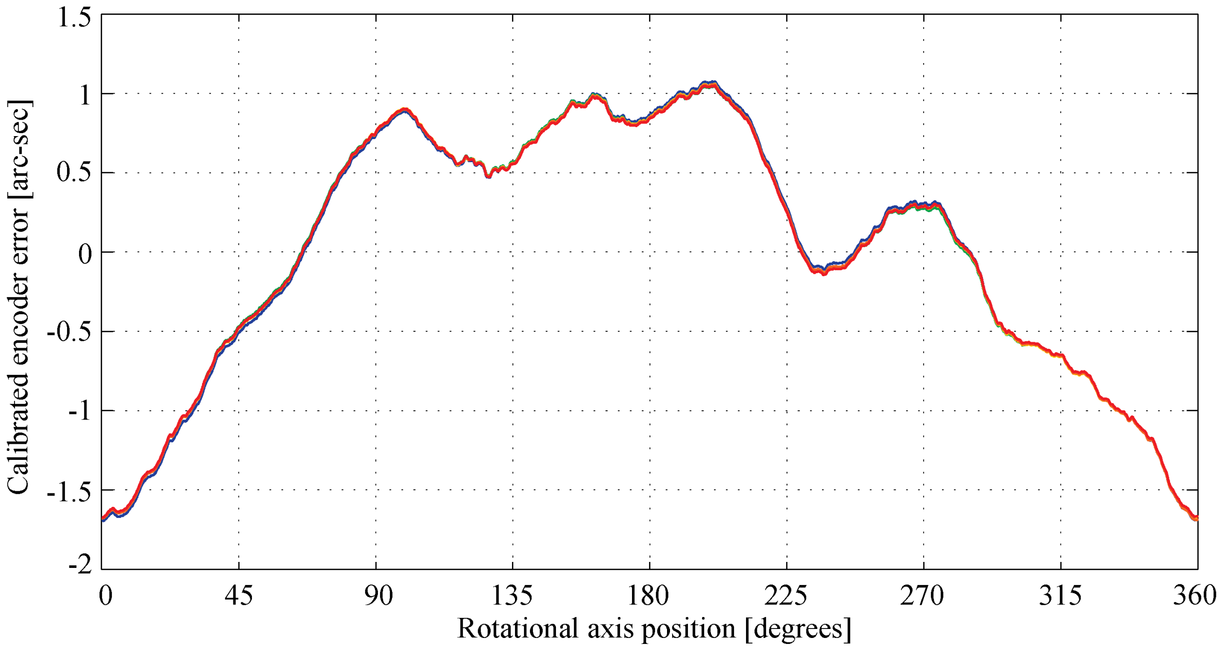

Figure 5.61: Calibrated error maps, showing only the first 500 cpr harmonics, from uncertainty experiment.

Figure 5.62 and Figure 5.63 show the error map differences between each calibrated error map and the mean error map, $q_i(k) - q_0(k)$. High frequency harmonic uncertainty, shown in Figure 5.62, are mainly caused by encoder signal noise and timing resolution. Low frequency harmonic uncertainty, shown in Figure 5.63, is believed to be caused by ambient temperature and pressure fluctuations uncontrolled in the environment.

The experiment uncertainty was found to be 0.03 arc-sec. If only the first 500cpr harmonics are considered the uncertainty drops to 0.02 arc-sec.

These uncertainties are believed to be caused by ambient temperature and pressure fluctuations uncontrolled in the environment. Ideally the experimental setup would be installed in a professional metrology facility. A clean room environment would guard from dust or foreign particles affecting the imaging of lines on the circular scale. Ambient temperature control and a dedicated air compressor would prevent large variations in the spindle dynamics. Ground floor installation would prevent building harmonics or floor vibrations from transmitting to the setup and affecting results.

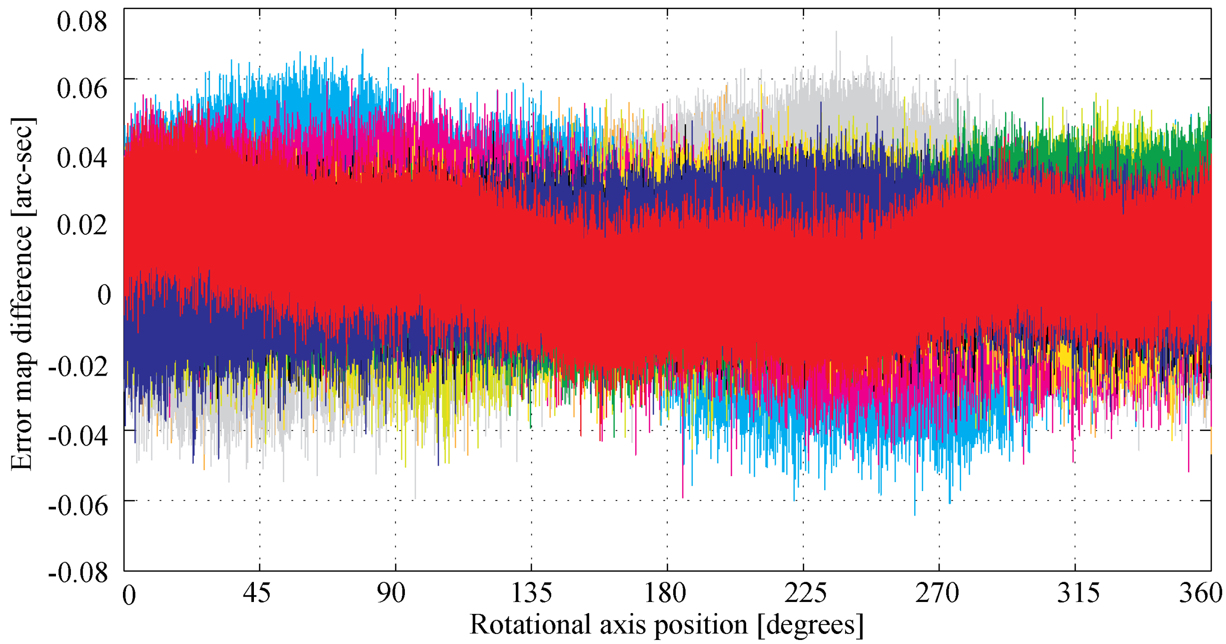

Figure 5.62: Sequential experiment error map differences from mean.

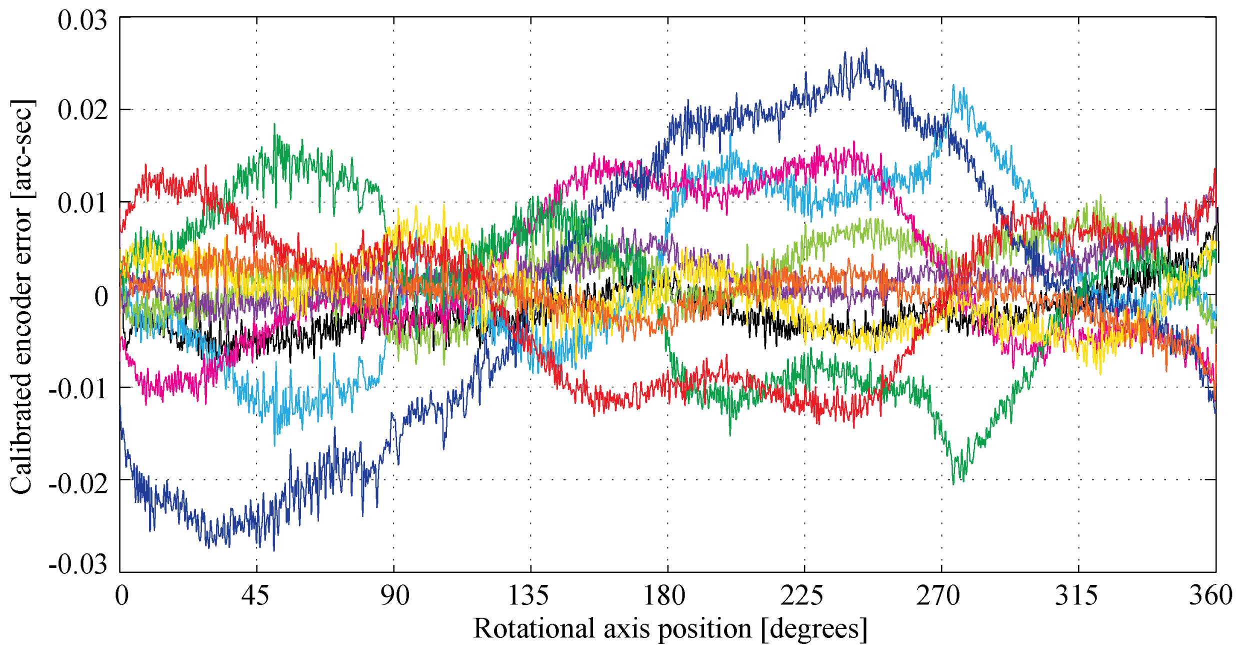

Figure 5.63: Sequential experiment error map differences from mean, with only first 500cpr harmonics.

5.6 Analog Encoder Signal Averaging

The repeatability of angle measurements from the rotary encoder is believed to be the limitation of the calibration results. One method to improve the repeatability of angle measurements without investing in a set of more expensive rotary encoders is to average the angle measurements from each scanning head.

Many precision rotary measurement axes, average the analog signals of multiple scanning units to cancel measurement error harmonics, rather than perform error calibration. The average of multiple scanning unit measurements, when evenly spaced around the circular scale, has a measurement error that is the sum of Fourier coefficients of the original measurement error only integer multiples of the number of scanning units. For the four head setup, the averaged signal will only show encoder measurement error harmonics that are multiple of four. The analog signals of each scanning unit must be precisely aligned to ensure proper error harmonic cancellation and signal summation. The same technique used to align the scanning units in the four setup ensures these conditions Section 4.5.

This averaging method provides the same benefits as calibration and compensation using the EDA self-calibratable encoder method. Only the error harmonics multiple of the number of scanning units remain. Many precision incremental encoders make use of this idea using a two scanning unit setup, that removes the dominant first order error harmonic, and subsequently all other harmonics not multiple of 2. The TDR calibration method can benefit from signal averaging due to the improvement in measurement repeatability.

The analog encoder signal averaging if performed on the daughter board electronics, with a summing amplifier, before the signal is digitized and sent to the mother board for time measurement, Figure 5.64.

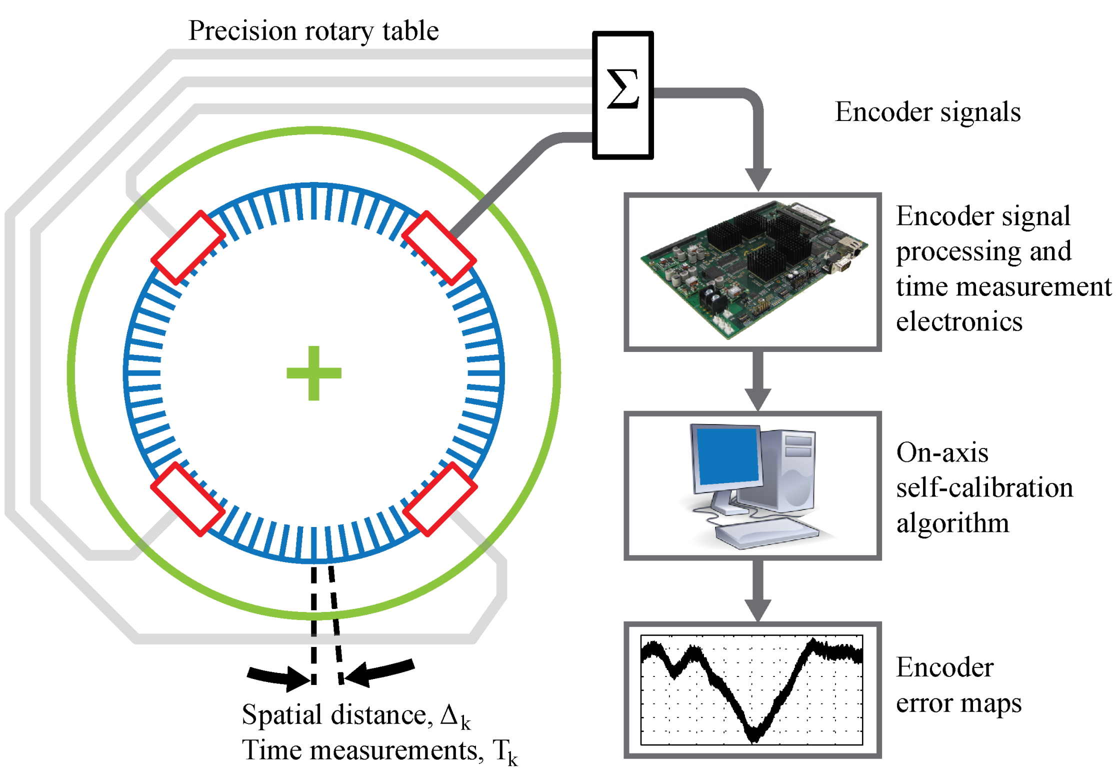

Figure 5.64: Averaging multiple scanning unit signals to improve calibration repeatability.

Calibration is performed for encoder signal averaging of two scanning units diametrically opposing each other shown in Figure 5.65. Most obvious in this calibration result is the lack of the dominant first order harmonic. The angle measurement error when averaging two scanning units is improved from 2.5 arc-sec down to 1.5 arc-sec. Further improvement down to 0.6 arc-sec is obtained with averaging four scanning units shown in Figure 5.66.

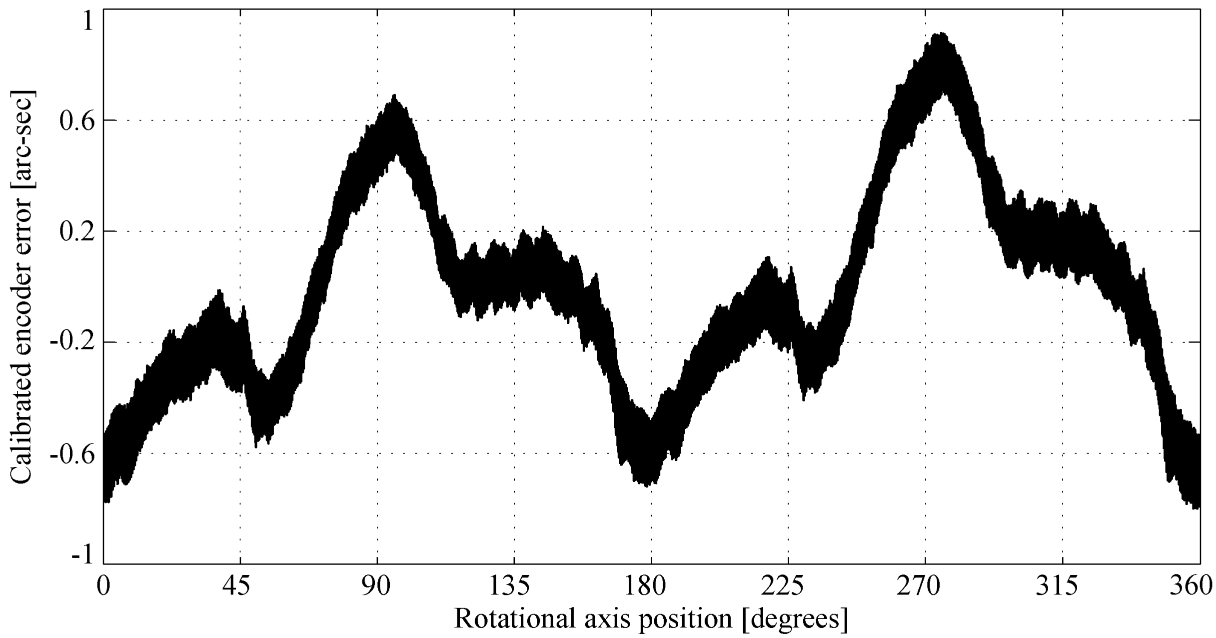

Figure 5.65: Experimentally calibrated error map from the analog signal average of two scanning unit signals.

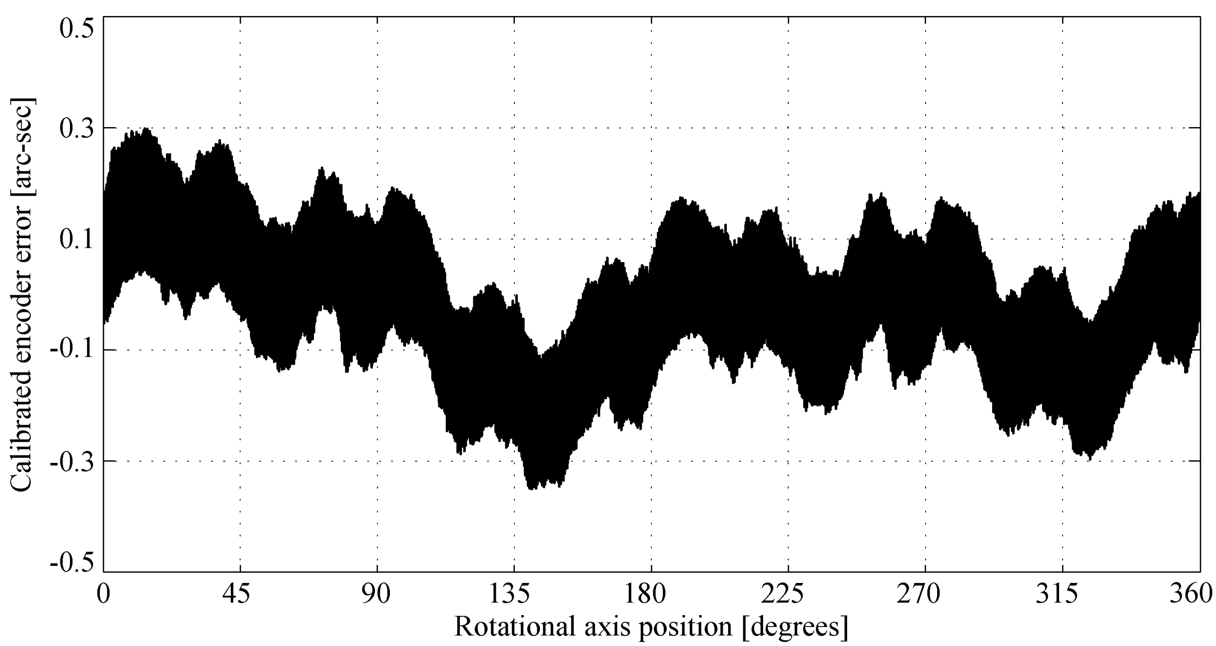

Figure 5.66: Experimentally calibrated error map from the analog signal average of four scanning unit signals.

Along with incremental improvements in measurement accuracy, averaging also results in improved repeatability of measurements. The repeatability of the measurements can be compared through the calibration performance metric, set repeatability. Figure 5.67 shows the rms set repeatability of calibration performed with a single scanning unit and averaging of two and four analog encoder signals. Using the analog signal

Figure 5.67: RMS set repeatability of calibration results with analog encoder signal averaging.

averaging of four scanning units, the set repeatability result is improved down to 5 thousandths of an arc-sec. This improvement in repeatability also shows that the calibration results are limited due to encoder angle measurement limitations rather than from the calibration algorithm itself. Further calibration performance should be investigated with more accurate and repeatable angle encoders.

Although this method results in improved calibration repeatability it has its disadvantages. The averaging of diametrically opposing scanning units, results in cancellation of the spindle radial error motion component. Without a spindle radial error motion component, the calibration accuracy cannot be verified through comparison with traditional capacitance probe error motion measurements Section 2.2. Another disadvantage of this method is that multiple scanning unit measurements cannot be used to isolate the rotary vibration component from the actual measurement error. Instead, the rotary vibration prediction method must be used, which can only predict rotary vibration caused by a torque disturbance and cannot predict constant rotary vibration as was found in experimental results (Section 5.3.1).

5.7 Calibration Installation Sensitivities

Early experimental calibration results on the air bearing spindle showed the sensitivity of encoder measurement error on the physical installation of the incremental encoder.

Initially $100\mu m$ shims were used to raise the height of the circular scale on the spindle rotor. This was required because the relative height between the mounting surface of the circular scale and the mounting surface of the scanning unit was smaller than the tolerance provided by the encoder manufacturer. This would cause the scanning unit to image the circular scale gratings at a lower height, possibly causing encoder signal issues. Shims were placed underneath the circular scale between each of the six bolts that secure the circular scale to the spindle rotor. The installation configuration of shim and bolt locations is shown in

Figure 5.68 As a result of the uneven mating surface, the circular scale was significantly deformed in this

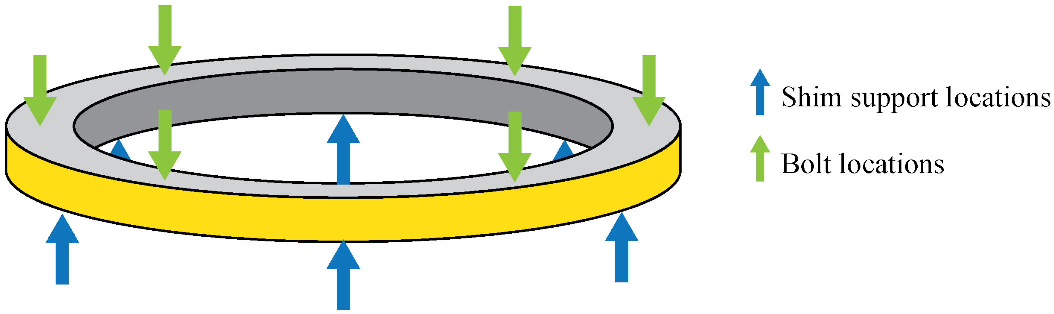

Figure 5.68: Initial installation of the circular scale on the spindle rotor with support shims.

installation, causing a deformation of the gratings on the scale. Figure 5.69 shows the calibrated error map with shims supporting the circular scale. The significant 6 cpr harmonic is due to deformation of the scale from the 6 mounting bolts securing the scale to the rotor. It was alternatively decided to perform calibration

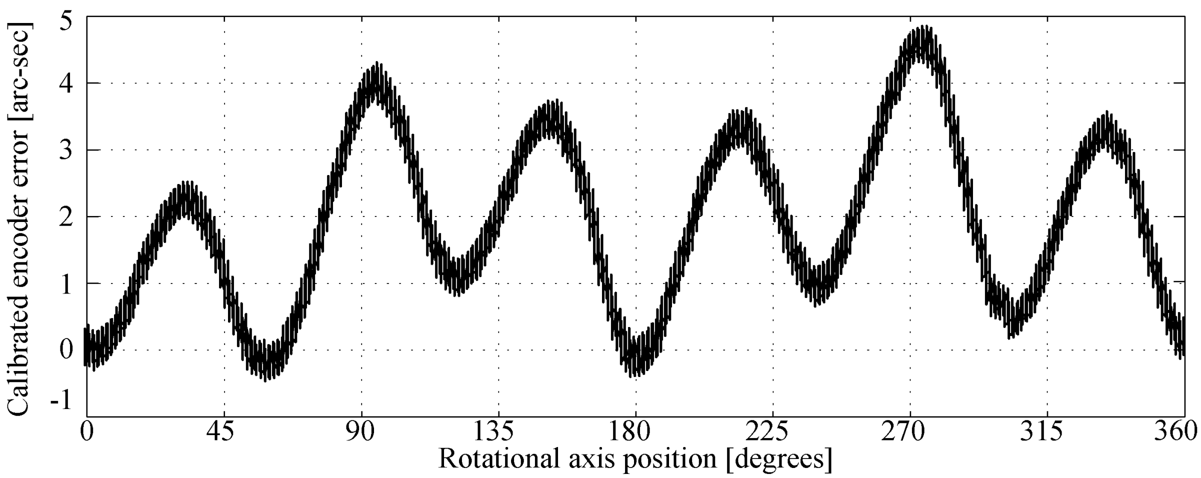

Figure 5.69: Experimentally calibrated error map for circular scale incorrectly installed, supported by shims.

experiments with the mating surfaces of circular scale and scanning unit out of tolerance rather than create large amounts of additional error due to installation with the shims. At a later date the mating surface of the scanning unit will be ground to solve both issues.

Another sensitivity to installation is due to uneven or uncontrolled torque of the bolts securing the circular scale to the spindle rotor. Fastening the bolts with too much torque or in an uneven pattern causes deformation of the circular scale, altering the encoder error map. Figure 5.70 shows an installation with uncontrolled and uneven installation torque on the mounting bolts in comparison to the proper installation technique. The result of proper installation, with a torque wrench and an alternating bolt tightening pattern, is a much smoother encoder error map.

Installation eccentricity is a large determining factor in measurement error (Section 1.2). Initial installation of the circular scale relied on centering measurement with a dial gauge. This method relies on physical contact of the dial gauge with the circular scale and centering on the order of $5\mu m$ was only achieved. As

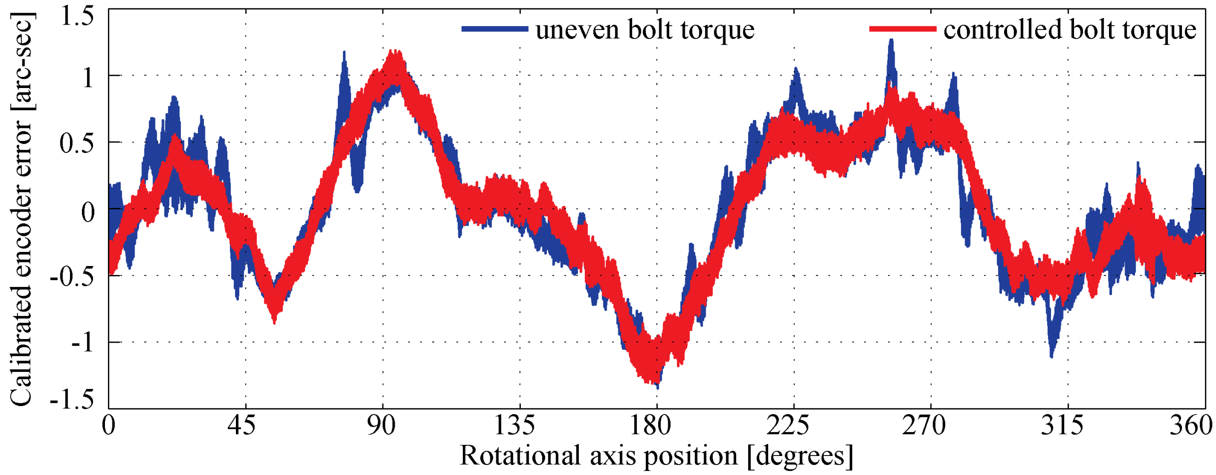

Figure 5.70: Experimentally calibrated error maps for circular scale correctly installed (red) and incorrectly installed with uncontrolled bolt torque (blue).

a result the calibration results show a dominant 1 cpr harmonic on the order of 10 arc-sec, Figure 5.71. To

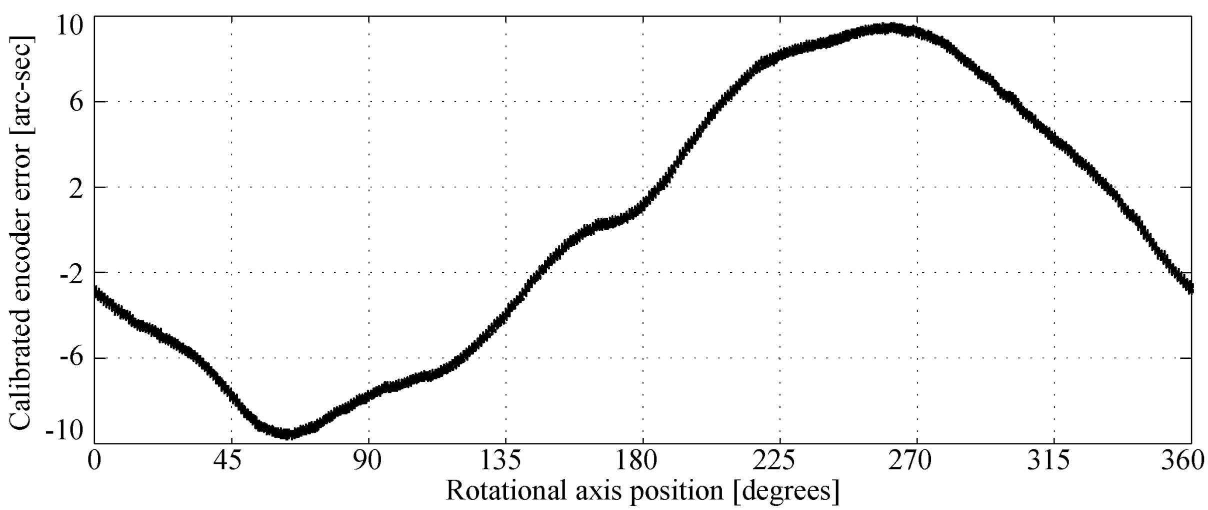

Figure 5.71: Calibration result with large 1cpr harmonic due to $5\mu m$ installation eccentricity.

achieve the best centering results a non-contact, capacitance probe sensor was used. This allowed centering to be done based on a measurement at the exact height of the scanning unit imaging. Centering of $0.3\mu m$ was readily achieved resulting in less than 0.6 arc-sec of encoder error.

Another sensitivity of error map calibration is due to the condition of the circular scale. If not in a clean room environment, dust and foreign particles can affect the imaging method of the encoder causing measurement error. Figure 5.72 shows the result of a dirty circular scale compared to a clean scale. A clean circular scale gives a more accurate measurement.

To obtain an accurate comparison of calibration between installations the circular scale must be mounted securely to the spindle rotor surface, using a torque wrench and alternating pattern for tightening the bolts. To avoid excessive installation eccentricity it is also recommended that a capacitance probe be used for precise centering.

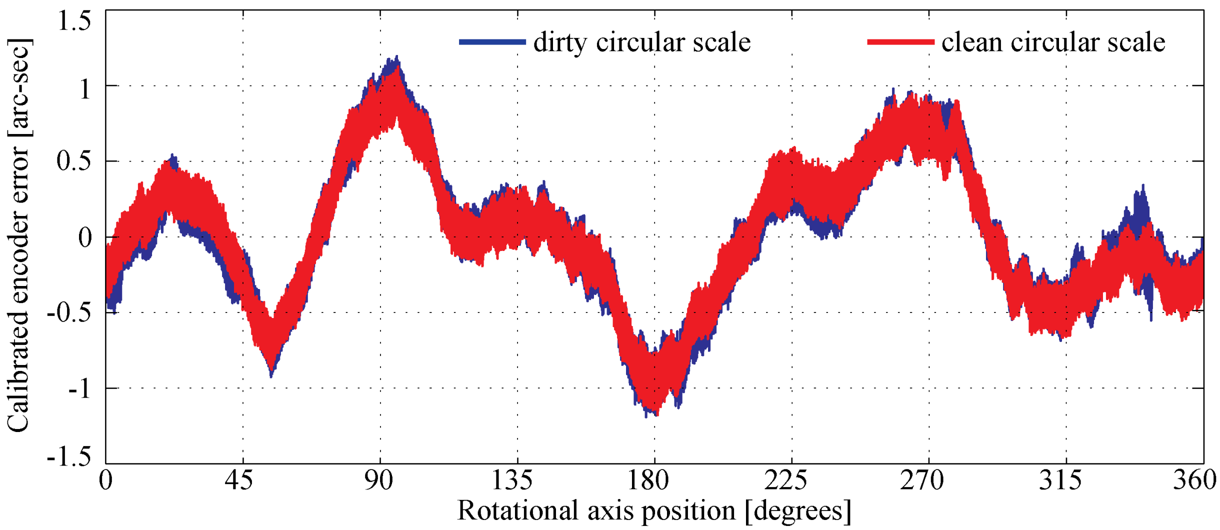

Figure 5.72: Experimentally calibrated error maps for clean circular scale (red, after cleaning) and dirty circular scale (blue, before cleaning).

Chapter 6

Conclusion

This thesis presents the development and experimental testing of an improve Time-Measurement Dynamic Reversal (TDR) calibration method for angle encoders. Uncertainties caused by limited time measurement resolution and an assumption of free-response dynamics are improved upon. This TDR calibration method can quickly calibrate angle measurement errors of the encoder installed on its application axis, providing the complete encoder error harmonics under arbitrary spindle working speeds. The calibrated encoder error map can be used in a lookup table to improve the accuracy of angle measurements, eliminating errors due to installation and alignment of the encoder, radial error motion of the application axis, and errors directly from the encoder such as grating or interpolation errors.

The simulation results show the only limitation on the accuracy of the TDR method is due to the repeatability of the time measurements. The TDR method is not limited in accuracy due to dynamics estimation, rather dominant uncertainties arise in reconstructing the error map from spindle speed compensated time measurements.

The experimental setup, designed by Darya Amin-Shahidi, was optimized to minimize measurement uncertainty. Custom electronics were designed with 1,500 MHz time measurement resolution, multiple filtering stages for encoder signal processing and simultaneous multiple scanning unit signal measurement. These improvements brought the set repeatability of calibration results from 0.033 arc-sec down to 0.014 arc-sec.

The experimental results show accurate and repeatable calibration of angle measurement errors to be within 0.006 to 0.01 arc-sec. The fundamental limitation in achieving more accurate results is due to uncertainties in the encoder angle measurement and not a function of the TDR calibration method. Improved calibration results were obtained by averaging multiple error maps at the same speed and using analog signal averaging. Ambient temperature and pressure fluctuation caused long term uncertainties in the calibration result of 0.03 arc-sec. Removal of the rotary vibration component was verified with calibration results obtained using the EDA method. The methods show agreement within 0.01 arc-sec due to higher, low frequency harmonic uncertainties in the TDR method. Due to a fundamental limitation of the EDA method, the TDR method is 0.3 arc-sec more accurate in calibration of this experimental setup.

6.1 Future Work

Several threads for future work in encoder calibration have emerged from this research.

The fundamental performance limitation of the TDR method has not been identified. Uncertainties in the experimental setup are currently limiting calibration performance. Ideally the experimental setup would be installed in a professional metrology facility with: (a) a clean room environment to guard from dust affecting the imaging of lines on the circular scale (b) ambient temperature control and a dedicated air compressor would prevent large variations in the spindle dynamics and (c) ground floor installation to prevent building harmonics or floor vibrations from transmitting to the setup. The repeatability of angle measurement errors can be improved by investing in more accurate and repeatable, commercially available rotary encoders. A rotary encoder based on the interferential scanning principle could lead to such improvements.

Collaborative research with encoder manufacturers could lead to more efficient rotary encoder designs that are not susceptible to encoder errors or have more repeatable angle measurements. The accuracy of the TDR method and its capability of determining all error map harmonics can be utilized, in working with encoder manufacturers to determine the physical causes of dominant error map harmonics.

This research is not restricted to encoder calibration, as the strength of the TDR method in determining encoder error is based on accurate spindle dynamics estimation. This can be used to characterize the performance of air bearing spindles: damping coefficients, rotary vibration, intrinsic disturbance torque and radial error motion. Theories have been developed but not proven for the existence of air bearing disturbance torque. In addition the cause of constant rotary vibration component, experimentally measured, has not been identified. If the air bearing design can be modified to minimize rotary vibration much more accurate calibration results can be found through encoder signal averaging.

Bibliography

[1] Canon Inc. Laser rotary encoder. http://usa.canon.com/CUSA/assets/app/pdf/encoder/LaserRotaryEncoder.pdf, February 2010. → pages 1, 8

[2] Dr. Johannes Heidenhain GmbH. Angle encoders without integral bearing. http://www.heidenhain.com/fileadmin/pdb/media/img/606_136-22.pdf, September 2007. → pages 7, 8, 51, 68

[3] Dr. Johannes Heidenhain GmbH. Angle encoders with integral bearing. http://www.heidenhain.com/fileadmin/pdb/media/img/591_109-21.pdf, June 2006. → pages 7, 8

[4] Renishaw. Rexm ulta-high accuracy angle encoder. http://resources.renishaw.com/download/(b8b80961ffd4414d877c6205cf35539e). → pages 1, 7

[5] Liang Pan, Yong-Shik Park, Yi Xiong, Erick Ulin-Avila, Li Zeng, Cheng Sun, David B. Bogy, and Xiang Zhang. Flying plasmonic lens at near field for high speed nanolithography. volume 7637, page 763713. SPIE, 2010. → pages 1

[6] Xiaodong Lu and David L. Trumper. Spindle rotary position estimation for fast tool servo trajectory generation. *International Journal of Machine Tools and Manufacture*, 47(9):1362 – 1367, 2007. Selected papers from the 2nd International Conference on High Performance Cutting, 2nd CIRP International Conference on High Performance Cutting. → pages 1

[7] W.T. Estler, Y.H. Queen, and J. Bryan. An advanced angle metrology system. *CIRP Annals - Manufacturing Technology*, 42(1):573 – 576, 1993. → pages 1, 9

[8] T. Masuda and M. Kajitani. An automatic calibration system for angular encoders. *Precision Engineering*, 11(2):95 – 100, 1989. → pages 9, 34

[9] Tsukasa Watanabe, Hiroyuki Fujimoto, Kan Nakayama, Tadashi Masuda, and Makoto Kajitani. Automatic high-precision calibration system for angle encoder. volume 4401, pages 267–274. SPIE, 2001. → pages 10

[10] Tsukasa Watanabe, Hiroyuki Fujimoto, Kan Nakayama, Tadashi Masuda, and Makoto Kajitani. Automatic high-precision calibration system for angle encoder (ii). volume 5190, pages 400–409. SPIE, 2003. → pages 10, 34

[11] R Probst. Self-calibration of divided circles on the basis of a prime factor algorithm. *Measurement Science and Technology*, 19(1):015101, 2008. → pages 10, 34

[12] R Probst, R Wittekopf, M Krause, H Dangschat, and A Ernst. The new ptb angle comparator. *Measurement Science and Technology*, 9(7):1059, 1998. → pages 10

[13] A. Just, M. Krause, R. Probst, H. Bosse, H. Haunerdinger, Ch. Spaeth, G. Metz, and W. Israel. Comparison of angle standards with the aid of a high-resolution angle encoder. *Precision Engineering*, 33(4):530 – 533, 2009. → pages 1, 9, 34

[14] D Amin-Shahidi. Ultra-precise on-axis encoder self-calibration for fast rotary platforms. Master's thesis, The University of British Columbia, 2009. → pages 1, 50, 51, 63

[15] G.E. Moore. Cramming more components onto integrated circuits. *Electronics Magazine*, 38, 1965. → pages 2

[16] International Technology Roadmap for Semiconductors. International technology roadmap for semiconductors 2009 edition - executive summary. Technical report, International Technology Roadmap for Semiconductors, 2009. → pages 2

[17] International Technology Roadmap for Semiconductors. International technology roadmap for semiconductors 2009 edition - lithography. Technical report, International Technology Roadmap for Semiconductors, 2009. → pages 2

[18] Dave Liu Ted Prescop Multibeam Corp., David Lam. E-beam direct write (ebdw) as complementary lithography. http://www.multibeamcorp.com/MultibeamEBDW.pdf. → pages 2

[19] G. de Boer P. Kruit* G.F. ten Berge A.M.C. Houkes R. Jager T. van de Peut J.J.M. Peijster S.W.H.K. Steenbrink T.F. Teepen A.H.V. van Veen B.J. Kampherbeek E. Slot, M.J. Wieland. Mapper: high throughput maskless lithography. volume 6921. SPIE, 2008. → pages

[20] B.J. Kampherbeek, M.J. Wieland, A. van Zuuk, and P. Kruit. An experimental setup to test the mapper electron lithography concept. *Microelectronic Engineering*, 53(1-4):279 – 282, 2000. → pages 2

[21] Physikalisch-Technische Bundesanstalt. The ptb angle comparator: primary standard for angle measurement. http://www.ptb.de/en/org/5/52/523/wmt_mess.htm, August 2001. → pages 10

[22] A. Ernst. European patent 0 440 833 b1. June 1994. → pages 10

[23] Ralf D Geckeler, Andreas Fricke, and Clemens Elster. Calibration of angle encoders using transfer functions. *Measurement Science and Technology*, 17(10):2811, 2006. → pages 10

[24] M. Krause R. Probst. Six nanoradian in 2pi radian: A primary standard for angle measurement. *Proceedings of 2nd euspen International Conference*, pages 326–329, 2001. → pages

[25] R. Probst R. Wittekopf A. Just, M. Krause. Calibration of high-resolution electronic autocollimators against an angle comparator. *Metrologia*, 40:288–294, 2003. → pages 10

[26] T Watanabe1, H Fujimoto, and T Masuda. Self-calibratable rotary encoder. *Journal of Physics: Conference Series*, 13:240–245, 2005. → pages 10, 11, 34

[27] P.A. Orton, J.F. Poliakoff, E. Hatiris, and P.D. Thomas. Automatic self-calibration of an incremental motion encoder. *IEEE Instrumentation and Measurement Technology Conference*, pages 1614–1618. → pages 11

[28] X.-D. Lu and D.L. Trumper. Self-calibration of on-axis rotary encoders. *CIRP Annals - Manufacturing Technology*, 56(1):499 – 504, 2007. → pages 11, 17, 37, 40

[29] Xiaodong Lu, Arash Jamalian, and Richard Graetz. A new method for characterizing axis of rotation radial error motion: Part 2. experimental results. *Precision Engineering*, 35(1):95 – 107, 2011. → pages 24, 40

[30] Xiaodong Lu and Arash Jamalian. A new method for characterizing axis of rotation radial error motion: Part 1. two-dimensional radial error motion theory. *Precision Engineering*, 35(1):73 – 94, 2011. → pages

[31] A Jamalian. A new method for characterizing spindle radial error motion : a two-dimensional point of view. Master's thesis, The University of British Columbia, 2010. → pages 24, 40

[32] High accuracy calibration system for angular encoders. *Journal of Robotics and Mechatronics*, 5:448–452, 1993. → pages 34

[33] K. Smeds and X.-D. Lu. A multirate multiprocessor control platform for high-speed precision motion control. *ASPE Annual General Meeting*, 2010. → pages 50, 63

Appendix A

Simultaneous Scanning Unit Damping Estimation

As discussed in Section 3.3.2 two potential limitations of the TDR calibration method exist: (a) damping estimation and (b) error map reconstruction from time measurements. It was identified through simulation that the second proposed limitation is dominant but some damping estimation inaccuracies exist. The second limitation can only be improved with better marking repeatability and time measurements, which are highly dependent on the experimental setup. It is also seen in simulation, that with more repeatable measurements damping estimation is improved as so the limitation of damping estimation is still not reached. However this has not been investigated in detail or through experiment. There may come a point when damping estimation is the calibration limitation.

Presented is a method for improving damping estimation for use in the TDR calibration technique when multiple scanning units are installed on the setup and when time measurements are made simultaneously. Previously, damping estimation is performed on data from a single scanning unit, Equation 2.26. With multiple scanning units installed on the setup the damping coefficients are treated separately, as if they were on individual spindles. Alternatively, if simultaneous time measurements of multiple scanning units are made, the damping estimation is improved through a least squares fit of data from all the installed scanning units. Equation 2.26 then becomes

$$\underbrace{\begin{bmatrix} int\begin{pmatrix} \mathbf{U_{1,H1}} & \mathbf{V_{1,H1}} & -\mathbf{U_{2,H1}} & -\mathbf{V_{2,H1}} \end{pmatrix} \\ int\begin{pmatrix} \mathbf{U_{1,H2}} & \mathbf{V_{1,H2}} & -\mathbf{U_{2,H2}} & -\mathbf{V_{2,H2}} \end{pmatrix} \\ int\begin{pmatrix} \mathbf{U_{1,H3}} & \mathbf{V_{1,H3}} & -\mathbf{U_{2,H3}} & -\mathbf{V_{2,H3}} \end{pmatrix} \\ int\begin{pmatrix} \mathbf{U_{1,H4}} & \mathbf{V_{1,H4}} & -\mathbf{U_{2,H4}} & -\mathbf{V_{2,H4}} \end{pmatrix} \end{bmatrix}}_{\mathbf{W}} \begin{bmatrix} a_1 \\ b_1 \\ a_2 \\ b_2 \end{bmatrix} = \begin{bmatrix} int\left(\mathbf{m_{1,H1}} - \mathbf{m_{2,H1}}\right) \\ int\left(\mathbf{m_{1,H2}} - \mathbf{m_{2,H2}}\right) \\ int\left(\mathbf{m_{1,H3}} - \mathbf{m_{2,H3}}\right) \\ int\left(\mathbf{m_{1,H4}} - \mathbf{m_{2,H4}}\right) \end{bmatrix}. \tag{A.1}$$

The data from each scanning unit is truncated together and the least squares fit is performed to solve for the damping coefficients

$$\begin{bmatrix} \overline{a_1} \\ \overline{b_1} \\ \overline{a_2} \\ \overline{b_2} \end{bmatrix} = \left(\mathbf{W}^T\mathbf{W}\right)^{-1} \begin{bmatrix} int\left(\mathbf{m_{1,H1}} - \mathbf{m_{2,H1}}\right) \\ int\left(\mathbf{m_{1,H2}} - \mathbf{m_{2,H2}}\right) \\ int\left(\mathbf{m_{1,H3}} - \mathbf{m_{2,H3}}\right) \\ int\left(\mathbf{m_{1,H4}} - \mathbf{m_{2,H4}}\right) \end{bmatrix}. \tag{A.2}$$

Appendix B

Encoder Signal Derivation

Steady State Encoder Response

The steady state component, $x - \frac{1}{f_w}\cos\left(f_w x\right)|_{x_{start}}^{x_{end}}$, contributes a small amount to offset of the encoder signals. Although for this theoretical model the steady state component is identical for both signals any mismatch in the window grating period from that derived in Equation 4.3 can result in differing common mode voltages between encoder signal A and B. This offset misalignment will lead to high frequency encoder error as discussed in Section 4.2.2. For encoder signal A

$$\left[x - \frac{1}{f_w}\cos\left(f_w x\right)\right]\Bigg|_{0\mu m}^{200\mu m} - \left[x - \frac{1}{f_w}\cos\left(f_w x\right)\right]\Bigg|_{400\mu m}^{600\mu m} = \frac{2}{f_w} \tag{B.1}$$

and for encoder signal B

$$\left[x - \frac{1}{f_w}\cos\left(f_w x\right)\right]\Bigg|_{200\mu m}^{400\mu m} - \left[x - \frac{1}{f_w}\cos\left(f_w x\right)\right]\Bigg|_{600\mu m}^{800\mu m} = \frac{2}{f_w}. \tag{B.2}$$

Middle Frequency Component Encoder Response

The component related to the harmonic of the circular scale, $-\frac{1}{f_s}\cos\left(f_s x\right)|_{x_{start}}^{x_{end}}$ and $\frac{1}{f_s}\sin\left(f_s x\right)|_{x_{start}}^{x_{end}}$, cancel between differential signals due to f_s being periodic over the individual photocell period T_p and thus do not contribute to the encoder signal.

Low Frequency Component Encoder Response

The low frequency component $\frac{1}{2(f_s-f_w)}\sin\left[(f_s-f_w)x\right]|_{x_{start}}^{x_{end}}$ and $\frac{1}{2(f_s-f_w)}\cos\left[(f_s-f_w)x\right]|_{x_{start}}^{x_{end}}$ provide the main contributions of magnitude and phase to the encoder signal. For encoder signal A

$$\begin{aligned}
\frac{\cos(N\theta)}{2(f_s-f_w)}\left[\sin\left[(f_s-f_w)x\right]\Big|_{0\mu m}^{200\mu m}-\sin\left[(f_s-f_w)x\right]\Big|_{400\mu m}^{600\mu m}\right]&=\frac{\cos(N\theta)}{(f_s-f_w)}\\
\frac{-\sin(N\theta)}{2(f_s-f_w)}\left[\cos\left[(f_s-f_w)x\right]\Big|_{0\mu m}^{200\mu m}-\cos\left[(f_s-f_w)x\right]\Big|_{400\mu m}^{600\mu m}\right]&=-\frac{\sin(N\theta)}{(f_s-f_w)}
\end{aligned}\tag{B.3}$$

and for encoder signal B

$$\begin{aligned}
\frac{\cos(N\theta)}{2(f_s-f_w)}\left[\sin\left[(f_s-f_w)x\right]\Big|_{200\mu m}^{400\mu m}-\sin\left[(f_s-f_w)x\right]\Big|_{600\mu m}^{800\mu m}\right]&=-\frac{\cos(N\theta)}{(f_s-f_w)}\\
\frac{-\sin(N\theta)}{2(f_s-f_w)}\left[\cos\left[(f_s-f_w)x\right]\Big|_{200\mu m}^{400\mu m}-\cos\left[(f_s-f_w)x\right]\Big|_{600\mu m}^{800\mu m}\right]&=-\frac{\sin(N\theta)}{(f_s-f_w)}.
\end{aligned}\tag{B.4}$$

High Frequency Component Encoder Response

The high frequency component $\frac{1}{2(f_s+f_w)}\sin\left[(f_s+f_w)x\right]|_{x_{start}}^{x_{end}}$ and $\frac{1}{2(f_s+f_w)}\cos\left[(f_s+f_w)x\right]|_{x_{start}}^{x_{end}}$, does no provide a significant contribution to magnitude or phase of the encoder signal but the small relative misalignment between encoder signal A and B will cause encoder error as discussed in Section 4.2.2. This high frequency contributes the following for encoder signal A

$$\begin{aligned}
\frac{\cos(N\theta)}{2(f_s+f_w)}\left[\sin\left[(f_s+f_w)x\right]\Big|_{0\mu m}^{200\mu m}-\sin\left[(f_s+f_w)x\right]\Big|_{400\mu m}^{600\mu m}\right]&=\frac{\cos(N\theta)}{(f_s+f_w)}\\
\frac{-\sin(N\theta)}{2(f_s+f_w)}\left[\cos\left[(f_s+f_w)x\right]\Big|_{0\mu m}^{200\mu m}-\cos\left[(f_s+f_w)x\right]\Big|_{400\mu m}^{600\mu m}\right]&=\frac{\sin(N\theta)}{(f_s+f_w)}
\end{aligned}\tag{B.5}$$

and for encoder signal B

$$\begin{aligned}
\frac{\cos(N\theta)}{2(f_s+f_w)}\left[\sin\left[(f_s+f_w)x\right]\Big|_{200\mu m}^{400\mu m}-\sin\left[(f_s+f_w)x\right]\Big|_{600\mu m}^{800\mu m}\right]&=-\frac{\cos(N\theta)}{(f_s+f_w)}\\
\frac{-\sin(N\theta)}{2(f_s+f_w)}\left[\cos\left[(f_s+f_w)x\right]\Big|_{200\mu m}^{400\mu m}-\cos\left[(f_s+f_w)x\right]\Big|_{600\mu m}^{800\mu m}\right]&=\frac{\sin(N\theta)}{(f_s+f_w)}.
\end{aligned}\tag{B.6}$$

The final encoder signals can be written as follows

$$\begin{aligned}
\text{encoder signal A} &= \frac{2}{f_w} + \cos(N\theta)\left(\frac{1}{fs-fw} + \frac{1}{fs+fw}\right) - \sin(N\theta)\left(\frac{1}{fs-fw} - \frac{1}{fs+fw}\right) \\
&= \frac{2}{f_w} + \cos(N\theta)\left(\frac{2f_s}{f_s^2-f_w^2}\right) - \sin(N\theta)\left(\frac{2f_w}{f_s^2-f_w^2}\right) \\
\text{encoder signal B} &= \frac{2}{f_w} - \cos(N\theta)\left(\frac{1}{fs-fw} + \frac{1}{fs+fw}\right) - \sin(N\theta)\left(\frac{1}{fs-fw} - \frac{1}{fs+fw}\right) \\
&= \frac{2}{f_w} - \cos(N\theta)\left(\frac{2f_s}{f_s^2-f_w^2}\right) - \sin(N\theta)\left(\frac{2f_w}{f_s^2-f_w^2}\right) \qquad \text{(B.7)}
\end{aligned}$$

The harmonics with differing amplitudes but identical frequencies can be added as follows,

$$\begin{aligned}
\text{encoder signal A} &= \frac{2}{f_w} + M_A \sin(N\theta + \phi_A) = 6.2 - 180\sin(N\theta - 45.73^\circ) \\
\text{encoder signal B} &= \frac{2}{f_w} + M_B \sin(N\theta + \phi_B) = 6.2 - 180\sin(N\theta + 45.73^\circ) \qquad \text{(B.8)}
\end{aligned}$$

where M_A and M_B the amplitude of the encoder signals is $-\frac{2\sqrt{f_s^2+f_w^2}}{f_s^2-f_w^2}$ and the phase of the encoder signals $\phi_A = -\tan^{-1}\frac{f_s}{f_w}$ and $\phi_B = \tan^{-1}\frac{f_s}{f_w}$.